Development of a low cost method to estimate the seismic signature of a geothermal field from ambient seismic noise analysis

Final Report

Institution:

University of Nevada, Reno

Principal Investigator:

Ileana M. Tibuleac

Contact information:

Nevada Seismological Laboratory, University of Nevada, Reno, 1664 N. Virginia St., MS 174, 89557, Tel. 775-784-6256, ileana@seismo.unr.edu

Project team:

David von Seggern, Nevada Seismological Laboratory, University of Nevada, Reno;

David Shaw, Nevada Seismological Laboratory, University of Nevada, Reno;

Holly McLahlan, Nevada Bureau of Mines and Geology, University of Nevada, Reno, NV 89557

Dr James Faulds, Director, Nevada Bureau of Mines and Geology, University of Nevada, Reno, NV 89557;

Consultant:

Joe Iovenitti, Geologica

Subcontractor:

Dr. Satish Pullammanappallil, Optim Inc., 200 S. Virginia Street, Suite 560 Reno, NV, 89

Collaborators:

Dr Fletcher H. Ibser, University of California at Berkeley

Mr. Monte Morrison, VP, Exploration and Chief Geologist, Magma Energy Corp., 5355 Kietzke Lane, Ste 100, Reno, NV 89511.

1. EXECUTIVE SUMMARY

A new, cost effective and non-invasive exploration method using ambient seismic noise has been tested at Soda Lake, NV, with promising results.

The material included in this report demonstrates that, with the advantage of initial S-velocity models estimated from ambient noise surface waves, the seismic reflection survey, although with lower resolution, reproduces the results of the active survey when the ambient seismic noise is not contaminated by strong cultural noise. Ambient noise resolution is less at depth (below 1000m) compared to the active survey. In general, the results are promising and useful information can be recovered from ambient seismic noise, including dipping features and fault locations.

Processing method tests are shown which have potential to improve the virtual reflection survey results. With the improvements made here and the introduction of certain novel methods, we argue for improved results in a site with less cultural noise, with a survey configuration adapted to the field-conditions and with a mixed set of high frequency, short period and broad-band instruments.

In addition to the 2D shear velocity models along Line 2, a 3D shear wave velocity model has been obtained in the Soda Lake study area using surface waves extracted from ambient seismic noise deeper than the depth of a typical reflection survey. Through innovative signal processing techniques, periods not typically analyzed with high frequency sensors were used in this study to obtain seismic velocity model information to a depth of 1.4km.

New seismic parameters such as Green's Function reflection component lateral variations, waveform entropy, stochastic parameters (Correlation Length and Hurst number) and spectral frequency content extracted from active and passive surveys have potential to indicate geothermal favorability through their correlation with high temperature anomalies, and are potential indicators of faults, thus reducing the uncertainty in fault identification. Attenuation for surface waves has not been estimated because of time constraints, however, P-wave attenuation results were not promising, for neither active and nor ambient noise survey data.

Qualitative and quantitative (geostatistics) correlations have been made between the seismic results and available gravity, magnetotelluric, and temperature data. Qualitatively, *Vs was* found to correlate with the high temperature and gravity anomalies at a depth of 0.3km; *Vp/Vs* was also correlated with the high temperature anomaly at 0.3km and a low *Vp/Vs* ratio was correlated with the steam cap present in the field; Power Spectral Density correlated with faulting identified by Magma (2011); Entropy correlated with faulting identified by both Optim (2015) and Magma (2011); Correlation Length and Hurst No. were also found to correlate with faulting. Fair to excellent quantitative relationships between the seismic parameters investigated and temperature, temperature residuals, lithology and faults were also identified by using all data along ambient seismic line 2 and using the only the well data locations along this line.

Favorability maps along ambient seismic line 2 were generated considering temperature, lithology and the seismic parameters investigated in this study. Pseudo-favorability maps were also generated using only the seismic parameters analyzed in this study.

A number of issues have been identified and solutions are proposed to solve (1) The need to speed up the computations by using parallel computer processing; (2) The need to identify processing methods such that the same results are obtained using less recording time than 20 days; (3) The need to use alternative waveform processing for extraction of P waves, as discussed in the text; (4) The need for innovative deployments for cultural noise reduction and for an ambient noise frequency band which includes enhanced amplitudes at periods lower than 5Hz; and (5) The need for preliminary studies of the ambient noise for optimal field deployments and results.

TABLE OF CONTENTS

LIST OF APPENDICES[1]

2 PROJECT OBJECTIVES AND PURPOSE

The primary objective of the proposed research is cost-effective characterization of geothermal reservoir properties from which drilling targets will be identified. To accomplish this objective, we:

1. Develop, test and calibrate a non-invasive and cost-effective seismic exploration method based on ambient-seismic noise analysis.
2. Investigated new, additional seismic parameters characteristic to geothermal reservoirs.
3. Used statistical methods to integrate new seismic information with other geophysical data in order to minimize the uncertainty and non-uniqueness associated with the drilling.

The project outcomes/deliverables are:

1. Testing and evaluation of a novel seismic exploration method based on analysis of body-waves and surface-waves extracted from ambient seismic noise. Specifically, we test whether the information provided by ambient noise seismic surveys has similar resolution, and favorability prediction power as the active survey information.
2. Development of a cost-effective technique, consisting of statistical integration of inexpensive seismic analysis techniques with other geological and geophysical data. Specifically, it is assessed whether preliminary, cost effective ambient noise surveys in conjunction with additional seismic parameters and other geophysical parameters indicate favorability areas that could be potentially explored in detail by active surveys.
3. An assessment of whether or not this new technique allows reliable geothermal reservoir characterization. Specifically, ambient seismic noise survey seismic parameters such as P/S velocity, stochastic parameters, attenuation, entropy and spectral properties are tested as geothermal favorability and fault indicators. Geo-statistical correlations are discussed.
4. Estimation of a drilling favorability map at Soda Lake, Nevada along Line 2.
5. Recommendations for further improvement of method cost-effectiveness, resolution and transportability.

Each of these project deliverables is discussed in detail in the text below and summarized in Section 6.

The purpose of our project is to "to develop and validate cost-competitive technologies and tools to accelerate the growth of geothermal energy in the United States", which is an objective of the US Department of Energy (DOE) Geothermal Technologies Program. Together with two industry partners, the University of Nevada Reno (UNR) developed an innovative and cost effective seismic exploration method to reduce "the high cost and risk of geothermal exploration and drilling" and "the cost of all geothermal energy so that it is competitive with conventional sources of electricity". Within the Geothermal Technologies Program, our project directly answered the Geophysical Exploration Technologies objectives: "advance exploration technologies to better locate potential geothermal resources that lack surface manifestations, thereby improving resource discovery" through development of "geophysical surveying tools, techniques and processing not previously utilized in geothermal exploration or only to a limited extent" and through "Improved data interpretation to minimize ambiguous geophysical signals."

3. TECHNICAL BARRIERS AND TARGETS

To date, no cost effective method had been developed to estimate compressional (*P)*, shear (*S*) velocity (*Vp and Vs,* respectively) models and buried fault location, which provide essential information in geothermal exploration. Because hydrothermal production relies on open fracture networks, highly localized geophysical information is critical for well location as well as for identification of the fracture network. Although active source reflection seismic experiments provide high resolution *Vp* models and direct information on the resource availability, widespread use is cost-prohibitive and must be used selectively, which is difficult when no background seismic information is available in the area. Thus,

developing an inexpensive seismic exploration method and identifying new seismic parameters (attenuation, spectral and stochastic properties, entropy) to be used for geothermal reservoir characterization is important for reducing geothermal exploration technology costs. Addition of *Vs* models to the *Vp* models is important, because studies of the *Vp* relative to *Vs* at the same location have the potential to provide supplementary information necessary to locate and drill productive wells. In addition, variations in Vs are larger, and thus easier to measure than variations in Vp in anomalous regions. To date, no widely accepted, technically feasible and cost-effective method for high-resolution *Vs* model estimation has been developed.

The UNR, Optim Inc. and Joe Iovenitti, an independent consultant, developed from 2012 to 2015 a new, non-invasive and cost-effective seismic velocity model estimation method, based on ambient noise analysis, which provides *Vp* and *Vs* models with a resolution of tens to hundreds of m^2, to a depth of at least 1km.

Out targets were:

A. Test whether the information provided by ambient noise seismic surveys can provide valuable preliminary information to be used in active survey investigations;
B. Test whether the method is promising for fault identification and geothermal reservoir characterization;
C. Test whether the ambient noise survey had similar resolution as the active survey information;
D. Statistically evaluate seismic geothermal favorability attributes such as attenuation, waveform spectral content, entropy and media stochastic properties, and compare to similar attributes for active source;
E. Develop a favorability map based on ambient noise and active source seismic attributes;
F. Make recommendations for further improvement of method usage, cost-effectiveness, resolution and transportability.

The study area is a relatively well-characterized geothermal resource at Soda Lake (SL), at Fallon, Nevada (Appendices 2-6), where evaluation and calibration of the new exploration method is possible. Extensive geological studies have been performed to date in the study area to characterize potential and existing hydrothermal resources, however, these studies did not provide a *Vs* model at a useful resolution. A *Vs* model is useful in a geothermal area because (as shown in Section 4): 1) Can be used as a starting model for an ambient noise seismic reflection survey when no Vp model is available in the area; 2) Can be used to identify anomalous areas, Vs model gradients appear to occur at the transition between areas with different geophysical properties and in the vicinity of faults (AltaRock, 2014b) and are stronger than Vp-gradients; 3) By comparison to the *Vp* models, it can provide information on geothermal favorability through *Vp/Vs* maps. In addition, *Vs* is much more sensitive than *Vp* to anomalies on the ray path and this is generally valid for Vs seismic attributes discussed in this study.

Barriers, Original hypotheses and Project Impact from departure from originally proposed technology

The initial hypothesis was that the ambient seismic noise and signal in a geothermal area were suitable for subsurface imaging using seismic interferometry. As shown in Section 5 below, we found that this hypothesis was valid in non-developed areas (geothermal field areas without much surface piping and plant facilities), however, when using this method in an area already developed for geothermal production (i.e. power plant), cultural noise was a challenge specifically for high-frequency phase identification and estimation of Vp models.

Another hypothesis was that ambient noise seismic reflection surveys, together with supplementary seismic parameter information and other geophysical information, can reduce the costs of an active seismic survey by narrowing down the scope of the active surveys to areas of enhanced geothermal favorability. Below we present arguments for the assessment that the results of this project support this hypothesis. Although unforeseen challenges occurred, as listed in Section 5, there was no significant departure from the originally proposed technology, and the method was adapted to newly established requirements, improving the results. Section 7 summarizes recommendations made throughout the report for further improvements of the method and highlights new research questions. A minor modification of the project plan

was not using the SL data recorded in 2010 to estimate the low-resolution Vs model, because the data was recorded for only two days. We estimate that this decision did not have any significant impact on the low-resolution Vs model. Although preliminary investigations show promising results, further investigations are necessary to improve the cost-effectiveness of the method by using reduced recording time and improving processing methods, as discussed in Section 5.

In the next sections, we discuss, address and propose solutions to overcome the following barriers:

A. Through Green's Function (GF) summation, the ambient noise virtual shot gathers are low-pass filtered and thus, lower frequency (8-20 Hz vs 50-100 Hz), than active survey shot gathers. Thus, the resolution of the seismic noise analysis is lower than the active survey resolution. We found that, however, additional seismic indicators can partially compensate for this problem, and we expect that additional data processing (Draganov et al, 2013, Appendix 4) has the potential to improve the results.
B. Using ambient noise some fault zones can be identified better than others, however, variations of the stochastic heterogeneity parameters, and of entropy and spectral energy may be useful indicators of faults zones. We proposed improved resolution Vs models for fault identification. Modifications of the technique are necessary to account for dipping faults, and to refine fault locations.
C. Data processing time length was the most important drawback in this study, due to high sample rates and because only one server has been used. We recommend parallelization of the codes.
D. P-arrival detection is not trivial, however, new algorithms are proposed here to extract useful P-arrivals (See Section 3.2).
E. Although remarkable results have been obtained extracting longer period (1-2s) from high frequency (5 Hz corner frequency) sensors, we recommend deployment of mixed sensor arrays to improve the long period GF extraction. The algorithms developed at UNR allow for processing data from multiple types of sensors (Tibuleac et al., 2011).

4. TECHNICAL APPROACH

We have organized our study into six-tasks.

Task 1. Permitting and environmental documentation

Permitting and environmental documentation were started in March 2013 and completed in November 2012. These activities included obtaining land usage approval from public and private land owners. The planned deployment was modified to accommodate the permitted locations, as shown in Appendix 1 and Figure 1. Appendix 1—Section A was submitted to, and approved by the US Bureau of Land Management (BLM). Appendix 1— B was a document submitted to the Department of Energy (DOE), showing the seismic deployment as permitted and discussing permitting issues, including private land approved access. Pending sponsor approval, this report will also be sent to all our collaborators and landowners who grated experiment permissions.

1.1 Study area

The study area (Figure 1A) is a relatively well-characterized geothermal resource in Fallon, Nevada, where evaluation and calibration of the new exploration method is possible (Tibuleac and Eneva, 2011, also shown in Appendix 2A) and active power is generated. SL is one of many geothermal systems hosted in the extensional Basin and Range Province, Nevada. This geothermal field is located about 100 km east of Reno and 10 km northwest of Fallon, along the Carson River Route of the Old California Trail. Soda was mined from SL in the middle to late 19th century. There might have been a hot spring discharging at that time as well (Hill et al., 1979). SL was identified as a geothermal resource in 1903 while drilling for a water well, which reached boiling water at depth of 18 m. This well was still emitting hot steam in 1974, while shallow subsurface boiling was indicated by alteration of Quaternary sediments to kaolinite and various iron oxides or hydroxides (Olmsted et al., 1975). The extent of the thermal anomaly in the shallow subsurface has been outlined by the drilling of temperature-gradient holes by the U.S. Geological Survey and the U.S. Bureau of Reclamation, as well as continued drilling of production, injection and monitoring wells by the Chevron Resources Company and Phillips Petroleum. The hottest parts of the SL thermal anomaly probably coincide with intersection of faults trending north-northeast and northwest. These faults provide steeply inclined conduits for thermal fluids that may be rising from depths of 3km to 7km (Olmsted et al., 1975). Although faults exposed on the surface are rare, some faults at depth were suggested, possibly along a rupture zone in the Tertiary or pre-Tertiary consolidated rocks. Faults exposed on the surface are inferred from silicified sediments and some faults at depth were suggested, possibly along a rupture zone in the Tertiary or pre-Tertiary consolidated rocks (Olmsted et al., 1975).

Magma (2011) reported on a comprehensive 3D geophysical model of the geothermal field using geological maps, locations and depths of wells, mud-logging and drilling data, temperature surveys, geophysical logs, LiDAR, resistivity, magnetic anomalies, microgravity, old seismic studies, existing well and precision gravity data. This collection of data has been interpreted, however, without application of a robust statistical analysis. One result of these investigations was the discovery of a steam cap (Appendix 2, Van Gundy et al., 2010). The location of the steam cap was associated with an Interferometric Synthetic Aperture Radar using Satellite Imagery (InSAR) low (Appendix2—Figure A2-3) indicating the area of largest subsidence. The InSAR anomaly marks the hottest and shallowest part of the geothermal field. The elevated temperatures actually cover an area with a diameter 4 to 5 times larger than that of the outer InSAR contour shown in Appendix2—Figure A2-3. Applying three dimensional - three component (3C) active source reflection seismic techniques to this data, to define transmisive geothermal structures at SL, has encountered difficulties (Echols, 2011). A method aiming to resolve the subsurface structure using P-to-S conversions at reflecting layers is under investigation, however, preliminary results were not encouraging (Echols et al., 2011).

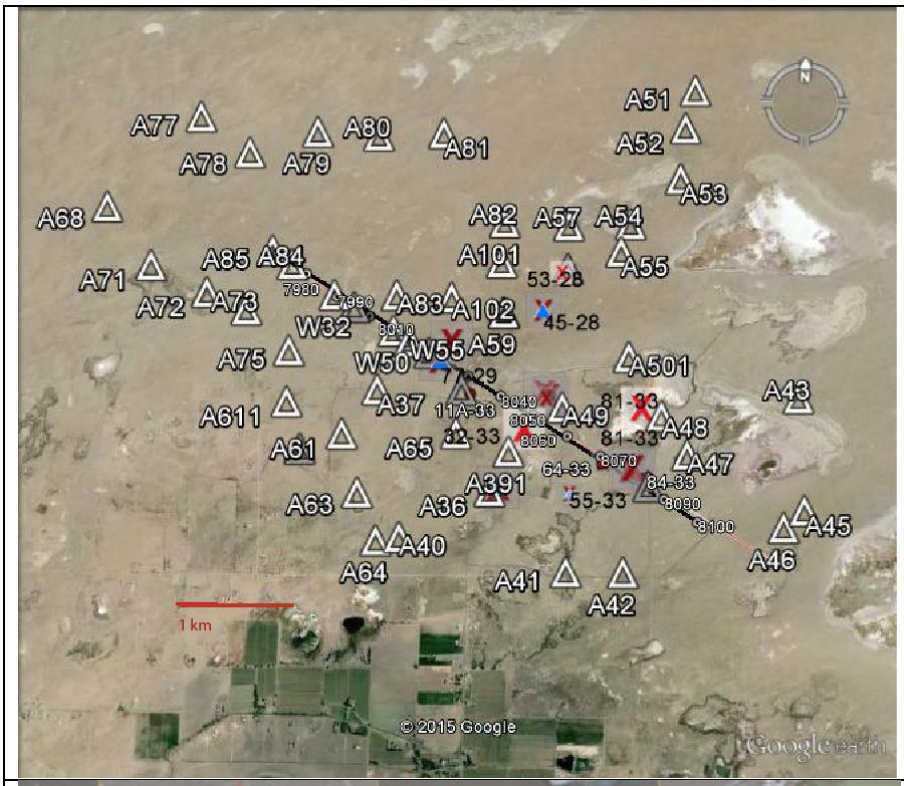

Figure 1A. Shows the map of the new passive ambient seismic deployment at Soda Lake, Fallon, NV. Triangles show array stations, and the black line shows the location of the ambient seismic noise 128 reflection survey stations. The inter-station distance was 34 meters. Proximal well locations to the ambient seismic line are shown as crosses, and the numbers along Line 2 show the Magma (2011) survey sensor numbers. The blue triangles show active wells. Note that 45-28 was active in 2010, until it corroded by steam production (SL personnel, 2012, personal communication).

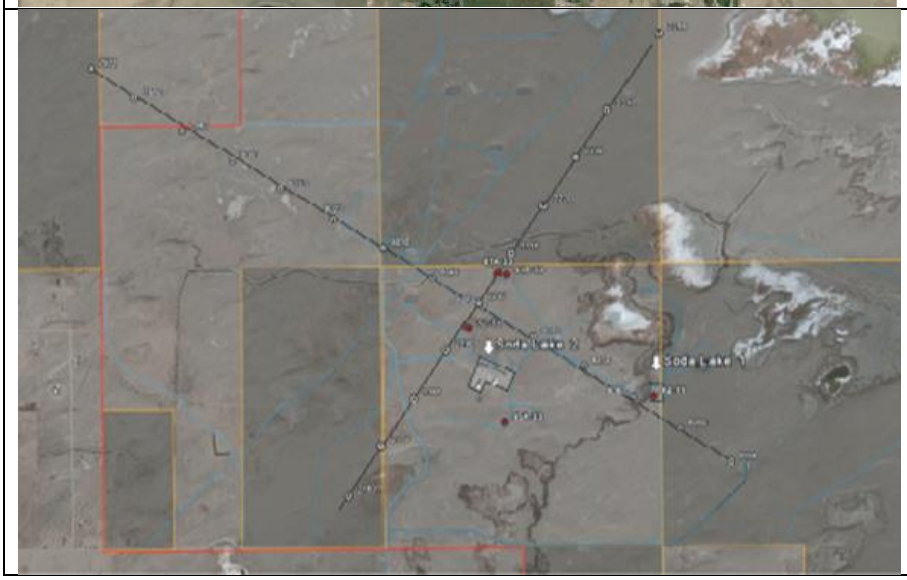

Figure 1B shows the 2010 active source test lines (black) as reported by Echols, (2011). Our ambient seismic noise deployment was at the same location as the Line 2 (black line trending northwest-southeast). This location was suggested by Mr. James Echols (formerly of Magma), as a location where faults were interpreted and where the active survey had inconclusive S-arrival results, specifically near the power plant (southeast portion of Line 2 (James Echols, personal communication).

We are using a new, independent method to estimate 2D P- and S-velocity models and to investigate the capability for fault identification along a 2D reflection profile. Our method has been tested at Pyramid Lake, NV (Tibuleac et al., 2010, Appendix 2B) and at Soda Lake in March 2010 (Tibuleac and Eneva, 2011, Appendix 2A). In SL, 1.3km2, 100m spaced high - frequency vertical geophone survey, conducted in March 2010 (Appendix 2), recorded ambient seismic noise (and available earthquake waveforms) for 3 days (Appendix 2A—Figure A2-3). This type of seismic survey aimed to resolve lateral seismic parameter variations at a resolution of approximately 100m. The deployment covered an area where depressurization of a shallow aquifer created a steam cap at SL. The array recorded ambient seismic noise (and small earthquake waveforms) for two days. The survey was aimed at resolving lateral seismic parameter variations at a resolution of approximately 100m. Although this preliminary demonstration of the method had encouraging results (Appendix 2), the survey was limited in time and space, and only sampled a subsurface region up to ~ 150m in depth. As shown in Appendix 2, applying cross correlation to ambient noise data recorded at pairs of sensors, and stacking the

results over the whole period of time, inter-station GFs were generated, with Rayleigh waves as dominant arrivals. The fundamental Rayleigh wave velocity (between 1-5Hz) was higher at pairs of stations in a transect outside a steam cap than at inter-station paths inside the anomaly. More scattering (complex GFs) has also been observed for paths crossing the steam cap discussed above.

1.2 Ambient noise deployment configuration and logistics

Unique, ambient seismic noise waveforms were collected, of unprecedented continuous recording duration (21 days as opposed to minutes-3 days), at the same location with an active survey. The seismic stations were provided by the Incorporated Research Institutions for Seismology (IRIS) Program for Array Seismic Studies of the Continental Lithosphere (PASSCAL) Instrument Center. With the goal to improve seismic velocity model resolution, in contrast with our previous surveys at a 100 samples per second (sps) sample rate, more than one terabyte of data were collected at 500sps during this survey along Line 2 at the L28 sensors, and at 250 sps at the high frequency geophones, as discussed in Chapter 5. It is our experience that a higher sample rate increases the accuracy of the GFs, because it increases the ambient noise bandwidth. Thus, although using 500sps (250Hz Nyquist frequency, ie 0-250 Hz frequency band) is best, it is shown below that the high end of the useable frequency band for the extracted GFs was 25Hz in this study, due to large cultural noise at 30Hz and 60Hz. When cultural noise is not present, we estimate that the useable frequency band is potentially higher, however, not much higher than 60Hz.

Continuous data was collected during a 1.3 month passive seismic survey at SL. The deployment, from October 20 2012 to December 1 2012, included two campaigns. The first campaign was of 21 days. The sensors were deployed in a line (referred to as Line 2) with 100ft inter-station distance (black line in Figure 1A, Appendix 3—Table A3-1) at the same locations as the locations on a 2010 Magma active seismic line reported by Magma (2011), the northwest-southeast line in Figure 1B. The second campaign consisted of 10 days of passive recording with the sensors deployed as an array, roughly at 600m inter-station distance (triangles in Figure 1A). Note that some of the sensors on the Line 2 (triangles in Figure 1A) recorded during both campaigns. The decision to deploy in two campaigns was a result of limited availability of this type of sensor from IRIS-PASCAL.

The deployment, with the line of sensors (Line 2) included:

30 Vertical 4.5Hz geophones with "Texan" digitizers at the northwest end of the line recording at 250sps. New “Texan” digitizers were switched with the ones in the field every three days for 21 days. The sample rate was chosen to meet digitizer memory constraints, and allow optimal storage during the 3-4 days recording time of each “Texan”.

96 three-component (3C) L28 sensors (4.5Hz) with Reftek RT130 dataloggers, which recorded continuously at 500 sps, being equipped with solar panels and 12.8 V batteries (Appendix 1A).

The seismic array (the array) included only L28 3C sensors and recorded for 10 days (second campaign). In this campaign, every fifth sensor (“W” station) on the Line 2 starting with W32 was left in place, while all the other sensors were moved to “A” locations or completely removed (Appendix 3—Table A3-2).

1.3 Method

Existing and newly acquired seismic survey data was used to test and validate a cost-effective, non-invasive, seismic exploration method (Figure 2), based on seismic interferometry (Campillo and Paul, 2003; Halliday and Curtis, 2008; Stehli et al., 2008; Gouedard et al., 2008). Seismic interferometry is a relatively new technique in seismology (Campillo and Paul, 2003) which is currently successfully applied to reflection surveys (Draganov et al., 2007, 2009, 2013; Irie and Brown, 2010). This technique is based on the theoretical result which states that, if A and B are two passive sensors (seismic sensors), the GF, or the signal that B would receive when A is given an impulsive excitation, can be recovered from the temporal cross-correlation of noise received at A and B. The impulse response or GF, with surface waves as the largest features is retrieved from crosscorrelation stacks of ambient seismic noise, at arrays or lines of sensors. This new

seismic exploration method (Tibuleac et al., 2010, 2011, 2012 and studies in Appendix 2) has had promising results when used for fault definition and P and S -velocity model estimation.

GFs are extracted from stacks of ambient noise and signal crosscorrelations and autocorrelations from pairs of sensors and at the same sensor. Data was processed using ambient seismic noise and signal autocorrelation and crosscorrelation algorithms in a package of optimized analysis codes (Tibuleac et al, 2011; Tibuleac and von Seggern, 2012). Algorithms for extracting ambient noise-derived GFs have been developed and are used at the Nevada Seismological Laboratory (NSL), Tibuleac et al. (2011), to derive P and S velocity models (i.e., Vp and Vs models) in the Reno Basin, for inter-station distance from 0.5km to 60km, for different sensor-types and to estimate the P/S reflection component of the GFs extracted from waveform autocorrelations (Tibuleac et al, 2012). The algorithms are using spectral whitening and sign-bit normalization.

As shown below, not only the surface wave portion of the GF could be retrieved from inter-station ambient noise cross-correlation, but also body-wave reflections (primaries as well as multiples) from layer interfaces (Draganov et al., 2009). Continuous waveform auto-correlation weres used to image the individual station substructure by extracting the GF reflection component at each station. Claerbout (1968) showed that for a horizontally layered medium the auto-correlation of the transmission response of a seismic noise source in the subsurface yields the reflection response. The ambient-noise autocorrelation at each station was interpreted as the collocated source–receiver elastic wave GF (i.e., the Earth's reflection response) and is used to distinguish reflecting layers beneath each station. Changes in the GFs along Line 2 were investigated in association to known faults. The GF P-reflection component resulted from Line 2 and array autocorrelations was compared to waveform modeling and used for an independent verification of the Vp model.

By applying cross-correlation to ambient noise data recorded at pairs of closely spaced (34 meters) seismic sensors along reflection lines, and stacking the results over a period of time, we generated virtual shot gathers as if one of the sensors was generating seismic waves, i.e., we retrieved the earth's reflection response (Draganov et al., 2009). Geothermal reservoir seismic spectral, stochastic and attenuation characteristics were estimated and statistically evaluated searching for the benefit for geothermal exploration of integration seismic and other geophysical results near SL. The virtual reflection survey was interpreted and compared to the active reflection survey. Because the initial velocity model is crucial in any inversion, before interpretation, information was extracted from the ambient seismic noise survey using array processing techniques (frequency – wavenumber or fk analysis) for P and fundamental mode Rayleigh phase velocity, and a set of programs named CPS3.0 (Herrmann and Ammon, 2002) for fundamental mode Rayleigh group velocity analysis.

The GF P-phases, surface wave and P reflection components were analyzed and discussed below.

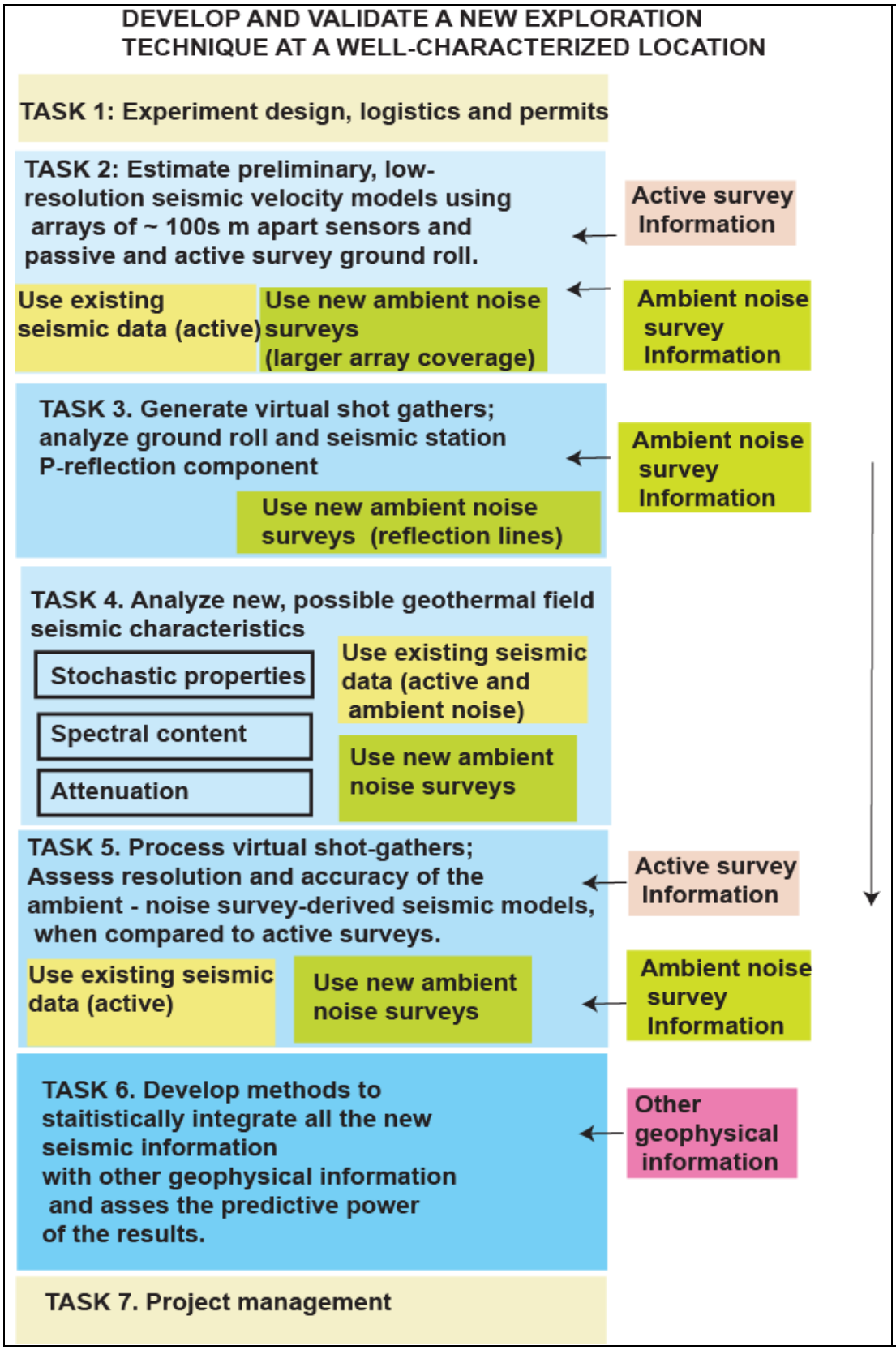

Figure 2. Project task flow-chart

Task 2. Ambient noise preliminary P/S-wave velocity models of the study area

The reason for this first investigation is to obtain an accurate preliminary velocity model, to be used as initial/input model with the reflection survey. This is a step essential for seismic survey interpretation. The lack of preliminary Vs models has proved to be a problem for the recent geothermal exploration studies in the SL area. A preliminary Vs model estimated using 6 km aperture seismic array and seismic interferometry will be compared in Section 6 with the geophysical measurements of the geothermal reservoir, to show that it has the potential to provide cost-effective preliminary information in the study area.

This task is organized as two subtasks:

1. Low resolution P/S seismic velocity model estimation from integration of a baseline seismic velocity model and models estimated from records of a 2D ambient noise seismic array;
2. Assessment of previous active survey usefulness for extracting a preliminary Vs model.

2.1 Ambient – noise preliminary S seismic velocity model estimation (SL_INITIAL MODEL_ARRAY)

A preliminary Vs model, SL_INITIAL MODEL_ARRAY, was estimated as a median of a model extracted using the ambient-noise seismic array records and a baseline seismic velocity model. The two models estimated using array data were obtained 1) by inversion of the fundamental Rayleigh (FR) wave group velocity (SL_GVEL_MOD discussed in Section 2.1.1) and 2) from fundamental Rayleigh phase velocity (SL_PHVEL_MOD discussed in Section 2.1.2) dispersion curves. This is the first estimate of a *Vs* velocity model using surface waves in the area, at best resolution of ~0.25km^2 with depth resolution of 0.2km, to a depth of 1.5km. A successful outcome of this experiment was extraction of periods of 1-2s using 5Hz corner frequency sensors. This was achieved by modification of the instrument response to simulate a broadband sensor.

2.1.1 The baseline P-velocity model SL_BP_MODEL

An initial, publicly available *Vp* model, was the best information in the upper 2.2km from an active survey study by Echols (2011). The model is referred to as ME in Table 1. Initial *Vs* velocities were estimated from *Vp* using a *Vp/Vs* ratio of 1.73 (i.e., for Poisson ratio 0.25). This initial model (ME) was the basis for an adjusted model, shown in Table 1 (SL Lake Model, or SLM). SLM was adjusted for the best fit of the data described in Section 2.1.2, and was the input model in Sections 2.1.2 to 2.1.3.

The ambient noise Vs models estimated using array data

New seismic data from the passive, 67 three-component geophone array (stations A31-A82 in Figure 1) was used to estimate *preliminary, lower resolution (~100m-500 m)* 3D *Vs* models. The models were estimated by inverting the dispersion curves of the fundamental model Rayleigh component of the GFs, which usually is the largest phase (ground roll), usually discarded in active surveys. The GFs were extracted from beams of continuous waveform crosscorrelations. The reflection component of the GFs was extracted from seismic noise autocorrelation beams.

**2.1.2. SL_GVEL_MOD Ambient Noise: ** The GFs extracted between 760 pairs of array stations (Figure 3) are shown in Figure 4. An approximate 0.25km^2 resolution S velocity model has been estimated using highest signal-to-noise ratio (SNR) inter-station GFs extracted in the SL project area. Using the CPS3.3 (Herrmann and Ammon, 2002) program do_mft, fundamental Rayleigh group velocity dispersion curves were manually picked. Using the CPS3.3 program surf96 the curves were inverted for shear wave velocity models. To estimate a group velocity model in each grid cell of the study area a the code named *gridsp was used* (Dr. Hafidh Ghalib, personal communication). *gridsp* used stochastic inversion, following a method by Feng and Teng (1983). The propagations paths were assumed to be straight rays. The fundamental mode Rayleigh group velocity maps are shown in Figure 5. The surface of the SL study area was partitioned into a grid with elements 0.005˚ (0.5km) on one side. A dispersion curve has been estimated for each of the 130 total grid elements in the SL. The inverted group velocity curves included only wavelengths less than half the interstation distance. The starting model was SLM for each grid cell. The results greatly depend on the starting model, and the best

starting model was estimated as a variation (through trial and error) of the ME Vs model. The goal was to obtain minimal difference between the observed and calculated dispersion curves. Another goal was to use the same SLM input model for the whole area, which was considered a best approach when assessing differences in the velocity model across grid cells.

Table 1. ME is the Vp model extracted from Echols (2011). SLM is the mean *Vp* and *Vs* extracted from the dispersion curves in Soda Lake (see text for an explanation) and the starting model for Soda Lake *Vs* inversion. SL_ACOR_MOD, was the model used to generate a synthetic reflection waveform in Figure 15.

ME				**SLM**				**Synthetic waveform empirical model: SL_ACOR_MOD**			
Layer Thickness	*Vp*	*Vs*	Rho (	Layer Thickness	*Vp*	*Vs*	Rho	Layer Thickness	*Vp*	*Vs*	*Rho*
(km)	*(km/s)*		*(g/cm³)*	*(km)*	*(km/s)*		*(g/cm³)*	*(km)*	*(km/s)*		*(g/cm³)*
0.2	*1.3*	0.75	2	0.1	1.3	0.7	2	0.2	1.5	0.7	2
0.05	1.647	0.95	2.53	0.1	1.3	0.7	2	0.3	1.9	0.8	2.53
0.3	2.344	1.35	2.64	0.15	1.647	0.8	2.53	0.3	2.344	1	2.64
0.3	2.77	1.6	2.64	0.15	2.344	1	2.64	0.3	2.77	1.2	2.64
0.3	4.06	2.34	2.64	0.15	2.344	1	2.64	3	4.06	1.5	2.64
4	5	2.89	2.64	0.3	2.77	1.2	2.64	-	-	-	-
-	-	-	-	0.5	4.06	1.5	2.64	-		-	-
-	-	-	-	0.5	4.06	1.5	2.64	-		-	-

The SL_GVEL_MOD was the product of an inversion by CPS3.3 program *surf96*. The inversion took place for each grid cell and required two estimates: an input model (SLM) and the dispersion curve. The program *surf96* varied the initial input model and estimated an output model to minimize the difference between the observed and calculated dispersion curves, for a given set of input parameters. The *surf96* input parameters, such as smoothing and damping values, were constant in this study and were as recommended by the CPS3.3 documentation. Variations of the smoothing and damping values may produce final model velocity variations on the order of tenths of km/s for *Vs*. For high smoothing the velocity discontinuities were less sharp between grid cells. The final output of the CPS3.3 algorithms was a velocity model with estimated values in *each depth slice i*. The number of depth slices was chosen by the analyst and was given in the input model SLM in Table 1. In our case, *surf96* first was applied first with constrained layer thickness looking for best layer velocity, and second, was applied with the previously estimated velocity fixed, however, looking for best layer thickness. The estimated layer thickness variations, however, were under 10m.

The mean dispersion curve for the entire SL study area is shown in Figure 6 in satisfactory comparison to a synthetic dispersion curve derived using SLM (Table 1), which was the input model. An example of inversion results in one grid cell is shown in Figure 7. Examples of the *Vs* models estimated by inversion of the velocity maps in Figure 5 at 0.3km, 0.8km and 1.4km depth from the surface are shown in Figure 8A.1 (A-C). The input model was SLM in Table 1. Because the Vp was estimated using an active survey, we considered Vp as an independent estimate and the Vp/Vs maps were shown in Figure 8A.1(D-E). It was observed that changes in sign of the anomalies were associated with fault projections on the surface as shown in Figure 8.2 (A-F). Also, the mean Vp/Vs values appear to increase with depth.

The fundamental mode Rayleigh group velocity model extracted along Line 2 is shown in Figure 10A with a superposed fault cross-section. Changes in Vs appear to be associated with the vicinity of the major faults (green), although at the low resolution provided by this measurement the Vs anomalies appear to have a vertical trend.

Trust factor estimation

In this section, we describe the empirical estimation of the S-velocity model trust factors (Figure 8B in each grid cell at each depth and Figure 10B along Line 2). Higher trust factors correspond to lower estimated errors.

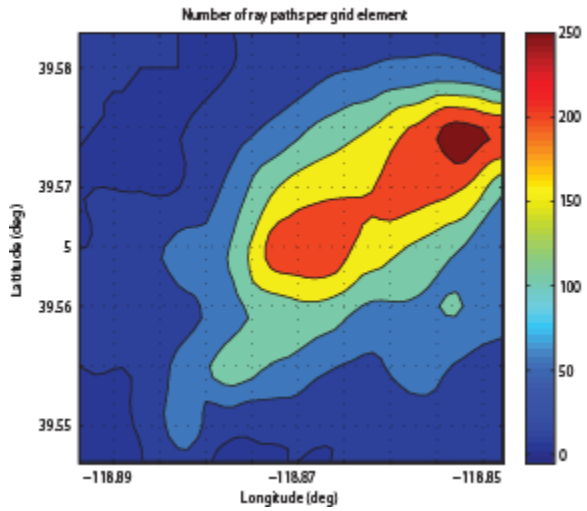

Figure 3. The number of inter-station ray paths for the ambient seismic survey station locations in the Soda Lake Area used for FR group velocity estimation. GFs were extracted on 739 inter-station paths, using data from 144 stations ("A" and "W"). A grid element was 0.5km on one side.

Errors for each component model are expressed as "trust" factors (the "trust" is higher when the errors are smaller) and are the assessment of the analyst, based on the model resolution, as described below. In each grid cell the input model has trust factors for *Vp, Vs, Rho* (density) and *Qp* and *Qs,* estimated at each depth *i* as the weighted mean of all the trust factors of all the models available at that depth.

The SL_GVEL_MODEL errors can be associated with:

1) The input model, SLM (Table 1)

The *Vp* in the input model SLM is based on active source results (Table 1), which incorporate unknown errors. Because the results were from active source reflection survey analysis, however, the value assigned to the *Vp* "trust" factor for this model was the same at each depth for all models and varies uniformly from 0.85 at the surface to 0.5 at 2.6 km depth. The *Vs* values in SLM were chosen by trial and error, starting with the ME Vs model, with the goal to obtain the best fit for the dispersion curves in all the grid cells (Figure 7B), and to use the same SLM values as an input model for all the grid cells. These errors could not be used in calculations.

2) The dispersion curve in each grid cell

In a grid cell, a dispersion curve was estimated using the CPSS3.3 program *do_mft* and had errors at each period. The main question was how these errors propagated into the inverted model. An analyst picked the fundamental mode Rayleigh dispersion curve which was usually the largest amplitude arrival. Errors could occur when several Rayleigh modes were present in the time series and they were misidentified. Mode identification was easier at an array, and that was the advantage of the SL array (Figure 1A). In addition, not only group velocity was used, a model (discussed below) of fundamental mode Rayleigh phase velocity was estimated, and the results compared well to synthetic dispersion curves (obtained from the SLM model).

Errors in velocity estimates occur when the GFs have low SNR. The errors were inversely proportional to the amplitude of the picked arrival at each period. The maximum amplitudes at each period were recorded for each dispersion curve and were input in the inversion program (*surf96*). Thus, these errors were taken into consideration in the resolution

matrix calculation (described below). A plot of all the estimated group velocity dispersion curves in SL is shown in Figure 6. In this figure, the mean of the standard deviations at all periods is 0.19km/s. These dispersion curves, however, are different most probably because of real crustal structure variations, thus their variation at each period should not be used as an estimate of errors.

Thus, an experiment has been conducted using these curves, to evaluate how errors in the dispersion curves translate into the final model at each depth. Assuming that these curves were random realizations of the same measurement, we investigated how the variation of these curves was mapped into the estimated model. Using these 140 dispersion curves, with what we considered random realizations of the dispersion curve velocity variations of 0.19km/s around a mean velocity at each period, and the same input model, realizations of the output model shown in Figure 9 were obtained. The normalized inverse standard deviation at each depth *i* was calculated as a trust vector $T_{surf96,i}/\max(T_{surf96,i})$ used in all the grids at depths *i.* The results were that the input model variations mapped into the output model variations, with larger variations deeper in the crust.

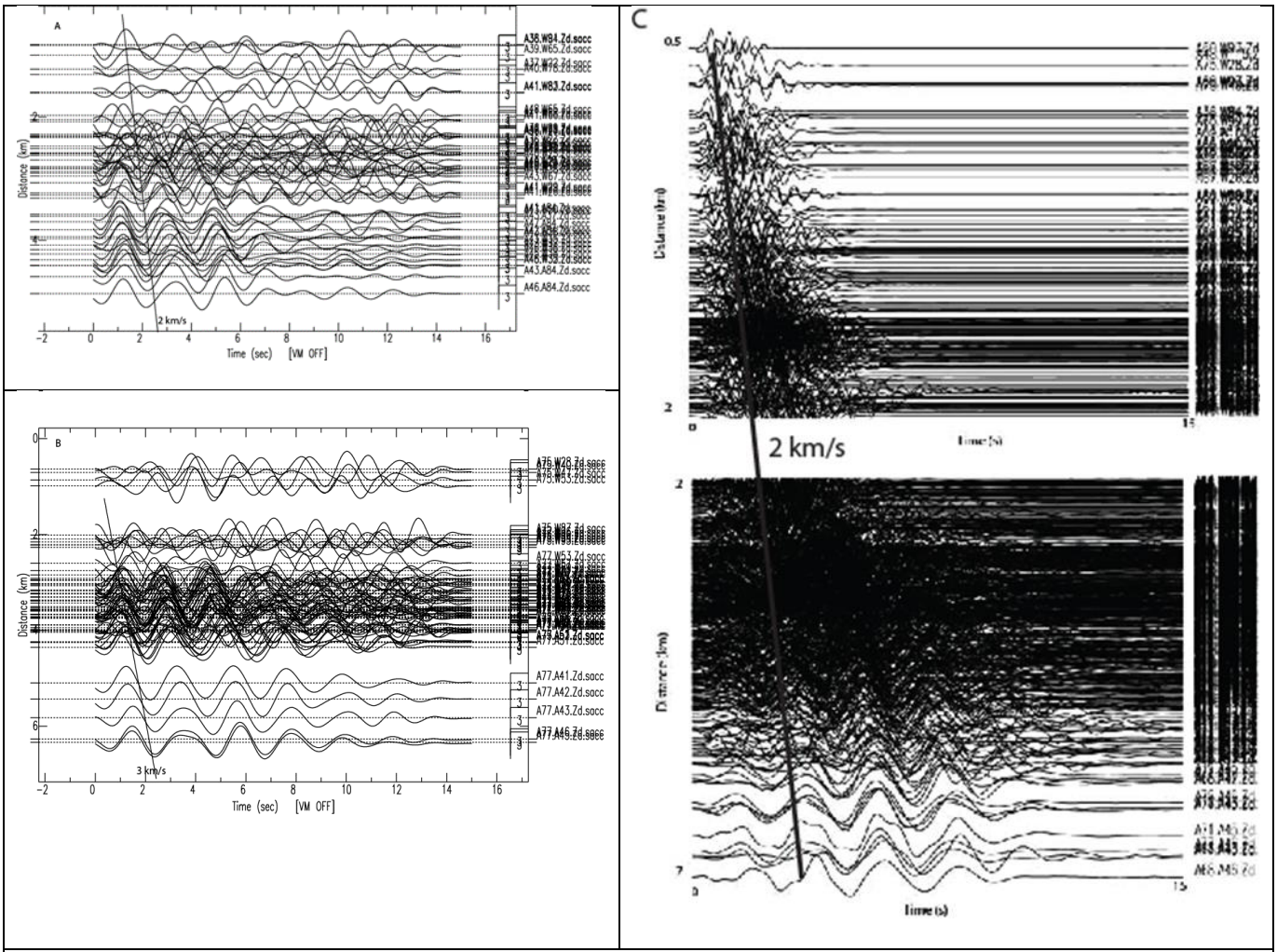

Figure 4. Record section of GF waveforms extracted in the Soda Lake area. The waveforms are filtered with a Butterworth, zero phase, 8 pole 0.4-0.8Hz filter. Figure 4A. Shows GFs extracted for virtual sources/stations in the eastern section of the array. Figure 4B. Shows GFs extracted for virtual sources to the north of the array. The vertical axis shows inter-station distance. A black line shows the 2km/s time lag (A) and 3km/s time lag (B). We interpret the largest arrivals at all distances as fundamental mode Rayleigh (ground roll). Figure 4C. Shows the waveforms after applying Phase Match Filters (PMF) twice: once on the raw data, and once again on the first-iteration dispersion curves. The black line is along the 2 km/s time lag.

According to the CPS3.3 documentation, if the group velocity dispersion curves were perfect, a "true model" would have been the result of the inversion. However, because the dispersion curves were not perfect, the estimated model (a vector of parameters, for example velocities, one parameter for each depth layer) was the resolution matrix (which was a square matrix) multiplied with the "true model". The resolution matrix is not symmetrical in the presence of smoothing and damping. In the following formula:

$$V_{i\ estimated} = \sum_{j} RijV_{j\ true}$$

where *i* is the depth interval number. The j'th column of the resolution matrix *Rij* showed how a unit perturbation in "Vj true" mapped into each of the elements of the Vj estimated. That means the true model was blurred by the inversion and the resolution matrix shows how this happens. Figure 7B shows an example of the estimated model and the observed (dots) and calculated (solid line) fundamental Rayleigh dispersion. Figure 7C shows an example of a resolution matrix representation for the same grid cell as in Figure 7A. For most of the layers, the resolution matrix value is largest at the layer depth, however, for some of the layers, a perturbation in the layer maps into perturbations in other depth layers, mostly when the depth resolution is lower than the depth interval of the model. Resolution matrices were calculated for each grid cell and a value was estimated for each depth layer. These are the trust factors *TR*.

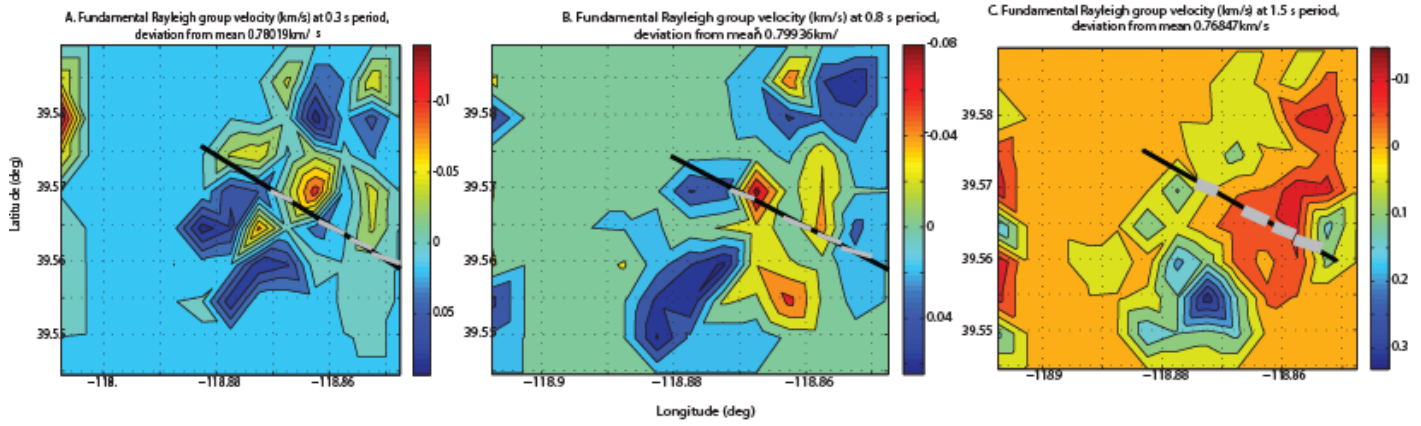

Figure 5. Maps of the deviation from the mean (at each period) of the fundamental Rayleigh group velocity at periods of 0.3s (A), 0.8s (B) and 1.5s (C) in the Soda Lake. The color scales on the right are in km/s. The Soda Lake Line 2 is shown as a black line in each plot and the surface projections of the fault zones (see also Figure 28) are shown as gray lines along Line 2. Note that the scale is not the same in A-C, because the group velocity is variable at different periods. Faults appear to be present near changes of *Vs* sign at depths <1km.

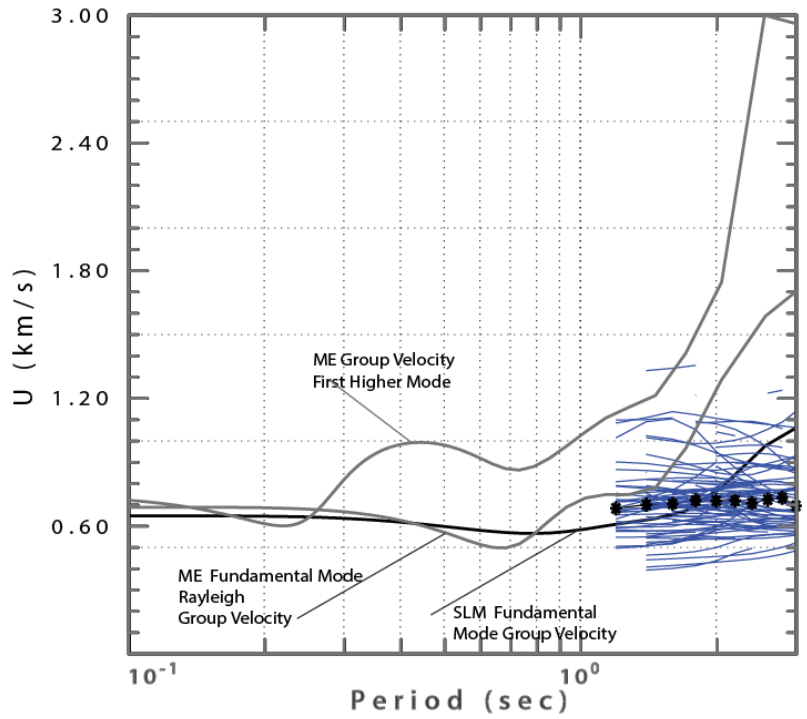

Figure 6. Estimated fundamental mode Rayleigh dispersion curves measured in Soda Lake (blue) and the calculated median dispersion curve (black dots) used in this study. In this figure, the mean of the standard deviations at all periods is 0.19km/s. Up to 2s period, note good correspondence between the mean Soda Lake fundamental mode Rayleigh group velocity (black dots) and the thin black curve which was the fundamental model Rayleigh group velocity as a function of period, estimated from the SLM-(Table 1). Note significantly lower group velocity at periods greater than 2s, which may be real, or errors due to using high-frequency sensors. This was one of the motives this study only used the models up to 1.4km depth. The ME dispersion curves for fundamental and first higher mode Rayleigh group velocity are shown for comparison (gray curves).

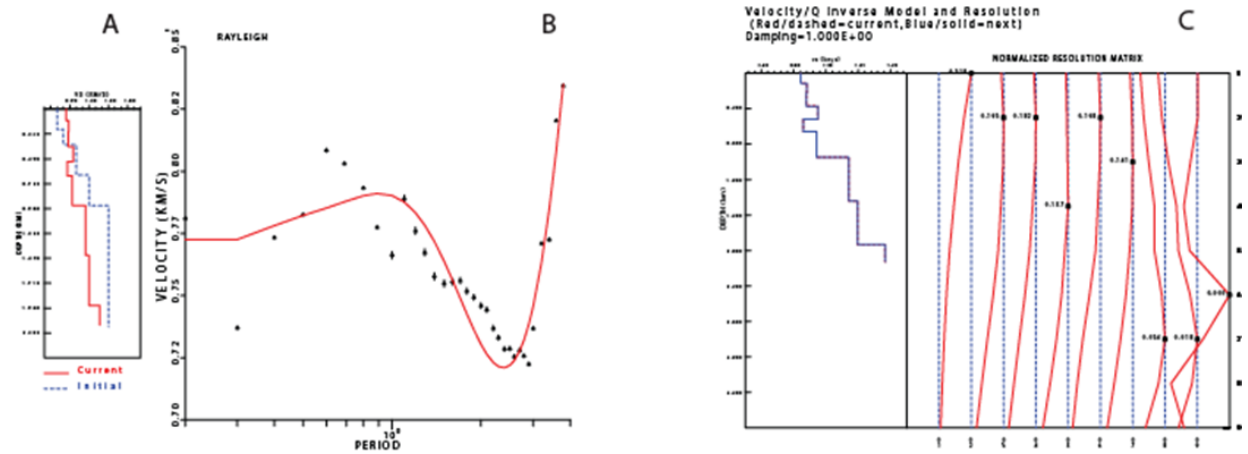

Figure 7. Example of velocity model inversion results, when using *surf96*. Figure 7A shows the starting model (blue) and the final inverted model (red), after at least ten iterations. Figure 7B. Black dots show the observed fundamental-mode Rayleigh dispersion curve in Soda Lake (black triangles) inverted to obtain the final model at grid cell with the location at 39.95745 N, 118.875 W. The dispersion curve was estimated using the *gridsp* program. Figure 7C. Shows the resolution kernels (Hermann and Ammon, 2002) for the inversion. Except for the deepest layers, the model is resolved, although the kernels suggest that the layering was possibly too thin because the kernels are wider than the layer thickness. The layer thickness of the SLM was chosen such that the inversion converged for the maxim number of cells.

1)

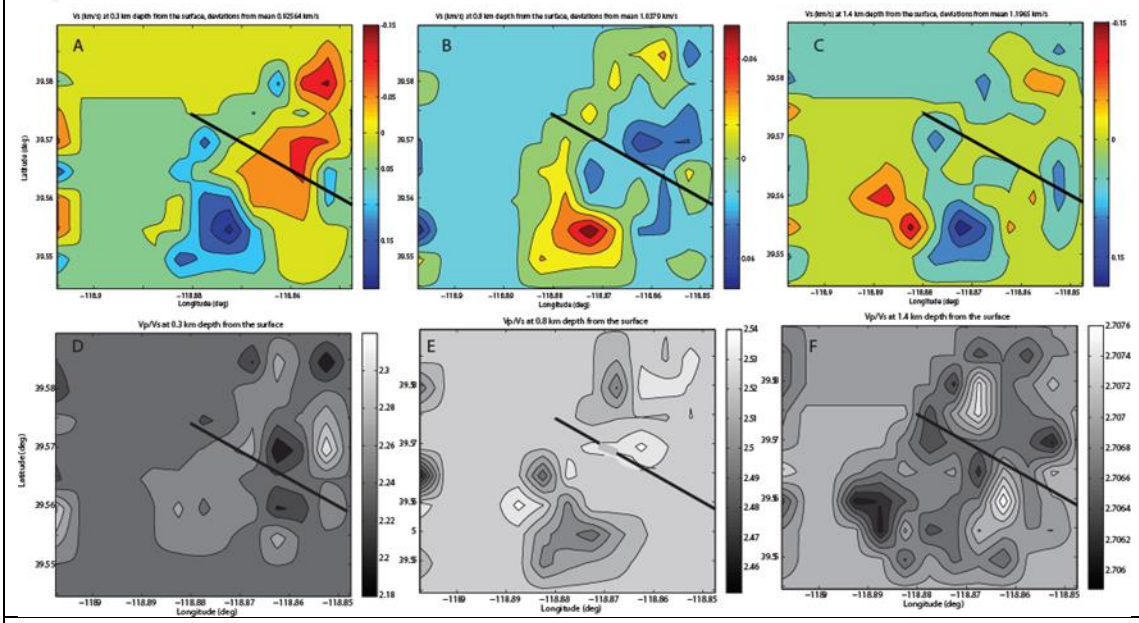

2) Notes: Images represent velocity maps produced for the current study overlain by a fault plane map from Magma (2011). Fault planes are from 0.18 - 1.2 km (600 – 4000 ft) and were based on a 3D-3C seismic reflection survey. Line 2 is represented by the black and gray line.

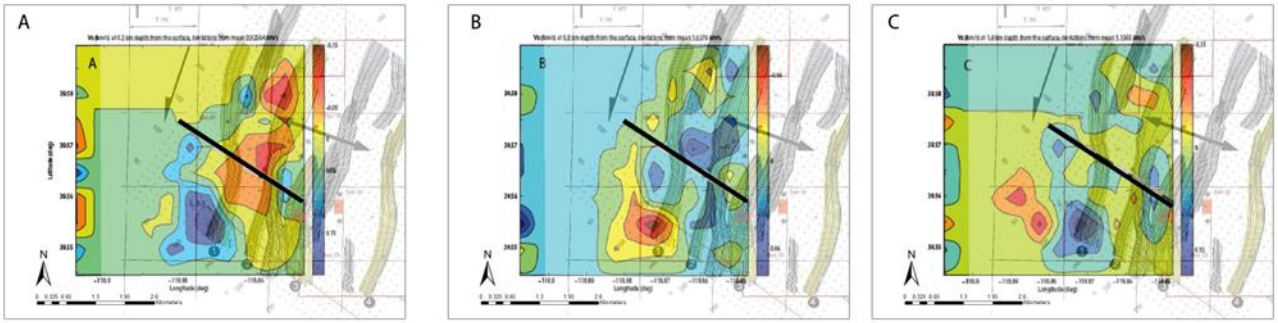

Vs map at a depth of 0.3 km

Vs map at a depth of 0.8 km

Vs map at a depth of 1.4 km

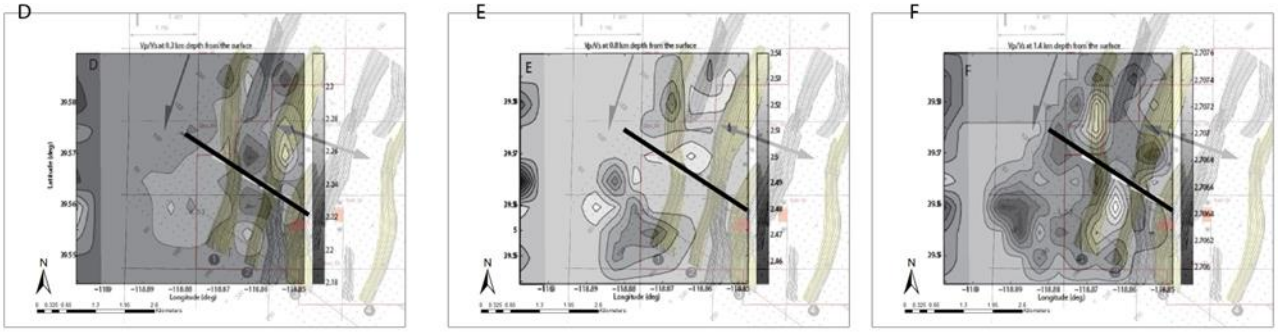

Vp/Vs ratio map at a depth of 0.3 km

Vp/Vs ratio map at a depth of 0.8 km

Vp/Vs ratio map at a depth of 1.4 km

Figure 8A.1. Vs maps (A-C) at depths of 0.3km (A), 0.8km (B) and 1.4km (C). Line 2 is shown as a black line in each plot. The Vp/Vs maps (D-F) shown in subplots D, E and F show changes in the vicinity of the faults (same plots in Figure 8.2). Figure 8A.2 shows the same plots in Figure 8.1 with fault maps superposed. These results provide important constraints for the SL_INITIAL_MODEL and can be used for comparison of the seismic experiment results with results of other geophysical methods (Section 6).

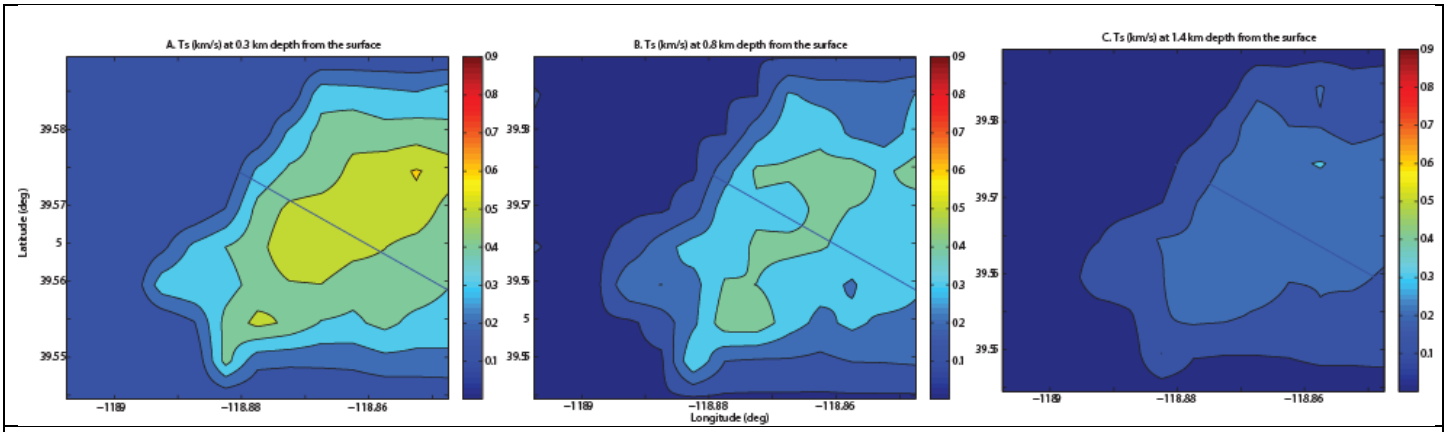

Figure 8B. Plots A-C show the trust factors for Vs. The trust factors for Vp/Vs are the trust factors for Vs multiplied in each grid cell with 0.805 at 0.3km depth, with 0.73 at 0.8km depth and with 0.64 at 1.4km depth from the surface.

3) Ray-path-density

A dispersion curve in each grid cell was best resolved by the group velocity tomography code, *gridsp*, when more paths intersected the grid cell. This was why the number of paths per grid cell (for all depths) shown in Figure 3 was an important indicator of how well resolved the model was in the respective cell. Thus, a normalized trust factor matrix T_{gc} (mn) = 1/(Nr Paths in cell *mn*)/max(T_{gc}) was assigned to each grid cell *mn* (m and n are the number of rows and columns in the grid matrix projection on the surface). We acknowledged the limitations of this trust factor estimate, which were due to ignoring the path density at different depths.

Considering all the above errors, an empirical trust factor has been estimated for each layer i in a cell *mn* as:

$$T_{i,\,mn}=(TR_{,i,\,mn} * T_{surf96,i} * T_{gc,mn})^{1/3}$$

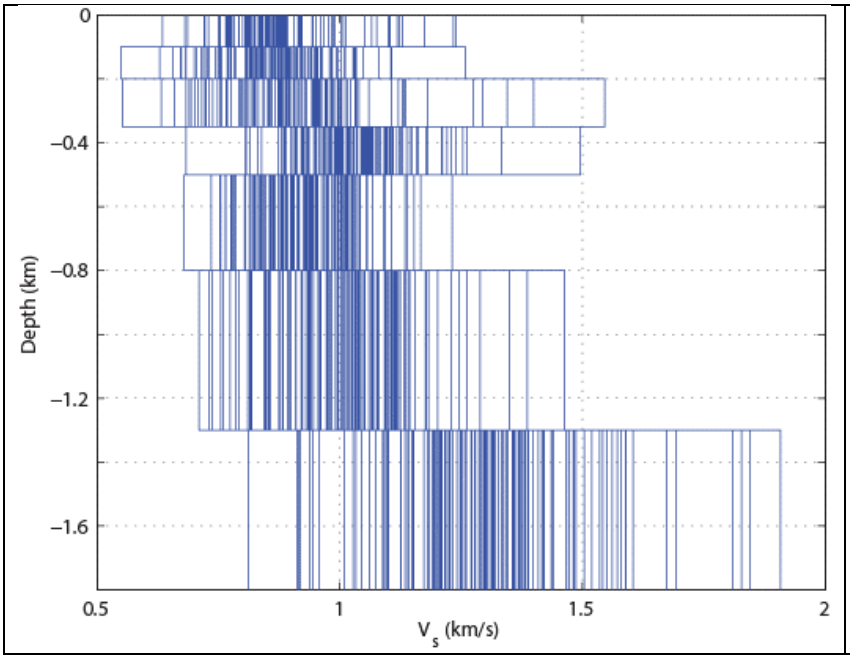

Figure 9. Realizations of the inverted shear-velocity models in Soda Lake when the input model randomly varies 0.19km/s around the mean velocity in Figure 6. The input model velocity variations produce output model variations of similar standard deviation relative to the mean, in the upper layers (<0.5km depth). The uncertainty of the model increases starting at 0.8km below the surface.

.

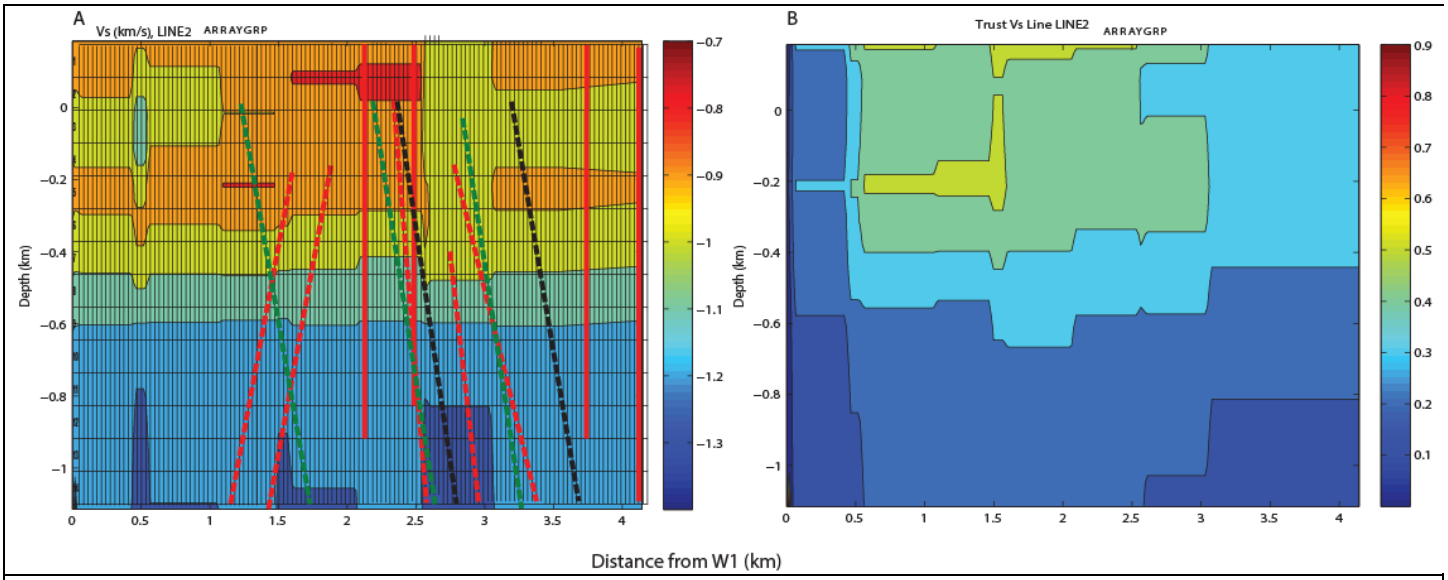

Figure 10A. SL_GVEL_MOD_LINE is the SL_GVEL_MODEL along Line 2, as a function of depth for Vs. Vs values are represented on this figure and vary from 0.7km/s to 1.4km/s. B. Trust factors for Figure 10A. Fault locations are indicated in Figure 10A: red lines are faults interpreted by Optim (Appendix 5) using the active survey data along Line 2, green lines are major faults interpreted by Magma (2011, see discussion in Task 6 and Figure 38) and black lines are minor faults interpreted by Magma (2011, Figure 38). Note changes in Vs near the major faults (green), although at the low resolution provided by this measurements the Vs anomalies appear vertical (see discussion in Section 3).

2.1.3. SL_PHVEL_MOD Ambient Noise

An alternative, array processing method to estimate the **Vs** model was applied in the larger project area to verify that the Rayleigh fundamental mode arrivals were correctly identified. The chosen array processing technique (Tibuleac et al., 2011) was frequency-wavenumber *(fk)* analysis of waveforms filtered using Continuous Wavelet Transforms (CWT). A GF was extracted for each path between an available SL array station and a station in an ad-hoc sub-array. The far SL station has been considered the virtual source of an "event" recorded at the ad-hoc SL sub-array. The sub-arrays were selected searching for groups of four stations or more in 45 degrees azimuth bins, increasing with a step of 22.5 degrees. Distances varied from 0km to 7km, starting at the virtual source and were chosen as 1km bins with step of 0.5km. A fundamental mode Rayleigh phase velocity dispersion curve was extracted, which subsequently was inverted to obtain the subsurface structure at the respective sub-array. Examples of the GFs estimated between the A77 SL array-station and stations in SL ad-hoc arrays, which included stations “A” and “W” were shown in Figure 11A. The individual station locations are given in Appendix 3—Tables A3-1 and A3-2. GFs were analyzed from paths including a total of 37 array-stations (“A” stations) as virtual sources (Figure 1, Appendix 3—Table A3-2), at 76 ad-hoc-arrays in the SL area. Figure 11B shows an example of waveforms processed at an adhoc array 1-2km and 292-337 degrees back azimuth from station A77. Figure 12 shows an example of processing fundamental mode Rayleigh phase velocity dispersion curves. Figure 12B shows an example of a dispersion curve obtained using frequency-wavenumber (fk) analysis for a virtual source at station A77 and virtual receivers in the SL, at distance from 1km to 2km and back azimuth from 315 to 360 degrees, corresponding to the area from 39.568989N to 39.571411N, from 118.874954W to 118.870468W. This area enclosed 14 receivers. Inversion for *Vs* models is shown in Figure 12A-B and Figure 12C shows the resolution kernels. The models for each subarray are integrated into the SL_PHVEL_MOD using MAT_MOD. Figure 13 shows the SL_PHV_MODEL at the same depths from the surface as the models in Figure 8: 0.3km, 0.8km and 1.4km and the trust maps at each depth. As previously observed in our Dixie Valley studies (AltaRock, 2014b), fault locations appear to be associated with sharp velocity gradients, even at lower resolution (hundreds of m^2). Note that, as a result of station configuration, and mostly because of short virtual station-sub array distance, for most of the sub-arrays the best model fit was obtained up to 600m from the surface. The shorter the wavelength of the Rayeligh waves, the shallower they

sample. The smooth kernels in Figure 12B, extending over multiple depths, also show that the depth resolution is lower than 0.2km. It was also observed that the best resolution was obtained in this case in the vicinity of Line 2, due to 150 m apart sensor availability. The extracted velocity model along Line 2 and the trust at each depth was shown in Figure 14.

Trust factor estimation

Trust factors (Figure 13 D-F) were estimated with a procedure similar to estimation of the trust factors in Section 2.1.1. The "bogus" model trust is the same as for the SL_GVEL_MODEL, however, the number of paths per grid element has been replaced with the number of stations in the ad-hoc array which were used by the *fk* algorithm.

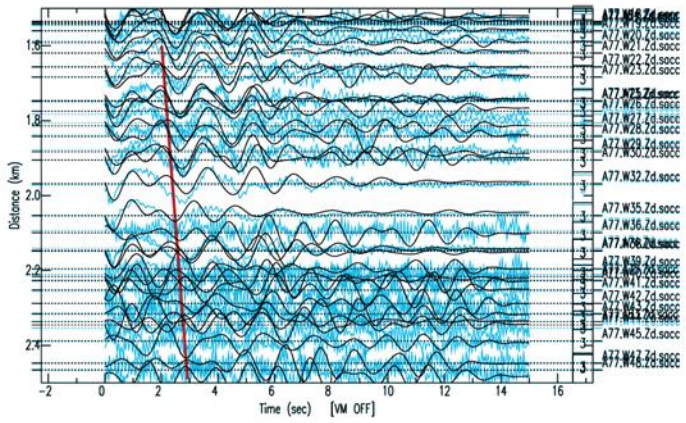

Figure 11A. Shows an example of the GFs estimated between the A77 Soda Lake array-station and stations in a SL ad-hoc array at distance from 1-5km to 2.5 km, as raw waveforms (blue) and black filtered waveforms (0.5–1Hz, zero phase, eight pole Butterworth filter). The line shows arrival times for 0.9 km/s velocity.

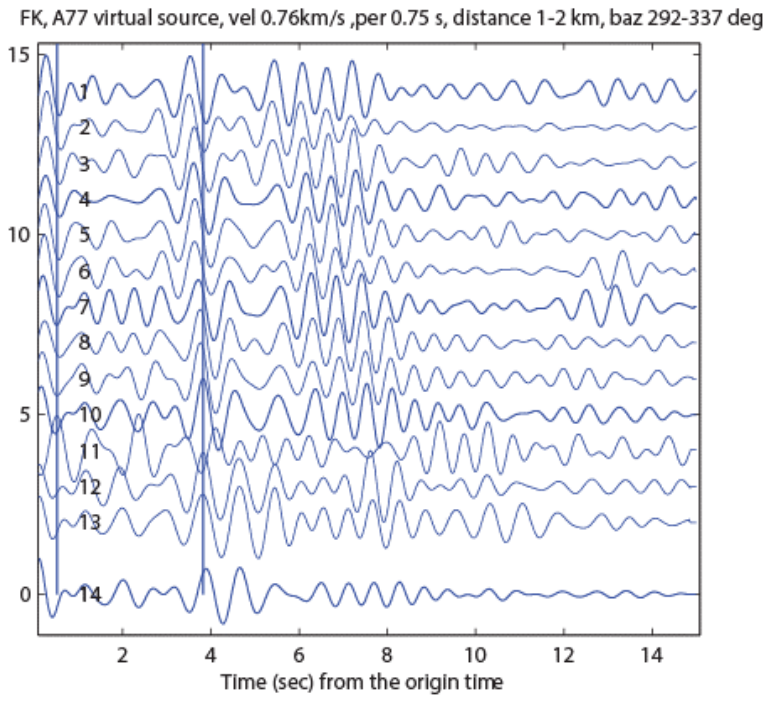

Figure 11B. Shows an example of GFs from A77 (virtual source) and sensors at distances 1-2km and in a back azimuth from 292-337 degrees. The waveforms are shifted for a phase velocity of 0.76km/s which was estimated as the velocity for which the summed waveform energy in the window (within the blue lines) was maxim. The arrival in the window is interpreted as the fundamental mode Rayleigh. The second arrival at ~ 6s time lag is an acoustic signal, which is not aligned because it has a horizontal velocity of ~0.34 km/s.

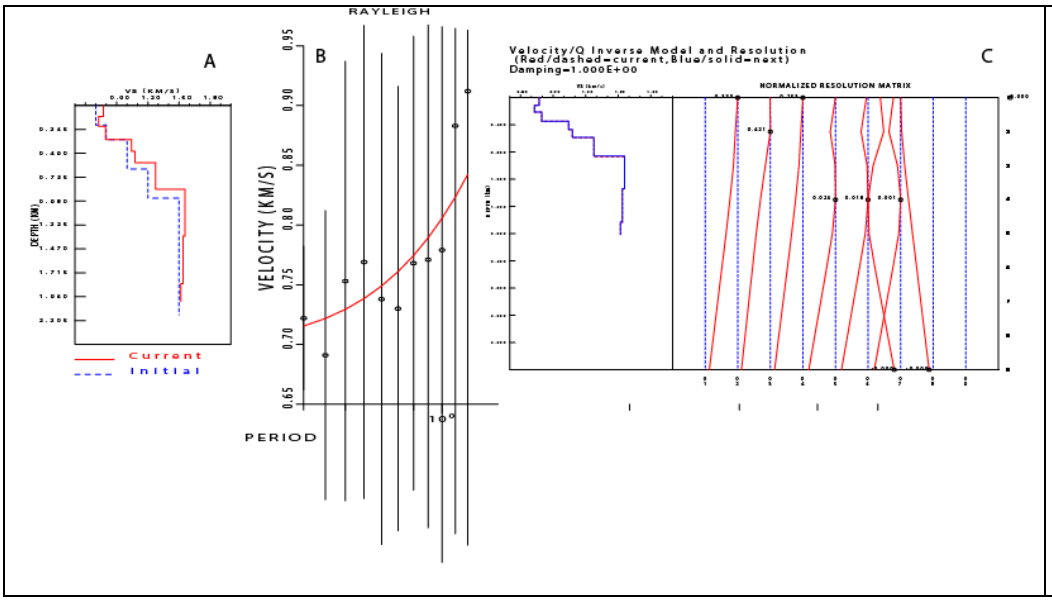

virtual station A77 and stations at 1 -2km distance, in a back azimuth range from 315 to 360 degrees. This is a fundamental mode phase velocity curve. B. The vertical bars are proportional to the width of the 75 percentile of the fk image maximum energy area, and are considered when estimating the phase velocity error. C. Similar to figure 7, the resolution kernels show that best resolution was obtained at depth < 0.6km.

2.1.4 Discussion of the low-resolution array-derived models

Two methods have been applied to extract Vs and the results (Figure 8, 13 and 6) compare well, while the dispersion curves are also comparable to the synthetic estimates. The above models estimated in Section 2.1.2-3 were integrated with *Vp* and *Vs* models estimated along Line 2, discussed in Task 3 below, using a set of algorithms named MAT_MOD. The MAT_MOD algorithms were particularly suitable for this study, because they allowed integration of independent information from multiple sources.

2.1.4.1 MAT_MOD

Each model we collected or estimated was stored into a Matlab@ structure. A "structure" is a named collection of data representing a single idea or "object". For anything in a computer more complicated than a list of numbers, structures can be used. The structure contains a list of fields, each being a variable name for some subset of data. Structures are similar to arrays in that they contain multiple data, but the main difference is, instead of an index to each piece of data, we have a "name"; and instead of every piece of data being the same type, we can have a different type for each "field". The fields of a MAT_MOD structure were: the reference to the model; the model area (which is a square oriented North-South, East-West; and the model matrix. The model matrix had eleven columns: depth, P velocity in km/s, S velocity in km/s, density (g/cm^3), P and S attenuation factors Qp and Qs and five trust factors, one for P, S, density, Qp and Qs. For "no information" the matrix element value was set to -99. The "trust" factor (a value from 0 to 1) was, for example, set by the analyst as high as 0.9 for reflection/refraction lines and is set to 0.01 for general (non-local) models. Using the "trust" parameter, seismic lines and local data were given higher weights than the global model weights. A "slack" number (in this case 0.005˚) for each model represents the area where the model is considered valid. When, for example, the P and S-velocity model at a point characterized by (latitude, longitude) is requested by the user, MAT_MOD finds all the models including a square centered on the respective point, i.e., within 0.005˚ from the respective point. A side of the square is twice the slack number value. For example, the resulting P-velocity at the respective point is a "trust" - parameter weighted mean, after the "-99" estimates are discarded. The choice of the "slack" factor can "sharpen" or "smooth" the P/S extracted velocity models.

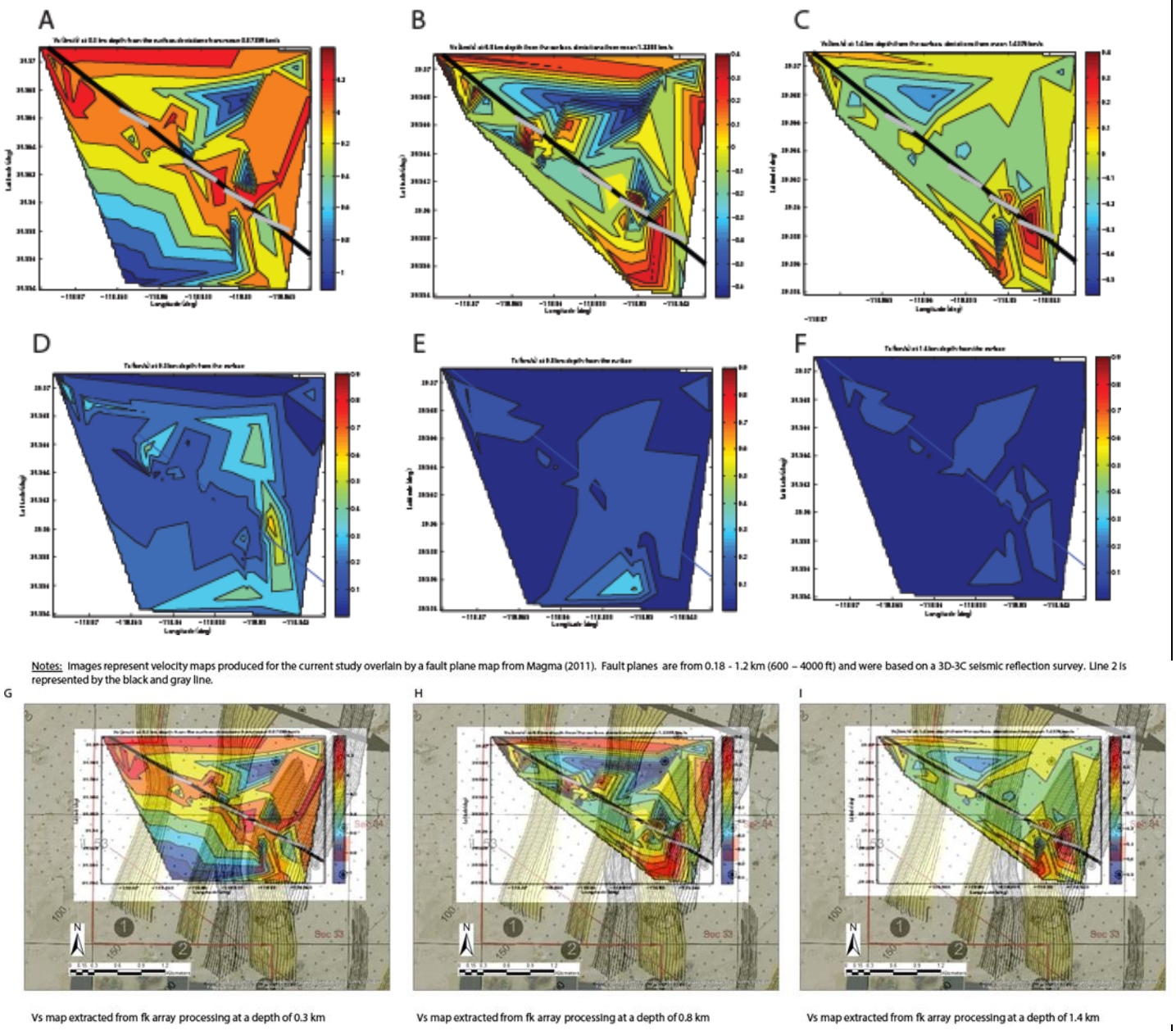

Figure 13. Difference from the mean at each depth for the *Vs* models extracted from fk array processing in the study area at depths of 0.3km (A), 0.8km (B) and 1.4km (C). The "trust" factors at the same depths 0.3km (D), 0.8km (E) and 1.4km (F) are shown in the lower plots. Note higher "trust" factors at shallowest depths and lowest trust factors away from Line 2, consistent with the lower density of stations away from Line 2. The location of the known faults along Line2 is shown by gray lines in plots G-I. Note the presence of the velocity gradients in the vicinity of the faults.

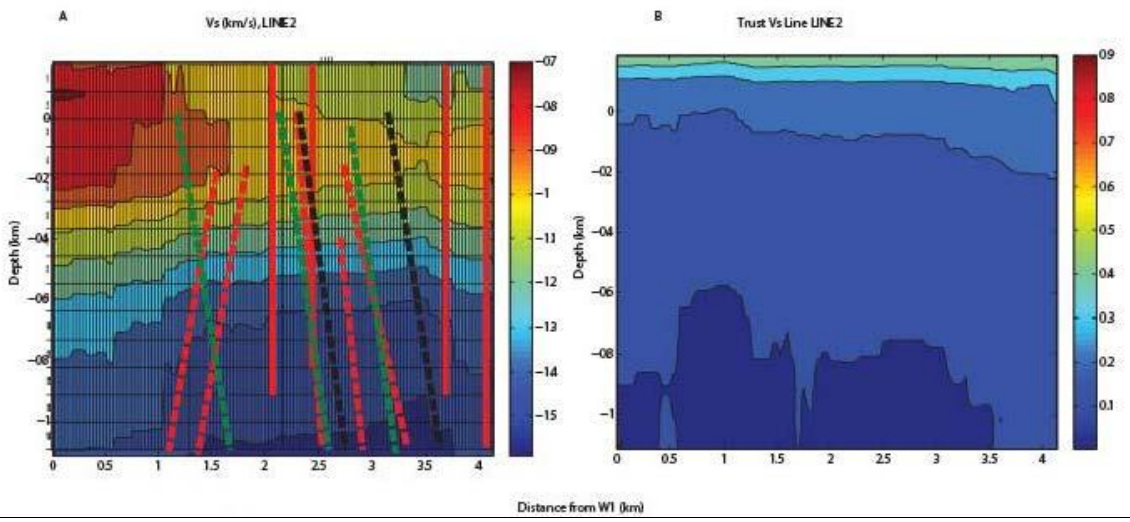

Figure 14. (A) SL_PHVEL_MOD_LINE: *Vs* as a function of depth, estimated from application of fk to adhoc subarrays. Note that this velocity model has best resolution in the upper 0.6 km and lower lateral resolution than SL_GVEL_MODEL. (B) The "trust" values for the *Vs* velocity mode in the left plot show higher confidence in the upper 800 m of this model.

2.1.4.2 Array- estimated Ambient Noise S-velocity (Vs) Data Discussion

The preliminary velocity models have an average resolution of ~0.25km^2.

A remarkable achievement of this preliminary survey was obtaining fundamental Rayleigh wave information at periods longer than 1s from sensors with a corner frequency of 5Hz, for an analysis duration of approximately one week. This was achieved through innovative adaptation of the seismic interferometry code to remove the instrument response of the geophones and replace it with a broadband sensor response.

A number of *Vs* anomalies were observed at the depths of this investigation, 0.3km to 1.4km. As shown in figure 28 and discussed in Section 6, low *Vs* velocity anomalies were observed (Figures 8 and 13) at the same locations as high temperature, low gravity and low resistivity anomalies estimated in previous geophysical studies. Also, according to Ramachandran (2011) "subsurface faults that are not clearly interpretable from velocity model plots can be identified by sharp contrasts in velocity gradient plots". Similar observations were reported in our previous study (AltaRock, 2014).

In this study it was also observed that *Vs* gradients were associated to known fault locations (Figures 10A and 14A).

The resolution of the *Vs* models extracted from seismic array processing (Figures 10 and 14) was lowest at depths greater than 800m. The SL_GVEL_MOD has better resolution at depths from 0.6 – 1.4km than the model SL_PHVEL_MOD.

Two low-resolution 2D velocity models (1) SL_GVEL_MOD_LINE from SL_GVEL_MOD and SL_PHVEL_MOD_LINE from SL_PHVEL_MOD, were extracted using the models estimated in Task 2 and along Line 2. Based on these models and on the Vp model from active survey (EM in Table 1) the SLM model in Table 2 was empirically estimated and was further used as initial/input velocity model to extract a high resolution *Vs* (and possibly *Vp*) along Line 2.

Task 3. Ambient noise reflection line analysis; Higher resolution (~0.045km^2) Vs and Vp model extraction from ambient noise

New records of ambient seismic noise along a passive or ambient noise reflection line at the same location as the Magma (2011) active Line 2 were processed with seismic interferometry (crosscorrelation and autocorrelation).

New *Vs* models were estimated along Line 2 using ambient noise: SL_LINE_FK_MOD and SL_LINE_3MOD. At Task 5, these ambient –noise extracted *Vs* models were converted to *Vp* models and were used to process the virtual shot gathers. Two cases were studied:

1) SL_LINE_FK_MOD was combined with SL_GVEL_MOD_LINE and SL_PHVEL_MOD_LINE into SL_LINE_3MOD without model weighting, however, the Vs in each grid cell was weighted with the trust factor;
2) SL_LINE_FK_MOD was used stand-alone.

A statistical comparison of the SL_LINE_3MOD and SL_LINE_FK_MOD can be found in Section 6.

Vp models are currently under construction, however, were not available in time for interpretation. Recommendations are made here for further P-arrival analysis.

A goal of this task is to assess whether the active survey could provide stand-alone information, comparable to active survey interpretations, at resolution better than 50-100 m on subsurface structure, and whether the Vp and Vs models obtained using array processing methods can be inverted at high enough resolution as to pinpoint potential fault zones.

3.1 Soda Lake Higher Resolution Ambient Noise Vs Models along Line 2

3.1.1. SL_LINE_FK_MOD

Along the line, ground roll has been recorded at all the sensors, at frequencies from 0.5Hz to 6Hz. Ground roll, i.e., fundamental-mode Rayleigh waves, is filtered out in typical reflection surveys. A novel approach in this study was to use ground roll, and array processing techniques, to extract a *Vs* model from data otherwise discarded.

A phase velocity model was estimated along the line using fk processing of the ground roll (fundamental mode Rayleigh waves). Starting at the northwest end of the line (station W1), groups of ten sensors (aperture ~300m), with 5-sensor overlap, were selected as virtual arrays. The GFs between these sensors and each other sensor on the line were analyzed as records of a virtual source at an array of geophones. Thus, for every virtual array the estimation of the dispersion curve potentially used data from 118 virtual sources (some of the virtual sources, especially near the power plant, did not have visible GF's and were discarded). The number of sensors was chosen empirically, as the maximum number of sensors for which the ground roll was relatively similar at all stations. A fundamental mode Rayleigh phase velocity dispersion curve was estimated for every group of 10-sensors.

The following criteria were used by an automatic algorithm to extract best dispersion curve data (1) The fk maxim should be narrow, such that the velocity error (calculated as the width of the 75 percentile of the energy maximum) does not exceed the velocity; (2) The SNR (estimated like in Tibuleac and Britton, 2006) of the beamed signal in the analysis window should be larger than 1, when the noise was chosen in an equal length window at the end of the record; and (3) The signal wavelength should not exceed twice the maximum distance between stations.

Once all the dispersion curves (usually over 50 with useful GFs) were estimated for one virtual array, the median velocity value at each period was calculated and the result was inverted for a velocity model with the same procedure as described in Section 2.1.3, using the SLM in Table 1 as initial model. An example of such a dispersion curve obtained for the subarray W1-W10 is shown in Figure 15, together with the theoretical dispersion curve estimated using SLM. The interquartile range of the velocity at each period for all the virtual stations was assigned as velocity error and was the input in *surf96*. An example of dispersion curve inversion for the W1-W10 virtual array is shown in Figure 16. The resulting model for Line 2, SL_LINE_FK_MOD is shown in Figure 17A with trust factors, discussed below, in (Figure 17B). Figure 17C shows the Vs differences from the mean (red are negative and blue positive) in percent.

Data contaminated by harmonic frequencies or by infrasound (Figure 18) was not used. The harmonic frequencies are the result of "leaked" energy from the removed cultural noise and affected frequencies as far as 5 Hz from the cultural

noise dominant frequency. The infrasound arrivals are observed on all the inter-station GFs and are propagating with a horizontal velocity from 0.32 to 0.36 km/s.

Trust factor estimation

A trust factor is estimated similar to the trust factor in Section 2.1.2 (Figure 17B). The "bogus" model trust was considered approximately the same as for the SL_GVEL_MODEL, however, the number of paths per grid element has been replaced with the number of virtual stations which were used to estimate the dispersion curve beneath every ad-hoc linear array.

3.1.3 Final Vs model in Soda Lake SL_LINE_3MOD

A final model was estimated in the study area, combining the SL_FK_LINE_MOD and the models along the line estimated in Task 2:SL_GVEL_MOD_LINE and SL_PHVEL_MOD_LINE. The model is shown in Figure 19A, with the trust factors in Figure 19B and the percent Vs anomalies relative to the mean at each depth shown in Figure 19B. . At each depth, and in each grid cell, the resulting velocity value was a median of the velocity in each of the three models, weighted with the respective trust value.

3.1.4 Processing challenges and solutions

1) **Waveform pre-filtering**. The fk methods were designed for strong SNR signal with energy in a frequency band broader than 2Hz. Ambient seismic noise GFs often have narrow frequency bands, mostly when extracted at short distances (Tibuleac, in preparation for BSSA[1]). This is why CWT was used in this case prior to fk analysis, thus avoiding the "ringing" typical for Fourier filtered signals when the filter is too narrow in frequency.
2) As shown in Figure 18, **strong contamination with acoustic waves** (0.32-0.36km/s) occurred at all stations. This is why all the velocities below 0.4km/s were discarded. This means that the model is valid deeper than ~150 m. Contamination with cultural noise was mitigated using data pre-filtering, before seismic interferometry was applied. Frequencies around 3Hz and 30Hz were filtered out, and the results significantly improved, however, as seen in Figure 18A, harmonic cultural noise leaked into frequencies around 3Hz (in this case 2.5 Hz) and measurements in this frequency range were also discarded. The cultural noise was higher in amplitude in the production area, and around the power plant, affecting the most the high frequency (>2.5 Hz) records at stations W90 to W128. Fortunately, in new exploration areas power plants are not present, however, these problems point out the importance of seismic noise evaluation at a site prior to the deployment.

All the figures generated for Line 2, as well as all the other figures generated in this project will be made available to the sponsor in a directory.

3.2 Ambient Noise Soda Lake Vp Models along Line 2

A first-order one-dimensional *Vp* model can be estimated along Line 2 using record sections of reflection GFs extracted from autocorrelation stacks, as shown in Section 3.2.1. In addition, we show that these record sections can be used in an initial investigation to delineate "zones of interest" for fault locations. A detailed *Vp* model could be extracted by finding the best fit of the GF synthetics with the observed GFs, however, due to time constraints, it is only recommended for future studies. Here it is only demonstrated that a Vp model SL_ACOR_VP_MOD (Table 1) extracted from autocorrelations is similar to ME, and fits the observed reflection component of autocorrelation-extracted GFs.

A second method for extracting a Vp model from ambient noise is discussed in Section 3.2.2, and is fk-analysis, possibly followed by 2D P-tomography. Due to time constraints, we only prove through examples that obtaining a Line 2 *Vp* model is possible with the recommendation to use this technique in future studies.

[1] Bulletin of the Seismological Society of America

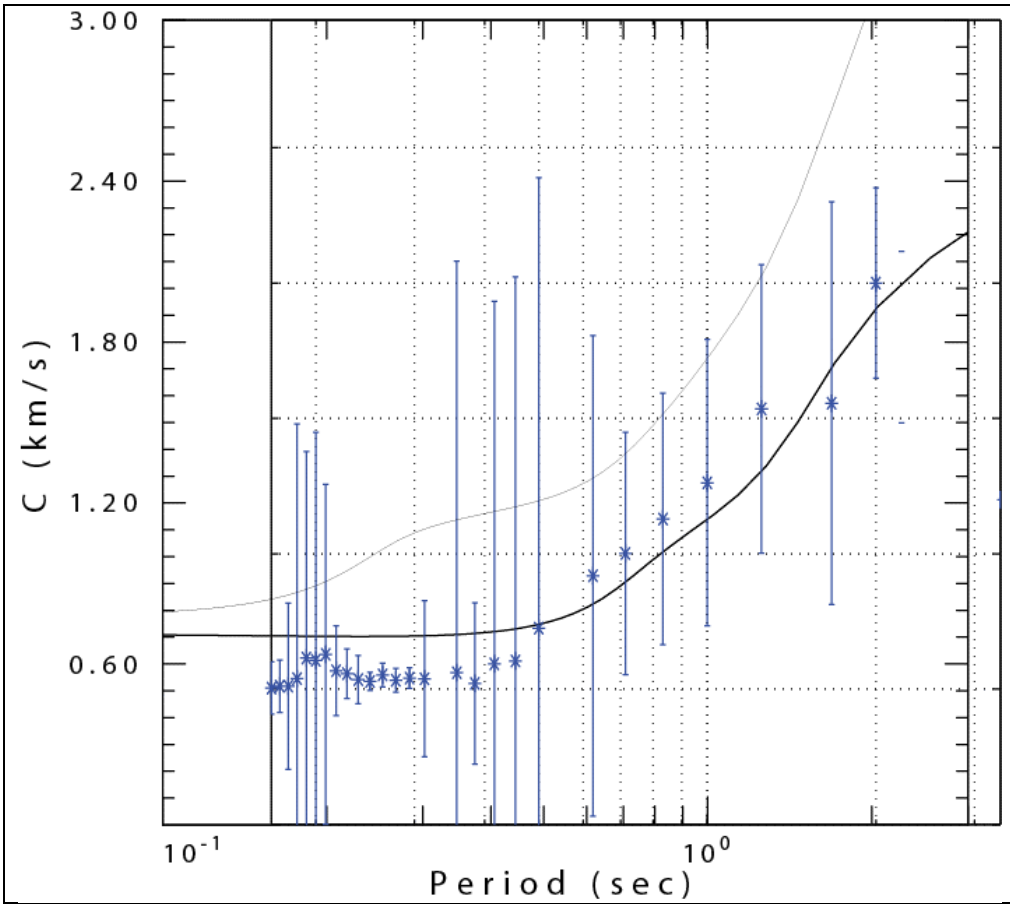

Figure 15. Example of a median dispersion curve estimated using *fk* processing for the W1-W10 subarray (stars) and 80 other sensors, each considered as virtual source. The length of the error bars are proportional to the interquartile range (iqr) of the velocity. The interquartile range is the difference between the 25 and 75 percentile of all the velocity values. Only the period values up to 2s were used in the inversion. Using ME (Table 1), a theoretical fundamental mode phase velocity dispersion curve was estimated (continuous black line) and a first higher mode dispersion curve (thin blue line). Note that the points with iqr larger than the velocity value were not considered for interpolation, as shown in Figure 16.

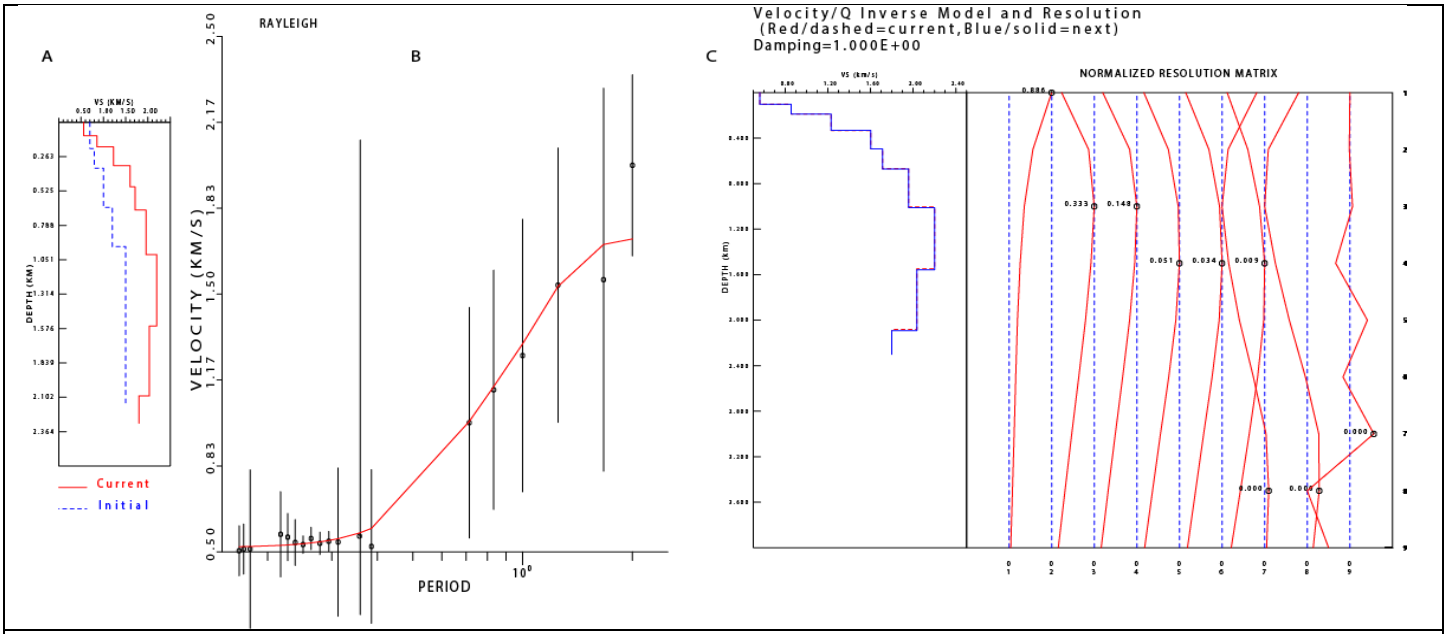

Figure 16 A. Same as in Figure 7, for the fundamental Rayleigh phase velocity dispersion curve estimated below the W1-W10 ad-hoc array. B. The observed dispersion curve (dots with bars of the length of the interquartile range) and the dispersion curve (red) estimated using the red "current" model in plot A. Note that some of the phase velocity values in Figure 15 have been discarded, because of too large errors. C. The smooth kernels extending over multiple depths, also show that the depth resolution is lower than 0.2km, and that resolution decreases significantly below 1km depth.

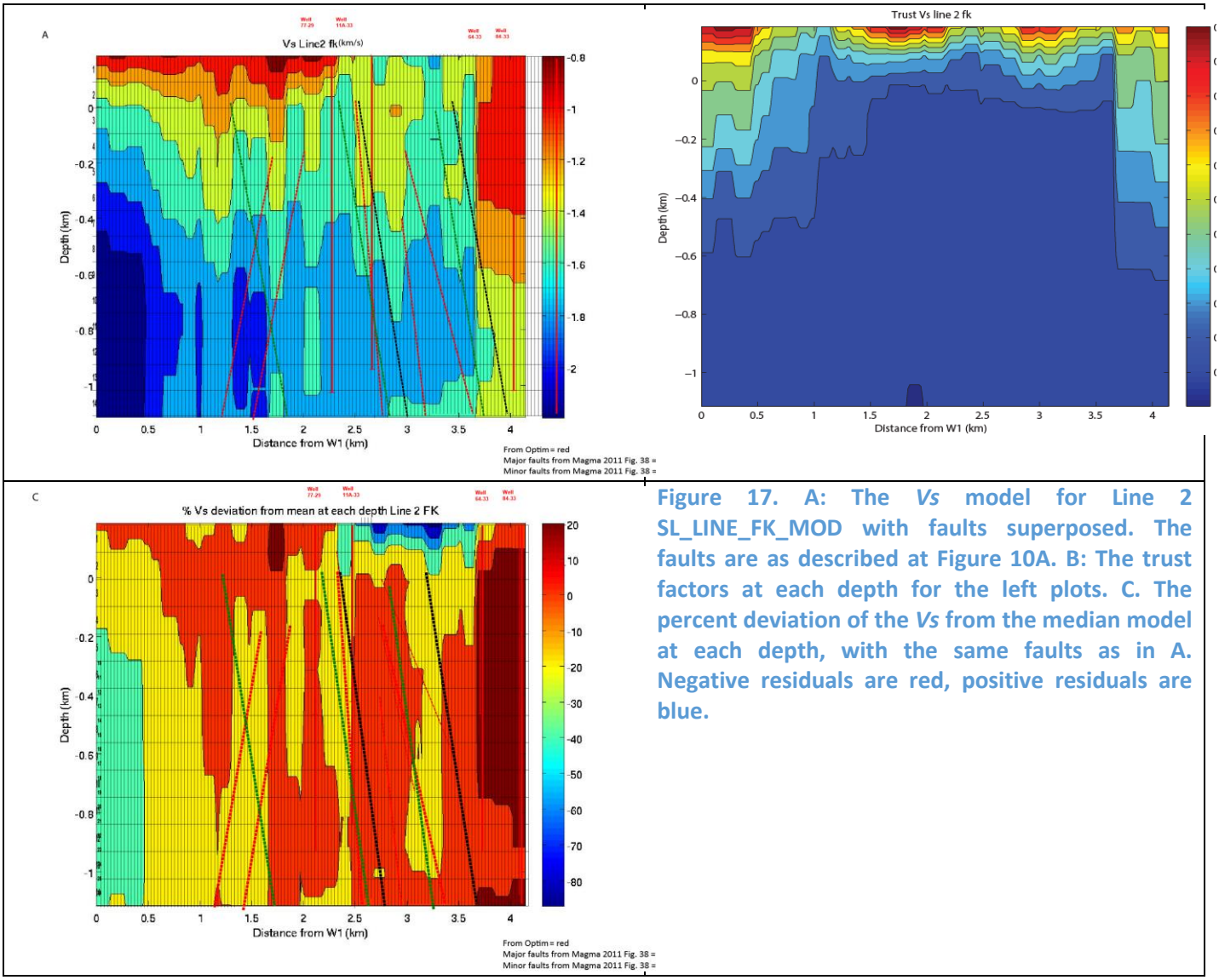

Figure 17. A: The *Vs* model for Line 2 SL_LINE_FK_MOD with faults superposed. The faults are as described at Figure 10A. B: The trust factors at each depth for the left plots. C. The percent deviation of the *Vs* from the median model at each depth, with the same faults as in A. Negative residuals are red, positive residuals are blue.

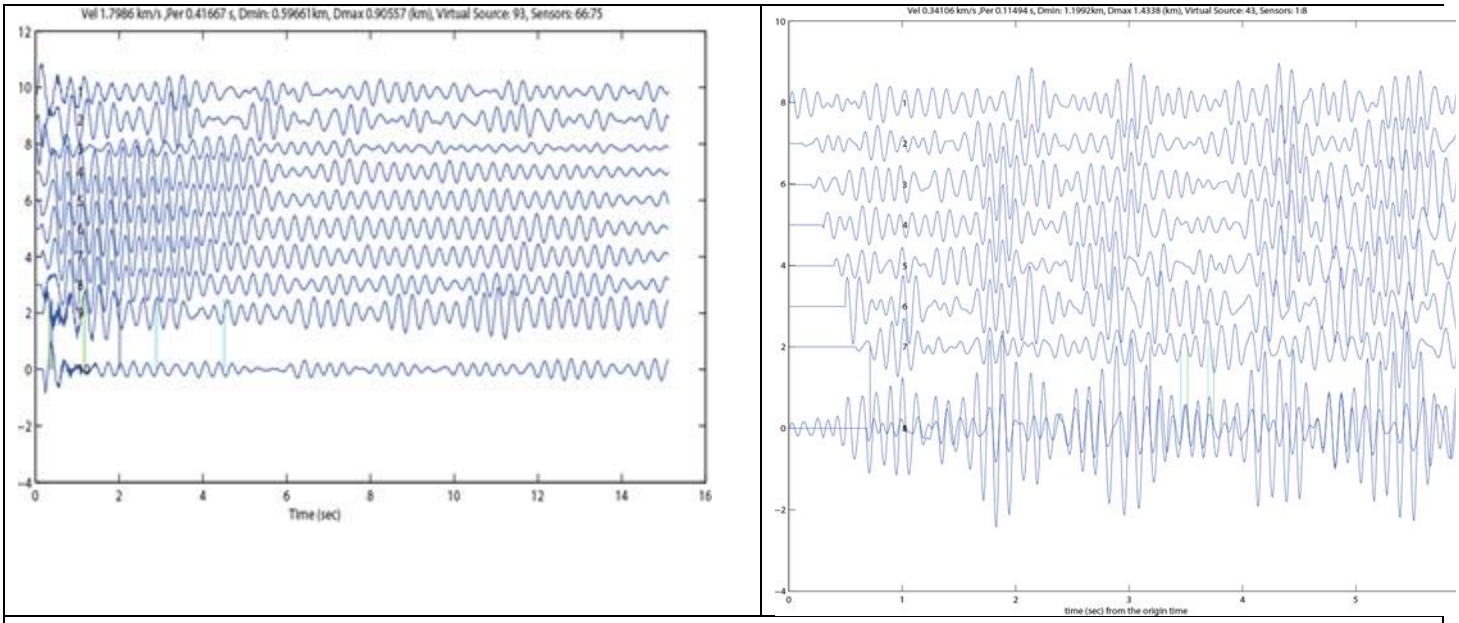

Figure 18. Plot A shows an example of cultural noise. Plot B shows an example of acoustic arrivals. Instances like these were discarded.

SL_ACOR_MOD

Ambient seismic noise survey and autocorrelation analysis were conducted to develop the SL_ACOR_MOD. The autocorrelations were estimated at all stations for a sample rate of 125sps. Each waveform represents the reflection GF extracted at the respective station over 21 days. Prior to processing, cultural frequencies at 30Hz and 60Hz were removed from the raw data using eight-pole, zero phase, band-stop Butterworth filters. The autocorrelation beams extracted at the Line 2 stations are shown in Figure 20. The E, N and Z-component autocorrelation beam record sections are shown in Figure 20 (A-C) for CWT center frequency of 0.16Hz and in Figure 20 (D-F) for CWT center frequency of 0.076 Hz. Note that CWT was used with a *sym8* wavelet, to extract signal in a very narrow frequency band. This type of analysis would have not been possible with Fourier filtering.

Arrivals were observed at 0.1s, 0.2s, 0.4s, 0.6d and 0.8s for sensors W1-W40. Using these arrivals, and assuming they were all P-arrivals, a velocity model (SL_ACOR_MOD in Table 1) was extracted from autocorrelations only. Synthetic waveforms estimated using the SL_ACOR_MOD model and CPS3.3 matched the W1-W40 GFs when filtered at the same center frequency, using CWT and a sym8 wavelet. The recommendation is, however, that synthetic waveforms should be generated for the middle and southeast sections of the line.

The variations in the layering in Figure 20 might be indicative of the shallow basalt layers below the line. Multiples are present in the section, and the velocity model varies significantly along the line. Dipping reflectors are usually difficult to distinguish in zero-offset sections, however, dipping layers are shown in Figure 20C and F (Z component). To understand all the reflections, detailed synthetic waveform modeling would be required, and the estimated model would have resolution of tens of m^2. A first-approximation model can be provided by the autocorrelations, however, this possibility needs more testing, and comparisons must be made between the E, N and Z components, to correctly identify all the reflection GF arrivals. For instance, it has been noted (Tibuleac and von Seggern, 2012) that P arrivals can be identified on all three-components when estimating reflection GFs, and this is evident in Figure 20. Differences, however, are observed between the horizontal (A and B and D and E) record sections and the vertical record sections, and these differences could be used to separate P and S arrivals at least for portions of Line 2.The autocorrelations images were also proof that the horizontal reflections seen in the ambient noise migration were real.

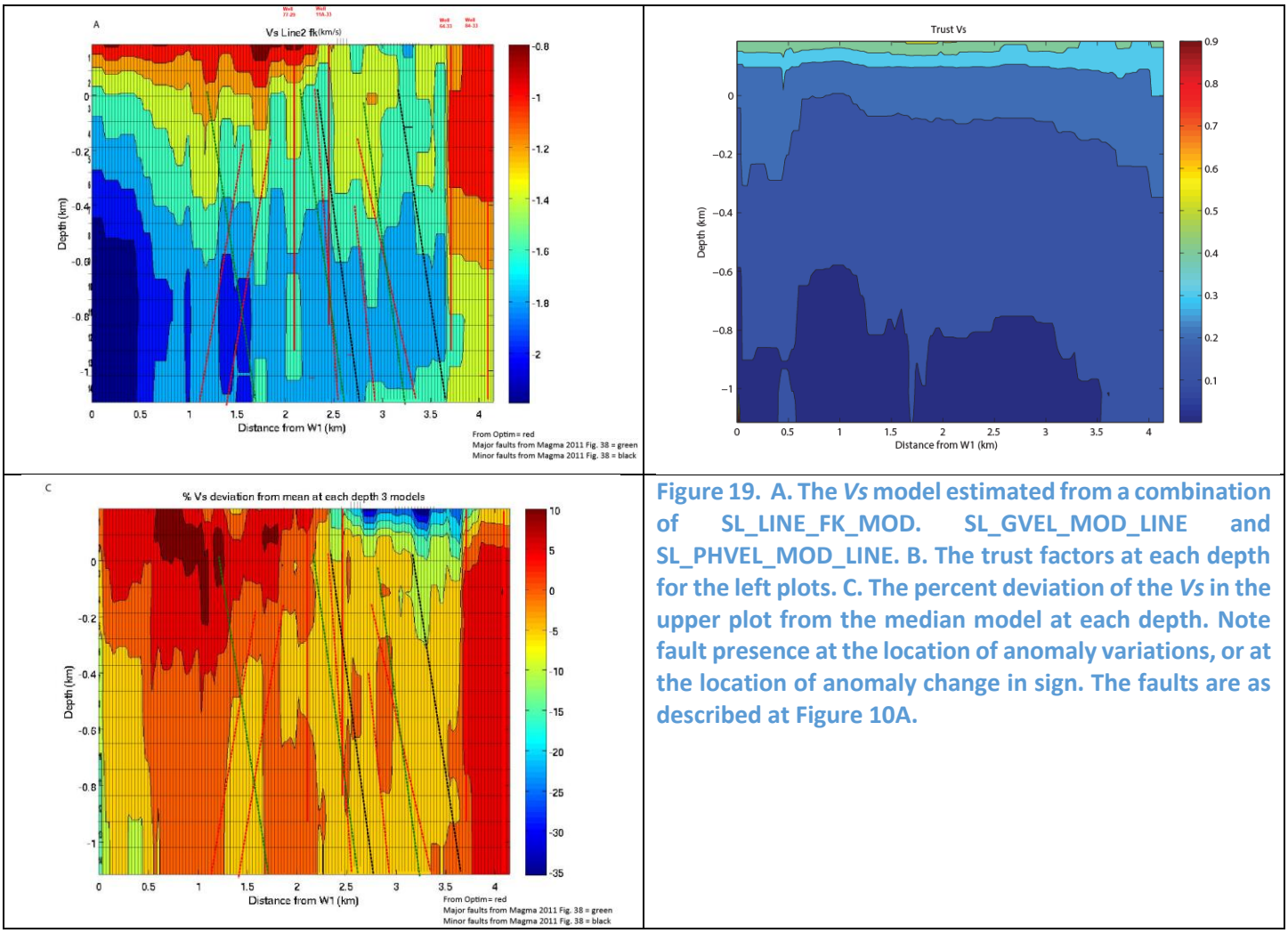

Figure 19. A. The *Vs* model estimated from a combination of SL_LINE_FK_MOD. SL_GVEL_MOD_LINE and SL_PHVEL_MOD_LINE. B. The trust factors at each depth for the left plots. C. The percent deviation of the *Vs* in the upper plot from the median model at each depth. Note fault presence at the location of anomaly variations, or at the location of anomaly change in sign. The faults are as described at Figure 10A.

3.2.2. SL_LINE_VP_MOD

High frequency (>20 Hz) P-waves are more difficult to extract than S-waves (Draganov et al., 2013), especially in conditions of similar frequency high cultural noise, such as in the southeast of the Line 2, which is actually the zone with most of the fractures, including 84-33, a productive well. It was also observed that the ambient noise extracted P-arrival can also have a very narrow frequency band, with lower frequencies when the inter-station distance increases. Frequency-wavelength analysis (fk) using waveforms filtered with CWT is a good alternative to fk using Fourier filtering because, as opposed to Fourier analysis, CWT extracts very narrow frequency signals without producing "ringing". This technique is also suitable when nothing is known about the potential P-arrival frequency range and it is usually used in nuclear monitoring array processing, to enhance coherent, however, weak event signals. An initial, low-resolution *Vp*-model could be extracted using fk analysis and P-tomography on Line 2, with the same virtual array and virtual station technique as described in section 2.1.4. In this case, however, the P-arrivals are beamed, as opposed to beaming fundamental Rayleigh waves. This analysis has been started, however, only initial results are available today. These results are discussed below are shown in Figure 21.

Overlapping groups of 6 stations are considered as virtual arrays along Line 2 with a step of 3 stations. Every other station on the line was assessed as virtual source. Note, however, that in this case, less virtual sources provided useful data when compared to the case discussed in Section 3.1.1. The *Vp* for a frequency range from 7Hz to 21Hz was estimated for each virtual array and virtual source. Initially, an analyst visually identified P-arrivals and chose a horizontal P-velocity which was close to the FK maximum energy (see Figure 21B for an example), and had high values of

the coherence, F-statistic and SNR in the analysis window. An automatic algorithm is currently tested for P-analysis, however, it is unclear whether the results will be available until this document is due. The results will be available on June 30, 2015.

3.2.3 P-arrival processing recommendations

1) Based on initial results, we find this array processing approach to Vp analysis promising and recommend that the approach is validated in future studies.

2) A wealth of information for P-arrivals can still be extracted using all three seismic components, as opposed to only the Z-component.

2. P-velocity analysis using array fk processing techniques and synthetic waveforms is possible along Line2, and the results should be compared to the active-source P-velocity model. We are currently investigating this possibility.

3. P-arrivals can be enhanced by using only the records proven (with array processing) to contain P-energy (Draganov et al., 2013). We are currently testing selective crosscorrelations of the data, and extracting GFs from only data with confirmed P-energy. These tests will be completed after this report is due.

4. Pre-filtering in narrow, empirically chosen frequency bands may enhance P-arrivals only when the cultural noise is very high (Appendix 4, Figure A4.1)

5. Using the crosscorrelations of the coda of the crosscorrelations (or C3) is a method developed first by Stehli et al. 2008, which has significant potential to improve P-extraction (Appendix 4, Figure A4.2).

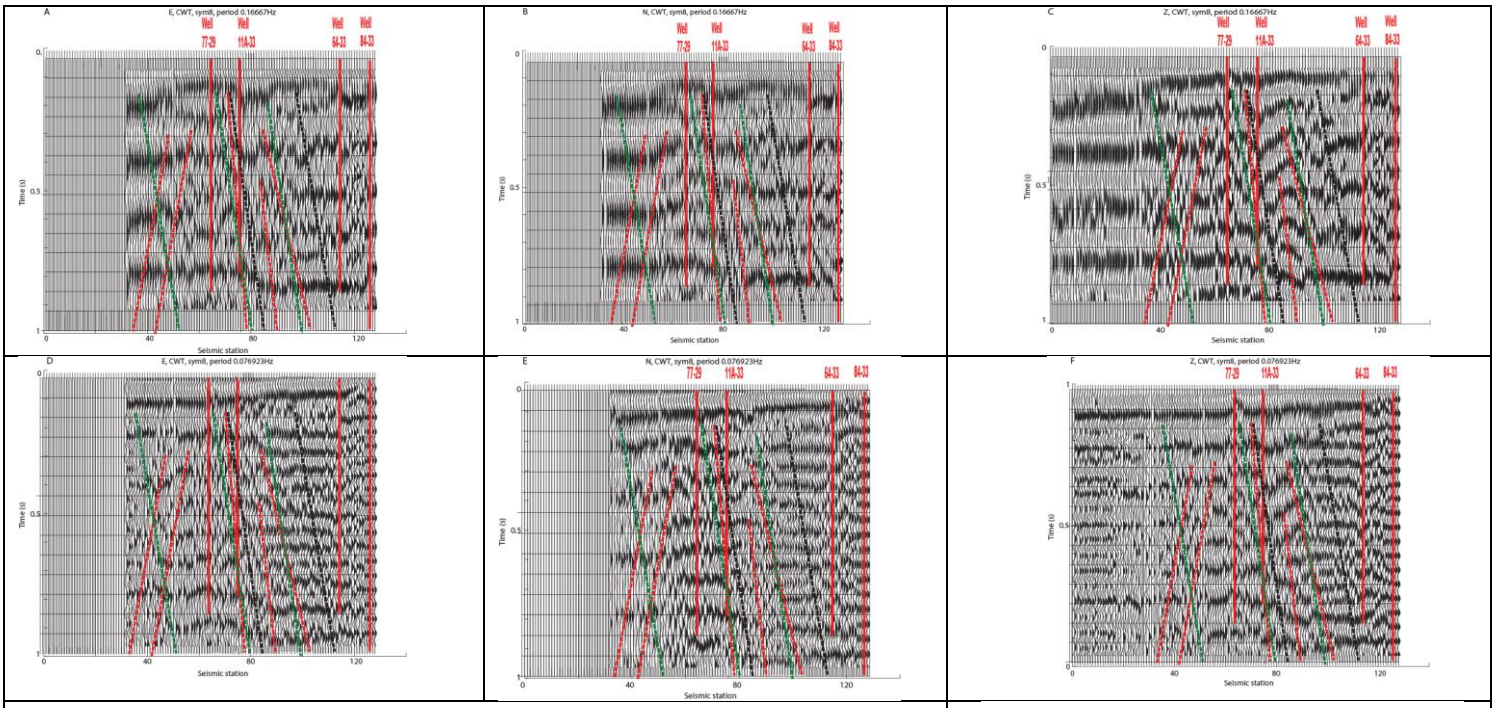

Figure 20. Record sections at CWT center frequency 0.17Hz (A-C) and 0.076Hz (D-F) of reflection GFs along Line 2 shows pattern changes at the fault locations. Note that higher frequency filters applied to the autocorrelations enhance shallower reflections. The faults are as described at Figure 10A and in all the figures are located where the GFs change lateral pattern. The P-arrivals have been observed before on the horizontal components (Tibuleac and von Seggern, 2012), however, the differences between arrivals on the vertical and horizontal components may show S-arrivals. This has not been investigated in detail, and is recommended for future research. Plot G shows the active source pre-stack depth migration analysis, also discussed in Chapter 5. Note similarities with plots C and F, although the plot G representation is currently available only as a function of depth. The box shows the portion of the plot G which corresponds to the upper plots.

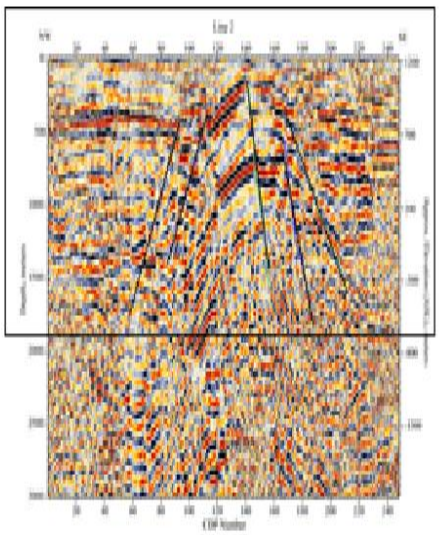

G

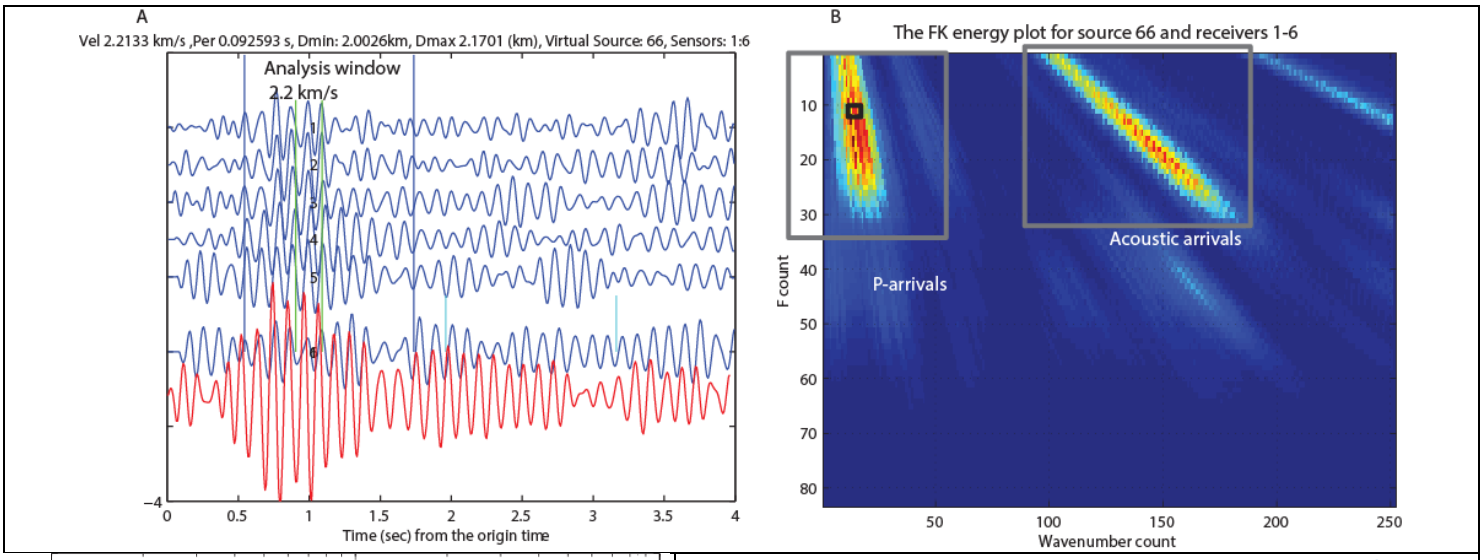

Figure 21A. P-arrivals with horizontal velocity 2.2km/s were identified by an analyst across a virtual array including the sensors W1 to W6. In this case W66 was the virtual source. Unlike surface waves, the P-waves are traveling deeper when the virtual source is far, and shallower when the virtual source is close. Thus P-arrival times are estimated for each virtual source and pair of receivers. B. FK energy plot showing the P-arrival energy (with the chosen velocity and frequency values in the black open square) and acoustic arrivals. Search frequencies vary from 7-21Hz, a band chosen empirically based on analyst – identified P-waves. Horizontal velocities across the virtual array W1-W6 were estimated at each of the frequencies 7-21Hz. As shown in (A), P-arrivals were identified at 2.2km/s and 0.09s period. Note that this analysis was not possible using conventional Fourier filtering, and was only possible using wavelet transforms. The black line in (C) shows the chosen P-velocity, also based on stability of the velocity values, on highest coherence of the waveforms in the window delineated by blue bars in plot A, and on high F-statistic values, as well as on the width of the energy beam (a narrow beam maxim is preferred).It is expected, bases on the Rayleigh wave analysis, that the first higher mode Rayleigh, which could be mistakenly identified as P-arrival, has a lower velocity than the cutoff P-search velocity (1.85 km/s).

Task 4. Analysis of New Geothermal Field Seismic Indicators along Line 2

New, possible geothermal field seismic characteristics indicating geothermal favorability were analyzed with regard to ambient-noise spectral content, scattering and attenuation, using data recorded at all sensors. We investigated the usefulness of stochastic heterogeneity, of spectral properties, of entropy and of attenuation variations for detecting productive geothermal reservoirs, and faults.

4.1 Stochastic heterogeneity analysis for active and ambient noise surveys

Crustal heterogeneities, mostly when compared to the seismic wavelength, influence the crustal seismic response. It was observed Holliger and Levander (1992) that the stochastic heterogeneity distributions found in the crustal

exposures and borehole logs followed the von Karman- or the 1/ f power law (self-similar) distributions. More specifically (Carpentier, 1979), autocorrelations and equivalently, the power spectra of the exposures and borehole logs were shaped according to these distributions. The von Karman function is an autocorrelation function whose power spectrum represents a probability distribution of heterogeneity in a stochastic (geological) sequence. It is parameterized by two 'fractal' parameters: correlation length, which is an upper limit for the scale invariance in the heterogeneity, and Hurst number, which is an exponent that controls the degree of scale invariance in heterogeneity below the correlation length scale. A segment of von Karman-type crustal fabric is therefore a segment of randomly distributed geological heterogeneity, whose autocorrelation follows a von Karman function, parameterized by correlation length and Hurst number. According to Frankel and Clayton (1986), a self-similar model of the crust is consistent with general observations concerning rocks and surface geology.

A seismic velocity model can be considered as a superposition of a deterministic model and of a stochastic model. Many studies suggest that the original stochastic parameters used to generate the velocity models, are (partially) retained in their seismic response - in this case the von Karman parameters (Frankel and Clayton 1986, Pullammanappallil et al., 1997). A series of 1D, vertical incidence, primaries only synthetic seismograms (Claerbout, 1985) is the standard conceptual model of subsurface reflectivity, is regarded as an ideal seismic image and has the same horizontal characteristics as the stochastic velocity model from which it is derived. Pullammanapalil et al., 1997 estimated that common offset gathers at zero offset closely approximate the correlation measure from the ideal wavefield response.

As shown in detail in Appendix 5, stochastic parameters were estimated from the depth migrated sections obtained from both active and ambient noise data. The stochastic parameters discussed here are correlation length and Hurst number, for a self-similar (von Karman) model of the crust. The objective was compare the active and ambient noise surveys and to investigate whether these parameters provide additional information that could be used as indicator of permeability/fragmentation within the subsurface. Lateral correlation functions were used to estimate the von Karman parameters, correlation length and Hurst number.

Figure 22A shows the correlation length parameter derived from the active source depth migration section. Figure 22B shows the correlation length parameter derived from the ambient noise depth migrated section. For all plots the correlation length varies from 20m which are shown blue colors to the maximum of 170m shown in red/purple colors. In Figure 22, the high correlation length (red/purple colors) match the horizontal and sub-horizontal reflectors while the dipping and incoherent reflectors have a low correlation length (blue). It is interesting to note some deeper horizontal reflectors own in the yellow. Even though the depth migrated image from the ambient noise data (Figure 22B, in the background) was not as clean as the image from the active source data (Figure 22A, in the background), the correlation lengths derived from ambient noise look remarkably similar to the section from the active source data.

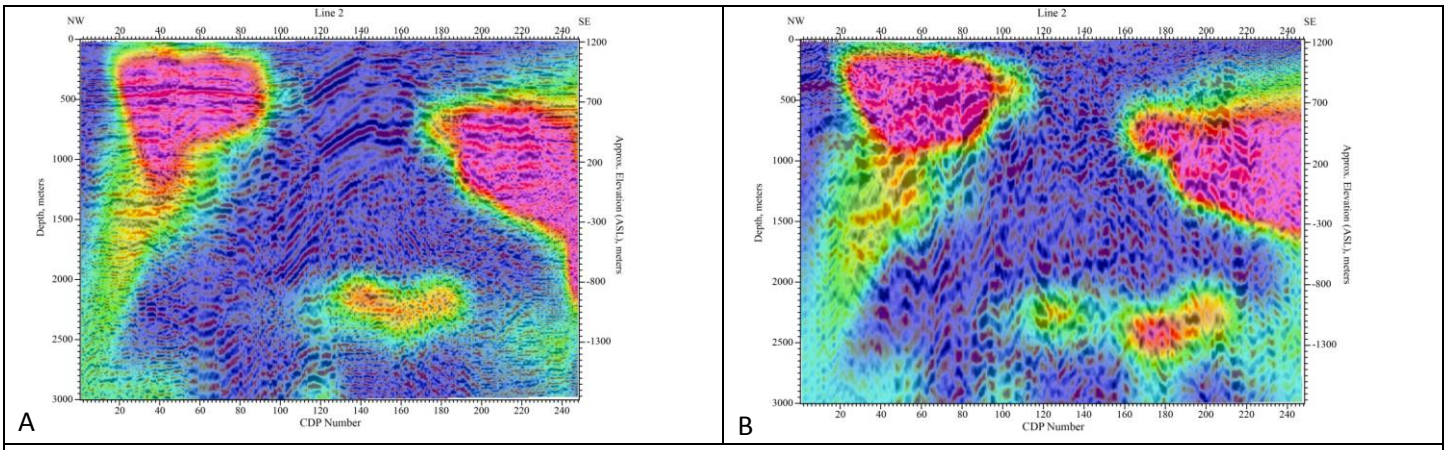

Figure 22: A. Correlation length estimate overlain on the active source depth migration image. Note how the high correlation length values (red/purple) match the horizontal reflectors whilst the blue, and low correlation length values overlay the dipping and incoherent reflectors. B. Correlation length estimate overlain on the ambient noise source depth migration image. Note remarkable similarity between the two measurements.

The Hurst number is related to the fractal dimension of the media. The lower the Hurst number higher the fractal dimension. The objective was to map its variations to see how they correlate with the anomalous zones. Like the correlation length estimation, the Hurst number estimates from the active source and ambient noise migrated data compare remarkably well. The high Hurst numbers highlight the strongly dipping reflectors. They reveal a NW dipping fabric that seem to extend in depth. It highlights the area where the subhorizontal reflectors truncate against this "dome" shaped structures.

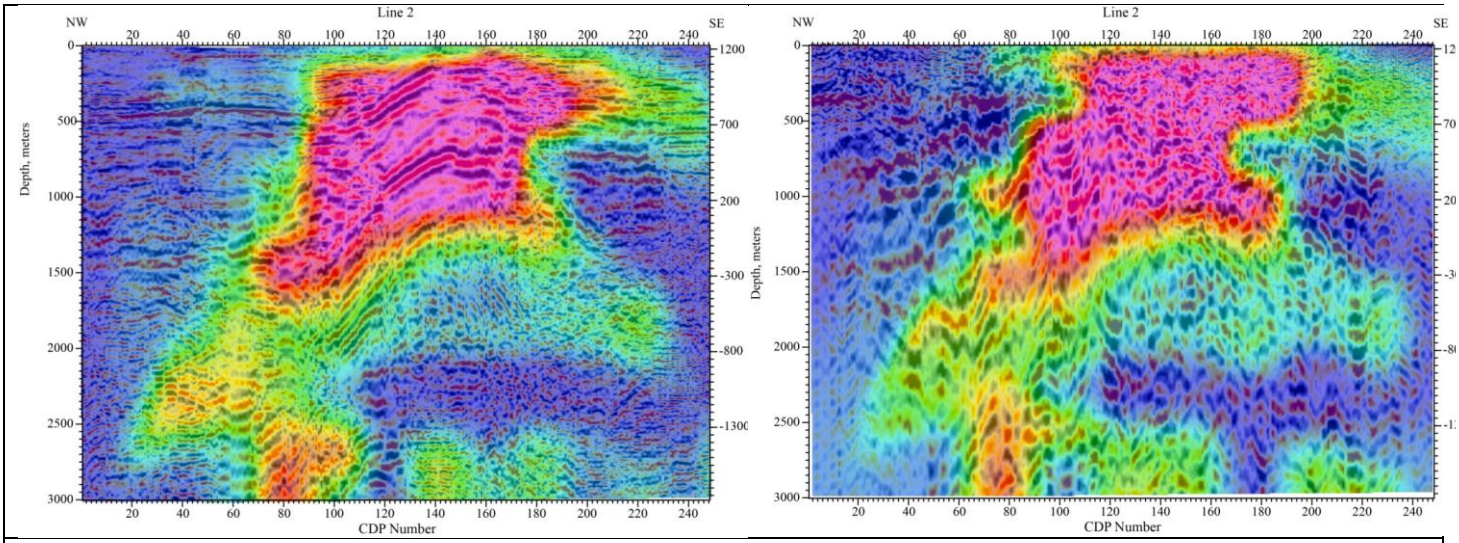

Figure 23. A. Hurst number variations overlain on the active source depth migrated image. The high Hurst number matches very well the strongly dipping reflectors. The values vary from 0 (blue) to 1 (red). B. Hurst number variations determined from the ambient noise depth migrated data (shown in the background). The values vary from 0 (blue) to 1 (red).

4.2. Spectral properties of the reflection components of the Green's functions for the ambient noise survey

A number of surveys over different oil and gas fields throughout the world have established the presence of spectral anomalies in the passive seismic wavefield, i.e., microtremors, with a high degree of correlation to the location of hydrocarbon reservoirs. For instance, Saenger et al. (2009) observed such an energy anomaly in the low-frequency band of passive seismic data between approximately 1Hz and 6 Hz. The exact nature of the physical mechanisms of these

observations above hydrocarbon reservoirs is not fully understood. Several explanations are proposed by Saenger et al.: first, that the hydrocarbon reservoir is partially saturated (e.g., with gas and water) whereas the surrounding rocks are fully saturated with water, that the low-frequency resonant scattering and amplification effects only occur within the reservoir and may modify the background seismic wave field in a way characteristic of the reservoir. These characteristic modifications can be observed in the spectral attributes above hydrocarbon reservoirs. Another possibility would be a higher intensity of low-frequency fracturing and/or fluid migration processes within the reservoir compared to outside the reservoir. Additionally, any kind of body waves hitting the reservoir could contribute to the excitation of resonance effects. In this study, we investigate whether energy anomalies can be observed in the production area along Line 2 (Echols et al., 2011). Hydrothermal reservoirs include fragmented areas and migrating fluids. The question we are trying to solve is whether these fluids have any surface manifestation in terms of energy anomalies.

Unlike other studies, we used the autocorrelations stacks at each station in SL, which are the time domain expressions of mean ambient noise and signal spectra at each site, estimated over 21 days. Using the sign bit representation prior to autocorrelation helps remove most of the cultural noise along Line 2. Three-component spectral analysis of the GF's extracted along Line 2 (Figure 24) shows the difference between the normalized reflection GF power spectral density (PSD) estimated using Welch's method and the mean normalized PSD for the entire line for four frequency intervals: 1-2 Hz, 1-4Hz, 1-6Hz and 7-10 Hz. The 1-2 Hz interval seems to be depleted of energy in the production (Echols, 2011) area (Figure 24A,C), however, only on the Z-component, is higher northwest of the line. On all components, the 7-10 Hz interval is characterized by larger energy in the production area and lower energy northwest of the line. The 1-6 Hz energy is larger in the vicinity of the faults, ie in most fragmented area and lower otherwise, for all components, similar to the 1-4 Hz data.

PSD was estimated in consecutive time windows. The length of the window was 0.2s on the E and N components, and 0.1s on the Z component, with a step of 0.2 of the window length, starting with the reflection GF origin time. The results were shown in Figure 25 for two frequency bands, 7-10 Hz (A-C) and 1-6 Hz (D-F), after the time series were related to depth using SLM in Table 1. When comparing the energy values, note that higher energy occurs above the faults in the production area and is similar, however, larger for the 7-10 Hz range, which is different from the observations in the hydrocarbon fields. It is believed that these observations are not cultural noise artifacts. The majority of the cultural noise occurred at 3 and 30Hz and was removed prior to processing, using band-stop filters. Also, the GF median power was removed in each window, which means any "leaked" cultural noise peaks which were still present were also removed.

At higher frequencies (7-10 Hz), PSD differences may also be attributed to very-near-surface properties, the so-called "site effect", and not to deeper characteristics related to geothermal potential. For instance, according to Figure 20, the depth of the first crustal layer (to 0.1 s) varies correlated to the 7-10 Hz spectral energy variations (lower 7-10 Hz energy is observed for thicker first layer). The 1-6Hz variations, however, are correlated with fault locations, and may be related to geothermal fluids having altered the shallow media. The entropy of differences from site to site, as shown in Section 4.4 and Figure 27B, would not be so large in the fault area if the differences were only due to site effects.

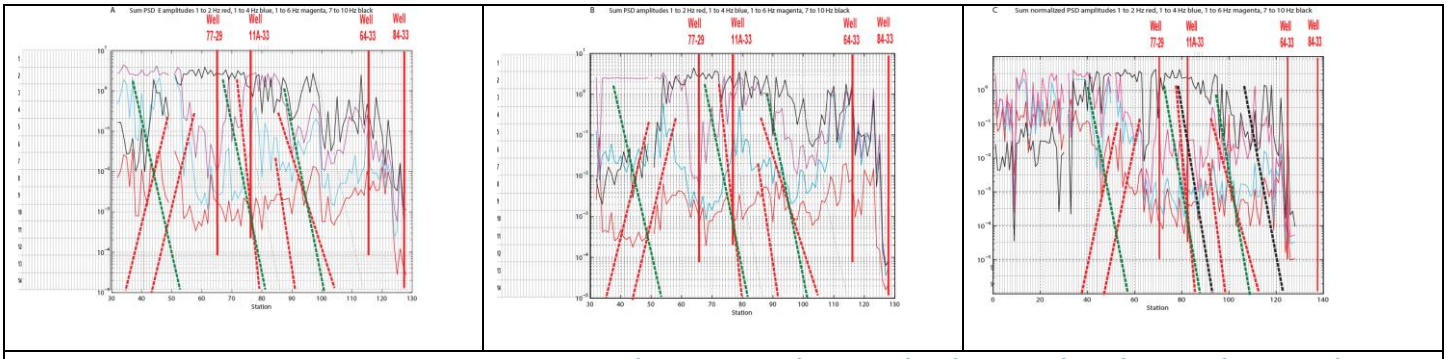

Figure 24. Spectral energy at each station location (on the x-axis): 1-2 Hz (red), 1-4 Hz (blue) 1-6 Hz (magenta) and 7-10 Hz black for the E-component (A), N-component (B) and Z-component (C). The E and N components were not available for the vertical (Z) high frequency geophones installed at W1-W30. The plots show the difference between the normalized reflection GF power spectral density (PSD) in each frequency band, estimated using Welch's method and the median PSD for the entire line.

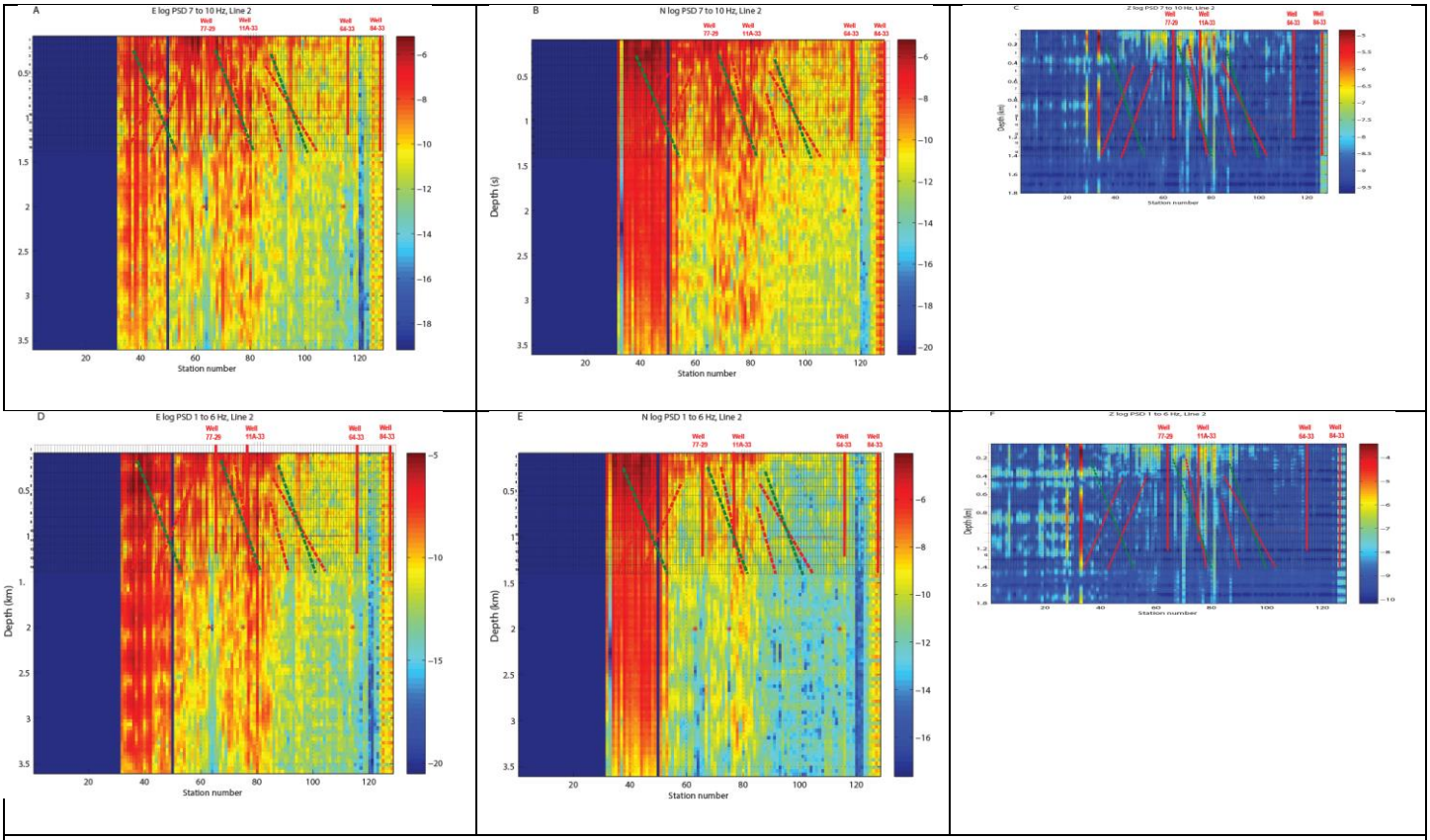

Figure 25. Spectral energy at each station location (on the x-axis) as a function of depth at frequencies from 1-6 Hz. Only vertical (Z) high frequency geophones were installed at W1-W30. The plots show the difference between the normalized reflection GF power spectral density (PSD) from 7-10 Hz (A-C) and for 1-6 Hz (D-F) and the median for all windows in the respective frequency band, estimated using Welch's method. Note higher energy associated with the fault zones, more obvious in the upper 300m. The depth has been related to time lag using the SLM model in Table 1. Note different figure scales due to different sample rates and lengths of the available waveforms. The Z-component was processed at 250 sps in this case, for only 6s, while the E and N components were processed at 125 sps for a waveform length of 15s.

4.3 Attenuation variation for the active and ambient noise surveys along Line 2

As shown in Figure 26, P-arrival attenuation estimated for active and ambient noise data does not show significant patterns. Thus, it was not used for favorability estimation. . Highlights of the analysis detailed in Appendix 5 are shown below. The analysis was performed on the depth migrated sections (see Appendix 5 and Task 5) obtained from both the ambient noise and active source data. Note that the migrated sections are for P-waves and thus the instantaneous Q estimated here are for P-waves only.

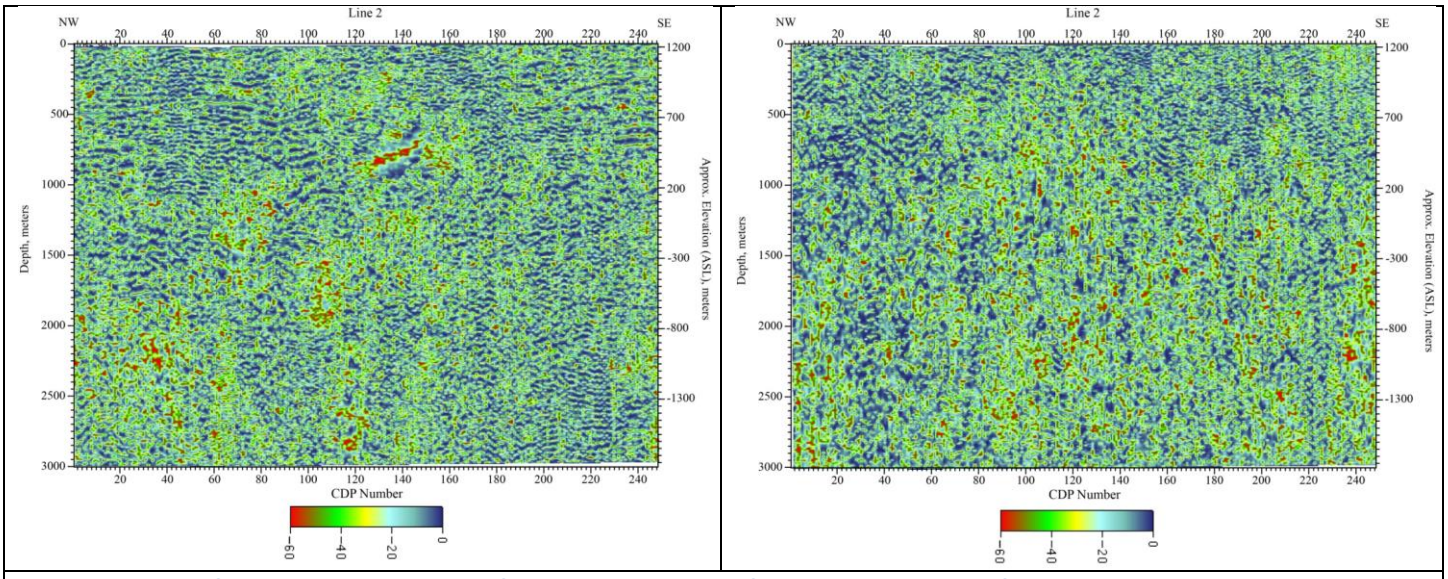

Figure 26. A.Q for P-waves estimated from instantaneous frequency analysis of the active source depth migrated section. The red colors represent higher attenuation. No patterns can be discerned except for the Q. A high attenuation was observed at CDP 140 (Appendix 5) and depth of about 500m. It is along one of the strong dipping reflectors. Values of Q go from 0 (blue) to -60 (red). B. Q for P-waves estimated from instantaneous frequency analysis of the ambient noise depth migrated section (Appendix 5). The red colors represent higher attenuation. No patterns can be discerned from this image. Values of Q go from 0 (blue) to -60 (red).

4.4 Entropy

The wavelet entropy carries information about the degree of order/disorder associated with a multi-frequency signal response. If all the reflection GFs in Figure 20 were similar, the entropy of the difference between any two GFs would be very low. If two successive GFs were very different, the entropy of their difference at each time lag would be large. Two entropy types were tested using the Matlab@ function “wentropy” applied on reflection GFs extracted from autocorrelation beams: Shannon entropy and Threshold entropy (Figure 27). Correspondence was found between high entropy and fault presence in the production area. The “threshold” entropy with a threshold value of 0.3, for the “sym8” wavelet was found to best correspond to the fault and well locations, and was estimated in a 25 sample (0.2s) window. The window moved with no overlap along the reflection GF waveforms. An example of whole record entropy variations using Shannon entropy is shown in Figure 27A. Tests using the two types of entropy show that threshold entropy is more suitable for this case, and the results are shown in Figure 27B.

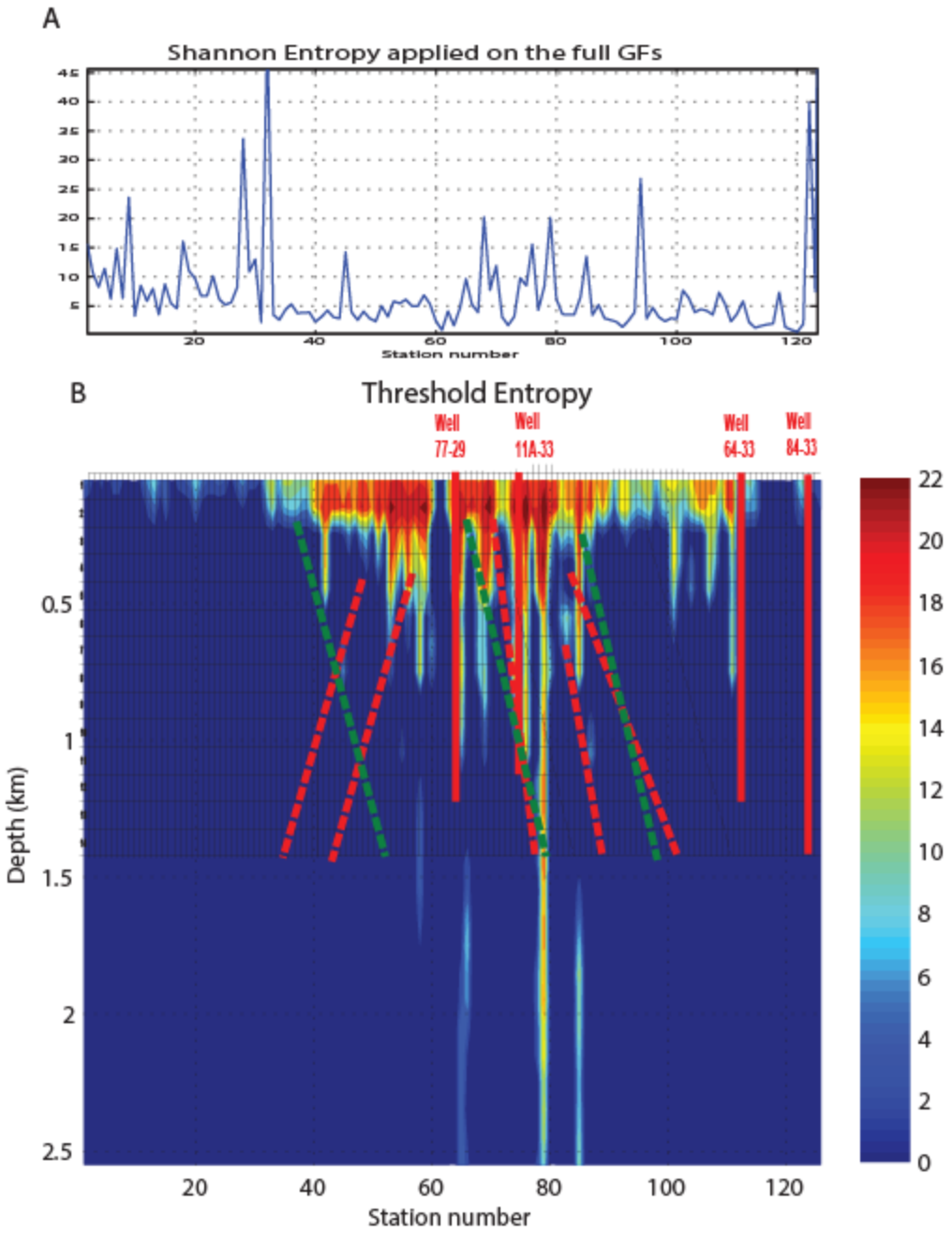

Figure 27 A. Shannon entropy increases for stations on the faults identified along Line 2. The entropy was estimated for the entire waveform, as opposed to consecutive windows in Figure 27B. Shannon entropy was estimated for each autocorrelation difference between two consecutive stations starting with W2-W1 and ending with W128-W127.

B. The entropy of differentiated reflection GFs. Threshold entropy was estimated for each autocorrelation difference between two consecutive stations starting with W2-W1 and ending with W128-W127. If the structure along Line 2 would be uniform, all GFs would be similar and the entropy would be low. The fragmented areas, however, have significant differences in structure and the scattered energy makes the waveforms different. The depth has been related to time lag using the SLM model in Table 1. Note the increase in entropy near the three major geothermal system faults (green lines) identified in Magma (2011) and Echols et al. (2010). Faults are also described at Figure 10B.

Task 5. Assess Seismic Model Resolution and Accuracy

We assess the resolution and accuracy of the ambient noise survey-derived seismic models, when compared to active survey-derived models and evaluate correlation of the seismic parameters described at Task 4 and other existing geophysical information on productive geothermal fields.

5.1 Correlation of Array-estimated Preliminary Seismic Velocity Models to Known Geophysical Features

Correlations of the plan view geoscience data (Figure 28) within the group (Vs and Vp/Vs) and phase (Vs fk analysis) model boundaries are presented below.

1. The area with the highest temperature at depths of 0.3km and 0.6 km (Figures 28A-C) contains the highest gravity anomaly. This anomaly is split by Line 2 and corresponds to the location of the basalt bodies from the gravity-based lithologic profile. A high gravity zone is depicted to the north of Line 2 and this area also corresponds to relatively high temperatures at depths of 0.15km, 0.3km and 0.6 km.
2. The high resistivity area on the MT-based map (Figure 28D) includes a relatively shallow (<400m deep) 3.4 ohm-m resistivity area that is located in the general vicinity of the gravity high, but slightly to the south. This anomaly corresponds to a low Vs anomaly at ~0.3km (Figure 28E) from the surface. Not that a reversed sign Vs anomaly is present at the same location at 800m depth (Figure 28F).
3. The high temperature anomaly (at 0.3km and 0.6km depth) that is split by Line 2 contains Faults 2 and 3 identified by Magma (2011). Magma Fault 1 does not appear to have an impact on temperatures at these three depths. The faults are shown in Figure 28D.
4. The area with the lowest *Vs* values at 0.3km (Figure 28E) is very well correlated with the most significant high temperature anomaly (and also contains Magma Faults 2 and 3 in Figure 28D) at 0.15km, 0.3km and 0.6km depth.
5. The location of the highest *Vp/Vs* ratio at 0.3km (Figure 28is very well correlated with the central portion of the high temperature anomaly at 0.3km and 0.6km. The area is also within the highest temperature isocontour at 0.15km. High *Vp/Vs* ratios are seen as indicators of fluid saturation. Although the 0.8km and 1.4km *Vp/Vs* models represent lower elevations than the thermal maps, these models exhibit similar characteristics with high *Vp/Vs* ratios near the high temperature anomaly. A low *Vp/Vs* is observed immediately north of the middle of the line at 0.3km depth, below which a high *Vp/Vs* area is observed at 0.8km depth. A steam cap was co-located with these anomalies.
6. The SL_PHVEL_MOD is shown in Figure 28 (J-L) and this model had best ray path coverage in the vicinity of the line, and better resolution at 0.3km depth than SL_GVEL_MOD. At 0.3km, which is the best resolved depth (Figure 28 J), *Vs* anomalies correspond to the high temperature along the line in Figures 28A and B.

Notes: The solid blue line superimposed onto the figures produced by Magma is Line 2. The boundary for the Vs and Vp/Vs models is represented by the dark blue dashed line and the light blue dashed line is the boundary for the Vs-fk models. Line 2 is the black and gray line on the velocity model figures. The Vs data represents the difference from mean with warmer (red) colors representing decreased velocities and cooler colors (blue) representing increased velocities.

A

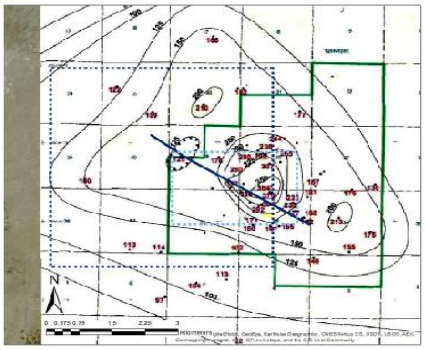

Measured and Extrapolated Temperatures (°F) at a depth of 0.30 km (1000 ft). Modified from Magma (2011).

B

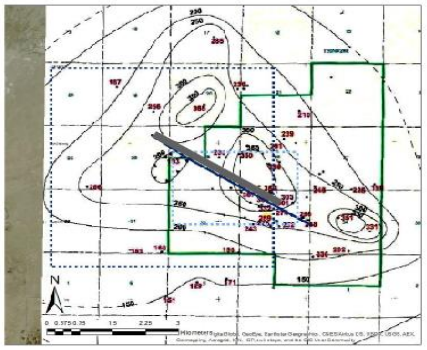

Measured and Extrapolated Temperatures (°F) at a depth of 0.61 km (2000 ft). Modified from Magma (2011).

C

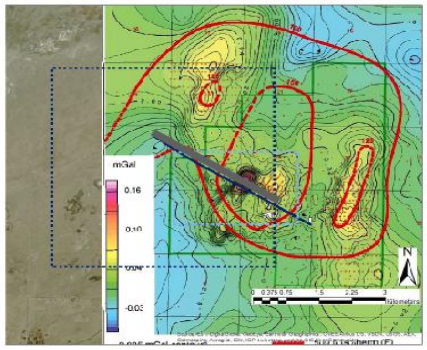

Residual Gravity Anomaly map with the 0.15 km (500 ft) temperature isocontours (°F) in red. Modified from Magma (2011).

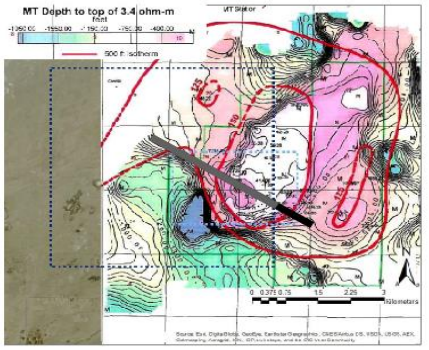

Depth to 3.4 ohm-m resistivity as defined by MT data with the 0.15 km (500ft) 100°F, 125°F and 150°F isocontours. Modified from Magma (2011).

D

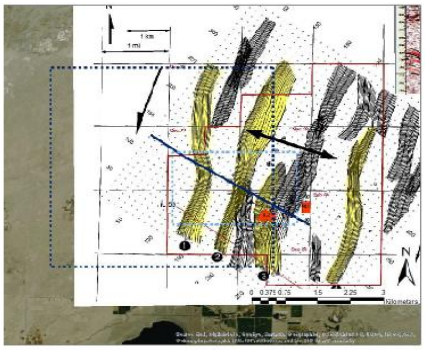

Fault plane map from 0.18 - 1.2 km (600 – 4000 ft) based on a 3D-3C seismic reflection survey. Modified from Magma (2011).

E

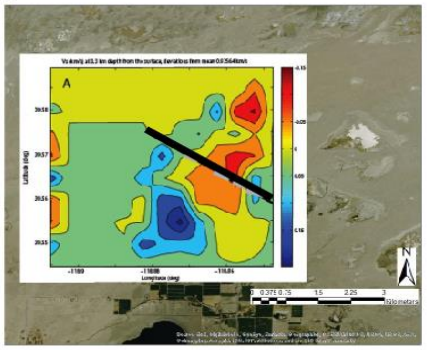

Vs map at a depth of 0.3 km (produced for current study).

F

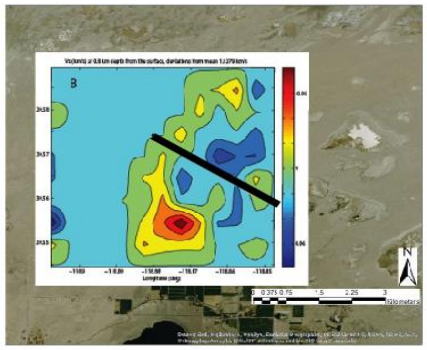

Vs map at a depth of 0.8 km (produced for current study).

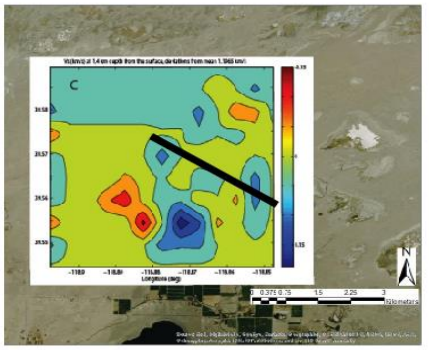

Vs map at a depth of 1.4 km (produced for current study).

Figure 28A-F. Plan view maps for temperature, gravity and temperature, MT resistivity, and faults (A-D) from Magma (2011) and Vs maps ay 0.3km, 0.8lm and 1.4km at Soda Lake

Note:. The black and gray line on the velocity model figures is Line 2. The Vs-fk data represents the difference from mean with warmer (red) colors representing decreased velocities and cooler colors (blue) representing increased velocities.

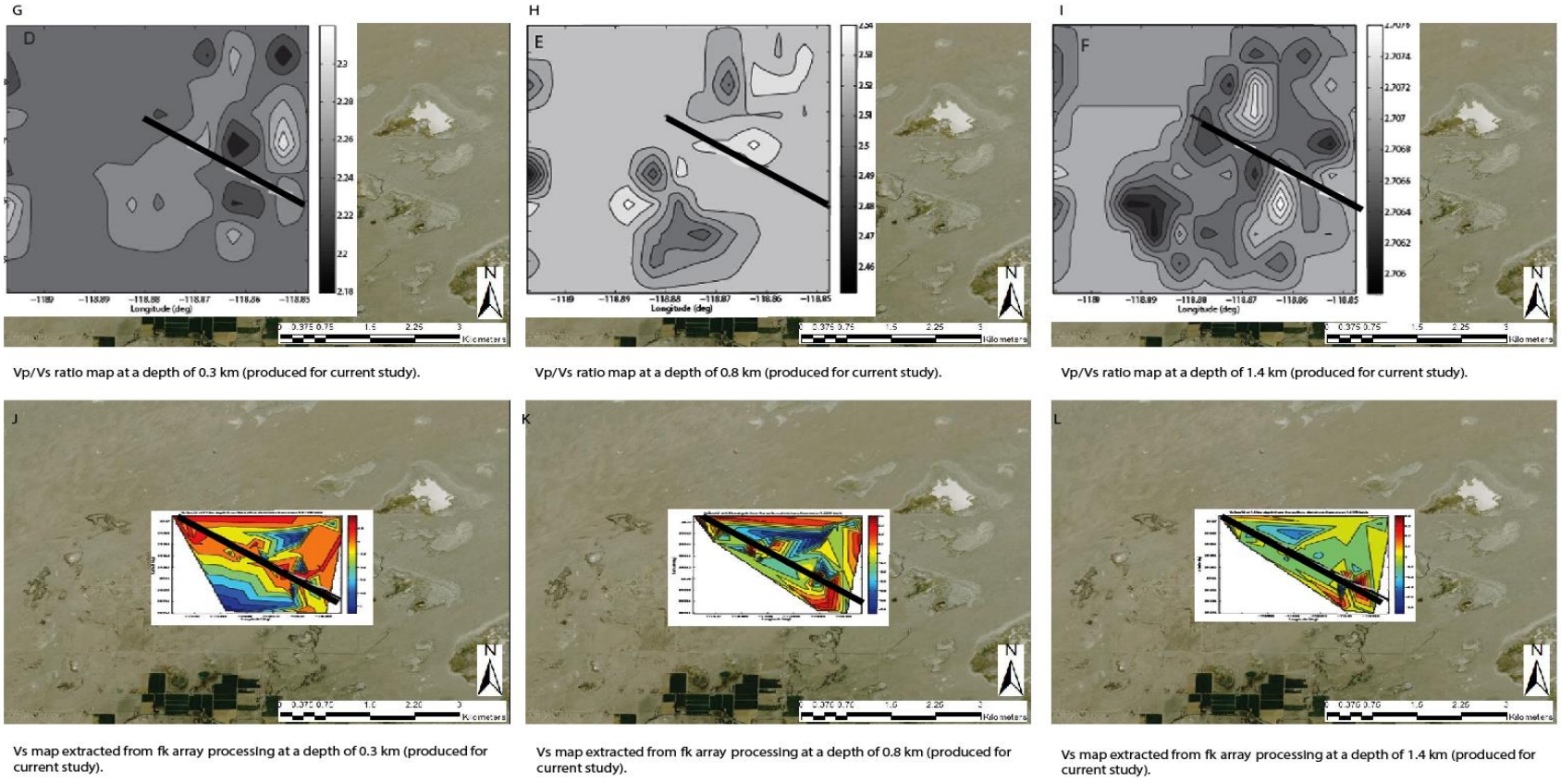

Vp/Vs ratio map at a depth of 0.3 km (produced for current study).

Vp/Vs ratio map at a depth of 0.8 km (produced for current study).

Vp/Vs ratio map at a depth of 1.4 km (produced for current study).

Vs map extracted from fk array processing at a depth of 0.3 km (produced for current study).

Vs map extracted from fk array processing at a depth of 0.8 km (produced for current study).

Vs map extracted from fk array processing at a depth of 1.4 km (produced for current study).

Figure 28G-L. *Vp/Vs* ratio maps at 0.3km, 08.km and 1.4km (G-I) and *Vs* maps at the same depths at Soda Lake, The black line indicates ambient seismic line 2.

5.2 Crosscorrelation stacks between each pair of stations

During this task, as described in detail in Appendix 5, we first derived P-wave velocity model from the active source data recorded along Line 2 and then used it in a pre-stack depth migration to directly image the reflectors in depth. The same model derived from the active source data was used for processing the ambient noise data as well. The S-wave velocity information derived from group-velocity dispersion analysis of the ambient noise data will also be used to process the data (after converting to P-wave velocities) at a later time and so those results are not included in this report. Velocity modeling was done using Optim's SeisOpt® Simulated Annealing Optimization method. SeisOpt® optimization uses only first arrivals from the raw data to accurately predict subsurface velocity structure.

The crosscorrelation stacks between each pair of stations, processed with the same geometry as the active source records, were arranged into virtual shot gathers and were compared to the active source gathers.

Figure 29 shows the depth migrated data using models SL_LINE_3MOD and SL_LINE_FK_MOD. Tests of scaling factors did lead to a value of *Vp/Vs* 2.8 to estimate *Vp* from the *Vs* models. This value was similar, and an independent confirmation of the values from 2.2 (at 0.3 km depth) to 2.7 (at 1.4 km) obtained from Vs analysis. This is a first approximation, and it is estimated that using a nonlinear scaling factor to convert the S- to P-wave velocities would produce even better comparisons. Using a low-resolution *Vp* model estimated from ambient noise would also help the interpretation. The depth migrations are quite comparable for both models, however, the SL_LINE_FK_MOD model produces slightly better results. In the upper 1000m the ambient noise survey compare well to active source. In both surveys, flat reflector(s) at 500m truncate against a dipping structure (around CDP 120, shown in Appendix 5). This is the "dome" structure observed in the active source results (Echols, 2011, Figure 5). The section becomes noisy southeast of CDP 160. Ambient noise resolution is less at depth (below 1500m) compared to the active source. In general, the results are very promising and Figure 29 shows that useful information can be recovered from ambient seismic noise, including dipping features. The migration of the active source data shows horizontal to sub-horizontal reflectors that truncate against a "dome" shaped structure between CDP's 120 and 180. This structure corresponds to the area that has the relatively low P-wave velocity. The resolution is good down to 2,300m or so before we start seeing deterioration of the image quality.

On the other hand, the ambient noise data does not show the dome shaped structure very well. We can see presence of dipping reflectors near CDP 120 and 180 and horizontal reflections truncating against it but the image resolution deteriorates rapidly below 1,000m or so. Deeper reflections are hard to discern. While the ambient noise autocorrelation data (Figure 20) shows clear variations of GF patterns with faults, the depth-migrated ambient noise crosscorrelation GF survey data is less clear.

Figure 29C shows a possible interpretation of faults on the depth migrated image from the active source reflection data. Truncations of sub-horizontal reflections against dipping structure and displacements within the dome shaped structure are interpreted as faults.

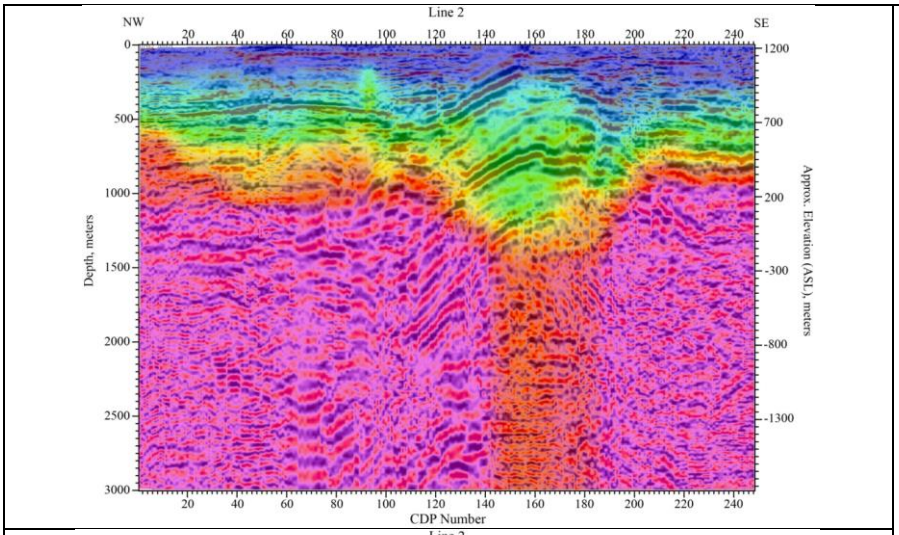

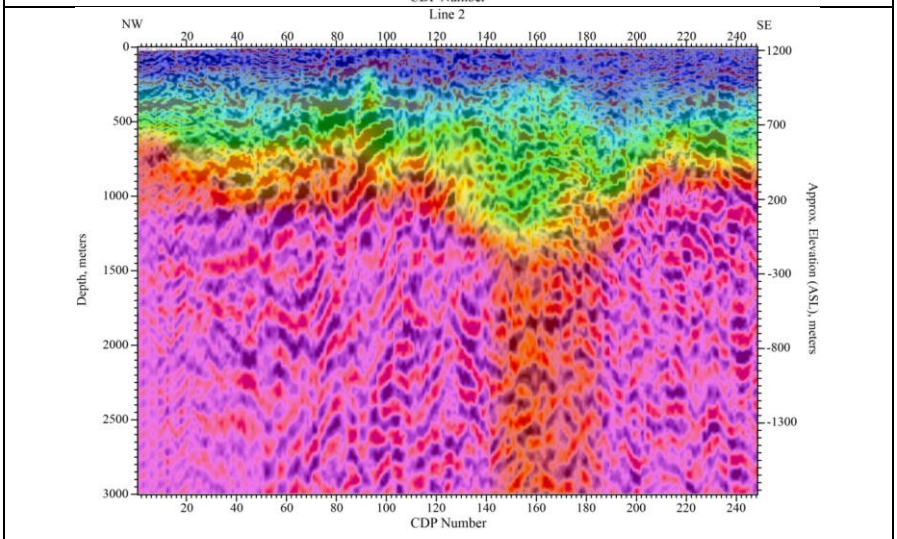

Figure 29A: P-wave velocity model overlain on the active source depth migrated section shown in Figure 7. The doming of reflectors corresponds to the relative low velocity zone between CDP's 120 and 180. The P-wave velocity model superposed here is obtained from the active source reflection data, using SeisOpt® velocity optimization along Line 2. Note the lower velocities between CDP's 120 and 180. Strong lateral velocity variations and in particular the "dip" in velocities are observed at the center of the line. P-wave velocities range from 1,850 m/s to 4,500m/s. The relative lower velocities between CDP's 120 and 180 are probably caused either due to fracturing or faulting.

Figure 29B: P-wave velocity model overlain on the depth migrated section shown in Figure 9. The resolution of the image deteriorates below 1,000m but shallower data show the horizontal and dipping reflections similar to those see in the active source data (Figure 29A). The depth migrated reflection sections are obtained using the velocity model SL_LINE_FK_MOD
Note similarities between the active and ambient noise surveys best in the upper 1000m when using a *Vp* model derived from the SL_LINE_FK_MOD. Also note less similarity between the active and passive survey at the stations near the southeast end of the line, where cultural noise was present.

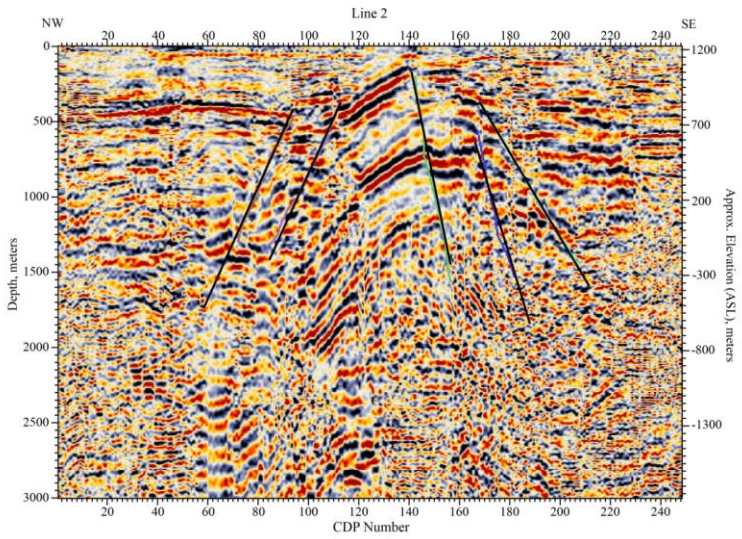

Figure 29C: Fault interpretation of the active source reflection data (Figure 29A). Truncations of horizontal and sub-horizontal reflections against dipping reflectors are interpreted as faults.

Task 6. Statistically Assess Geothermal Reservoir Favorability

We generated gridded sections of all the key geoscience data. We conducted a qualitative examination of the geoscience sections and a geostatistical analysis of the geoscience parameter relationships. Favorability maps were generated for all the active and passive seismic survey estimated attributes coupled with temperature and lithology.

6.1 Geologic and Geophysical Setting

This section has been based on the two Magma Energy Corp. (Magma) reports: Magma (2011) and Magma (2012) as well as McLachlan et al. (2011) and McLachlan et al. (2013).

6.1.1 Soda Lake Geothermal field background

In 1971, the US Geological Survey (USGS) identified the SL area as a Known Geothermal Resource Area (KGRA) based on the presence of an extinct fumarole or an area of steaming ground, small and scattered amounts of silica cemented Quaternary alluvium, and the young SL and Upsal Hogback volcanic features. The regional setting of the SL resource is shown in Figure 30. Phillips Petroleum Company, partnered with Chevron Resources Company, drilled up to 36 temperature gradient holes(TGHs) up to about 153m (500ft) deep over an area of 35-40 mi^2 (Figure 31). The USGS also drilled a few slightly deeper TGHS (Magma, 2011).

The TGHs defined an approximately circular temperature anomaly aligned along a postulated NNE-trending structure connecting SL and Upsal Hogback. Several deep geothermal wells were drilled by Phillips/Chevron including 77-29 to a total depth of 1329m (4306ft) with a maximum temperature of 172°C (342°F). The deepest and hottest well in the field, 84-33, was drilled to a total depth of 2584m (8489ft) and a maximum temperature of 203°C (397°F) at 8100ft. In December 1977, Ormat and Chevron began commercial geothermal electrical generation (SL 1 power plant, 3.6 MW gross) at SL using 77-29 and 84-33 as the injection and production wells, respectively (McNitt, 1990). Given the success of this first plant, Ormat started development drilling for an 18 MW gross SL 2 power plant and an additional 1.5 MW (gross) at SL 1. A total of 15 wells and 2 redrillls were drilled by Ormat (March 1990-June 1991) located between 77-29 and 84-33. Ormat drilled 15 consecutive wells and two redrills at SL between March 1990 and June 1991. Adequate fluid supply to operate both power plants at full output was not achieved. Ormat drilled its last and successful well, 32-33, in October 1993 and then sold its interest in the project to Constellation Energy who drilled an unsuccessful well, 22-33 and its redrill in 2002. In 2008, Magma Energy (U.S.) Corp. (Magma) purchased the project from Constellation and

drilled three deep wells (2009-2010) within the existing field. Given the rapid expansion of the field, the initial conditions of the resource were not

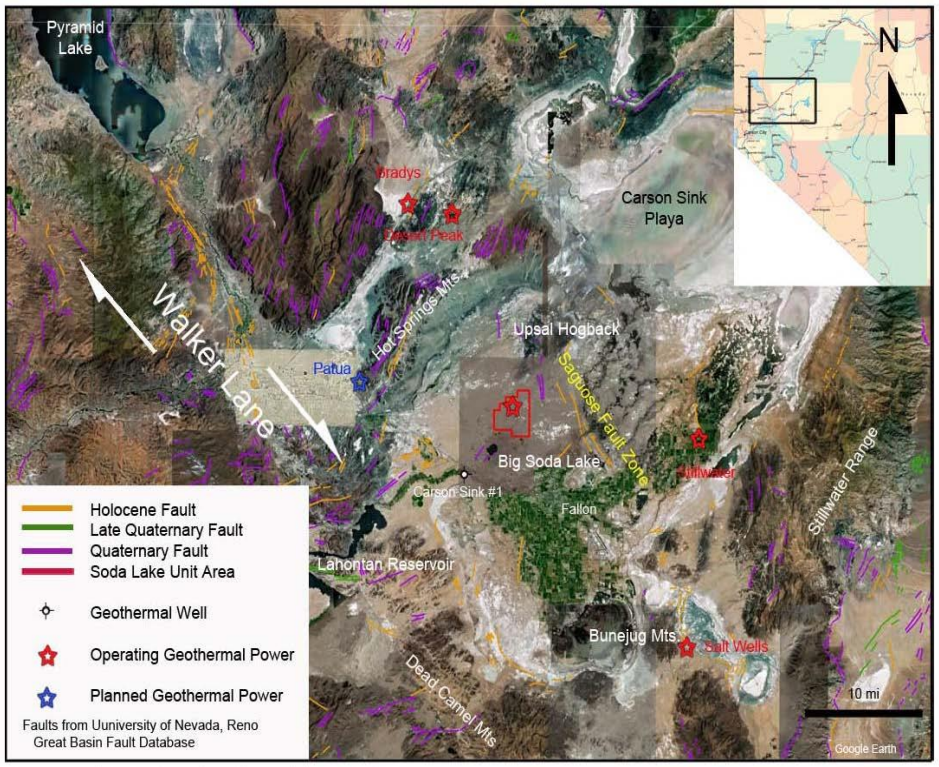

Figure 30. Regional setting of the Soda Lake Geothermal resource (from Magma, 2011)

adequately characterized and its overall pressure history is poorly documented and poorly understood (Magma, 2011). Two small diameter geothermal observations holes were drilled by Magma as part of their US Department of Energy (DOE) Phase 1 Project, DOE contract no. DE-EE0002832: 44B-34 and 46A-20 (Magma, 2012). As of 2012, a total of 23 geothermal wells and six redrills have been completed but only five wells were utilized for production and five for injection (Magma, 2011).

6.1.2 Geology

6.1.2.1 Regional Geology and Tectonic Environment

The following description is excerpted from Magma (2011).

> "The Soda Lake geothermal field lies directly between the… Big Soda Lake volcanic explosion crater, and the mafic Quaternary Upsal Hogback volcanic complex…*[Figure 30]…* These…*[three]*…features define a narrow NNE trending 11 mile-long feature that presumably is the surface expression of a buried deep-seated feature. *[McLachlan et al. (2011) reported that the Sold Lake explosion crater (a maar is ~6000 years-old and the Upsol Hogback is about 600,000-700,00 years-old, Figure 32).]*…The surface of the Carson Sink is covered by Quaternary alluvium, sand dunes, silt, and a large playa surface. There are only four small and widely scattered outcrops of Tertiary or Quaternary mafic volcanic rocks within the Carson Sink, which is the widest valley in Western Nevada… The southern part of the Carson Sink is bounded to the northwest by the low relief and irregularly shaped Hot Spring Mountains and unnamed hills southwest of Patua…*[Figure 30]* …The Carson Sink defines a major change in topography from the classical Basin and Range mountains and valleys to the east to the lower relief and irregular topography typical of far western Nevada. These surrounding lower relief ranges are composed primarily of Miocene and Pliocene mafic lava flows, tuffs and lacustrine sedimentary rocks which vary considerably from range to range… Beneath the Miocene mafic rocks in the surrounding ranges there is a variable sequence of Miocene and Oligocene rhyolitic ash flow

tuffs which can be the oldest rocks exposed in the individual ranges…These basement rocks have been penetrated in the 81-33 and 84-33 wells at depths of 7500 and 7800 ft, beneath 3000 to 4000 ft of Tertiary volcanic and sedimentary material.

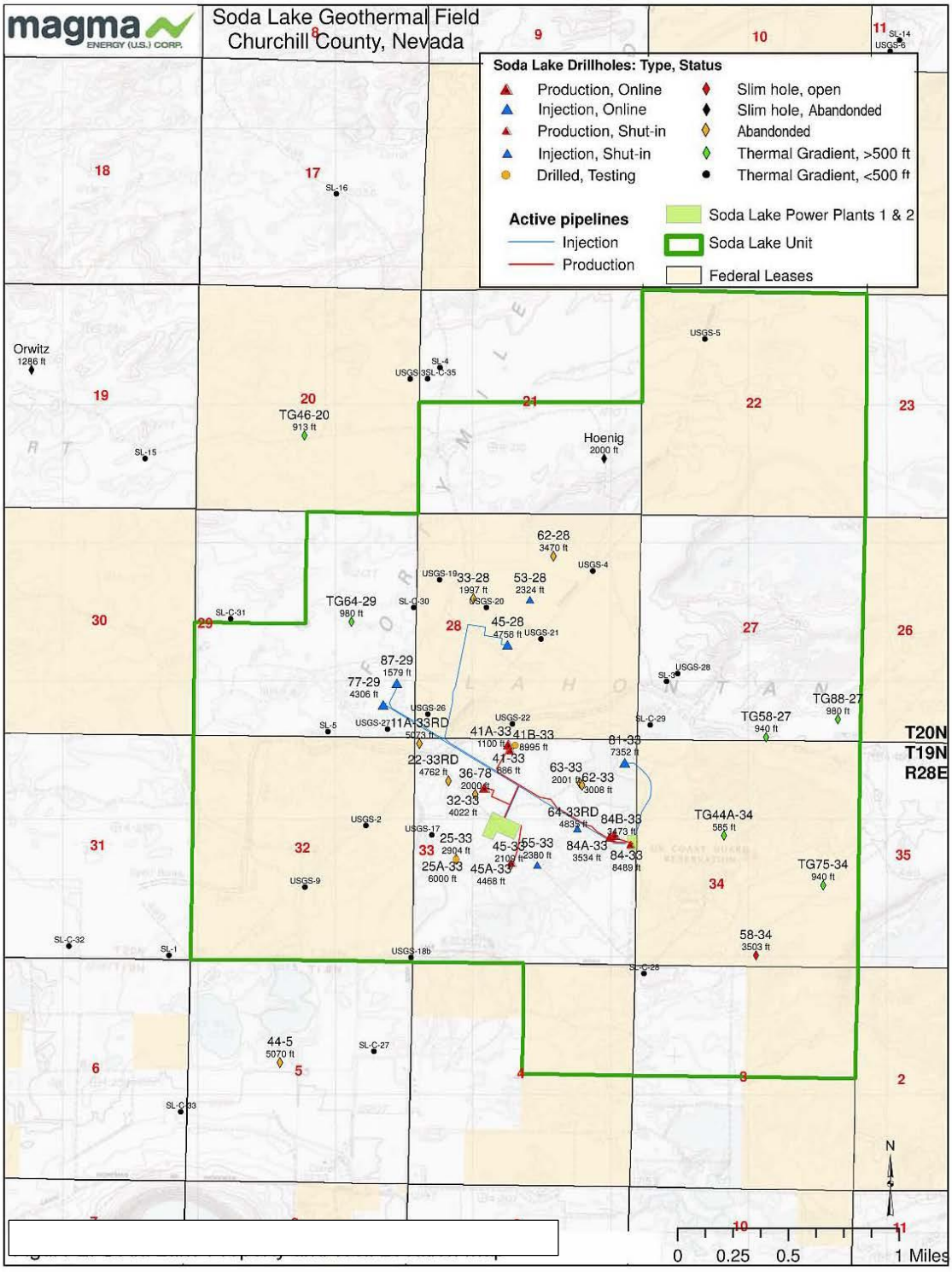

Figure 31. Soda Lake geothermal wellfield (from Magma, 2010)

The Soda Lake geothermal field is located on top of a gravity high defining a semi-circular ridge or ring about six miles across…*[Figure 32]*…Hill et al., (1979) with a much smaller gravity data set described the field as being on the east rim of a two mile-wide circular low. Gravity anomaly shapes near Soda Lake are more representative of the irregular topography currently surrounding the southwestern part of the Carson Sink than of classical NNE trending basin and range topography. Deeper drill holes in the Soda Lake area, with the exceptions of well 81-33, which reached pre-Tertiary sedimentary rocks, and 84-33, which terminated in granite, were completed in Tertiary volcanic rocks. This suggests the gravity high represents a relatively shallow buried Tertiary volcanic basement surface covered by Quaternary sediments of the Carson River delta, NE of Lahontan Reservoir, and the Pleistocene-age Lake Lahontan. On a more detailed level the Soda Lake resource lies within the northwest trending portion of this gravity high. The Soda Lake field is the only geothermal system associated with this buried gravity high.

The Walker Lane, a region defined by northwest-striking, right lateral strike-slip faults, is recognized as being the easternmost expression of lateral motion between the North American and Pacific plates and accommodates +20% of the dextral motion between the two plates. The northern edge of the Walker Lane has historically been viewed as being located seven or eight miles southwest of the Soda Lake geothermal field (Hill et al., 1979). There are no mapped surficial indications of the Walker Lane's presence south of Soda Lake…*[Figure 30]*…The poorly defined and little-studied Sagouse fault zone (Adams and Sawyer, 1999) is located sub parallel to the Walker Lane and passes through the Upsal Hogback area several miles north of the Soda Lake geothermal field…*[Figure 30]*…This opens the possibility that the Soda Lake field could be within an outer fringe of shear along the Walker Lane."

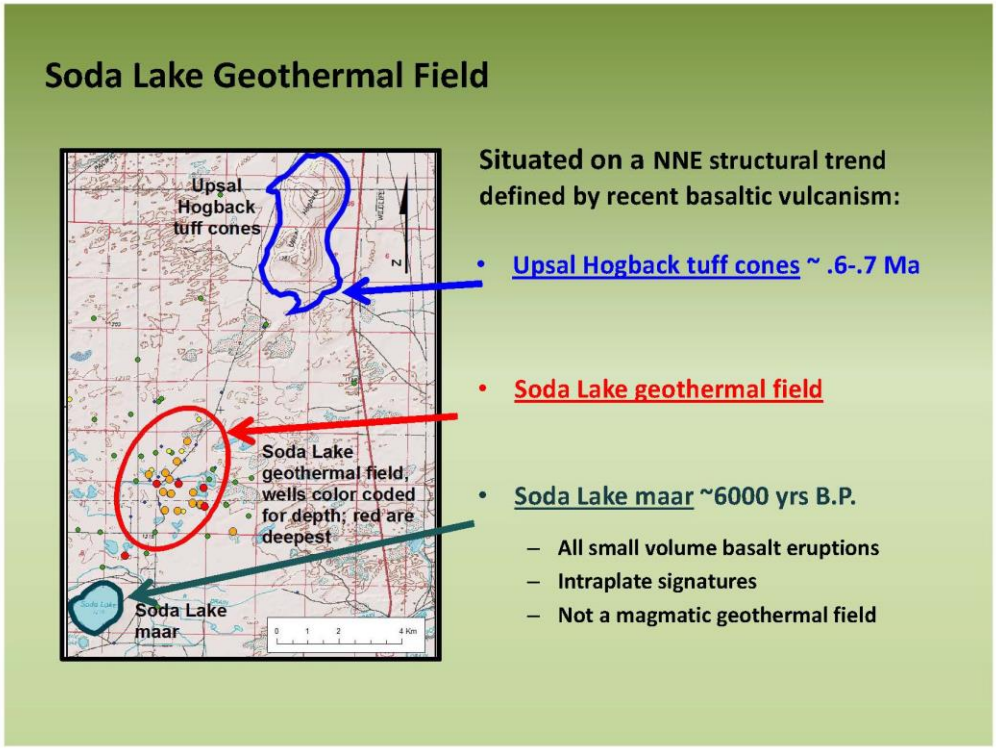

Figure 32. Local setting of the Soda Lake geothermal field (from McLachlan et al. 2013)

6.1.2.2. Local Geology

Based on a detailed review of the lithology from 50,000+ ft of drill cuttings and gravity data, McLachlan et al. (2013) defined a coherent subsurface 3-unit stratigraphy (i.e., basin fill, basalt and basement) for the SL geothermal field wells based on both re-logging the drill cuttings and the density of the lithologies in the field. This stratigraphic model is the

most comprehensive and accurate model to data given the numerous and varied contributors to the lithologic logging over about 30 years of assessment. The current authors have adopted this stratigraphy for their analysis of the ambient seismic noise line investigated in this study. This stratigraphic-density model was used to interpret the subsurface stratigraphic correlations in the vicinity of Line 2 (Figure 33).

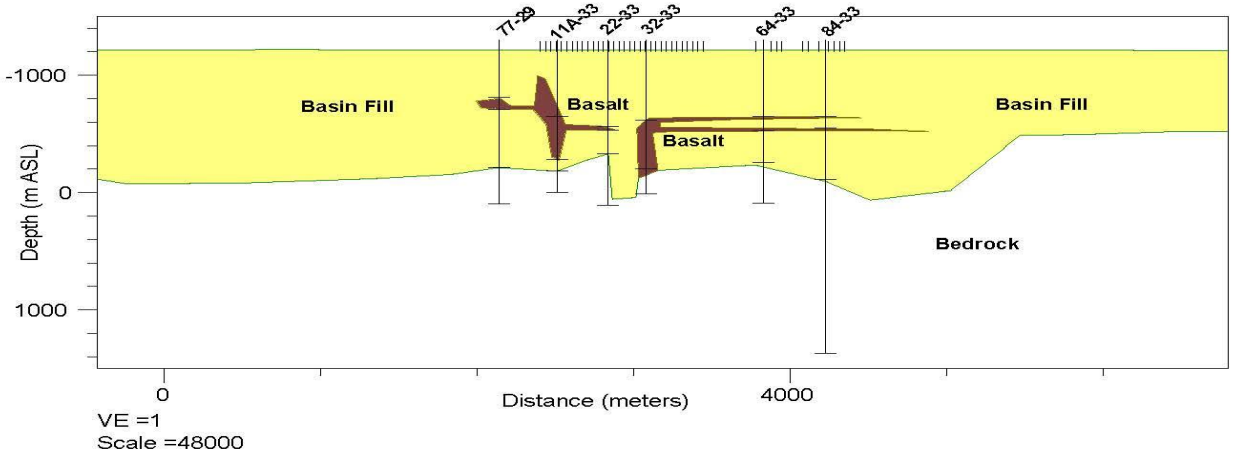

Figure 33. Combined stratigraphic-gravity model for Line 2 (ambient seismic noise investigation line) at the Soda Lake geothermal field (courtesy of Holly McLachlan [PhD candidate at the University of Nevada Reno, 2015).

The 3-unit, gravity-constrained lithologic cross section (Figure 33) was developed based on the presence of 3 distinct density packages identified by forward modeling of gravity data in Oasis montaj GM-SYS 2D software. A similar 3-unit density approach was described by Magma (2011) and clastic compaction curves from borehole data provided densities of 2.1 g/cc for the unconsolidated basin fill, 2.6 g/cc for the basalt, and 2.7 g/cc for the basin floor rocks. Location of the basalt body was an iterative process, performed repeatedly until its location matched the gravity data within acceptable tolerances.

Three previously documented Magma (2011) major faults (1, 2 and 3) intersect Line 2 and a discussion of these structures is included in the discussion in Section 6.1.3.1.

6.1.3 Geophysics

6.1.3.1 Thermal Structure

As reported by Magma (2011), the SL shallow thermal anomaly to 153m (500ft) was generally outlined in the 1970s. It is approximately circular covering 30-35 mi^2 (Figure 34) Measured temperatures at this depth are 21°C to 170°C (69°F to 338°F). The high shallow temperatures and temperature gradients focused exploration and development for more than three decades in the south half of Section 28, the north half of Section 33, and the southeast corner of Section 29 (Figure 34). Not well thermally-defined are the eastern, northern, and western boundaries of thermal anomaly. The southern boundary is relatively well-defined with shallow flow of cold water toward the north. Reanalysis of these data by Magma indicated that (1) the western portion of the shallow thermal anomaly probably contains a NNE-trending sub-anomaly and the area east of the operating field in Section 34 around the discovery well, 84-33, was never further explored. As a result, Magma drilled additional TGHs up to 305m (1000ft) to the east and northeast of the operating plant area. Measured and extrapolated temperatures to 305m (1000 ft), Figure 35, have a comparable thermal anomaly as (Figure 34) but the subsidiary thermal anomalies in Sections 20 and 34 are more apparent with maximum measured temperatures of ~100°C (~212°F). Comparable temperatures at 610m (2000ft) in the subsidiary thermal anomalies approximate the central anomaly measured temperatures at the same depth (Figure 36).

Three thermal aquifers have been defined by Magma at (1) depths of 122-305m (400-1000ft), Figure 37, in unconsolidated Quaternary alluvium; (2) a depth of 605m (2000ft), Figure 38, where a weakly-flowing and relatively poorly-defined intermediate-depth thermal aquifer occur generally associated with the basaltic unit and not significantly utilized for production or injection; and (3) depths of 1006-1219m (3300-4000 ft), Figure 39, where the deepest and hottest of the sub-horizontal aquifers occurs in basement unit.

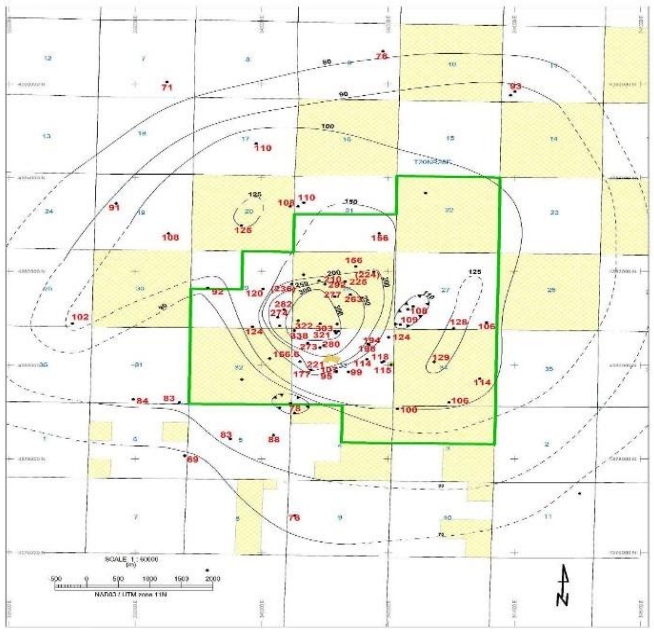

Figure 34. Measured Soda Lake thermal anomaly in °F at 153m (500ft). The figure is from Magma, 2011).

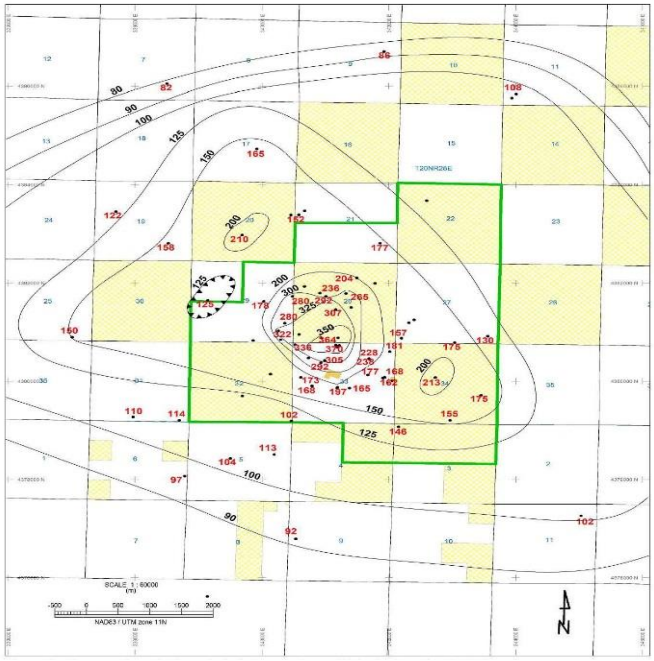

Figure 35. Measured Soda Lake thermal anomaly in °F at 305m (1000ft). The figure is from Magma, 2011).

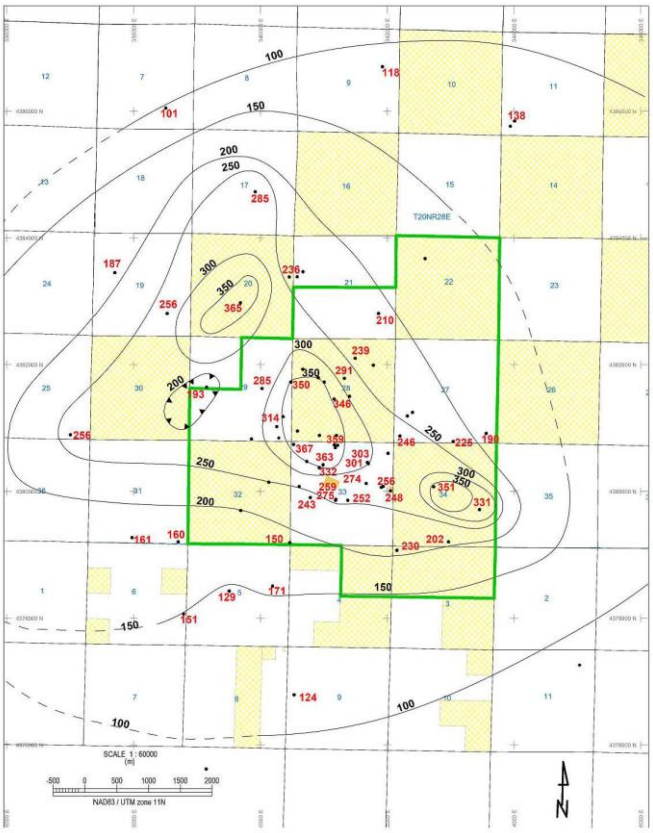

Figure 36. Measured Soda Lake thermal anomaly in °F at 610m (2000ft). The figure is from Magma, 2011).

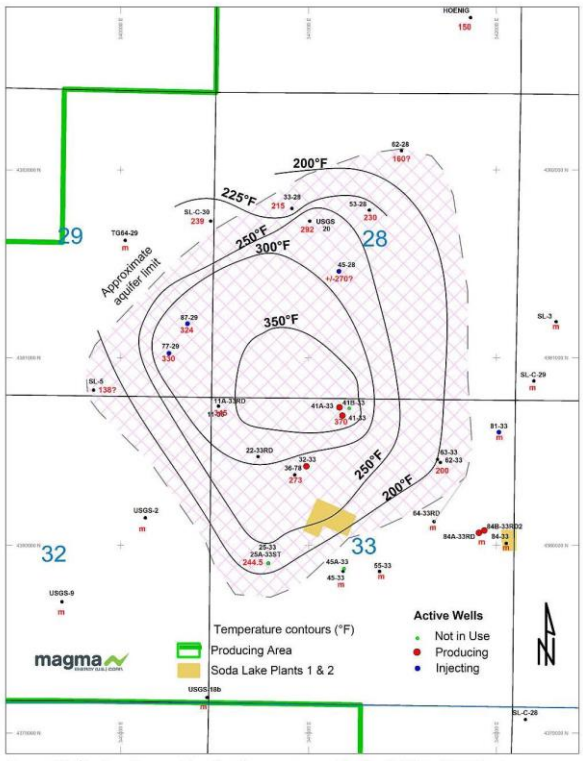

Figure 37. Shallow thermal aquifer between 122-305m (400-1000ft) in the basin-fill unit. The figure is from Magma, 2011).

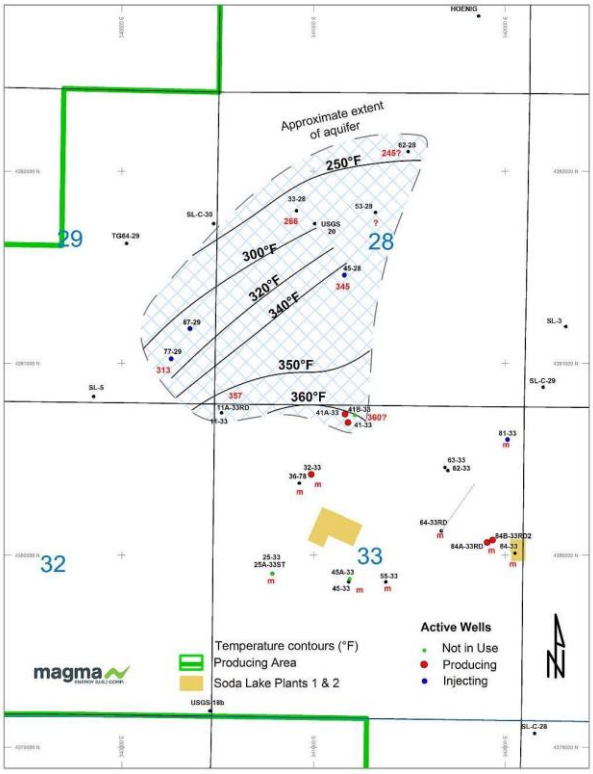

Figure 38. Intermediate thermal aquifer at approximately 605m (2000ft) in the basalt unit. The figure is from Magma, 2011).

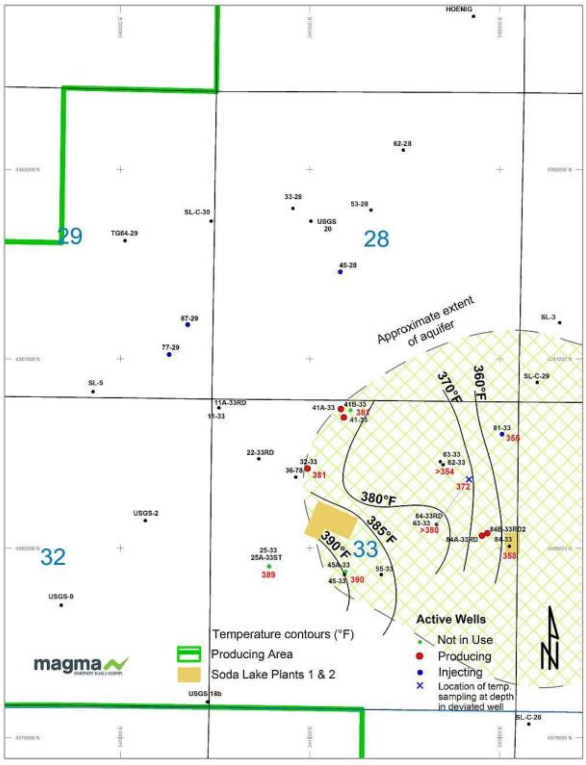

Figure 39. Deep thermal aquifer at approximately1067-1524m (3500-5000ft) in the basement unit. The figure is from Magma, 2011).

At the depths of 1245-1509m (4100-4950 ft) temperatures >390°F are encountered in 25A-33 and 45A-33. These wells are interpreted to be near a deep near-vertical upflow zone but they only have modest permeability. It appears that the hottest wells at SL are in proximity to the southern margin of the thermal anomaly. Chemical geothermometry is reported to have a maximum temperatures of slightly greater than 204°C (400°F) which is slightly greater than the 203°C (397°F) measured near the bottom of 84-33.

Magma reported that the vertical permeability in the field, allowing temperatures of 189°C (372°F) at 259m (850ft), must connect these three aquifers to the deeper thermal water. This vertical permeability is found to be most pronounced at shallow depths near 41-33 and dips southerly toward the 25A-33 and 45A-33 with depth. Results from four tracer tests in 2009 indicated no flow between the western (area of 32-33 and 41A-33) and eastern (area of 84A and 84B-33) parts of the field. The tracers travelled in a N-S direction instead of an anticipated E-W direction indicating some compartmentalization in the reservoir at a 244-1219m (800-4000ft) depth.

For this investigation the thermal data was extracted from a 3D block model compiled by Magma using Oasis Montaj software. The model represents the most complete data set available to this project at the time of this writing and it includes multiple geophysical and geologic data layers. The thermal model along the ambient seismic line2 is included as Figure 40 along with wells within 100 m of this seismic line. GIS software was used to georeference a plan-view fault plane map (Figure 41) with major fault locations along the line identified by Magma (2011) and the line was overlain on this image to estimate fault locations beneath Line 2. Major fault locations estimated from the structural contour map (previously interpreted by Magma) were superimposed onto all gridded data profiles analyzed for the current study. Individual structural contours from the 2011 map were not sufficiently discernable to allow for an estimation of fault plane curvature beneath Line 2 and, as such, faults included on the gridded profiles represent straight lines joining Magma's uppermost (600ft) and lowermost (4,000 ft) fault plane contours.

Fault interpretations from the active source reflection data provided by Optim (2015), provided in Appendix 5)and Magma (2011) were both considered for the current study. As shown in Figure 29C, Optim interpreted truncations of horizontal and sub-horizontal reflections against dipping reflectors as faults. The gridded profiles presented in this section include faults interpreted by both Magma and Optim. Magma (2011) included seismic reflection profiles (from areas not coincident with Line 2) with their fault interpretations and smaller faults included on their seismic profile figures were not presented with their structural contour map (Figure 41). The ambient seismic noise analyses are capable of identifying faults and inclusion of faults from Magma and Optim allowed for an assessment of qualitative and quantitative relationships between identified seismic attributes and the faults identified by both sources.

Figure 40 is the first of a number of geoscience parameters gridded for statistical and favorability analysis for this study. The following discussion of the Optim and Magma identified faults applies to all the gridded figures where both of these fault sets are shown. Optim interpreted a fault immediately to the east of Well 77-29 and this fault may correspond to Magma Fault 2 or an adjacent minor fault identified by Magma. Optim also interpreted a fault to the east of Well 11A-33 that is likely correlated with Fault 3 identified by Magma. One fault solely identified by Optim and another fault only identified by Magma are present in the portion of Line 2 between Wells 77-29 and 64-33. However, all recognized faults to the east of Well 77-29 have similar, east-dipping inclinations. Optim interpreted two west dipping faults west of Well 77-29 that were not identified by Magma. Optim's analysis did not resolve the presence of Fault 1 (Magma), which dips to the east and is also located to the west of Well 77-29.

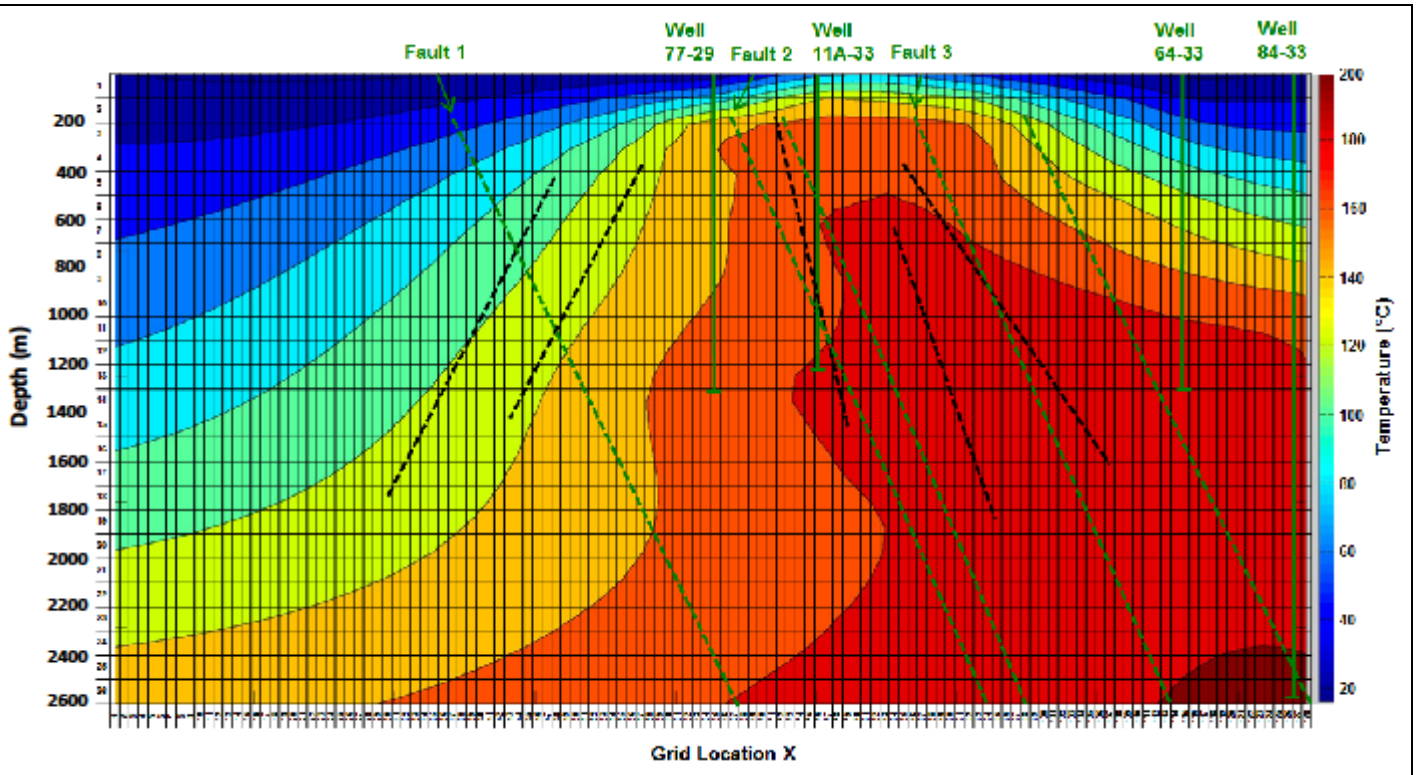

Figure 40. Gridded temperature distribution along the ambient seismic line2 with key fault locations estimated from Optim (2015), see text, and Magma (2011). Optim faults are presented in black while major (Faults 1, 2 and 3) and minor Magma (2011) faults are shown in green.

6.1.3.2 Distribution of Permeability

Magma (2001) reported that permeability at the SL geothermal field at all depths has proven difficult to locate and understand. For example, circulation losses in 77-29 were only partial when the shallow thermal aquifer was penetrated during drilling but complete losses occurred while running 13 3/8" casing. This permeability interval was cemented behind casing but later perforations restored high productivity and injectivity. Similarlily, the 84-33 producing zone was put behind casing and drilling of 84A-33 and 84B-33 within meters of the 84-33 production zone required three redrills to access permeability. No major lost circulation was encountered during drilling of 81-33 but when the well was changed over from mud to water, total lost circulation developed and the injectivity greatly improved over time as it was used for injection. In Orhen et al. (2011) reported 25A-33 sustained permeability in 25A-33 only developed after deflagration and injected for a few weeks. It has been postulated by McNitt (1990) that the SL geothermal reservoir primarily consists of thermal fluid movement along stratigraphic horizons. Drilling since 1990 has not resolved whether the permeability is primarily sub-horizontal or near-vertical in nature.

A permeability map for the SL reservoir was not available to this study.

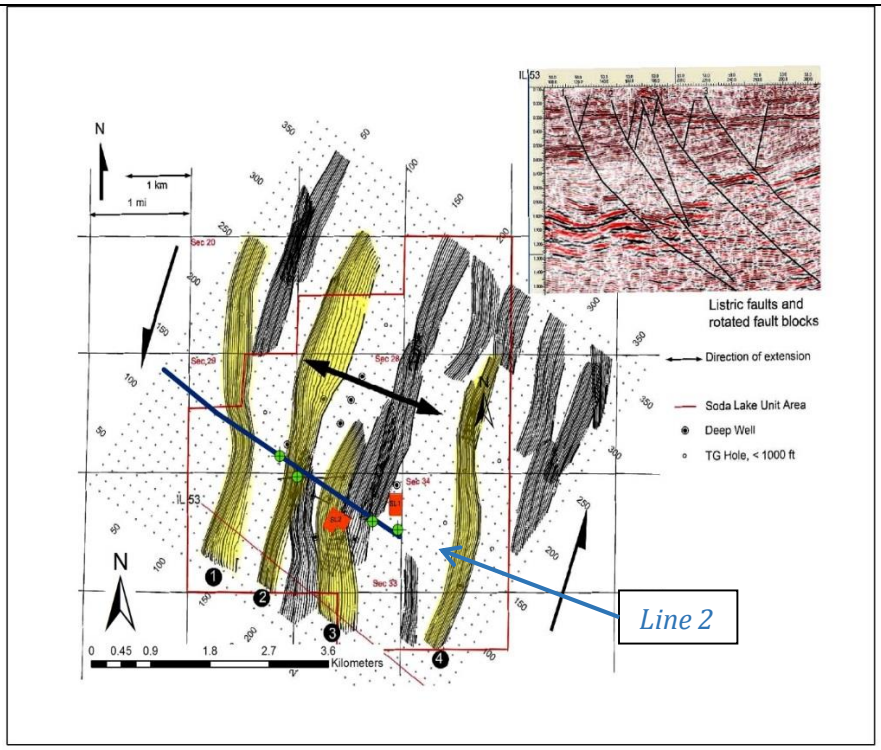

Figure 41. Fault plane map from 600-4000ft based on the 3D-3C seismic reflection survey (modified from Magma, 2011). Seismic line2 is shown in blue. Figure 45 includes the corresponding well ID numbers.

6.1.3.3 Gravity Surveys

An initial gravity survey identified a NW-trending gravity ridge in the field (Figure 42; McNitt, 1990) leading to a "poorly supported hypothesis of a NW-trending structure (Magma, 2011). Teplow (2011) in an unpublished report on a more precise and detailed gravity survey, documented in Magma (2011), identified local positive gravity anomalies on the order of milligals on top of the NW-trending ridge. A detailed microgravity survey in 2008 with a resolution of 0.03-0.05 mgal by Magma identified and corrected mislocated 2001 gravity stations and the relocated small positive gravity anomalies were reported to be spatially related to small and scattered surface silicified alluvial deposits. This recognition by Magma resulted in an additional microgravity survey with a resolution of 0.003-0.005 mgal which reconfirmed the existence of small residual gravity anomalies sitting on top of the larger previously known gravity ridge. Figure 43 is the Complete Bouguer Anomaly (CBA) of these data. The producing portion of the field has a gravity relief of 0.8 mgal and is defined by the 96 Mgal contour (Figure 43). It was also noted by Magma that similar size and magnitude CBAs occur within the shallow thermal anomaly (Figure 34) in Section 20 (northwest of field) and Section 34 (east of the field).

Figure 44 presents a filtered residual gravity anomaly (RGA) map (Magma, 2011) with the 152m (500ft) temperature isocontours emphasizing small-contrast density anomalies from the surface to 198m (650ft). Two distinct slightly elongated anomalies occur in the producing field supporting the possibility of two upflow zones or alternately one major upflow zone with a physical separation in the upper 198m (650ft). Much longer densified intervals occur in Sections 20 and 17 as well as Sections 34 and 27 correlating with elevated thermal conditions supporting the hypothesis of shallow hydrothermal flow and silicification of Quaternary alluvium in these areas.

A gravity cross-section prepared by Ms. Holly McLachlan, a PhD candidate at the University of Nevada Reno is presented in Figure 33 and the gridded profile with the faults discussed above is presented in Figure 45.

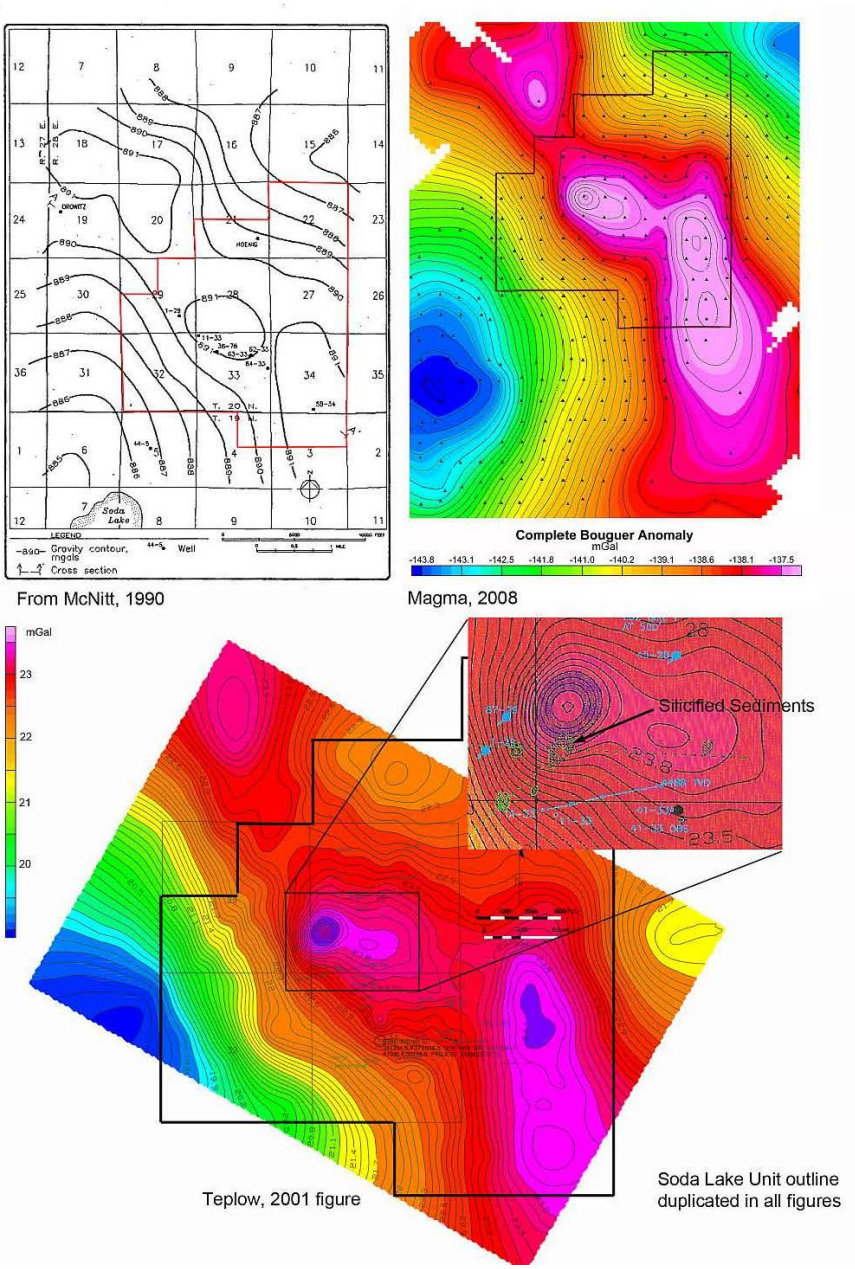

Figure 42. Results of a Soda Lake gravity survey conducted in 1990-2008. Note that the gravity values (mgal) vary with the surveys reported (from Magma, 2011).

6.1.3.4 Magnetotellurics

Magma conducted a 74-station Tensor Magnetotelluric (MT) survey in 2009 with a station spacing of 488-976m (1600-3200ft). Figure 46 presents the 3.4 ohm-meter (Ω-m) iso-resisitivty map for the SL geothermal system along with the section lines for two MT cross-sections shown in Figures 47 and 48. Note that Mama (2011) reported that only a 3D grid of 1D inversion of the MT data is available given problems with data noise and errors in 1D inversions, Figures 47 and 48.

To about a depth of 1km (+3000ft), the resistivities are <15-20 ohm-meter (Ohm-m) and vertically stratified. Magma found that this low resistivity correlates with horizontally layered meteoric water with a resistivity generally from 10-50 ohm meters and is absent in the heart of the geothermal field where geothermal fluids are close to the surface. Magma (2011) reported that:

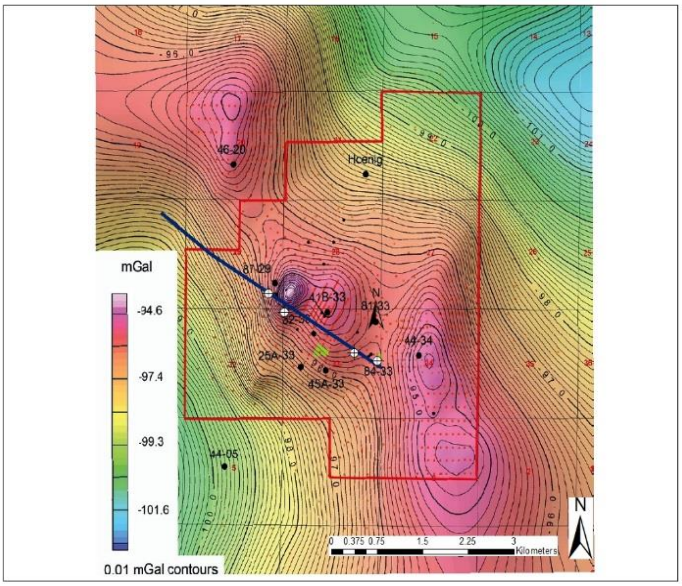

Figure 43. Complete Bouguer Anomaly map for the Soda Lake geothermal area (modified from Magma, 2011). Seismic line2 is shown in blue. Figure 44 includes the corresponding well ID numbers.

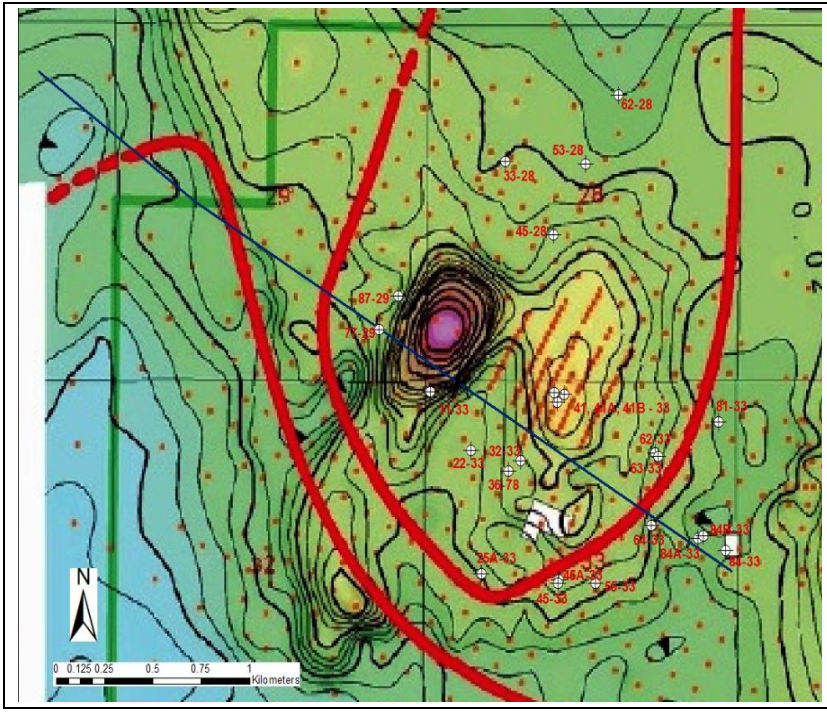

Figure 44. Residual Gravity Anomaly map for the Soda Lake geothermal area with the 152m (500ft) temperature isocontours in °F (modified from Magma, 2011). Seismic line2 is shown in blue and well ID numbers are included.

1. The thermal contours on the Figures 48 and 49 correlate with resistivity values showing that the resistivity reflects active geothermal fluid movement in the producing field area and not some older alteration feature.
2. The 3.4 ohm-m iso-resistivity surface may reflect the boundary between the meteoric and thermal waters evidences a marked NW-trending boundary at the southern edge of the geothermal field (Figure 46).
3. At shallower depths north of the southern boundary, the 3.4 ohm-m contours correspond with the producing geothermal field and greater depths to the south correspond with a known cooler non-geothermal area. This resistivity feature correlates closely with rapidly declining temperatures at the southern margin of the geothermal field.

4. A marked correspondence exists between the 3.4 ohm-m iso-resistivity surface and plan view temperatures at 152m (500ft) depth including the subsidiary thermal anomalies northwest and east of the core area (Figure 46).
5. The 3.4 ohm-m iso-resistivity surface occurs at greater depth in Section 20 and 34 than in the core thermal area possibly reflecting the a mudstone unit in the basin fill unit being a more effective cap in these outlying areas.

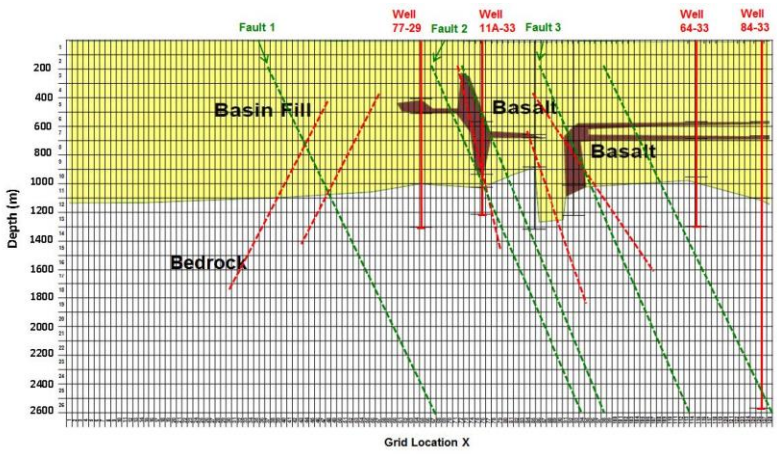

Figure 45. Gridded gravity model from Holly McLachlan (University of Nevada Reno Ph.D. candidate). Optim faults are presented in red while major (Faults 1, 2 and 3) and minor Magma (2011) faults are shown in green.

The MT model data beneath ambient seismic line 2 was extracted for the current project from Magma's block model and a gridded profile of this data is included as Figure 49. The contoured MT profiles included as Figures 47 and 48 represent data from nearby parallel profile lines, as depicted in Figure 46. The gridded MT profile used for the current analysis and the nearby profile produced by Magma demonstrate similar trends in data, with only minor discrepancies likely due to a slight variation in data extraction locations and/ or contour threshold values.

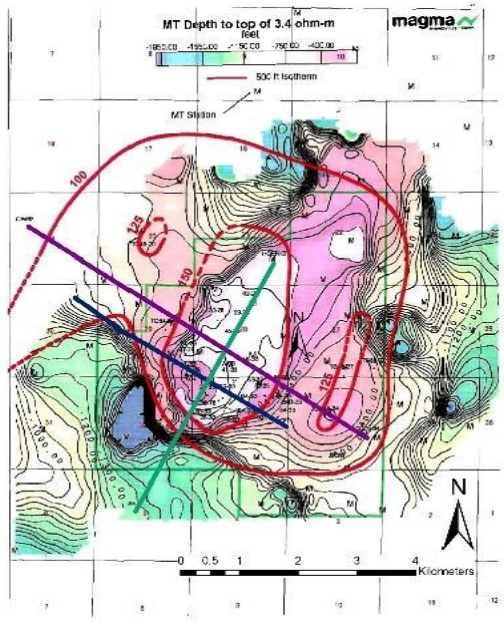

Figure 46. Depth to the 3.4 ohm-m at the Soda Lake geothermal area as defined by the 1D inversion of the MT data with the 152m (500ft) 100°F, 125°F and 150°F isocontours (from Magma, 2011). Note that the two magnetotelluric profiles shown in this Figures 47 and 48 are indicated in green and purple, respectively. Ambient seismic line 2 is shown in blue.

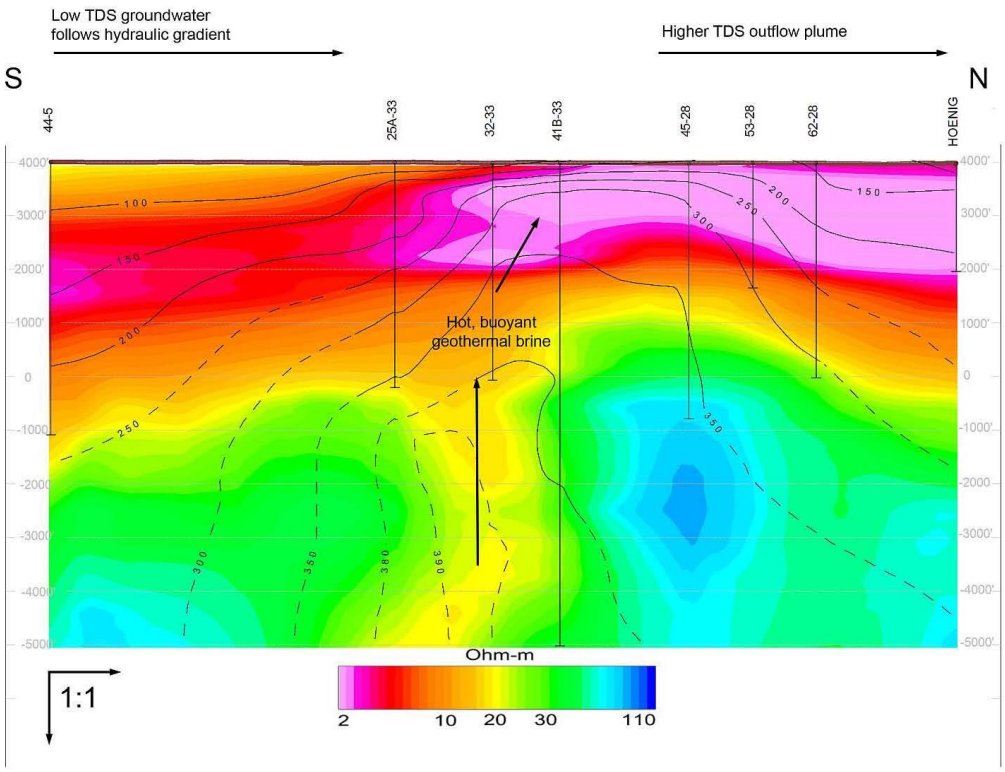

Figure 47. North-South magnetotelluric 1D profile through the Soda Lake Geothermal area with temperature contours in °F (from Magma, 2011). The location for this section is shown in Figure 46.

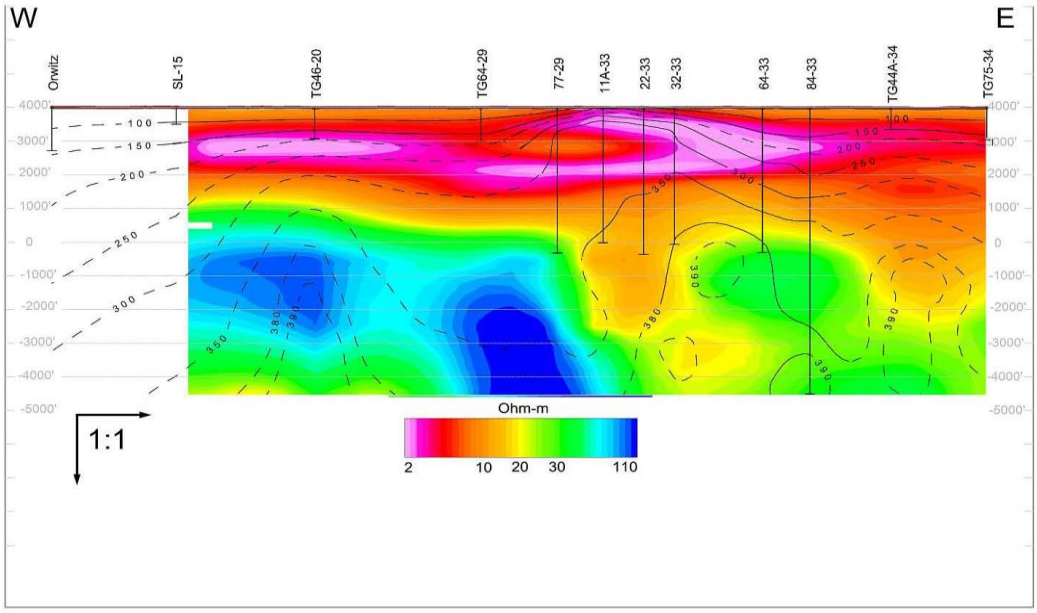

Figure 48. East-West South magnetotelluric 1D profile through the Soda Lake Geothermal area with temperature contours in °F (from Magma, 2011). The location for this section is shown in Figure 46.

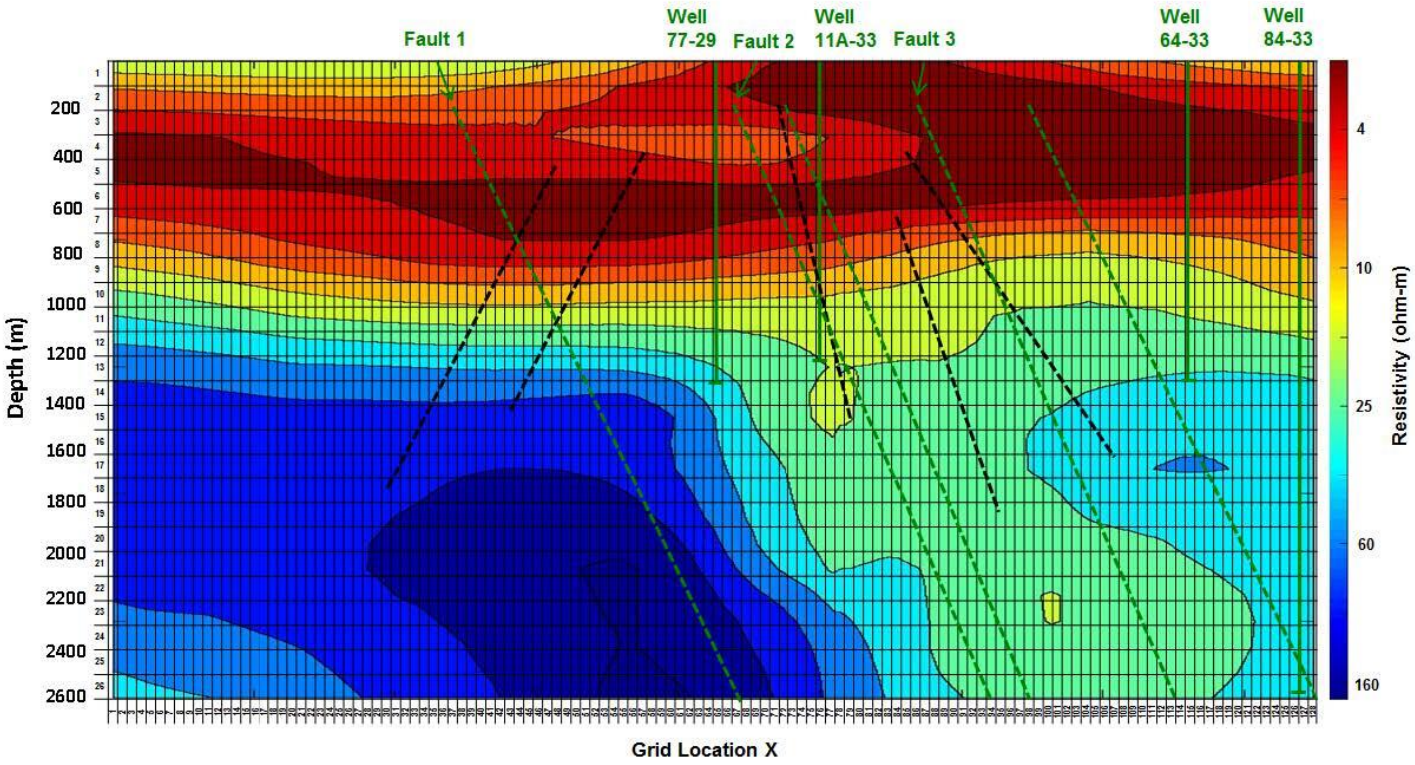

Figure 49. Gridded ID MT inversion data along the ambient seismic noise line 2 with key fault locations estimated from Holly McLachlan (Ph.D. candidate at the University of Nevada Reno) who was provided the data from Magma. Optim faults are presented in black while major (Faults 1, 2 and 3) and minor Magma (2011) faults are shown in green.

6.1.3.5 3D-3C Seismic Reflection Survey

Magma conducted a 3D seismic reflection survey was conducted in 2010. The shot lines were parallel to the anticipated NNE strike of normal faults in the area with perpendicular receiver lines (Figure 50).

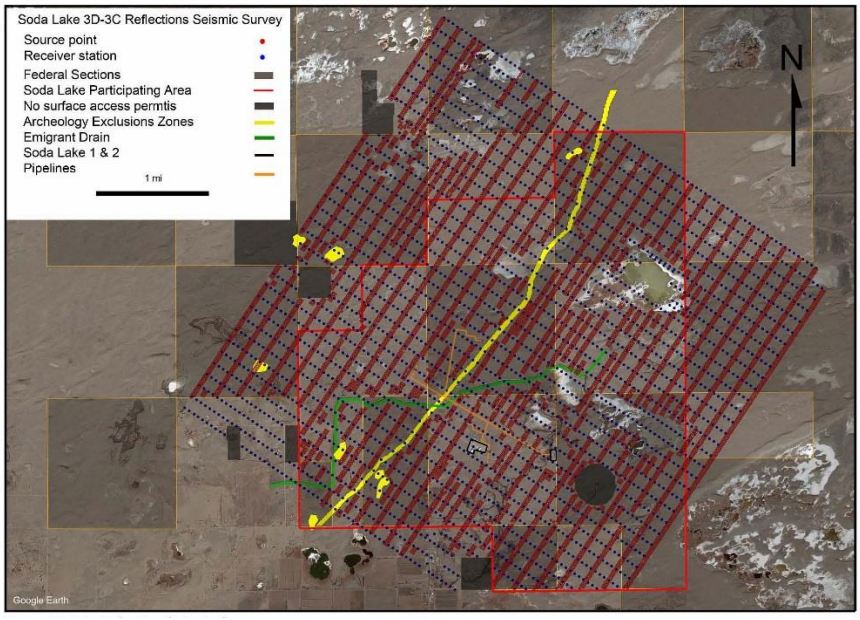

Figure 50. 3D-3C seismic reflection survey layout (from Magma, 2011)

According to Magma (2011), the centerpiece of this survey was to identify fluid-filled fractures and permeability through a calibrated surface seismic data set achieved by having checkshots or time-depth surveys and synthetic seismograms. Numerous problems were identified in this survey and these are detailed in Magma (2011).

The most significant results of this survey are:

1. The mudstone reflector in the basin fill unit provides the best depiction of the three mile-wide NNE-trending fault zone in the SL area. Within this fault zone, identified faults 1-4 were most significant. Faults 1-3 have been used in the ambient seismic noise Line 2 investigation (Magma, 2011). However, the mudstone reflector was not resolved in the gravity model and as such is of limited use, other than the identification of the aforementioned faults.
2. The basaltic unit, thought to be the best reflector in the survey, did not produce a strong or consistent reflection.
3. The basement unit was also not detected with respect to coherent reflectors.
4. Filtered and unfiltered gravity profiles plotted against the seismic data. Gravity highs were associated with elevated the elevated basement unit and elevated shallow temperatures (Magma, 2011).
5. A total of 19 largest vertical offset faults identified at ~91m (~300ft) depth all dip 60-70° to the east. Figure 41 shows these fault planes at 183-1219m (600-4000ft).
6. The seismic signature associated with permeability either through a structural relationship or shear-wave anisotropy was not identified to the degradation of the seismic data over the producing area.
7. A regional structural model was developed (Figure 51) identifying a three mile-wide, NNE-trending fault zone thought to connect Big SL and Upsal Hogback. The majority of individual faults in this fault zone are not geothermally active. Magma (2011) reported that the intersection of this fault zone and the Tertiary volcanic basement ridge regionally controls the location of the SL geothermal system. Figure 52 presents a possible model of the fault zone which includes left-lateral movement does not cause recognizable gravity displacement of the identified gravity ridge.
8. Magma (2011) concluded that the basement high assumed to be an antiform is the source of the geothermal fluids at depths of 3218-4828m (2-3 miles).
9. A 3D conceptual geologic model showing the 4 major faults identified by the seismic reflection survey (and of which 3 intersect the ambient seismic line 2) is presented in Figure 52.

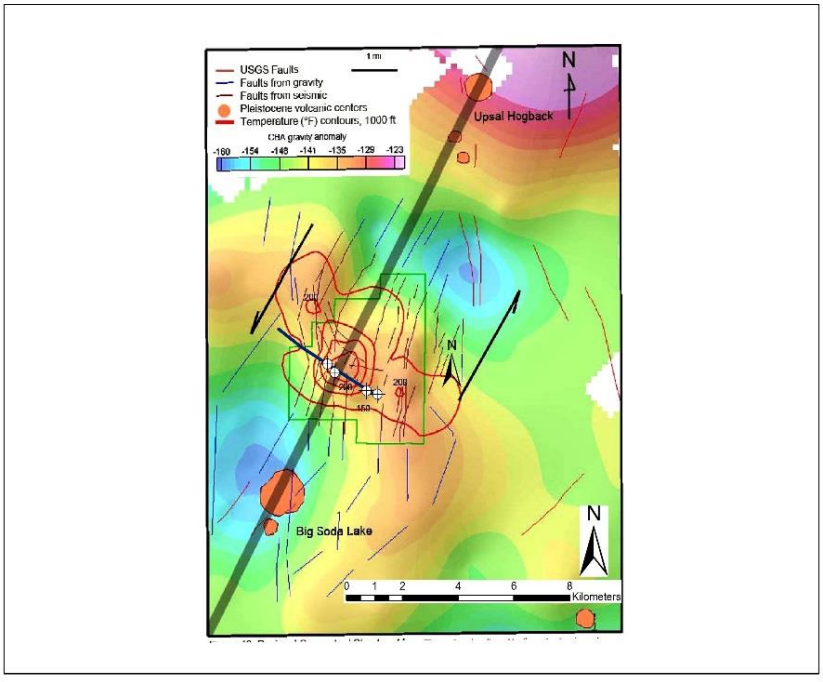

Figure 51. Regional structural model based on gravity, seismic and USGS faults (from Magma, 2011). The seismic line2 is shown in black. The white squares are wells along ambient noise seismic line 2 which are identified in Figure 44.

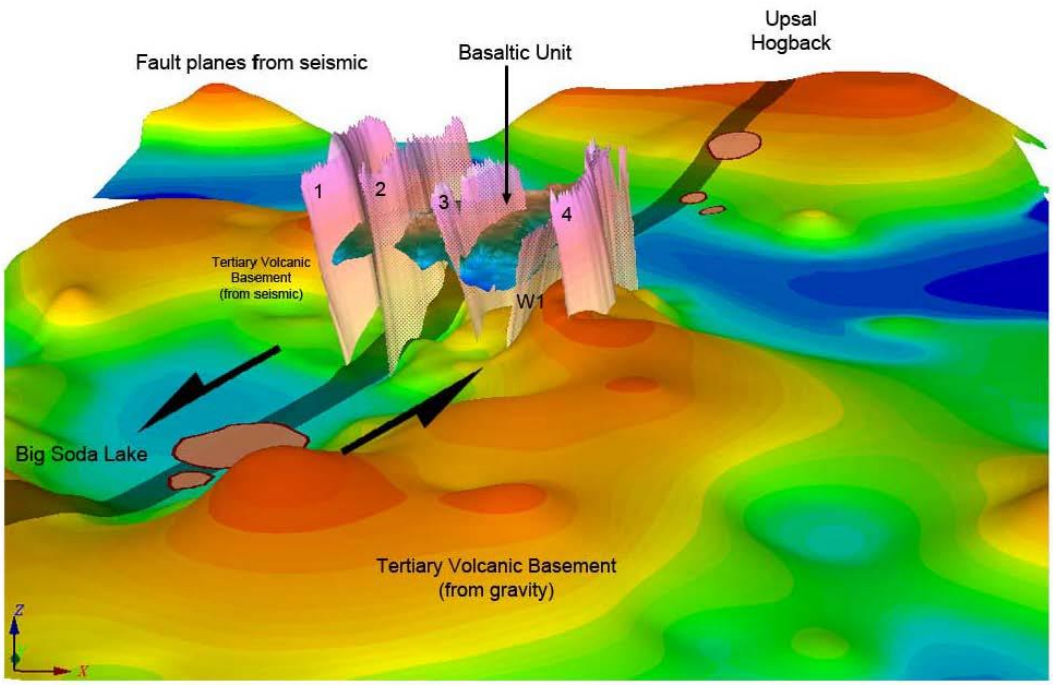

Figure 52. 3D oblique view of the conceptual geologic model (from Magma, 2011)

6.1.3.6 Current Ambient Seismic Noise Analysis

Several seismic parameters were assessed for Line2 and detailed descriptions of data acquisition and processing techniques are included in Sections 2 and 3 of this report. The following figures represent gridded, subsurface profiles of data sets incorporated into the statistical and favorability analyses. Active source data sets include: P-wave % anomaly (Figure 53), attenuation (Figure 54), correlation length (Figure 55), and Hurst number (Figure 56). Ambient seismic noise data sets include: S-wave fk % anomaly (Figure 57), 3-model S-wave % anomaly (Figure 58), attenuation (Figure 59), correlation length (Figure 60), Hurst number (Figure 61), entropy (Figure 62), 3-model analysis S-wave velocity (Figure 63), fk analysis S-wave velocity (Figure 64), and power spectral density (Figure 65).

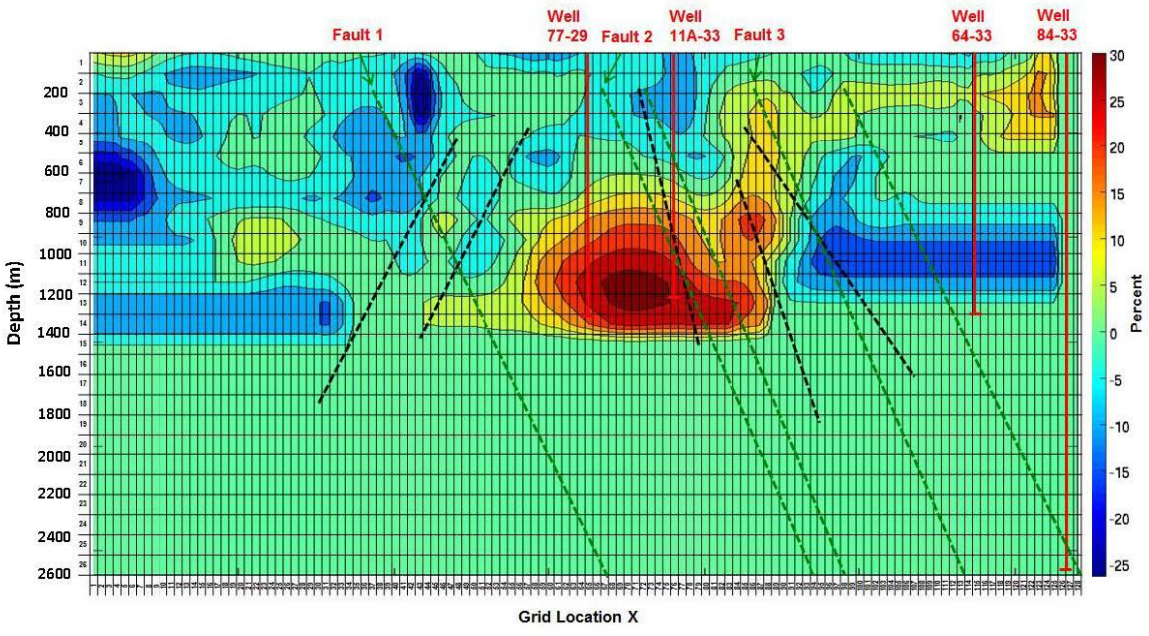

Figure 53. Gridded profile of active source *Vp* % anomaly along Line2. Optim faults are presented in black while major (Faults 1, 2 and 3) and minor Magma (2011) faults are shown in green.

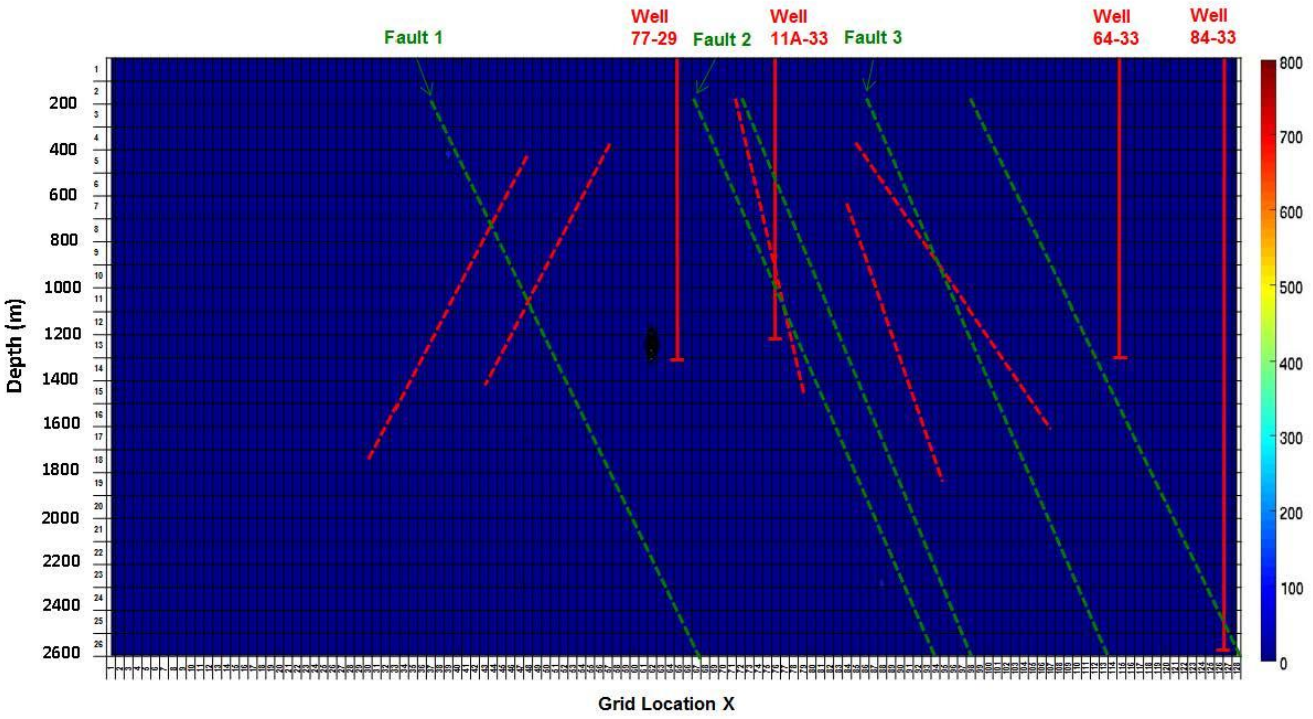

Figure 54. Gridded profile of active source P-phase Q along Line2. Optim faults are presented in red while major (Faults 1, 2 and 3) and minor Magma (2011) faults are shown in green.

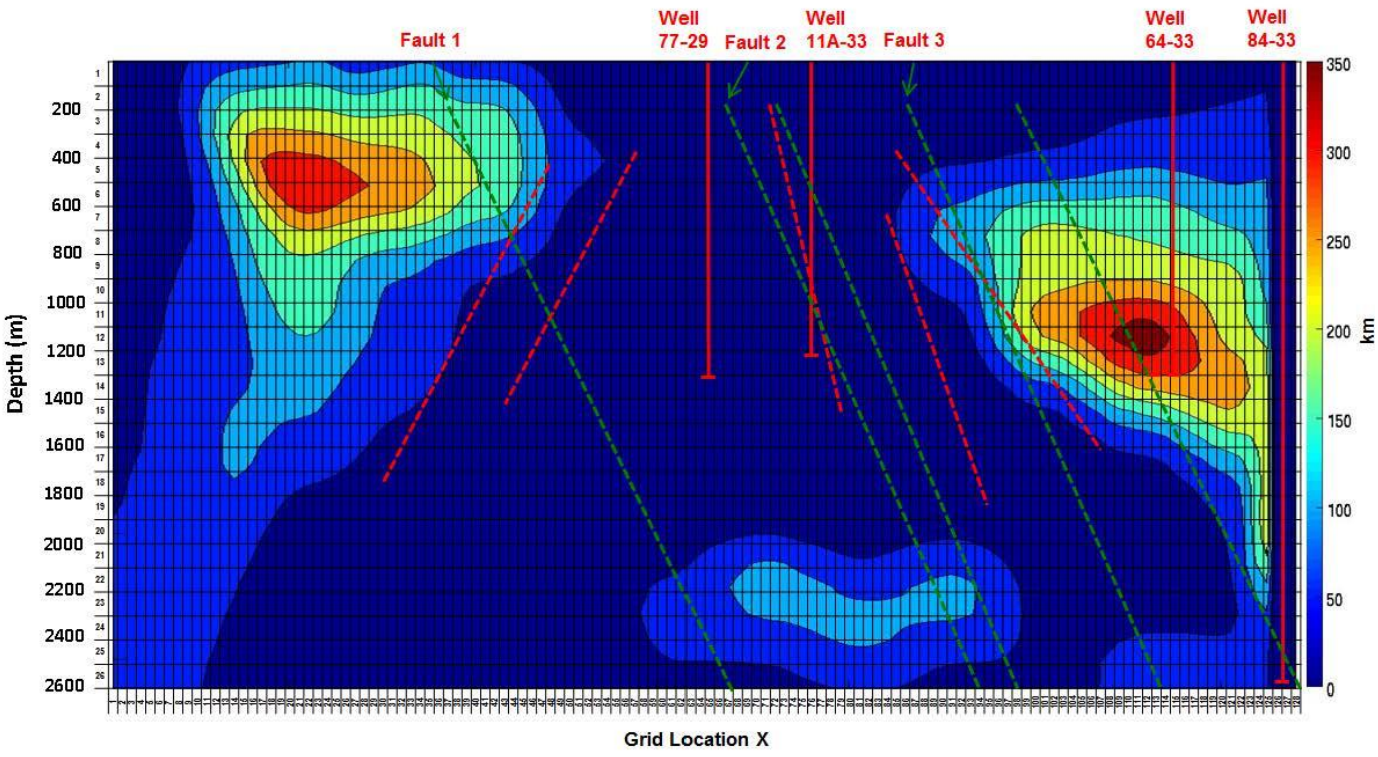

Figure 55. Gridded profile of active source correlation length along Line2. Optim faults are presented in red while major (Faults 1, 2 and 3) and minor Magma (2011) faults are shown in green.

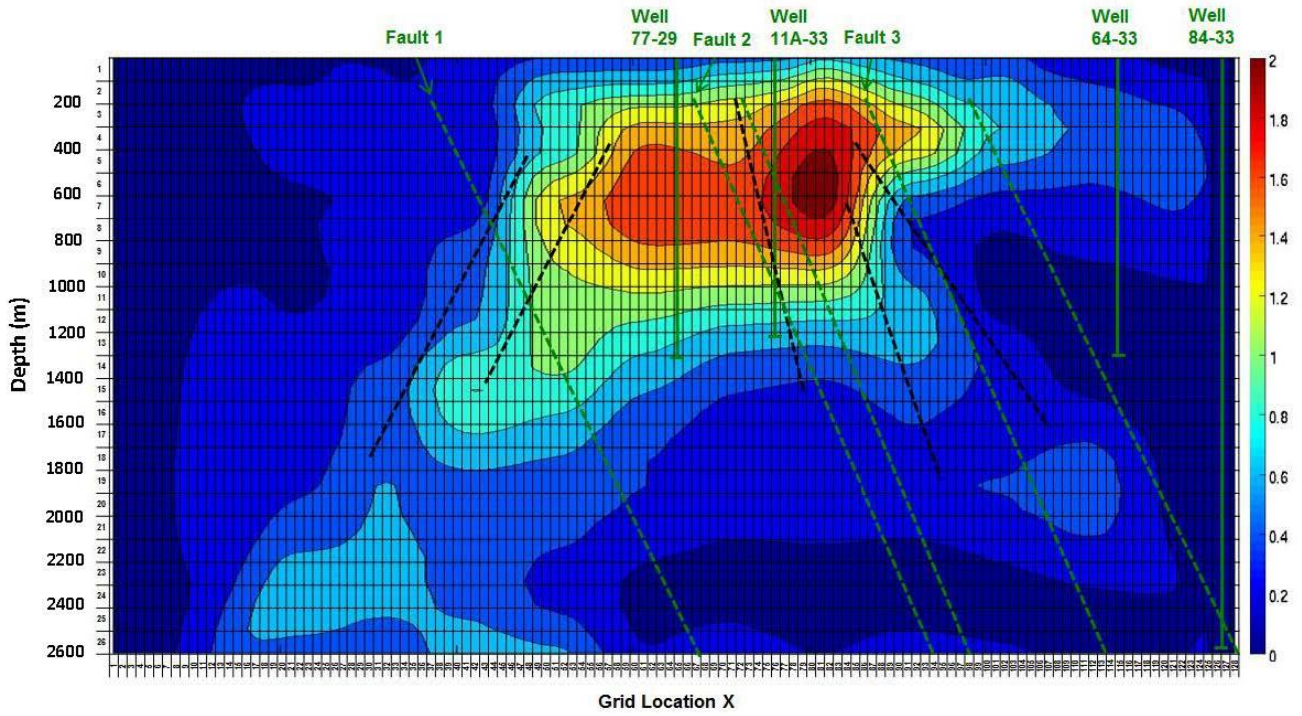

Figure 56. Gridded profile of active source Hurst number along Line2. Optim faults are presented in black while major (Faults 1, 2 and 3) and minor Magma (2011) faults are shown in green.

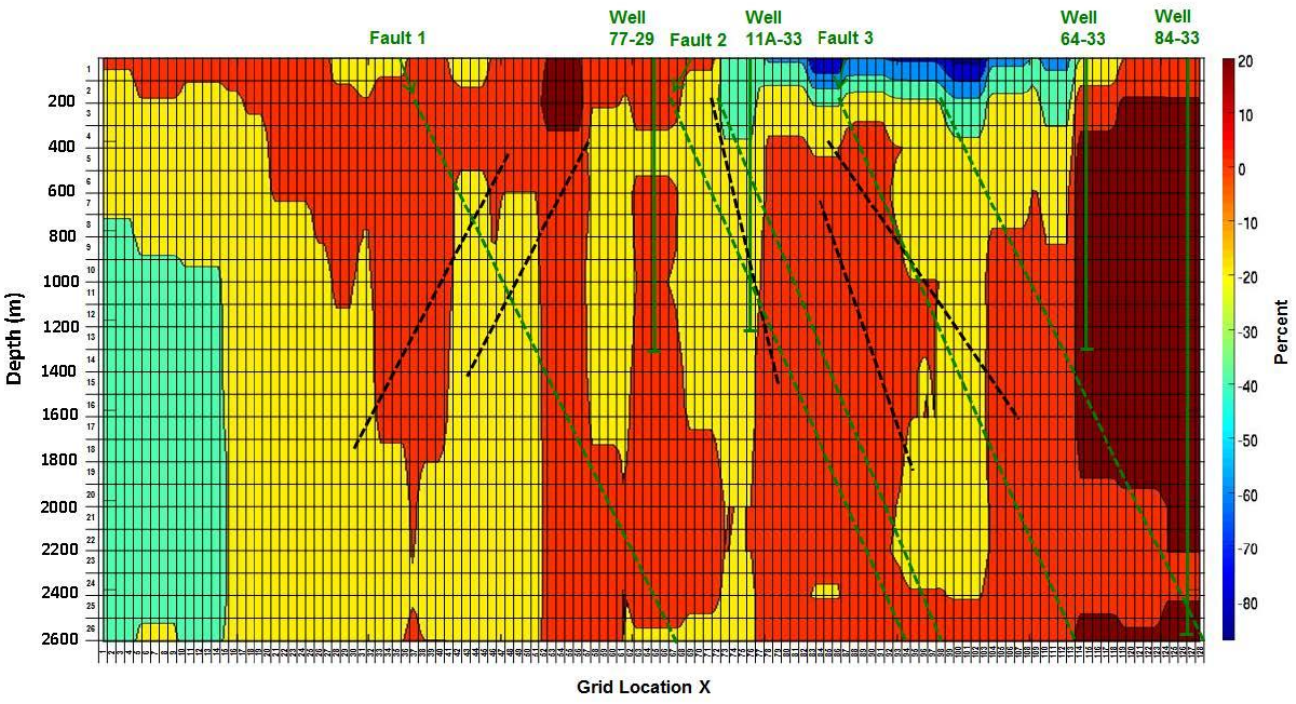

Figure 57. Gridded profile of ambient seismic noise *Vs* fk % anomaly along Line 2. Optim faults are presented in black while major (Faults 1, 2 and 3) and minor Magma (2011) faults are shown in green.

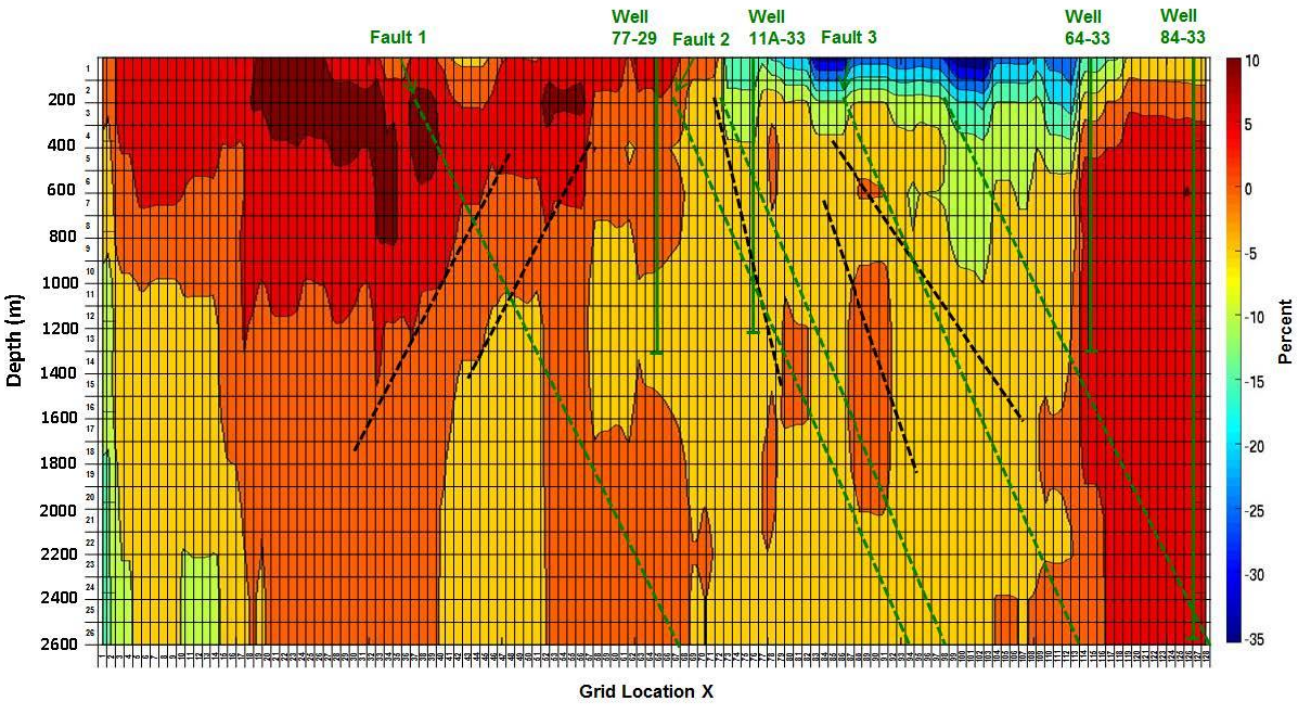

Figure 58. Gridded profile of ambient seismic noise 3-model *Vs* % anomaly along Line 2. Optim faults are presented in black while major (Faults 1, 2 and 3) and minor Magma (2011) faults are shown in green.

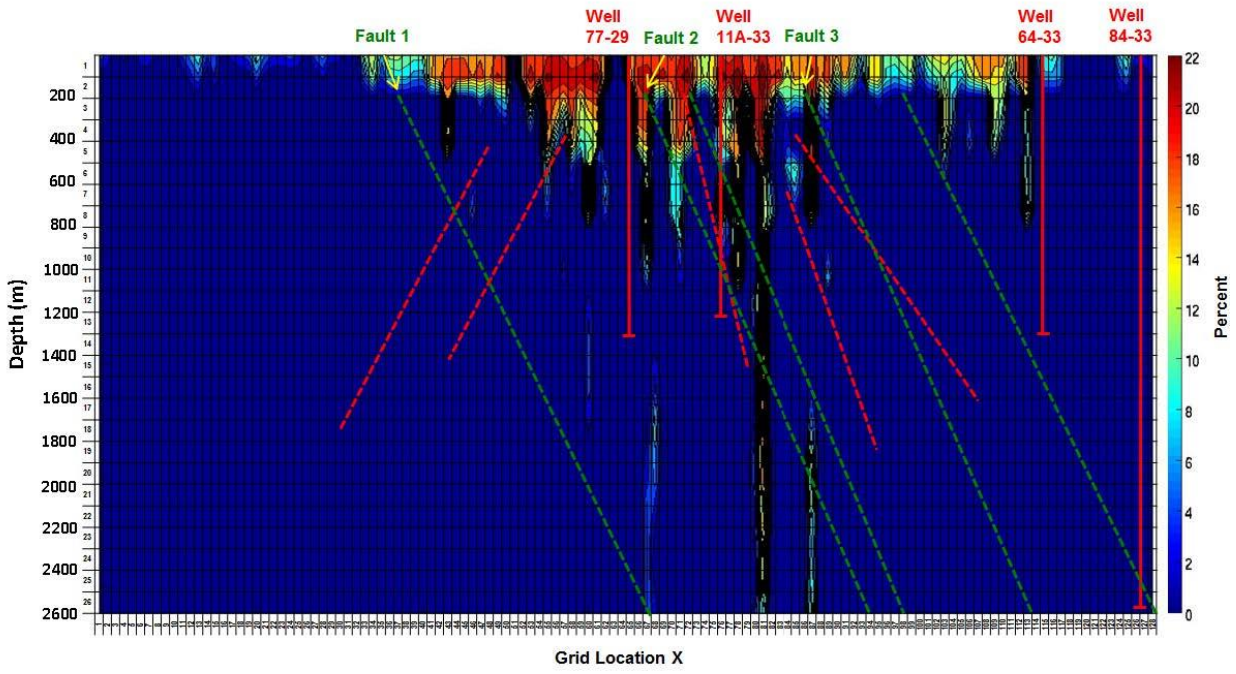

Figure 59. Gridded profile of ambient seismic noise P-phase Q along Line2. Optim faults are presented in red while major (Faults 1, 2 and 3) and minor Magma (2011) faults are shown in green.

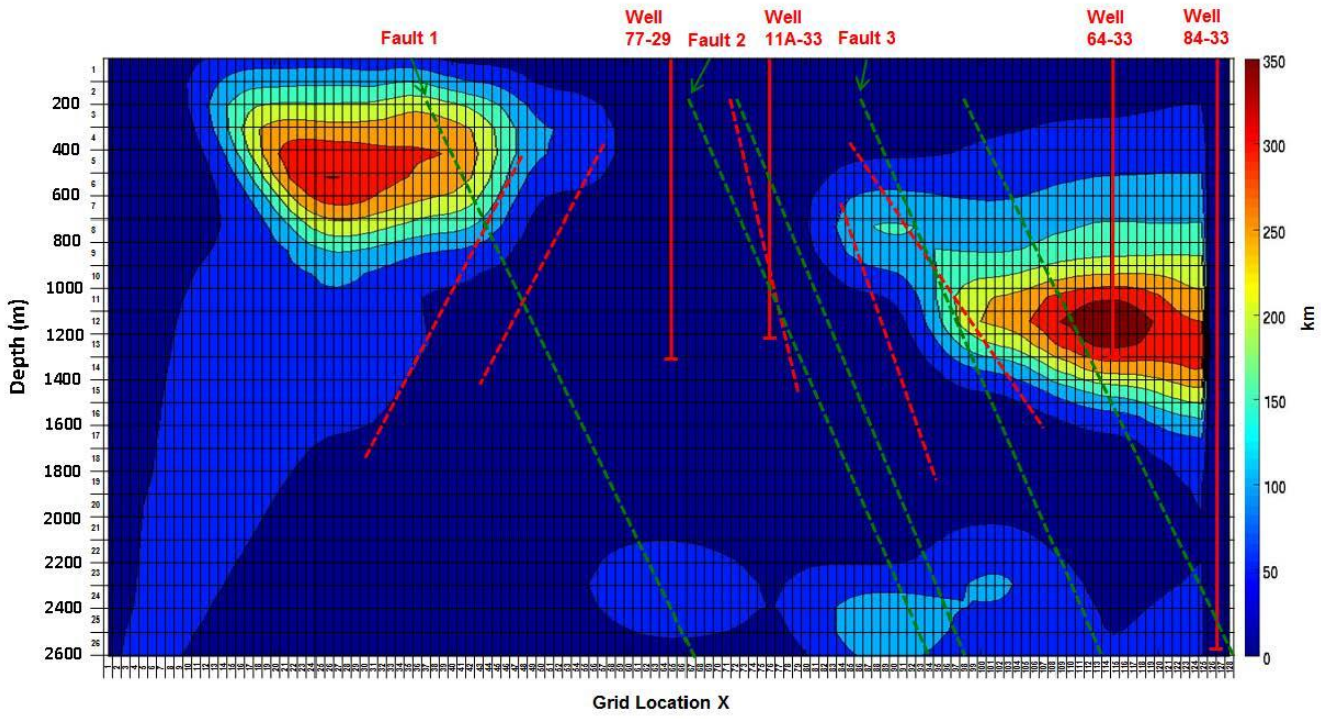

Figure 60. Gridded profile of ambient seismic noise correlation length along Line2. Optim faults are presented in red while major (Faults 1, 2 and 3) and minor Magma (2011) faults are shown in green.

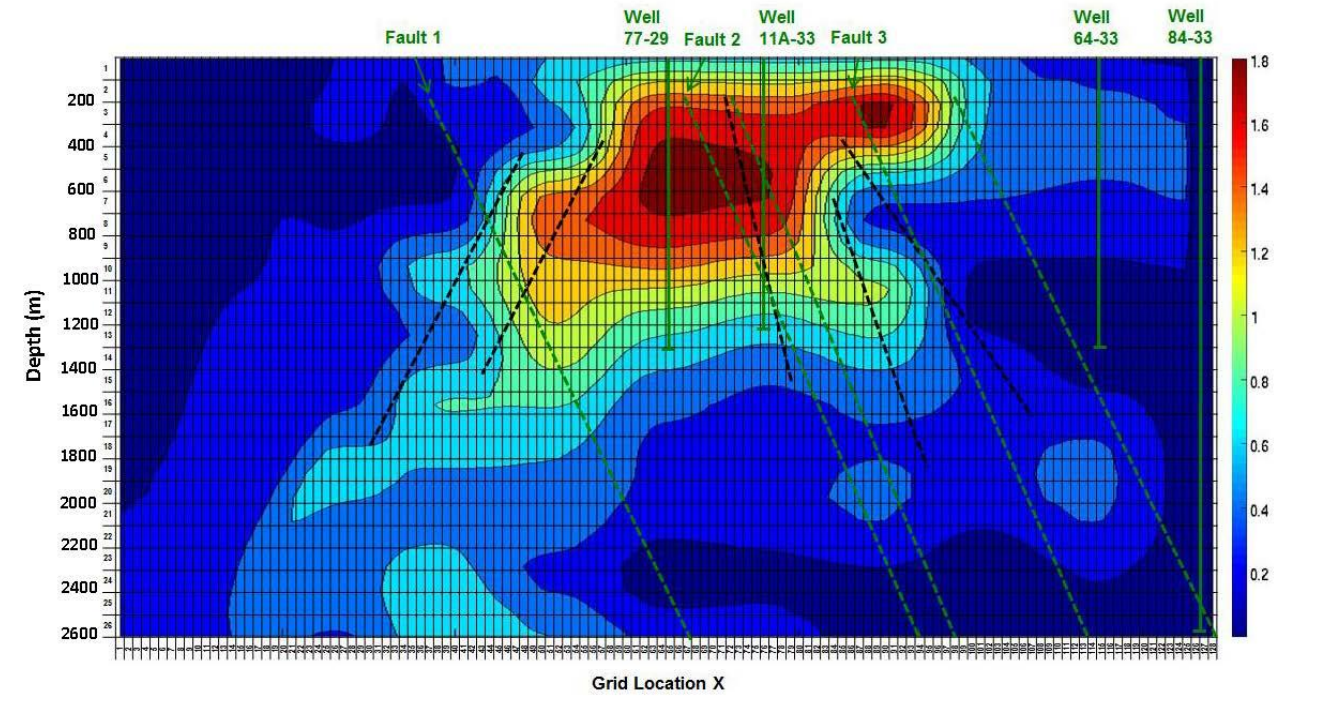

Figure 61. Gridded profile of ambient seismic noise Hurst number along Line2. Optim faults are presented in black while major (Faults 1, 2 and 3) and minor Magma (2011) faults are shown in green.

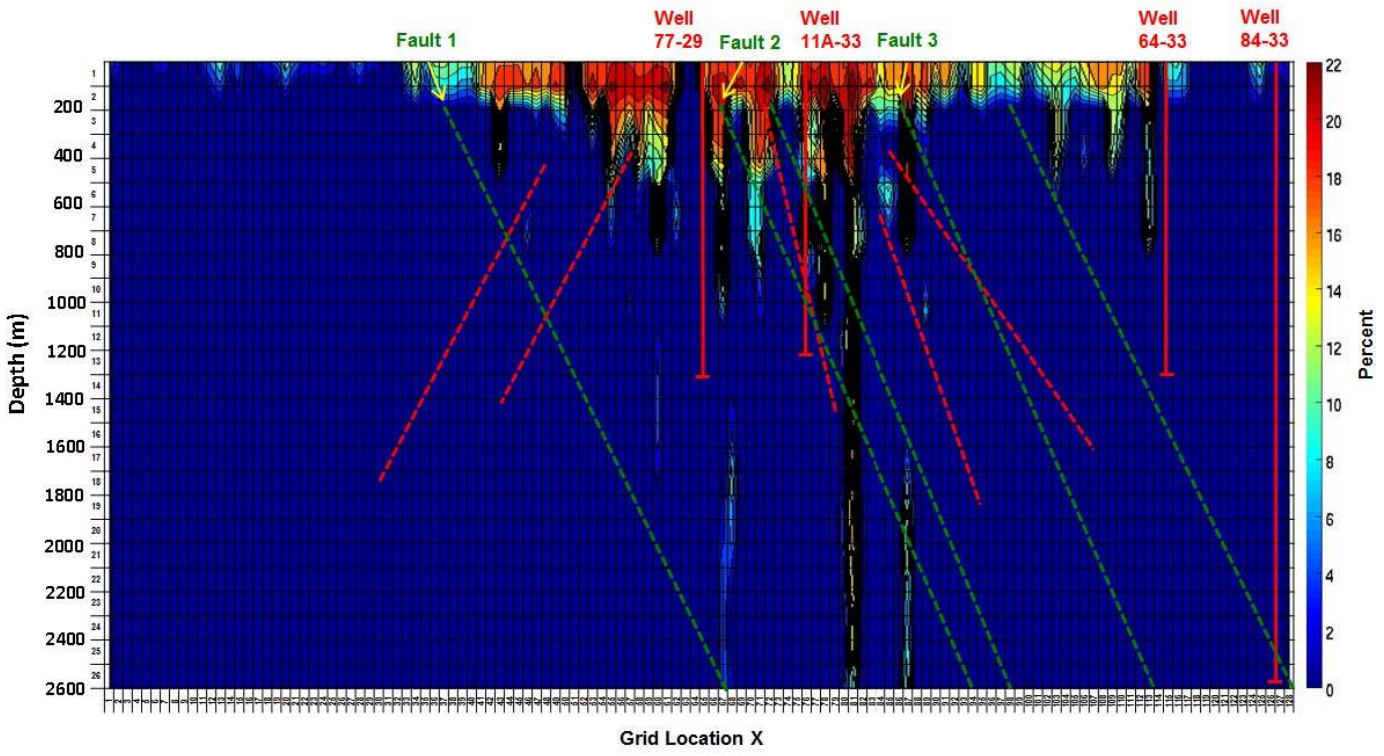

Figure 62. Gridded profile of ambient seismic noise entropy along Line2. Optim faults are presented in red while major (Faults 1, 2 and 3) and minor Magma (2011) faults are shown in green.

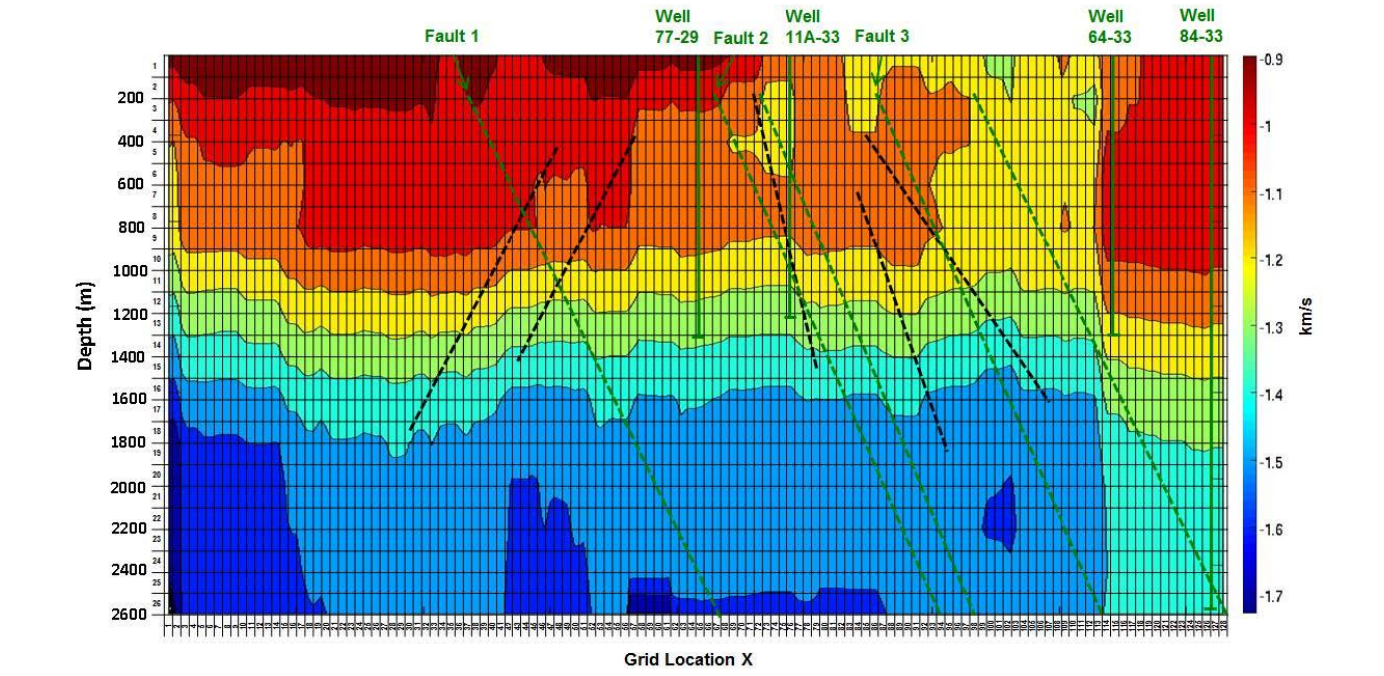

Figure 63. Gridded profile of ambient seismic noise 3-model *Vs* along Line2. Optim faults are presented in red while major (Faults 1, 2 and 3) and minor Magma (2011) faults are shown in green.

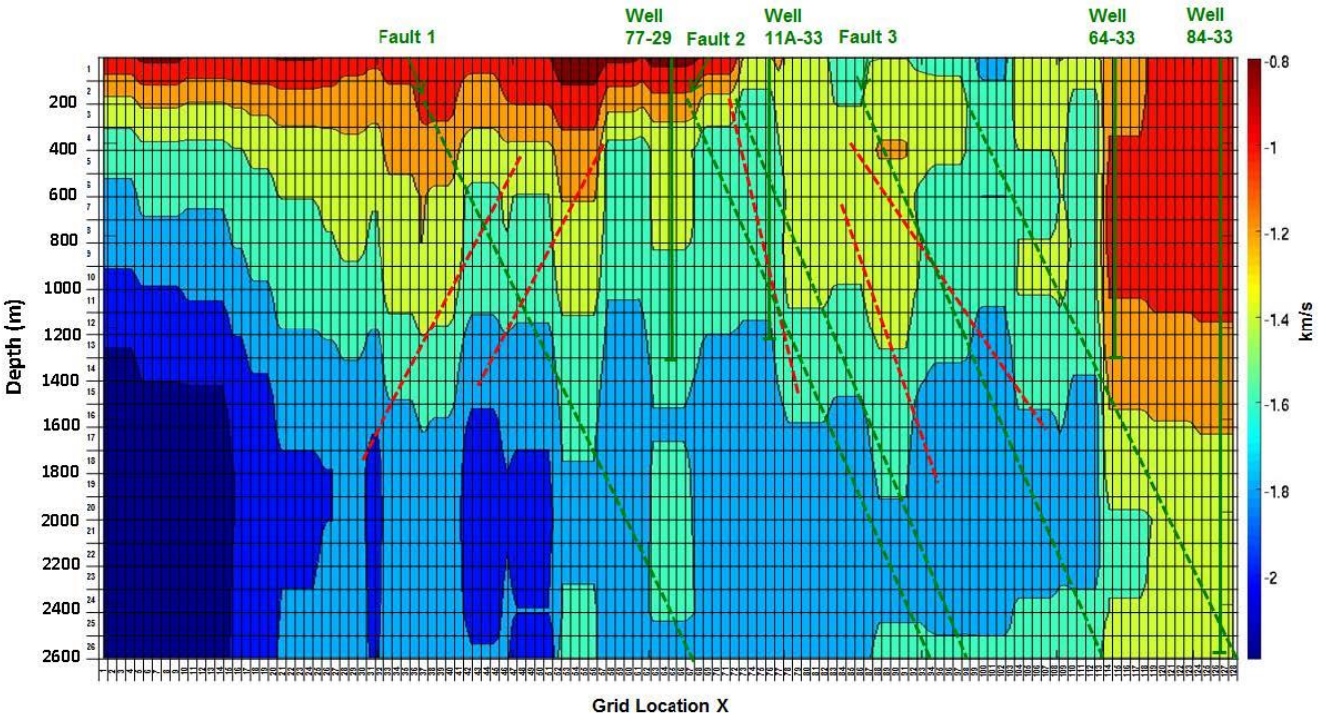

Figure 64. Gridded profile of ambient *Vs* fk along Line2. Optim faults are presented in red while major (Faults 1, 2 and 3) and minor Magma (2011) faults are shown in green.

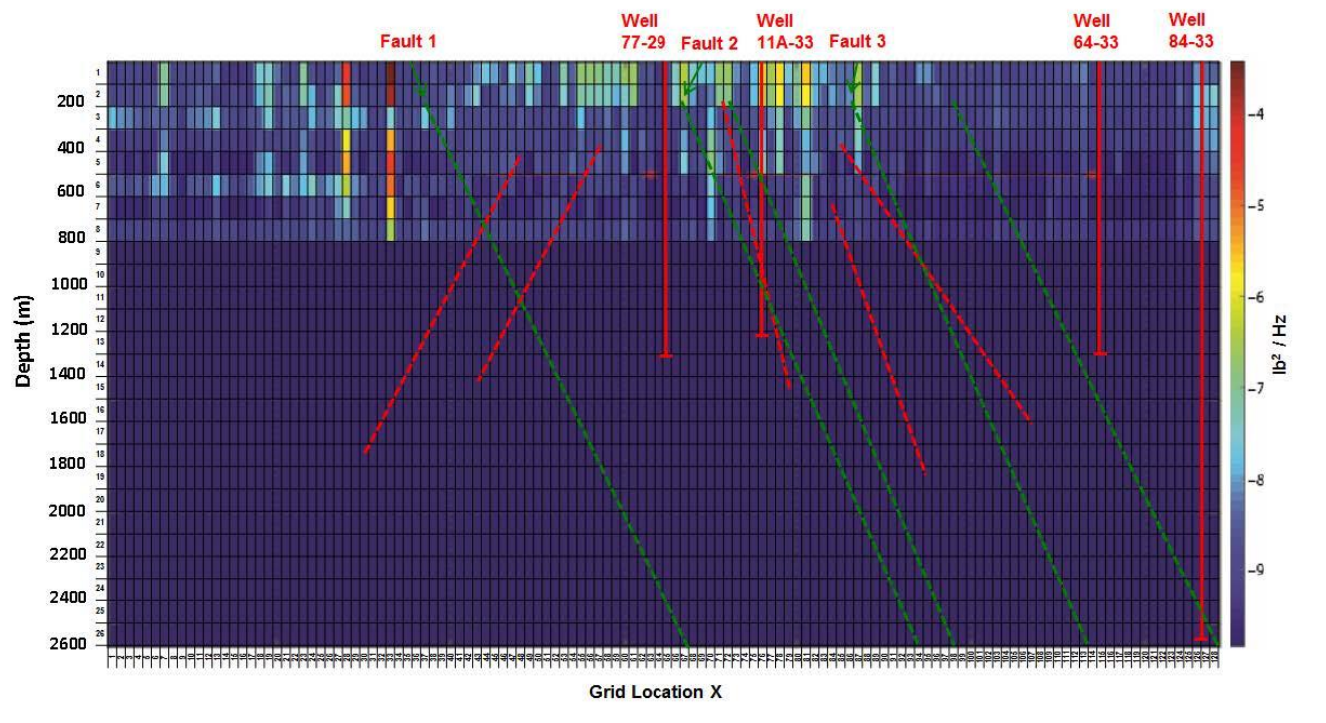

Figure 65. Gridded profile of ambient power spectral density along Line2. Optim faults are presented in red while major (Faults 1, 2 and 3) and minor Magma (2011) faults are shown in green.

Table 2 presents a summary of the seismic attributes derived from the passive seismic analysis and the active seismic survey described above 4 and their geoscience significance. The qualitative and quantitative geoscience correlations of these seismic and other geophysical attributes (e.g., MT) at SL are described in Sections 6.2 and 6.3, respectively. At the end of these sections, the results of these correlations are compared to the Table 2 geological significance.

6.2 Qualitative Geoscience Correlations

Analysis of the gridded geologic and geophysical data profiles (presented in Section 6.1) was performed to qualitatively asses correlations between datasets previously collected by others and the seismic data collected for the current study. A summary of these findings follows:

6.2.1 Plan View Map Correlations

Plan view map correlations are described in Section 5.1

6.2.2 Ambient Seismic Line 2 Correlations

Correlations of the geoscience data along Line 2 are presented below. Note that structural correlations are principally made with respect to both the Optim (2015), Appendix 5, reported faults as well as the Magma (2011) faults for reasons discussed in Section 6.1.3.1 discussion about Figure 40.

1. Comparison of the temperature section (Figure 40) indicates that the high temperature zone originates in the bedrock at depth below well 84-33 on the eastside of the profile flows up in the region of faulting between the Magma (2011) defined major Faults 2 and 3.
2. The MT low resistivity (Figure 49) is correlated with the basin fill which is typical in sedimentary deposits containing significant amounts of clay. The lowermost third of the basin fill exhibits the lowest resistivity values within the alluvium, possibly suggesting the presence of a clay cap. The MT is vertically stratified within the basin fill which Magma (2011) attributed to meteoric groundwater. The ~20 ohm-m zone is well correlated with the faulting in the Magma (2011) Fault 2 area.

Table 2. Geological Significance of various seismic attributes measured or modeled in this study.

Seismic parameter	**Geology Significance**
Vp, Vp anomalies, Vs, Vs anomalies, Vs % and Vs fk anomalies	Conventional interpretation is that low P and S velocities are associated with unconsolidated rocks and/or rocks having higher temperature (Wang et al., 1990) and/or with higher degree of rock fracturing, and/or water saturated rocks. Faults not always clearly interpretable from velocity models (depending on model resolution)but can be identified by sharp contrasts in velocity gradients (Ramachandran, 2011).
Vp/Vs	High Vp/Vs ratio may indicate fluid-saturated rock (Wang et al, 1990).
Attenuation (Q)	All the other parameters constant, attenuation increases as temperature increases and/or with faulting and/or fracturing.
Power Spectral Density	Scattering of wavelengths indicates fragmentation which may be indicative of faults and/or fracturing.
Entropy	Lateral and vertical dimension of fragmentation may be indicate of faults and/or fracturing.
Correlation Length	Upper limit of fractal dimension of heterogeneity. Related to fragmentation in the medium. If the correlation length is low this may be indicative of fault and/or fracturing.
Hurst Number	Fractal measure of medium may be indicative of fault and/or fracturing. Small fractal dimension may be indicative of dipping layers.

3. The basalt body indicated by the gravity model (Figure 45) does is not resolved by the MT model possibly this apparent lava flow is too small to be detected.
4. The active source (AS) *Vp* anomaly section (Figure 53) shows a high at the area of the bedrock-basin fill contact in the area of Magma (2011) Fault 2.
5. The AS Q profile for P-waves (Figure 59) does not show any anomalies.
6. The AS correlation length section (Figure 60) shows a high in the region of multiple identified faults. Lows in this data set are related to the basin fill to the west of Magma (2011) Fault 3 and in the basin fill bedrock contact area in the area of well 64-33. The Magma (2011) Fault 3 appears to bound this anomaly on its western side and possibly along its base since this is a known listric fault (see discussion in Section 6.1.3.1).
7. The AS Hurst number section (Figure 56) is inversely correlated to the active source correlation length profile. Comparison of the AS Hurst number, AS *Vp* % anomaly (Figure 53), and gravity-based lithologic profiles (Figure 45) indicates that the area with the largest AS Hurst number and AS *Vp* % anomaly values is approximately correlated with the basalt location.
8. A low velocity zone within the upper 0.3km of the ASN *Vs* fk % anomaly profile (Figure 57) corresponds to the area of the high temperature anomaly but the correlation is not apparent below this elevation.
9. The low velocity zone shown by the ASN 3-model *Vs* % anomaly profile (Figure 58) is well correlated with the high temperature anomaly and also corresponds to the basalt location estimated from the gravity data. The correlation with the thermal anomaly is more pronounced at depth with this model than with the Vs fk % anomaly model.
10. The ASN Q profile (Figure 62) does not identify any anomalies, similar to the AS case.
11. The ASN correlation length (Figure 60) and ambient seismic noise Hurst number sections (Figure 61) have an excellent correlation with the active profiles for these seismic parameters (see item nos. 6 and 7 above).
12. The ASN entropy section (Figure 62) shows relatively high entropy values are present near the ground surface between Magma Faults 1 and 3, which corresponds to the zone with the majority of faults in the subsurface. This observation suggests that larger entropy values in the shallow subsurface may be indicative of more highly fractured zones at depth.
13. The ASN *Vs* 3-model section (Figure 63) shows lower S-wave velocities between Wells 77-29 and 64-33, which corresponds to the more densely faulted portion of the profile and the high temperature anomaly.
14. The ASN *Vs* fk section (Figure 64) also shows lower shear wave velocities between Wells 77-29 and 64-33, which corresponds to the more densely faulted portion of the profile and the high temperature anomaly. The Vs fk model suggests an increase in shear velocity in the vicinity of the basalt body.
15. ASN power spectral density section (Figure 65) shows a good correlation with faulting in the uppermost portion of the profile as well as the area east of Magma (2011) Fault 1.

6.2.3 Seismic Parameter – Qualitative Correlation Summary

Table 3 cross-correlates the geologic significance of the various geoscience parameters with the qualitative geoscience correlations. In summary, some of the seismic parameters clearly show the effects of faulting.

6.3 Geostatistical Analysis of Available Geoscience Data

6.3.1 Temperature

The correlation and the statistical significance of the correlation (p-values) between selected geoscience parameters in this study and temperature as well as temperature residual was calculated. The calculation was done both for the full dataset along ambient seismic Line2 (“all data”) and also for the well location data along said line alone (“well data”). For the “well data”, some of the correlations are not available (NA) if there wasn’t enough data to obtain a correlation,

and also some of the correlations reported are large because of the lack of data. The correlation results are shown in Table 4. Note that for statistical significance the p-values are calculated under the assumption of independence between cells. Although this is clearly not true, the p-values are so small that most of the correlations are certainly difficult to explain by chance. That is, the p-value is the chance of randomly obtaining a statistic (in this case correlation), given that in fact there is no underlying true relationship. The p-values for the correlations are two-sided (double what they would be for one-sided). This is consistent with the assumption that we have no particularly strong a priori beliefs about the direction of any of the correlations. Since most p-values are so small, doubling the p-values or not makes little difference, and doubling them is more conservative.

Table 3. Cross-correlation of the geological Significance of various seismic attributes measured or modeled in this study with the qualitative geoscience correlations.

Seismic parameter	Geological Significance	Qualitative Geoscience
Vp, Vp anomalies, Vs, Vs anomalies, Vs % and Vs fk anomalies	Conventional interpretation is that low P and S velocities are associated with unconsolidated rocks and/or rocks having higher temperature (Wang et al., 1990) and/or with higher degree of rock fracturing, and/or water saturated rocks. Faults not always clearly interpretable from velocity models but can be identified by sharp contrasts in velocity gradients (Ramachandran, 2011).	The Vs models (3-model and fk) indicate an increase in velocity with depth, which correlates with denser media as indicated from the gravity data. Both Vs modeling approaches show decreased velocities in the area of known faulting and high temperatures. The Vp anomaly model shows an area of increased velocity near the basalt body (located with gravity data). The Vs fk model also suggests a velocity increase in the area of the lava flows.
Vp/Vs	High Vp/Vs ratio may indicate fluid-saturated rock (Wang et al, 1990).	Highest Vp/Vs ratio at 0.3km is correlated with the central portion of the high temperature anomaly at 0.3km and 0.6 km. A low Vp/Vs ratio occurs north of the middle of the ambient seismic Line 2 at 0.3km depth where a steam cap was co-located with these anomalies. High Vp/Vs ratios indicated by the 2D models are well correlated with the area of the known high temperature anomaly. Differences in Vp/Vs ratios at 0.3km (low Vp/Vs) and 0.8 km (high Vp/Vs) suggested the presence of a steam cap immediately north of the central portion of Line 2.
Attenuation (Q)	All the other parameters constant, attenuation increases as temperature increases and/or with faulting and/or fracturing.	P-wave attenuation in this study did not provide any meaningful data. Note that S-attenuation has not been estimated because of time constraints.
Power Spectral Density	Scattering of wavelengths indicates fragmentation which may be indicative of faults and/or fracturing.	Correlates with the area of known faulting between Magma Fault 1 and 84-33, but the strongest correlations are located at higher elevations the fault origins defined by Optim and Magma (2011). Power Spectral Density (see also the discussion at Task4) at 1-6Hz suggests faulting in the area west of Fault 1, however, there was no supporting data from Magma (2011). This may be due to the lack of investigation by in this area by various operators of the field (also the land is private). However, there is a north-northeast trending thermal and gravity anomaly to the north of this area and the power spectral data lies along this trend.
Entropy	Lateral and vertical dimension of fragmentation may be indicate of faults and/or fracturing.	Correlates with the area of faulting defined by Optim (2015) in this study and Magma (2011). Assuming that the time lag-depth conversion is correct, the strongest correlations appear exist at higher elevations than the estimated fault origins. Significant Shannon entropy increases, however, are observed

Seismic parameter	Geological Significance	Qualitative Geoscience
		when the whole waveform is considered (Figure 20A). Also, when using threshold entropy and the full reflection GF, with no automatic gain control (AGC), mixed reflection multiples may carry mixed information from different depths, thus later GF arrivals may be less useful. Figure 20 shows that the best entropy information at depth may be obtained from data after AGC was applied. This may be the reason PSD does not show a significant depth variation as well.
Correlation Length	Upper limit of fractal dimension of heterogeneity. Related to fragmentation in the medium. If the correlation length is low this may be indicative of fault and/or fracturing.	Approximately correlates with the area of intense faulting as defined by Magma Faults 1, 2 and 3 as well as Optim (2015) in this study.
Hurst Number	Fractal measure of medium may be indicative of fault and/or fracturing. Small fractal dimension may be indicative of dipping layers.	Approximately correlates with the area of intense faulting as defined by Magma Faults 1, 2 and 3 as well as Optim (2015) in this study defined faults. Excellent correlation with dipping beds as defined by Optim (2015) in this study.

Table 4. Correlation Coefficients and corresponding p-values for the geoscience parameters, temperature (Temp) and temperature residuals (TempRes) using "all data" and "well data" (see text for an explanation) at Soda Lake. Note that all correlations indicated are statistically significant except those highlighted in yellow. We classified correlation coefficients with absolute values between 0.4 and 0.5 as fair, between 0.5 and 0.7 as good, and >0.7 as excellent. All fair and good/excellent correlation coefficients (|x|>.5) are highlighted in light and dark green, respectively. P-values, an indicator of statistical significance are two-sided (see text for an explanation) and rounded to nearest ten-thousandth. Large p-values (>0.05) indicate that the correlation is not significant.

Geoscience Parameter	Correlation Coefficient -Using "All Data"		Corresponding p-values		Correlation Coefficient - Using "Well Data"		Corresponding p-values	
	Temp	*TempRes*	*Temp*	*TempRes*	*Temp*	*TempRes*	*Temp*	*TempRes*
Vpactive[1]	0.459	0.204	0	0	0.698	0.496	0	0
Vpanom[2]	-0.31	-0.301	0	0	-0.236	-0.053	0	0.0246
Clactive[3]	-0.13	0.002	0	0.9216	0.247	0.136	0	0
Hurstactive[4]	0.184	0.479	0	0	0.331	0.492	0	0
Vsanom[5]	0.154	0.177	0	0	-0.138	-0.054	0	0.0282
Vsambient.noise[6]	0.535	0.298	0	0	0.666	0.439	0	0
Vsanomambientfk[7]	-0.267	-0.289	0	0	0.016	0.129	0.486	0
Vsfkambient[8]	0.287	0.095	0	0	0.791	0.729	0	0
Clambient[9]	-0.079	0.066	0	0.0002	0.279	0.165	0	0
Hurstambient[10]	0.173	0.463	0	0	0.263	0.447	0	0
MT[11]	0.186	-0.288	0	0	0.582	0.176	0	0
FP_Opt15[12]	0.075	0.153	0	0	0.121	0.164	0	0
FP_M11[13]	0.178	0.201	0	0	0.214	0.122	0	0
Entropy[14]	-0.237	0.024	0	0.1734	-0.263	-0.031	0	0.0706
Spectral[15]	-0.463	-0.305	0	0	-0.239	0.023	0	0.256
Vp/Vs[16]	0.329	0.113	0	0	0.535	0.423	0	0

1 - *Vp* active survey (AS
2 - *Vp %* anomaly
3 - Correlation Length AS
4 - Hurst No. AS
5 - *Vs* anomaly 3-model ambient seismic noise (ASN)
6 - *Vs* 3-model anomaly ASN
7 - *Vs* anomaly fk ASN
8 - *Vs* fk ASN
9 - Correlation Length ASN
10 - Hurst No. ASN
11 - Magnetotelluric resistivity
12 - Fault planes by Optim (2015)
13 - Fault plane by Magma (2011)
14 - Entropy
15 - Power Spectral Density
16 – Vp/Vs ratio

For the temperature correlation using all the data along ambient seismic Line 2, the *Vp* active survey (AS) and Power Spectral Density ambient seismic noise survey (ASN) have a fair correlation coefficient (0.4>|x|<0.5) while *Vs* ambient noise has a good correlation. Note that Power Spectral Density has a negative correlation with temperature. However, we know that temperature at SL Lake increases with depth (Figures 40 and 66) and we attempted to remove this effect by determining the correlation coefficient for temperature residual in the same manner as reported in AltaRock, 2014). Figure 66 shows that temperature at SL is highly correlated with depth, consequently to control for this parameter, temperature was regressed on depth and the residuals were used to get correlations with each of the other variables. The intention of this method is to determine if unusually hot spots at a particular depth are correlated with any of the variables. The values for TempRes are the distances above or below the blue line in Figure 66. Thus if a correlation coefficient with TempRes is large, this is an indication that the variable is a good predictor of locations where it is hot compared to other locations at the same depth. The temperature residual correlation coefficient using all the data along ambient seismic Line 2, the only geoscience parameter with a "high" correlation coefficient, 0.462, is the Hurst No. ASN which is classified as a fair correlation.

Using “well data” along ambient seismic Line 2, we find that the temperature correlation coefficient is good for MT (0.598) and excellent for *Vp* AS (0.724) and *Vs* ASN (0.776). All these are statistically significant. The comparison between using “all data” versus “well data” was done because the temperature “well data” is a hard data set while the “all data” set is a mix of hard data and modeled temperature data.

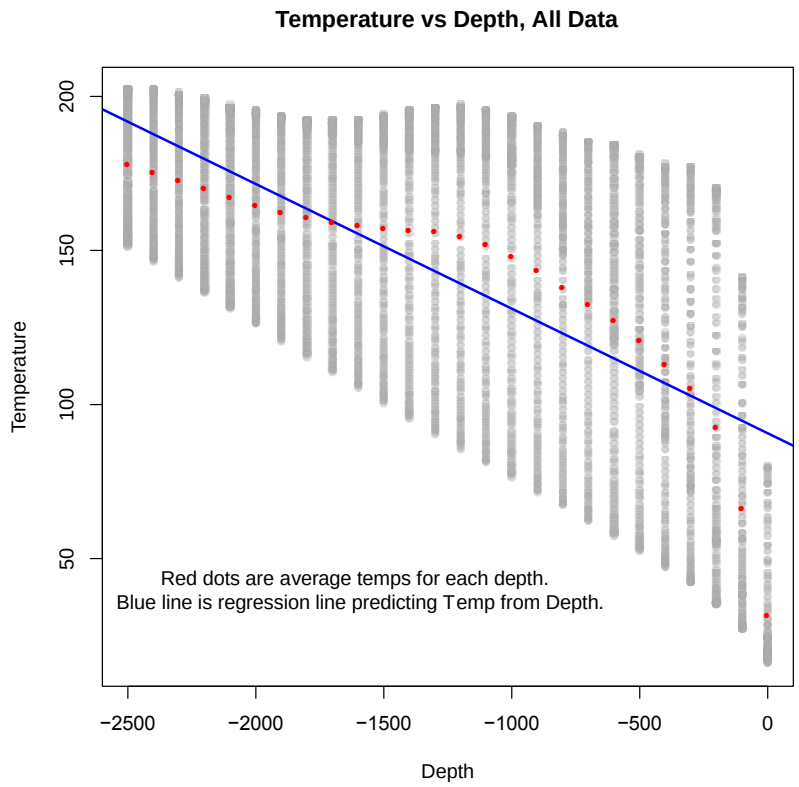

Figure 66. Temperature-depth relationship for data along ambient seismic line2

6.3.2 Temperature-Depth-Lithology Relationships

Figure 67 shows the temperature-depth-lithology relationship along ambient seismic line2 using “all data”. Within the figure, hotter temperatures are shown in red, cooler temperatures in blue. The white region in the lower right is missing data. In addition, the regions are shown based on lithology, with small dots indicating basin fill, vertical lines for basalt, and horizontal lines for bedrock. The figure shows that the hottest shallow regions tend to be basalt.

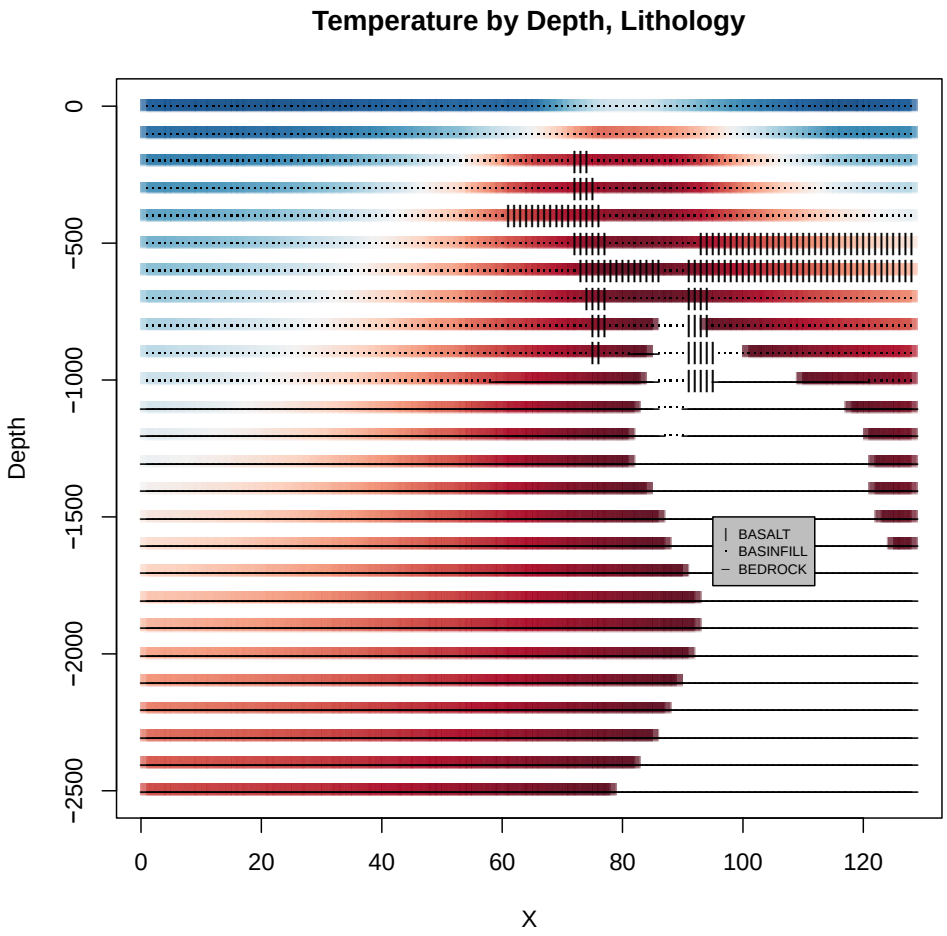

Figure 67. Temperature-depth-lithology relationship along ambient seismic line2

6.3.3 Lithology Correlations

The various geostatistical variables were also broken down by lithology. Since lithology is a categorical rather than a numerical variable, we looked at average values within each lithology rather than at correlations. The results are summarized in Table 5 using "all data" and in Table 6 using "well data" both along ambient seismic line 2.

As for the correlation results, some of the averages detectable where data was missing for particular variables and lithology combinations and are identified as NA. Perhaps the most interesting findings from the data in Tables 5 and 6 without consideration of statistical significance are:

1. The basalt seems to have quite large values for TempRes, meaning that basalt has average TempRes over 40°C higher than would be predicted at that depth using "all data" and over 37°C for the "well data".
2. The bedrock shows a similar a similar relationship to that in item no. 1 above for the bedrock using the "well data".
3. The *Vp* active is higher in the bedrock relative to the other two formations using "all data" and slightly higher using the "well data".
4. The *Vp* anomaly is lowest in the bedrock for "all data" and "well data".
5. The Correlation Length (AS) is lowest in the bedrock for "all data" and highest for the "well data".
6. The Hurst No, (AS) has the same relationship as item no. 5 above.,
7. The *Vs anomaly* is somehat higher using "all data" but significantly lower using the "well data".
8. The *Vs* ASN is slightly higher in the bedrock using "all data".
9. The *Vs* anomaly fk ASN shows significant differences between all three units using all data but is only slightly different for the three formations using "well data".

Table 5. Average geoscience parameter values (see text for an explanation) for each of the three formations identified at Soda lake and the p-values (see text for an explanation) for the differences between the averages using "all data". P-values are rounded to nearest ten-thousandth and the ones greater than 0.05 are not statistically significant and are highlighted in yellow.

Geoscience Parameter	Correlation Coefficient -Using All Section Data			Corresponding p-values for the different average values for formation comparison		
	Basalt	*BASINFILL*	*BEDROCK*	*Basalt-BasFill*	*Basalt-Bedrock*	*BasFill-Bedrock*
Temperature (Temp)	157.85	102.57	163.58	0	0.0027	0
Vpactive[1]	2.79	2.7	4.33	0.0163	0	0
Vpanom[2]	-1.6	-0.23	-4.49	0.0051	0.0002	0
Clactive[3]	82.85	88.37	58.97	0.1529	0	0
Hurstactive[4]	0.95	0.63	0.39	0	0	0
Vsanom[5]	-0.18	-0.92	0.04	0.0226	0.2658	0
Vsambient.noise[6]	1.21	1.18	1.52	0.013	0	0
Vsanomambientfk[7]	-5.79	1.98	0.43	0	0	0.019
Vsfkambient[8]	1.43	1.45	1.69	0.3014	0	0
Clambient[9]	75.78	85.95	56.24	0.014	0	0
Hurstambient[10]	0.94	0.64	0.4	0	0	0
MT[11]	4.23	5.61	55.29	0	0	0
FP_Opt15[12]	0.14	0.04	0.03	0.0002	0	0.0736
FP_M11[13]	0.17	0.05	0.08	0	0.0007	0.0003
Entropy[14]	2.21	3.73	0.29	0.0002	0	0
Spectral[15]	-11.08	-9.73	-11.33	0	0.0619	0
Vp/Vs[16]	2.31	2.26	2.85	0.0055	0	0
TempResidual	43.86	-7.18	1.08	0	0	0

1 - *Vp* active survey (AS
2 - *Vp %* anomaly
3 - Correlation Length AS
4 - Hurst No. AS
5 - *Vs* anomaly 3-model ambient seismic noise (ASN)
6 - *Vs* 3-model anomaly ASN
7 - *Vs* anomaly fk ASN
8 - *Vs* fk ASN
9 - Correlation Length ASN
10 - Hurst No. ASN
11 - Magnetotelluric resistivity
12 - Fault planes by Optim (2015)
13 - Fault plane by Magma (2011)
14 - Entropy
15 - Power Spectral Density
16 – Vp/Vs ratio

10. The *Vs* fk ASN shows comparable results for all three formations using all the data sets considered.
11. The Correlation Length ASN is highest for the basin fill using "all data" but highest for the bedrock using "well data".
12. The Hurst No. is lowest for bedrock using both data sets.
13. The MT resisitivity shows a comparable relationship as item 12 above, but highest instead of lowest in bedrock.
14. The fault plane parameter using Optim (2015) data is highest in the basalt using both data sets.
15. The fault plane parameter using Magma (2011) data is comparable to item 14 above.
16. The Entropy parameter is the lowest in the bedrock using both data sets.
17. The TemRes is highest for the basalt using "all data" and the basalt and bedrock are comparable using the "well data".

6.3.4 Fault Relationships

The various geostatistical variables were also broken down with respect to the Optim (2015) and Magma (2011) faults being present or not in Table 7 using "all data" and Table 8 using "well data". The data is approximately comparable in both data sets. We observed many relationships with the fault data that are consistent with our geological expectations

across both the "all data" and the "well data". For faults based both on Optim and Magma, the following observations are made:

1. Temperature is higher in the faults, both measured by raw temperature and by the temperature residuals. In particular, in the "all data" based on both Optim and Magma faults, the temperature residuals are ~30˚C higher than for non-fault cells, indicating that compared to cells at a similar depth, the faults are considerably hotter.
2. Correlation length active is lower in faults, Hurst number (both active and ambient) is higher in faults. These results are consistent with having more fractures in the fault areas, and are encouraging in that these parameters may be useful in predicting fault locations.
3. For other parameters, the relationship with the faults is somewhat less consistent, though for the "all data" both sets of faults: Vs anomaly, Vs ambient.noise, and Vs fk ambient are all higher, while Vs anomaly fk ambient and MT are lower.

Table 6. Average geoscience parameter values (see text for an explanation) for each formation at Soda lake and the p-values (see text for an explanation) for the differences between the averages using "well data". The geoscience parameters and the three geologic units include "all data" along the ambient seismic line 2. P-values are rounded to nearest ten-thousandth and the ones greater than 0.05 are not statistically significant and are highlighted in yellow.

Geoscience Parameters	**Correlation Coefficients using "Well Data"**			**Corresponding p-values**		
	BASALT	*BASINFILL*	*BEDROCK*	*Basalt-BasinFill*	*Basalt-Bedrock*	*BasinFill-Bedrock*
Temp	154.64	115.9	185.77	0.0012	0.0001	0
Vpactive[1]	2.68	2.47	3.81	0.0999	0	0
Vpanom[2]	-5.76	-0.58	-14.3	0.063	0.0714	0.0048
Clactive[3]	45	53.43	124.9	0.3651	0.0526	0.0687
Hurstactive[4]	1.41	0.93	0.59	0.021	0.0002	0.029
Vsanom[5]	-0.98	-1.05	-2.06	0.4831	0.2165	0.2351
Vsambient.noise[6]	1.21	1.13	1.46	0.1086	0	0
Vsanomambientfk[7]	-7.98	-6.9	-8.87	0.4288	0.4335	0.338
Vsfkambient[8]	1.42	1.25	1.54	0.0448	0.1007	0
Clambient[9]	39.32	47.16	135.19	0.3527	0.0338	0.0462
Hurstambient[10]	1.4	1.04	0.59	0.0703	0.0003	0.0086
MT[11]	4	4.77	26.46	0.1849	0	0
FP_Opt15[12]	0.18	0	0.04	0.068	0.1312	0.1587
FP_M11[13]	0.18	0	0.12	0.068	0.3147	0.0355
Entropy[14]	5.05	4.23	0	0.354	0.0016	0.0008
Spectral[15]	-10.43	-10.91	-11.72	0.1048	0.0001	0.0053
Vp/Vs[16]	2.24	2.17	2.63	0.2695	0.0148	0.0077
TempRes	40.07	8.38	33.67	0.0025	0.2183	0.0014

1 - *Vp* active survey (AS
2 - *Vp %* anomaly
3 - Correlation Length AS
4 - Hurst No. AS
5 - *Vs* anomaly 3-model ambient seismic noise (ASN)
6 - *Vs* 3-model anomaly ASN
7 - *Vs* anomaly fk ASN
8 - *Vs* fk ASN
9 - Correlation Length ASN
10 - Hurst No. ASN
11 - Magnetotelluric resistivity
12 - Fault planes by Optim (2015)
13 - Fault plane by Magma (2011)
14 - Entropy
15 - Power Spectral Density
16 – Vp/Vs ratio

6.3.5 Seismic Parameter – Qualitative and Quantitative Correlation Summary

Table 9 summarizes the seismic parameter geologic significance with the qualitative and quanitiative correlation results.

6.4 Favorability Trust Mapping

6.4.1 Mapping Approach

Existing geologic and geophysical data including ambient seismic data collected for the current study were incorporated into SL geothermal resource assessment along seismic Line2, similar to the analysis performed by Iovenitti et al. (2012) for the Dixie Valley geothermal system. A 2D favorability cross-section was constructed for SL along Line 2 with 33-meter horizontal grid cell lengths, which was selected to represent the mean spacing of the ambient seismic line receivers. Each grid cell extends to an incremental depth of 100m and contoured, gridded profiles representing the data sets considered for the favorability analysis were presented in the Task 6 discussion above.

Parameters and weights for the active and passive seismic survey data along with temperature and lithology are presented in Tables 10a and 10b, respectively. The following equation provided weighted favorability values for each cell along ambient seismic line2:

$$F_V = (d_0 * w_0) + (d_1 * w_1) + (d_n * w_n)$$

where F_v is the overall favorability value for the cell, favorability values for individual geoscience parameters considered (Tables 10 and 11) at each cell location are represented by d_0 through d_n, and w is a weighting parameter assigned for each geoscience data set. Figures 68 and 69 the favorability maps for the active and passive survey, respectively. Figures 70 and 71 present pseudo-favorability maps based on solely the seismic parameters identified in this section.

Table 7. Average values for geoscience parameters and the lack of faults or the presence of faults as indicated by Optim, (2015) and Magma (2011) at Soda Lake using "all data" along ambient seismic line 2. p-values correspond to the differences between the means between the groups (e.g., no fault present/fault present) analyzed. P-values are rounded to nearest ten-thousandth and the values greater than 0.05 are not statistically significant) and are highlighted in yellow.

Geoscience Parameters	No Fault Present based on the Optim, Inc. Analysis	Fault Present based on the Optim, Inc. analysis	Corresponding p-values	No Fault Present based on (Magma, 2011)	Fault Present based on (Magma, 2011)	Corresponding p-values
Temperature (Temp)	140.16	159.24	0	138.54	172.85	0
Vpactive[1]	3.08	3.42	0	3.09	3.17	0.1651
Vpanom[2]	-1.21	-4.08	0.0017	-1.17	-4.22	0.0009
Clactive[3]	71.56	53.58	0	71.17	66.62	0.184
Hurstactive[4]	0.49	0.81	0	0.49	0.59	0.002
Vsanom[5]	-0.76	0.72	0	-0.8	0.95	0
Vsambient.noise[6]	1.26	1.37	0	1.26	1.33	0.0002
Vsanomambientfk[7]	0.98	0.74	0.3788	1.03	0.12	0.1487
Vsfkambient[8]	1.5	1.62	0	1.5	1.57	0.0001
Clambient[9]	68.23	63.53	0.1838	67.94	69.38	0.3932
Hurstambient[10]	0.5	0.81	0	0.51	0.63	0.0002
MT[11]	35.33	19.28	0	35.39	25.56	0
Entropy[12]	1.65	1.33	0.2092	1.65	1.48	0.2921
Spectral[13]	-10.8	-9.88	0	-10.72	-11.11	0.0088
Vp/Vs[14]	2.4	2.46	0.0521	2.41	2.37	0.1523
TempResidual	-1.17	29.27	0	-2.1	28.25	0

1 - *Vp* active survey (AS
2 - *Vp %* anomaly
3 - Correlation Length AS
4 - Hurst No. AS
5 - *Vs* anomaly 3-model ambient seismic noise (ASN)
6 - *Vs* 3-model anomaly ASN
7 - *Vs* anomaly fk ASN
8 - *Vs* fk ASN
9 - Correlation Length ASN
10 - Hurst No. ASN
11 - Magnetotelluric resistivity
12 - Entropy)
13 – Power Spectral Density
14 - Vp/Vs ratio

Table 8. Average values for geoscience parameters and the lack of faults or the presence of faults as indicated by Optim, (2015) and Magma (2011) at Soda Lake using "well data" along ambient seismic line 2. p-values correspond to the differences between the means between the groups (e.g., no fault present/fault present) analyzed. P-values are rounded to nearest ten-thousandth and the values greater than 0.05 are not statistically significant) and are highlighted in yellow.

Geoscience Parameters	No Fault Present based on the Optim, Inc. Analysis	Fault Present based on the Optim, Inc. analysis	Corresponding p-values	No Fault Present based on (Magma, 2011)	Fault Present based on (Magma, 2011)	Corresponding p-values
Temperature (Temp)	148.09	176.67	0	146.39	186.4	0
Vpactive[1]	2.88	2.89	0.4533	2.88	2.85	0.4206
Vpanom[2]	-4.15	-21.2	0	-4.69	-14.31	0.1348
Clactive[3]	75.02	16.7	0.0002	75.02	16.73	0.0002
Hurstactive[4]	0.92	1.35	0.0091	0.91	1.43	0.0175
Vsanom[5]	-1.38	0.08	0.0299	-1.41	0.46	0.0224
Vsambient.noise[6]	1.22	1.45	0	1.22	1.37	0.0953
Vsanomambientfk[7]	-8.07	-2.52	0.0122	-8.15	-1.55	0.0072
Vsfkambient[8]	1.34	1.65	0	1.35	1.59	0.0005
Clambient[9]	73.16	17.03	0.0007	73.17	16.97	0.0007
Hurstambient[10]	0.97	1.29	0.0414	0.96	1.38	0.0516
MT[11]	13.23	9.33	0.0631	12.77	16.6	0.2535
Entropy[12]	2.68	3.67	0.3256	2.76	2.24	0.3755
Spectral[13]	-11.21	-9.87	0	-11.16	-11.01	0.4003
Vp/Vs[14]	2.33	1.99	0	2.33	2.1	0.0415
TempResidual	22.17	49.6	0	22.19	38.31	0.0694

1- *Vp* active survey (AS)
2- *Vp %* anomaly
3- Correlation Length AS
4- Hurst No. AS
5- *Vs* 3-model anomaly ASN
6- *Vs* 3-model ambient noise survey (ASN)
7- *Vs* anomaly fk ASN
8- *Vs* fk ASN
9- Correlation Length ASN
10- Hurst No. ASN
11- Magnetotelluric resistivity
12- Entropy
13- Power Spectral Density
14- Vp/Vs ratio

Table 9. Cross-correlation of the geological Significance of various seismic attributes measured or modeled in this study with the qualitative geoscience correlations.

Seismic parameter	Geological Significance	Qualitative Geoscience Correlations	Quantitative Geoscience Correlations
Vp, Vp anomalies, Vs, Vs anomalies, Vs % and Vs fk anomalies	Conventional interpretation is that low P and S velocities are associated with unconsolidated rocks and/or rocks having higher temperature (Wang et al., 1990) and/or with higher degree of rock fracturing, and/or water saturated rocks. Faults not always clearly interpretable from velocity models but can be identified by sharp contrasts in velocity gradients (Ramachandran, 2011).	The Vs models (3-model and fk) indicate an increase in velocity with depth, which correlates with denser media as indicated from the gravity data. Both Vs modeling approaches show decreased velocities in the area of known faulting and high temperatures. The Vp anomaly model shows an area of increased velocity near the basalt body (located with gravity data). The Vs fk model also suggests a velocity increase in the area of the lava flows.	Fair to good correlations (see Section 6.3 for definitions of correlations rank) exist between the *Vp* and thermal data. The Vs (3-model) has good correlations and the *Vs* (fk) values has excellent correlations with temperature. *Vp* is higher in the bedrock than the basin fill and basalt. *Vp* anomalies are the lowest in the bedrock. *Vp* anomaly indicates a decrease in *Vp* in the faulted areas but a relationship between Vs anomalies and faults was less clear.
Vp/Vs	High Vp/Vs ratio may indicate fluid-saturated rock (Wang et al, 1990).	Highest Vp/Vs ratio at 0.3km is correlated with the central portion of the high temperature anomaly at 0.3km and 0.6 km. A low Vp/Vs ratio occurs north of the middle of the ambient seismic Line 2 at 0.3km depth where a steam cap was co-located with these anomalies. High Vp/Vs ratios indicated by the 2D models are well correlated with the area of the known high temperature anomaly. Differences in Vp/Vs ratios at 0.3km (low Vp/Vs) and 0.8 km (high Vp/Vs) suggested the presence of a steam cap immediately north of the central portion of Line 2.	Fair to good correlations exist between the Vp/Vs ratios and temperature.
Attenuation (Q)	All the other parameters constant, attenuation increases as temperature increases and/or with faulting and/or fracturing.	Attenuation in this study did not provide any meaningful data.	P-wave attenuation in this study did not provide any meaningful data.
Power Spectral Density	Scattering of wavelengths indicates fragmentation which may be indicative of faults and/or fracturing.	Correlates with the area od known faulting between Magma Fault 1 and 84-33. Power Spectral Density suggests faulting in the area west of Fault 1 but there was no supporting data from Magma (2011). This may be due to the lack of investigation by Magma in this area.	No quantitative correlation was found between faults and power spectral density at depth. This may be due to weaker coda of the reflection GF.
Entropy	Lateral and vertical dimension of fragmentation may be indicate of faults and/or fracturing.	Correlates with the area of faulting defined by Optim (2015) in this study and Magma (2011).	No quantitative correlation was found between faults and entropy at depth. The lowest entropy values are located within bedrock. This may be due to weaker coda of the reflection GF.

Seismic parameter	Geological Significance	Qualitative Geoscience Correlations	Quantitative Geoscience Correlations
Correlation Length	Upper limit of fractal dimension of heterogeneity. Related to fragmentation in the medium. If the correlation length is low this may be indicative of fault and/or fracturing.	Approximate correlation with Magma (2011) and Optim (2015) in this study faults in the area around Magma Fault 3.	AS correlation length is lower in the faulted areas.
Hurst Number	Fractal measure of medium may be indicative of fault and/or fracturing. Small fractal dimension may be indicative of dipping layers.	Approximately correlates with the area of intense faulting as defined by Magma Faults 1, 2 and 3 as well as Optim (2015) in this study defined faults. Excellent correlation with dipping beds as defined by Optim (2015) in this study.	AS and ASN Hurst Numbers are higher in the faulted areas. The lowest values (AS and ASN) are located within bedrock. A fair correlation exists between the data (AS and ASN) and temperature residuals.

6.4.2 Mapping Results

Figures 68and 69 present the combined results from favorability mapping with the temperature, and gravity-based lithologic data along with the active and passive seismic data, respectively. The contributions of only the active seismic data (Figure70) and only the passive seismic data (Figure 71) are also presented as pseudo-favorability maps because not all the favorability parameters were considered.

Table 10a. Favorability Mapping Parameters of Interest and Their Favorability Values - Active Survey

Temp (□C, 0.50 w[2])	Fav Value[1]	Lith-ology[3] (0.20 w)	Fav Value	Seismic Parameters ((0.30 w)									
				Vp anomaly (0.09 w)	Fav Value	*Q (0.01 w)*	Fav Value	*Correlation length (0.07 w)*	Fav Value	*Hurst number (0.06 w)*	Fav Value	*Entropy Coef. (0.07 w)*	Fav Value
<100	1	Basin Fill	1	<-15%	3	>0 & < 10	1	>100	2	>0.8	3	>6	3
100	1	Basalt	5	<0	2	>10	2	<100	3	<0.8	2	<6	1
110	1	Bedrock	5	>15%	1	<0	0						
120	2												
130	3												
140	4												
150	5												

[1]Favorability Value (1-5 with 5 being the highest)
[2]Favorability weights
[3]Represented by the generalized formations in Soda Lake

Table 10b. Favorability Mapping Parameters of Interest and Their Favorability Values - Passive Survey

Temp (°C, 0.50 w[2])	Fav Values[1]	Lith-ology[3] (0.30 w)	Fav Value	Seismic Parameters (0.30 w)					
				Vp anomaly active survey	Fav Value	Vs anomaly from Line2 fk	Fav value	*Q from active source**	Fav Value
<100	1	Basin Fill	1	<-15%	3	<-15%	3	>0 & < 10	1
100	1	Basalt	5	<0	2	<0	2	>10	2
110	1	Bedrock	5	> 15%	1	>.15%	1	<0	0
120	2	---		---	---	---		---	---
130	3	---		---	---	---		---	---
140	4	---		---		---		---	---
150	5	---		---		---		---	---

Seismic Parameters (0.30 w)											
Correlation length active source	Fav Value	*Hurst number. Active source*	Fav Value	Q from ambient noise*	Fav Value	Cor-relation length ambient noise	Fav Value	Stochastic Coef. ambient noise	Fav Value	*Entropy Coef. From ambient noise*	Fav Value
>100	2	>0.8	3	>0 & < 10	1	>100	2	>0.8	3	>6	3
<100	3	<0.8	2	>10	2	<100	3	<0.8	2	<6	1
---	---	---	---	<0	0	---		---	---	---	---
---	---	---	---	---	---	---	---	---	---	---	---
---	---	---	---	---	---	---	---	---	---	---	---
---	---	---	---	---	---	---	---	---	---	---	---

[1]Favorability Value (1-5 with 5 being the highest)
[2]Favorability weights
[3]Represented by the generalized formations in Soda Lake

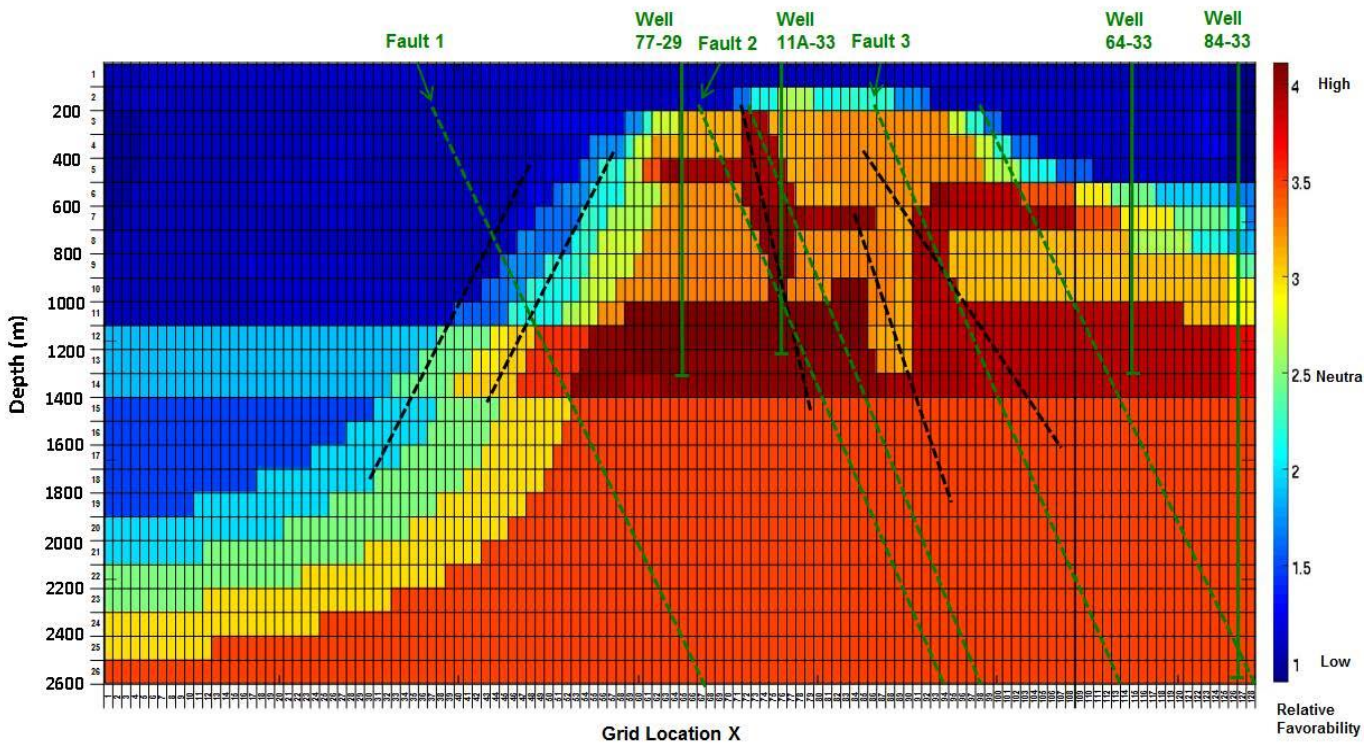

Figure 68. Favorability map produced with active seismic survey temperature, and gravity-based lithologic parameters. Optim (2015) faults are presented in black while major (Faults 1, 2 and 3) and minor Magma (2011) faults are shown in green.

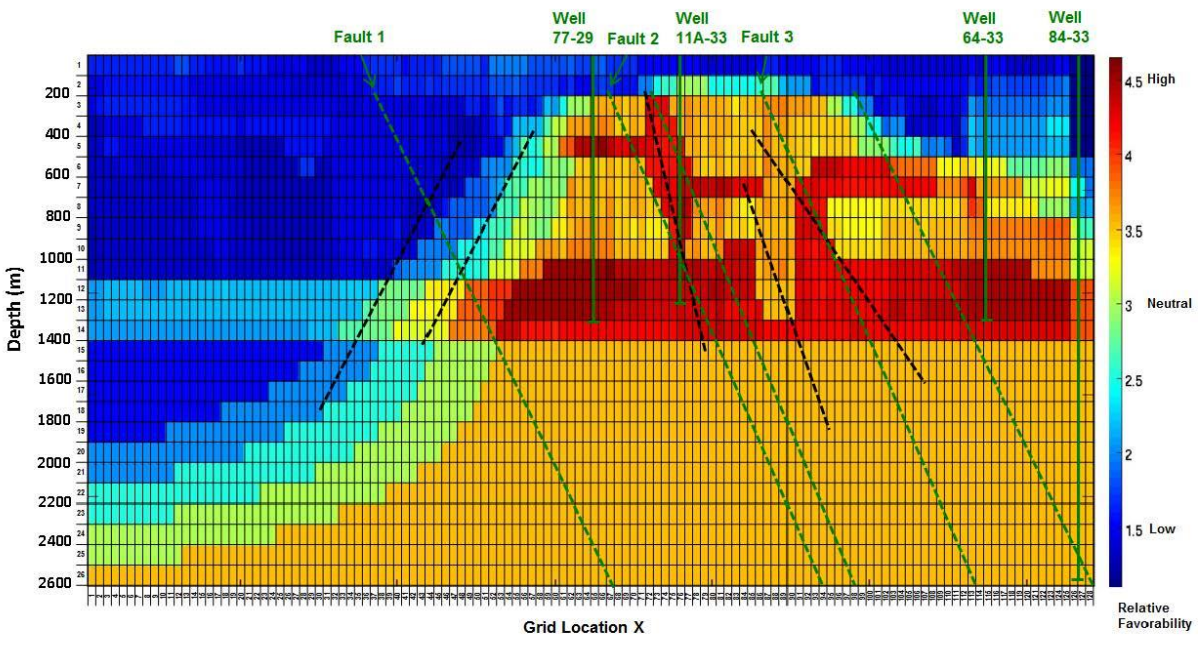

Figure 69. Favorability map produced with passive seismic Survey, temperature, and gravity-based lithologic parameters. Optim (2015) faults are presented in black while major (Faults 1, 2 and 3) and minor Magma (2011) faults are shown in green.

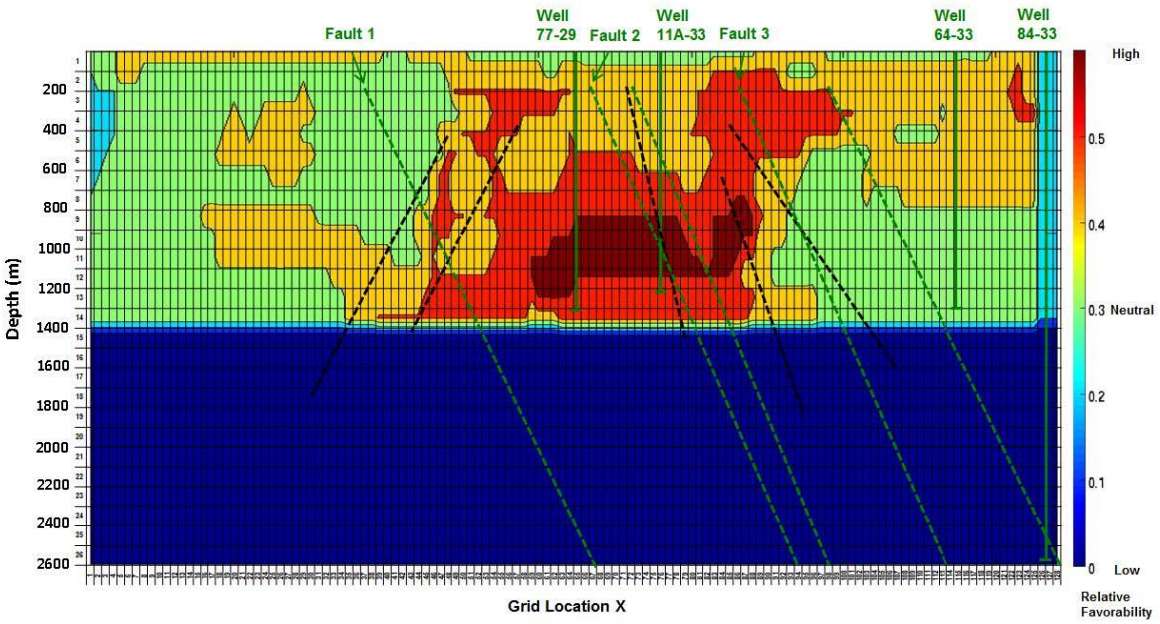

Figure 69. Pseudo-favorability map produced with active seismic survey without consideration of the temperature or lithology parameters. Optim (2015) faults are presented in black while major (Faults 1, 2 and 3) and minor Magma (2011) faults are shown in green.

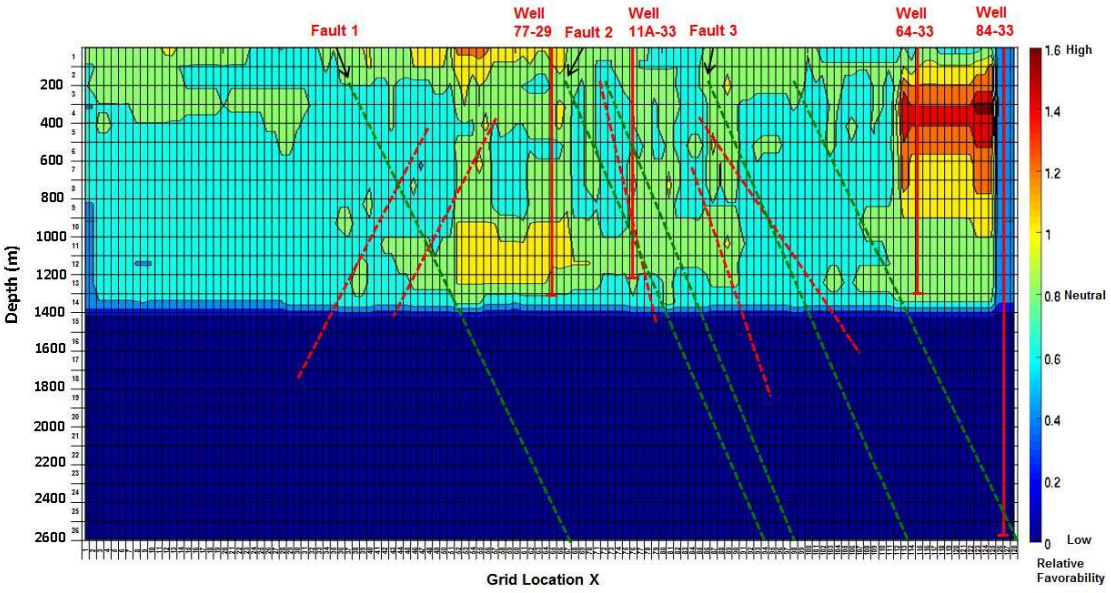

Figure 70. Pseudo-favorability map produced with passive seismic survey without consideration of the temperature or lithology parameters. Optim (2015) faults are presented in black while major (Faults 1, 2 and 3) and minor Magma (2011) faults are shown in green.

5 CHALLENGES AND LESSONS LEARNED

1) **Sample rate:** It is our experience that a higher sample rate increases the accuracy (better resolution) of the extracted GFs, because it increases the ambient noise bandwidth. Thus, although using 500sps (250Hz Nyquist frequency, i.e., 0-250Hz frequency band) is best, it is shown below that the high end of the useable frequency band for the extracted GFs at Soda Lake was 25Hz, due to large amplitude cultural noise at 30Hz and 60Hz. When cultural noise is not present, we estimate that the useable frequency band is potentially higher, however, not much higher than 60Hz.

2) **Waveform pre-filtering:** The fk methods were designed for strong SNR signal with energy in a frequency band broader than 2Hz. Ambient seismic noise GFs often have narrow frequency bands, mostly when extracted at short distances (Tibuleac, in preparation for BSSA). This is why CWT was used in this case prior to fk analysis, thus avoiding the "ringing" typical for Fourier filtered signals when the filter is too narrow in frequency.

2) **Strong contamination with acoustic waves:** As shown in Figure 18, strong GF contamination with acoustic waves (0.32-0.36km/s) occurred at all stations. This is why all the velocities below 0.4km/s were discarded. This means that the SL_FK_LINE_MOD is valid deeper than ~150 m. Contamination with acoustic waves may be avoided by burying the sensors deeper.

3) **Contamination with cultural noise:** Noise was mitigated using data pre-filtering, before seismic interferometry was applied. Frequencies around 3Hz and 30Hz were filtered out, and the results significantly improved, however, as seen in Figure 18A, harmonic cultural noise leaked into frequencies around 3Hz (in this case 2.5Hz) and measurements in this frequency range were also discarded. Consequently, all the crosscorrelations including these stations' waveforms were also affected, leading to weak P-arrivals. The cultural noise was higher in amplitude in the production area, and around the power plant, affecting the most the high frequency (>2.5Hz) records at stations W90 to W128. Fortunately, in new exploration areas power plants are not present, however, these problems point out the importance of seismic noise evaluation at a site prior to the deployment.

3) **Identification of Rayleigh velocity fundamental and higher modes:** Surface wave dispersion data obtained in field surveys are inherently incomplete, which makes identification of Rayleigh velocity fundamental and higher modes difficult at times. Insufficiently constrained dispersion curves, truncated frequency range, and inclusion of data from higher-mode dispersion curves can produce erroneous inversion results (Zhang and Chan, 2003). Our attempts to mitigate this problem included inversion of both phase and group velocity for the same area, and comparison of the synthetic and observed dispersion curves (Figure 6 and Figure 15). While at the current model resolution we consider the errors acceptable, for improved resolution we recommend supplementary tests, such as using three – component elipticity information and modifications of the fk-methods to eliminate higher modes iteratively, using the synthetic higher-mode dispersion curve information. Further tests of the automatic algorithms created for this project will include improved phase velocity analysis, using synthetic data. On the other hand, errors associated with high frequency velocity data have almost no effects on the inversion.

4) **Wider band sensors:** Because accurate phase velocity data at low frequency range are crucial to the reconstruction of the ground model, the use of wider band sensors is recommended.

5) **IRIS/PASSCAL sensor availability and available sensor specification:** Constraints determined the timing and the configuration of the seismic surveys. Different sensors than initially required were available to us due to delays in permitting and in the project start.

6) **Competitive calculations:** Due to the very high sample rate, despite algorithm improvements, the calculations were not competitive to the active survey calculations. This is a problem that will be solved using parallel computers.

7) **Mixed sensor types:** A mixed set of sensors, including broadband and short period would have enhanced the resolution deeper than 1000m.

8) **Cultural noise mitigation:** To mitigate cultural noise effects, the sensors deployed near the power plant should have been buried deeper, and deployed farther from the well-field pipelines and from the road. Some of the best data was obtained using deeply buried high frequency geophones in a quiet setting, even if the total recording time was as short as 6 days.

9) **Field conditions testing:** Extended tests of the field conditions and analysis of the ambient noise composition are recommended before any future deployment.

8) **Different *Vp* and *Vs:*** Because of the nature of the subsurface structure, the *Vp* and *Vs* anomalies may differ significantly at the same location.

10) **GF P-component:** We have outlined possibilities for extraction and characterization of the P-component of the GFs, which we recommend as the subject of future research.

11) ***Vp, Vs,* and *Vp/Vs* by ambient noise:** We recommend that the possibility of obtaining a Vp, Vs and Vp/Vs velocity model using only ambient noise autocorrelations is evaluated in the future, as well as fault identification, because of high potential to provide reliable and independent model information.

12). **Solutions to reduce the length of processing time** Due to the large amount of data processing time needed for interferometry application to 500sps seismic waveforms, questions regarding the optimal amount of time for a seismic survey and an assessment of the best processing time window (with or without overlap) are pending. Solutions are suggested below.

One solution is to process data separately for P and fundamental Rayleigh arrivals. Using a higher sample rate and shorter windows (in this case 3s) substantially shortened the processing time for P-arrivals. Second, using a lower sample rate and longer windows for Rayleigh wave processing would also shorten the analysis time, because the fundamental mode Rayleigh was observed at longer periods (lower frequency).

A third solution is to shorten the experiment duration. A shorter experiment duration (3 days) using a crosscorrelation window of 20s, with 10% overlap (named here OWL) resulted in similar GFs when compared to a long (21 day) experiment duration, with 1 day time windows, and no overlap, only in the absence of significant cultural noise (Figure 71A compared to Figure 71B). These results are not enough to draw a conclusion and further investigation is necessary, for instance to estimate the best window length, overlap, and pre-filtering, however, this approach is promising for reducing processing time and method costs.

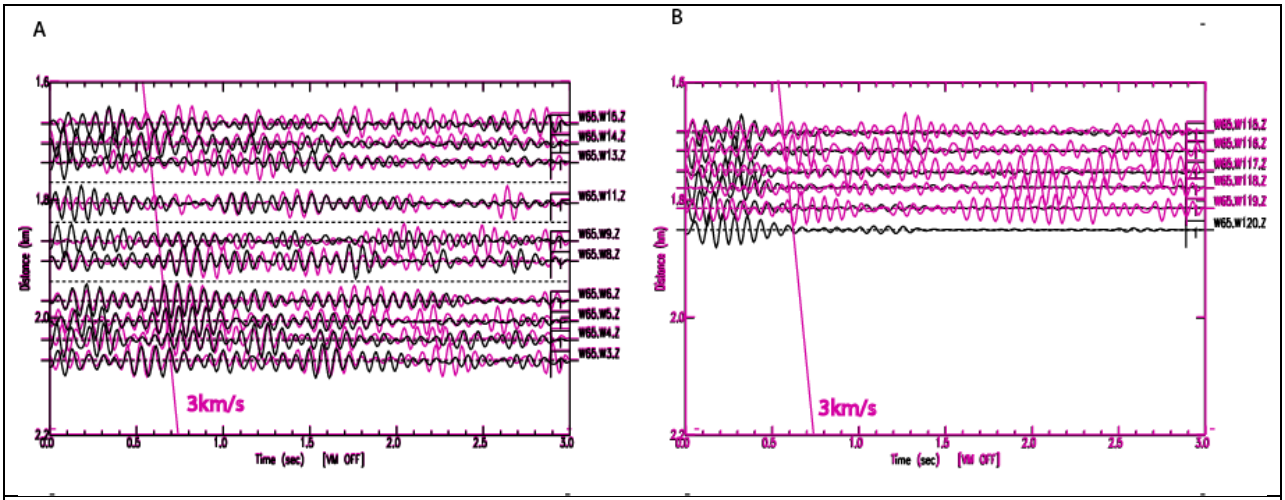

Figure 71 A shows that using overlapped windows (OWL) for three days of recording potentially produces similar results with a longer duration of the experiment to the north of W65, however not to the south, where data was contaminated with cultural noise. The black traces show OWL – extracted GFs in both A and B plots. The magenta traces are the same traces as in Figure 71 C and D and show (see text for explanation) B. In the case of waveforms contaminated with cultural noise, the window overlap appears to enhance the unwanted noise.

6 CONCLUSIONS

We tested and evaluated a novel seismic exploration method based on analysis of body-waves and surface-waves extracted from ambient seismic noise. The merit of the ambient noise seismic survey at SL when compared to an active survey is in a combination of multiple seismic parameter measurements which we assess as useful, as a cost-effective preliminary analysis of geothermal favorability. This technique allows first-order geothermal reservoir characterization. When the waveforms are not affected by cultural noise, the method is comparable, however, of lower resolution than the active survey results. Improvements are suggested for this method, pending further investigations. The method can provide first-order geothermal favorability estimates, and potential areas of interest for detailed investigations with active surveys, through statistical integration of inexpensive seismic analysis results with information from other geological and geophysical data.

The P-components of the GFs extracted from ambient noise crosscorrelations were significantly affected by cultural noise near the power plant at frequencies higher than 20Hz. This was an unexpected result, considering the removal of the largest cultural noise energy bands prior to processing and the promising results of the Pyramid Lake experiment (Appendix 2B). Reflection GF's extracted from waveform autocorrelations were more promising for fault identification than the crosscorrelation GFs analysis. The Vs analysis was lower frequency, and thus less affected by cultural noise, and, even at lower resolution, showed promise for fault identification. Other seismic parameters designated by the geostatistic studies as highly correlated to temperature, however, were not affected by the cultural noise. A successful outcome of this experiment was extraction of periods of 1- 2 s using 5Hz corner frequency sensors. This was achieved by modification of the instrument response to simulate a broadband sensor. A first-approximation seismic velocity model can be provided by the autocorrelations, however, this possibility needs more testing, and comparisons must be made between the E, N and Z components, to correctly identify all the reflection GF arrivals. P-arrival identification and analysis is possible using array processing and is recommended for future studies. Recommendations were made to improve the P-wave extraction using array processing techniques and crosscorrelations of the coda of crosscorrelations.

Method cost-effectiveness It is estimated (Echols personal communication) that the total cost of this complete study was at least 5 times less than the cost of the active survey at the same location. The costs can be further lowered by reducing the duration of the experiment.

Method resolution Low-resolution model: SL_GVEL_MOD and SL_PHVEL_MOD had lateral resolution of ~ 500m. The depth resolution was better in the upper 300 m (~ 100 m resolution), however, the resolution was lower than 200 m for the deeper velocity values. The resolution of the Vs models extracted from seismic array processing (Figures 10 and 14) was lowest at depths greater than 800m. The SL_GVEL_MOD has better resolution at depths from 0.6 – 1.4km than the model SL_PHVEL_MOD. Higher resolution models: Although much more accurate (more ray paths) than the array models, the Line 2 model SL_LINE_FK_MOD had lateral resolution of ~ 150 m, and depth resolution variable, from ~ 100 m in the upper 300m, to less than 200 m deeper than 300m. Reflection GFs are extracted from autocorrelations every 34 m on the horizontal, thus changes in the GFs have the potential to identify faults with a ~ 30m resolution.

Method transportability We assess that the method works best in areas without significant monochromatic cultural noise. Noise assessment is a critical task prior to deployments and use in new locations.

Fault identification High resolution tomography, whether 2D or 3D appears to have the potential to delineate faults at the locations of velocity anomaly gradients. Investigations of lateral variations of the GF reflections shows changes in the GF reflection component patterns at locations coincident to fault locations.

Geostatistic analysis Qualitative and Quantitative correlations of have been made between the seismic parameters reported in this study and the gravity, magnetotelluric resistivity and temperature data reported by Magma (2011) and the faults identified by Magma as well as Optim (2015). Correlations range from being absent as is the case for attenuation to excellent, as in the case of the Hurst Number. Favorability maps were generated for the active and passive (ambient seismic noise survey) data parameters coupled with temperature and lithology. Additionally, pseudo-favorability maps were made using the seismic parameters alone for the two cited surveys. The favorability map of the ambient noise seismic survey identifies a “zone of interest” of spatial extent comparable to the zone of interest identified by the active survey, despite the difficulties due to cultural noise. A summary of cross-correlation of the geological significance of various seismic attributes measured or modeled in this study with the qualitative geoscience correlations is in Table 9.

7 PUBLICATIONS AND PRESENTATIONS

Paper and Poster presentation at the Geothermal Resource Council meeting, 2012.

Presentation at the 2015 Seismological Society of America annual meeting.

8 ACKNOWLEDGEMENTS

This project is made possible by the Department of Energy, Geothermal Technologies Office, contract EE0005518. During the seismic deployments we have received help and cooperation from Mr. Monte Morisson, Mr. Greg Champneys and the personnel at the Alterra Power Corp and from Fallon, NV land owners in the project area. UNR undergraduate students Jehren Boehm, Kegan Rahe, Darcy Fisher, Kelly Elloyan and Kate Schnoor and Michael Johnson from IRIS-PASSCAL were essential personnel during the field work. For all our field trips we used the UNR Mackay School of Science terrain vehicles and we were helped by Mrs. Melodie Gander. We are also expressing our gratitude to Drs. Mariana Eneva and Jim Echols, who were our partners at the start of the project and whose expertise and advice were essential in obtaining the contract.

9 REFERENCES

AltaRock Energy Inc., 2014a, EGS Exploration Methodology Project using the Dixie Valley Geothermal System, Nevada as a Calibration Site Part I—Final Scientific Report Baseline Conceptual Model, US Department of Energy DOE Award: DE-EE0002778, submitted to the National Geothermal Data Repository.

Altarock, 2014b, Exploration Methodology Project using the Dixie Valley Geothermal System, Nevada as a Calibration Site Part II—Final Scientific Report Enhanced Conceptual Model, US Department of Energy DOE Award: DE-EE0002778, submitted to the National Geothermal Data Repository, 2 January.

Campillo, Michel, and Anne Paul. "Long-range correlations in the diffuse seismic coda." Science 299.5606 (2003): 547-549.

Claerbout, Jon F. "Synthesis of a layered medium from its acoustic transmission response." Geophysics 33.2 (1968): 264-269.

Draganov D., Campman, X., Thorbecke, J., Verdel, A., and Wapenaar, K., 2009. Geophysics 74, p. A63–A67, 10.1190/1.3193529

Draganov, D., Campman, X., Thorbecke, J., Verdel, A., 2013. Seismic exploration-scale velocities and structure from ambient seismic noise (> 1 Hz), Journal of Geophysical Research: Solid Earth, 118, p. 4345-4360.

Echols, J., Benoit, D., Ohren, M., Oppliger, G., and T. Van Gundy, 2011. Integration of a 3D-3C reflection seismic survey over a known geothermal resource: Soda Lake, Churchill County, Nevada, GRC Transactions, 35.

Feng, C. and Teng, T., 1983. Three-dimensional crust and upper mantle structure of the Eurasian continent. Journal of Geophysical Research 88: doi: 10.1029/JB088iB03p02261. issn: 0148-0227.

Georgsson, L. S., Fridleifsson, G. Ó., Ólafsson, M., and Flóvenz, O.G., 2000. The geothermal exploration of the Öxarfjördur high-temperature area, NE-Iceland, Proc. World Geothermal Congress, Kyushu - Tohoku, Japan, May 28 - June 10, p. 1157-1162.

Gouedard P., Stehly, L., Brenguier, F., Campillo, M., Colin de Verdiere, Y., Larose, E., Margerin, L., Roux, P., Sanchez-Sesma, P.J., Shapiro, N.M. and Weaver, R.L., 2008. Cross-correlation of random fields: mathematical approach and applications, Geophysical Prospecting, 56, p. 375–393.

Halliday D. and Curtis, A., 2008. Seismic interferometry, surface waves, and source distribution. Geophys. J. Int., doi: 10.1111/j.1365-246X.2008.03918

Herrmann, R.B., Ammon, C.J., 2002. Computer Programs in Seismology, http://www.eas.slu.edu/People/RBHerrmann/ComputerPrograms.html.

Iovenitti, J., Tibuleac, I.M., Blackwell, D., Cladouhos, T., Karlin, R., Mack Kennedy, B., Issaks, E., P. Wannamaker, M. Clyne, O. Callahan (2010). Development of Exploration Methods for Engineered Geothermal Systems (vol. 33). Geothermal Resources Council Transactions, v. 33, p. 437-440.

Irie, K. and L. Brown, 2009. Extraction and analysis of seismic body waves from ambient noise recorded for crustal imaging in Montserrat, American Geophysical Union, Paper # V23D-2106, abstract and poster.

Olmsted, F.H., P.A. Glancy, J.R. Harrill, F.E. Rush, and A.S. Van Denburgh, 1975. Preliminary hydrogeologic appraisal of selected hydrothermal systems in northern and central Nevada, USGS Open File Report, 75-56.

Magma Energy Corporation (Magma), 2011. Soda Lake DOE Phase I Report Soda Lake 3D-3C Reflection Seismic Survey, report released to the US. Department of Energy Geothermal Technologies Offices and obtained for this report from Mr. James Echols, formerly of Magma, 13 May.

Pullammanappallil, S., Levander, A., Larkin, S., 1997. Estimation of crustal stochastic parameters from seismic exploration data, Journal of Geophysical Resources, 102, 15, 269-286.

Saenger, E., Lambert, H., Nguyen, M.A., and Schmalholz, S.M., 2009, 71st EAGE Conference & Exhibition — Amsterdam, The Netherlands, 8 - 11 June.

Schechinger, A., Goertz, B., Artman, 2009. Extracting subsurface information from ambient seismic noise – an example from Germany, 79th Society of Exploration Geophysics, Int. Exp. and An. Meet. Houston, Texas, USA, 25 - 30 October p. 1617-1621.

Stehli, L., Campillo, M., Froment, B., Weaver, R.L., 2008. Reconstructing Green's function by crosscorrelation of Coda of the Correlation (C3) of Ambient Seismic Noise, Journal Geophysical Research, 113, B11306, doi:10.1029/2008JB005693.

Tibuleac, I.M., Pullammanappallil, S., von Seggern, D. H., Pancha, A., Louie, J. N., 2010. Retrieval of Earth's reflection response from ambient seismic noise - a Nevada experiment, American Geophysical Union Fall Meeting, abstract #S33A-2071.

Tibuleac, I.M., von Seggern, D.H., Anderson, J.G., and Louie, J.N., 2011. Computing Green's Functions from Ambient Noise Recorded by Narrow-Band Seismometers, Accelerometers, and Analog Seismometers, doi: 10.1785/gssrl.82.5.661 Seismological Research Letters, September/October, v. 82, no. 5, p. 661-675.

Tibuleac, I., and Eneva, M., 2011. Seismic Signature of the Geothermal Field at Soda Lake, Nevada, from Ambient Noise Analysis, Geothermal Reservoir Council Transactions, 35, p. 1767-1772.

Tibuleac, I.M. and von Seggern, D.H., 2012, Crust-mantle boundary reflectors in Nevada from noise auto-correlations, Geophys. J. Int., v189, issue 1, p. 493-500.

Tibuleac, I.M. and Britton, J., 2006. An automatic regional surface wave detection algorithm, Bulletin of the Seismological Society of America, 96, p. 334 - 343.

Van Gundy, T., G. Oppliger, M. Ohren, D. Benoit, and M. Morrisson, 2010. Utilizing a comprehensive 3-D model to understand, maintain, and expand the Soda Lake geothermal resource, Nevada USA, GRC Transactions, 34, 1185-1189.

Zhang, S.X. and L.S. Chan, 2003. Possible effects of misidentified mode number on Rayleigh wave inversion, Journal of Applied Geophysics 53, 17–29

Zhang, J. and X. Yang, 2013. Extracting surface wave attenuation from seismic noise using correlation of the coda of correlation, JOURNAL OF GEOPHYSICAL RESEARCH: SOLID EARTH, VOL. 118, 2191–2205, doi:10.1002/jgrb.50186.

APPENDIX 1

AMBIENT SEISMIC LINE PERMITTING

Below is documentation on experiment permitting.

A. PROPOSED WEST-FALLON SURVEY DESCRIPTION SUBMITTED TO THE BUREAU OF LAND MANAGEMENT

This is a possible survey, pending a positive outcome of our Phase 1 research at Soda Lake. The survey location is only proposed, and will be changed as recommended. The sensor type is also subject to change, as a function of sensor availability from the Incorporated Research Institutions for Seismology, however, we are discussing below the sensors which would require the maximum site disturbance. Finally, the start date of the survey depends on: 1) The success of Phase 1 work; 2) The sensor availability from IRIS; 3) The possibility to use the sensors in conjunction with another DOE project.

The purpose of the survey

The purpose of the experiment will be to gather passive seismic data. We have developed methods of processing the seismic ambient noise which could diminish or eliminate the need for active seismic surveys. In addition, a larger aperture array of instruments will be installed around the line, to gather lower resolution velocity model information. This project is purely scientific research. No induced seismicity and no vibroseis trucks will be used.

Start date and end date

The start date and end dates are to be determined. ***We estimate the earliest deployment date as December 2014, and the latest date, March 2014.***

Relationships to Statues, Regulations, and Other Plans

The project will not interfere with the industrial or private activities in the area. The proposed project is also consistent with State of Nevada and Churchill County ordinances, policies and plans. The proposed passive survey is consistent with the National Energy Policy which encourages the development of energy resources including geothermal resources on federally managed lands.

Proposed Project Area

The figure below shows the proposed line in red and an approximate boundary for the larger seismic array as a thick black enclosure, which is roughly defined. After passively recording using stations on the line (deployment phase 1), we would redistribute the sensors as an array (deployment phase 2). To accomplish this task, some of the stations would be left on the line, and some of the stations would be moved outside the line, at more than 100 m interstation distance. The stations would be placed as close to existing roads as possible. While the line would follow the red line in the figure below, the array would be deployed in the black rectangle in Figure A1 below.

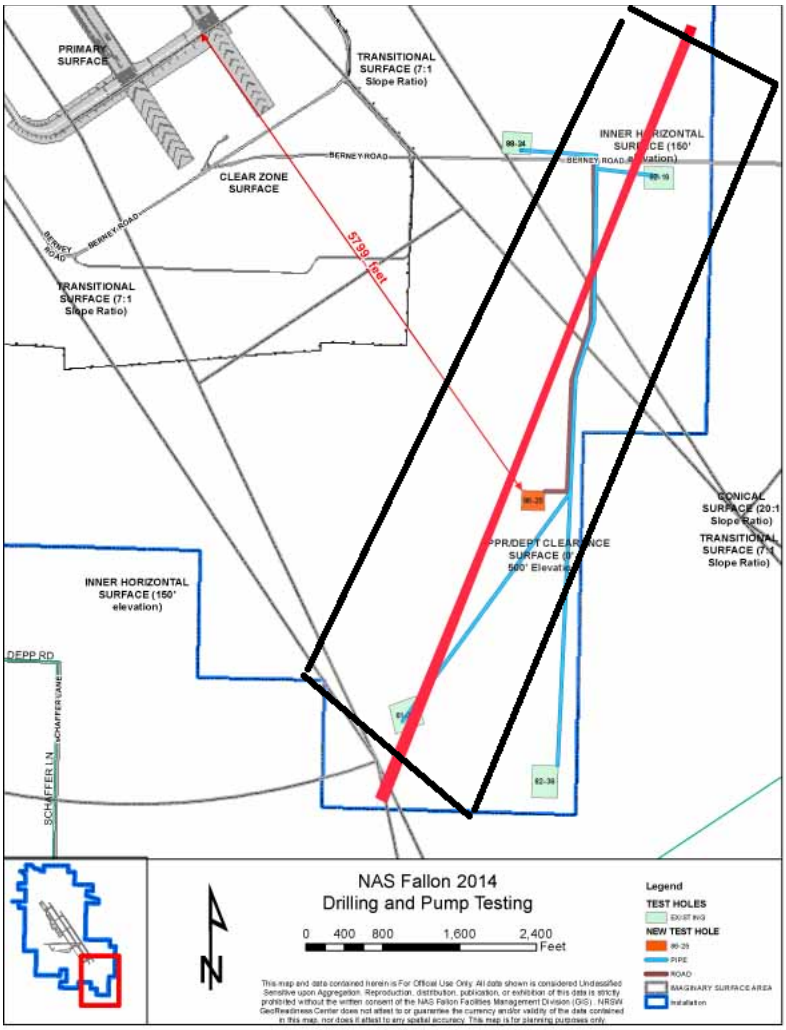

Figure A1. Proposed deployment area

Detailed description of equipment to be used including size and weight of vehicles. Description of staging, and lay down areas.

The vehicles we intend to use are: truck Ford 150 and other UNR field vehicles (same or smaller dimensions). A rental truck will be used to transport all the sensors at the start of the experiment.

Staging area All the equipment will be transported in vehicles. No sensors or boxes will be stored on the ground. UNR will rent a unit in Fallon for overnight storage of the equipment.

Considering the setting in Figure A1, we anticipate using 80-160 sensors. We anticipate that the entire activity will have maximum a month duration.

The stations will be deployed as two arrays:

A. Seismic pseudo-reflection line (named like this because it does not use an active source) from now on named SL, with sensors spaced at ~ 60 ft – *note that the separation may change (30-90ft) as a result of Phase 1 research.*

B. Large Aperture (~4 km) from now on named LA with sensors spaced at ~ 100 m or more, depending on obtaining land use permissions.

Lay-down areas would be every 15-60 ft along a red line shown in Figure 1, and every 100-400 m in a grid covering the surface within the black enclosure in Figure 1.

Length and width of access roads

The LA stations will be accessed for deployment, for data collection once and for deployment dismantling (estimated 3-4 times). The SL stations will be accessed over ~~10 trips. We will access the stations from the existing roads such that UNR will not interfere with existing installations.

Photographs of the equipment to be used and photos of the disturbance created by the equipment.

We intend to request from IRIS 160 sensors. These sensors can be (1) **v**ertical 4.5Hz geophones with Texan digitizers, as shown in Figure A2 or (2) 3-component L28 sensors (4.5Hz) with Reftek RT130 dataloggers in BIHO boxes, as shown in Figures A3-A6.

Figure A2 shows a vertical 4.5 Hz geophone (https://www.passcal.nmt.edu/content/instrumentation/sensors/high-frequency-sensors/geophones-45hz-hf-sensor) . The spike is ~ 3" long and it is stuck in the ground. The RT130 digitizer (https://www.passcal.nmt.edu/content/instrumentation/dataloggers/1-channel-texan-dataloggers) is 3"x7" .

Figure A3 shows an L28 sensor (https://www.passcal.nmt.edu/webfm_send/1186) which works with a RT130 digitizer (https://www.passcal.nmt.edu/content/instrumentation/dataloggers/3-channel-dataloggers/reftek-rt-130-datalogger). The sensor dimensions are 8x20x6 cm with 8 cm spikes. The sensor is stored in a BIHO box as in Figure A4.

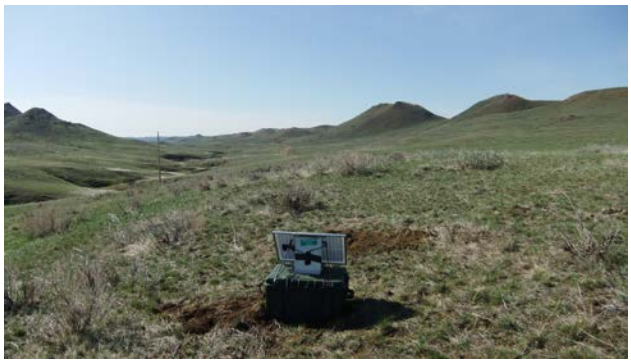

Figure A4. Shows a deployed station (a BIHO box) with the battery and digitizer on the ground and a buried short-period sensor.

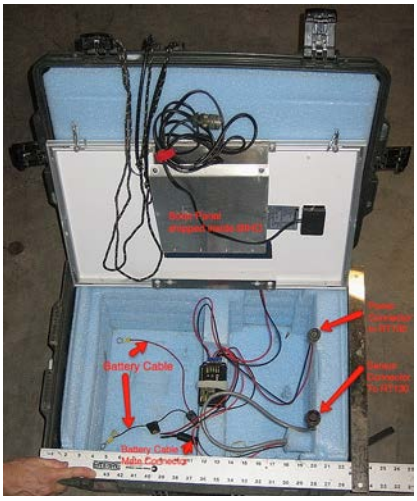

Figure A5 shows the BIHO box in Figure A4 and its content.

Figure A6 shows the BIHO box solar panel and a short-period sensor larger than the one we would use.

Estimate of acres to be disturbed, including dimension of disturbance.

The vertical geophones have needle-like metallic parts about 3 inches long which stick in the ground. The L28 short period sensors would be buried ~6 inches deep and ~12 inches in diameter.

Environmental protection measures and best management practices

Air Quality Prudent speed limits would be observed on unpaved roads throughout the project area in order to reduce dust emissions.

Cultural Resources UNR will limit vehicle and equipment travel to previously-identified established roads and to paths agreed upon with the land owners or administrators. Any unplanned discovery of cultural resources, items of cultural patrimony, sacred objects or funerary items requires that all activity in the vicinity of the find ceases, and the Field Manager be notified immediately by phone with written confirmation to follow. The location of the find would not be publicly disclosed, and any human remains must be secured and preserved in the place until a Notice to Proceed is issued by the authorized officer.

Wildlife Trash and other waste products would be properly managed and UNR would control garbage that could attract wildlife. All trash would be removed from the sites and disposed of at an authorized landfill. Reclamation of the disturbed areas would be completed in order to return these areas to a productive wildlife habitat.

Noxious Weeds, Invasive, and Non-Native Species Because the cars will be used only on existing roads, the probability of vehicle contamination with noxious weed populations will be very low, close to zero.

Affected environment and environmental consequences

This section describes the affected environment in the vicinity of the proposed passive survey and the potential impacts from implementation of the proposed passive survey. The project area lies at the north end of the Lahontan Valley, southeast of the Hot Springs Mountains and northwest of Fallon in Churchill County, Nevada.
The following resources may be present and potentially impacted by the proposed passive survey:

Cultural Resources;
Invasive, Non-Native and Noxious Species;
Migratory Birds;
Native American Religious Concerns;
Soils;
Vegetation;
Wildlife

Cultural resources The projects would be approved by the land owner prior to project initiation, thereby avoiding or mitigating adverse effects on identified cultural sites. The activities would avoid or mitigate, to the extent possible, all known and discovered resources. No incremental cumulative effects would occur to cultural resources as a result of the proposed passive survey.
Invasive, non-native and noxious weed species The proposed passive survey does not have the potential to create conditions favorable for the invasion of invasive, non-native, and noxious species.
Migratory birds Habitat within the study area supports low abundance and nesting density for migratory birds. Disturbance from the proposed passive survey, may displace birds into adjacent habitat, of which there is an abundance; therefore impacts to species stemming from resource competition (food, forage, cover) should be minimal. Impacts to migratory birds from dispersed recreation within the study area, as well as in areas of the proposed passive survey that do not realize further development, should be temporary. Consequently, minimal incremental cumulative impacts would occur to migratory birds from the proposed passive survey.
Native american religious concerns There are no Native American Religious concerns relative to this project.
Soil Soil disturbance within the study area from the activities would be minimal, with no increased potential for erosion of soils.
Vegetation The project would impact vegetation resources by the removal of vegetation. Cumulative impacts to vegetation will be minimized by installing the stations at locations without vegetation.
Wildlife Wildlife would be minimally affected by a temporary increase in traffic, however a very small area will be disturbed, thus having a negligible contribution to cumulative effects.

Methods to reclaim the surface.

The geophones will be pulled out and the 3 inch hole with 1/2 inch diameter will be filled. Each 6 inch deep short-period sensor hole with ~12 inch diameter will be filled.

B. PERMITTED SODA LAKE DEPLOYMENT – DOCUMENT SUBMITTED TO GTO DOE

We assess that the experiment can be performed using the current permitted sensor configuration (white triangles and cyan/white circles in Figure 1), even if it is not the ideal deployment. There is enough station coverage (white triangles) to extract a preliminary, low resolution P/S seismic velocity model.

As shown in Figure A7, the ideal deployment at Soda Lake was a square array of sensors 300 m apart and a line duplicating a previous experiment by Magma Energy and collaborators. The permitted stations are shown as white/cyan circles and white triangles. The yellow/white arrows show the 2010 Magma Energy exploration experiment sensor location (named Magma locations and shown in Figure A8). Duplicating the 2010 Magma experiment configuration is necessary. Only four of the 2010 Magma locations have not yet been permitted (thick white arrows). Our experiment will be three times denser than the Magma experiment, because one of the project tasks is to assess the best sensor deployment configuration.

The red circles and the red triangles show the stations which were not permitted. In an effort to obtain the ideal configuration, we are still working with the land owners to permit the sites shown as blue color symbols, however, even if we obtain no further permission to deploy, we expect that the experiment will not be significantly affected. The two green triangles are stations for which we may request BLM permission, if it can be obtained prior to the experiment.

Granted permissions:

BLM - has approved our request to deploy sensors on the BLM administered land, and the approval letter has been sent to the sponsor.

The Truckee-Carson irrigation district, P O BOX 1356, 89407-1356 has given written approval for the deployment on their properties and the approval has been sent to the sponsor.

The seismic line passes through several private properties, as listed below.

Kupfer Moshe & Dale , POBox 1204 , Lake Arrowhead CA, 92352-1204, owners of parcel 10 have approved access in writing.

Hansen Jim and Leo, 1149 Sewell Dr., Elko, NV, 89801-2963 own parcel 15 and have verbally approved the deployment.

Owens Marquerite's son (64460 Rock Springs Rd., Bend OR, 97701-9155 has verbally approved the deployment on Sept 5 2012 at ~ 4:30 pm and has agreed to send the approval in writing.

According to discussions in April 2012, we assume permission to deploy sensors on the Magma property. We have contacted Magma related to obtaining permission to access the property from October 15 to November 15 and we will deploy pending approval.

Pending requests for approval:

We are still trying to contact the following land owners:
Powelson Robert et al., address: Marilyn Grillo, 5938 N Walnut Grove Ave, San Gabriel CA, 91775-2528, owners of parcel 14. This property includes the red circles in the middle of the line.

The blue triangles in the southwest of the array would be deployed along three roads, with no property interference. The roads are maintained by the residents, thus we need to have deployment permissions. On Monday, Sept 9 we will travel to Fallon to talk to the families listed below. One sensor would be placed close to the road, outside the property line of each family.

WILSON MARVIN D & JUNE E, 6877 VICTOR DR, FALLON, NV, 89406-8358
(775) 867 4596

BAYLEY SHAWN, 6330 VICTOR DRIVE, 89406-6355

TOLLEY RANDY J & ANN M, 5750 JUNE DR, FALLON NV, 89406-4365

BROOKS RALPH WAYNE & PEGGY 6165 JACOBS RD, FALLON NV, Tel 775-423-5148

COX CASEY, 6707 VICTOR DR., FALLON, NV, 89406 - 775 867 5351 - contacted today and expecting our visit on Sept 9, 2012. We have received approval, however, the seismic array was reconfigured and no sensor was stored on this property.

Denied permissions
The northeast line portion passes through the Torvik John and Vella L., 455 N. Harmon Rd., Fallon, NV, 89406-9187 - parcel 42, and it is represented by red circles because the owners have not approved access.

BLM did not approve the line passing through the Coast Guard's property (southeast-most white arrows).

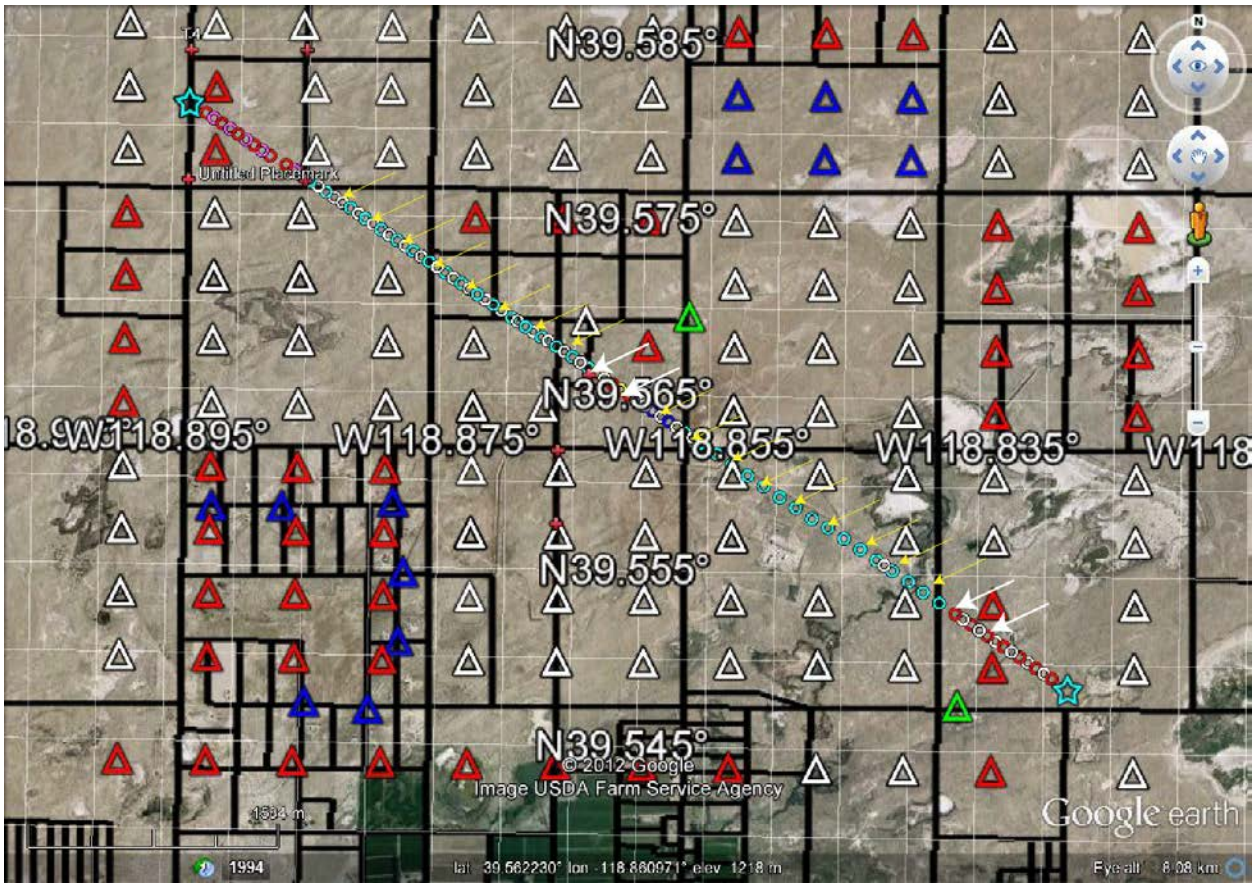

Figure A7. Ideal array deployment and permitted stations (white triangles, and white or cyan circles). Desired station locations, currently not permitted, are shown with red symbols. Green symbols show stations for which permission <u>may be</u> requested from BLM, if time allows. Blue shows stations which <u>may be</u> deployed, if we obtain landowner permissions. The arrows show the 2010 Magma Energy exploration experiment sensor location (named Magma locations and shown in Figure A8). Duplicating the 2010 Magma experiment configuration is necessary. Only four of the 2010 Magma locations have not yet been permitted (thick white arrows). Our experiment will be three times denser than the Magma experiment, because one of the project tasks is to assess the best sensor deployment configuration.

Figure A8. The 2010 Magma Energy deployment at Soda Lake. We are trying to duplicate the northwest - southeast line. Note that we will not duplicate the northeast-southwest line.

APPENDIX 2

A. GEOTHERMAL RESOURCES COUNCIL TRANSACTION 2011 PAPER - SEISMIC SIGNATURE OF THE GEOTHERMAL FIELD AT SODA LAKE, NEVADA, FROM AMBIENT NOISE ANALYSIS (pp 1)
B. FINAL REPORT AMBIENT SEISMIC NOISE (pp 13)
   RETRIEVAL OF REFLECTIONS FROM AMBIENT SEISMIC NOISE - EXPERIMENT NEAR RENO, NV

Seismic signature of the geothermal field at Soda Lake, Nevada, from ambient noise analysis

Ileana M. Tibuleac[1] and Mariana Eneva[2]
[1]*Nevada Seismological Laboratory, University of Nevada Reno, Reno, NV 89557*
[2]*Imageair Inc, 10513 Caminito Westchester, San Diego, CA 92126*

ABSTRACT

Our objective is to estimate geothermal reservoir indicators, such as: P and S seismic velocity models to a depth of ~300 m, ambient noise spectral energy and media stochastic properties. An important advantage of our method is estimating the shear velocity model, which, unlike the P-velocity model, is not yet accomplished by conventional reflection surveys. We analyze ambient seismic noise recorded by a 3 day, 1.3 km^2, 100 m spaced vertical geophone survey as well as four 12 m-separation seismic lines. The survey was conducted by UNR and Imageair Inc. in March 2010 at Soda Lake, Nevada, geothermal field operated by Magma Energy Corporation.

We use seismic interferometry, a new imaging method, to generate subsurface images without any larger seismic sources, such as explosions or earthquakes. One application of seismic interferometry is to retrieve the impulse response or Green's Function (GF) from crosscorrelation of ambient seismic noise. The ambient-noise autocorrelation at each station is interpreted as the collocated source–receiver elastic wave Green's Function (i.e. the Earth's reflection response).

Stacks of ambient noise crosscorrelations at pairs of sensors over three days result in inter-station GF's, with Rayleigh waves as dominant arrivals. A preliminary estimation of the velocity of phases which we interpret as fundamental Rayleigh waves shows lower surface wave velocity and higher scattering within the geothermal production field, at frequencies of 1-5 Hz. Using array processing techniques, such as frequency-wavelength (fk) analysis, we will estimate Rayleigh-wave phase velocity dispersion curves. The dispersion estimates will be inverted for surface wave velocity models using the Computer Programs in Seismology (CPS3.0) surf96 algorithm. Stacks of autocorrelations of ambient noise data recorded at individual sensors result in retrieval of the Earth's reflection response at the location of each sensor. The autocorrelation traces are interpreted in terms of reflection GF phase composition and crustal reflector properties. By applying crosscorrelation to ambient noise data recorded at pairs of sensors located 12 m apart we generate virtual shot gathers as if one of the sensors is generating seismic waves, i.e. we retrieve the Earth's reflection response.

We will also investigate whether differences between production and non-production geothermal reservoir areas could be assessed by measuring seismic scattering. We will compare the stochastic parameters (Hurst number, characteristic length) from the ambient noise autocorrelations and crosscorrelations and the ambient noise spectral energy differences above the geothermal reservoir to similar parameters outside the geothermal reservoir area.

Keywords: geothermal, seismic, ambient-noise, shear wave velocity, Soda Lake, shear velocity models, autocorrelation, crosscorrelation

INTRODUCTION

We report work in progress for the development of a new, cost-effective method, based on ambient seismic noise analysis, to estimate geothermal reservoir indicators such as: P and S seismic velocity models to a depth of ~300 m, ambient noise spectral energy and media stochastic properties at the location of a geothermal exploration area operated by Magma Energy Corporation, near Soda Lake. An important advantage of our method is estimating the shear velocity model of the Soda Lake geothermal field, which, unlike the P-velocity model, is not accomplished by conventional reflection surveys.

Soda Lake is one of many geothermal systems hosted in the extensional Basin and Range Province, Nevada. This geothermal field is located about 100 km east of Reno and 10 km northwest of Fallon (Figure 1), along the Carson River Route of the Old California Trail (Figure 2). Soda was mined from Soda Lake in the middle to late 19th century. There might have been a hot spring discharging at that time as well (Hill et al., 1979). Soda Lake was identified as a geothermal resource in 1903 while drilling for a water well, which reached boiling water at depth of 18 m. This well was still emitting hot steam in 1974, while shallow subsurface boiling was indicated by alteration of Quaternary sediments to kaolinite and various iron oxides or hydroxides (Olmsted et al., 1975). The extent of the thermal anomaly in the shallow subsurface has been outlined by the drilling of temperature-gradient holes by the U.S. Geological Survey and the U.S. Bureau of Reclamation, as well as continued drilling of production, injection and monitoring wells. The hottest parts of the Soda Lake thermal anomaly probably coincide with intersection of faults trending north-northeast and northwest. These faults provide steeply inclined conduits for thermal fluids that may be rising from depths 3 to 7 km (Olmsted et al., 1984). Although faults exposed on the surface are rare, some faults at depth were suggested, possibly along a rupture zone in the Tertiary or pre-Tertiary consolidated rocks (Olmsted et al., 1975).

Two binary plants came on-line at the Soda Lake geothermal field in 1987 and 1991. Their gross installed capacity is 23.1 MW, with estimated net capacity ~16 MW. However, when Magma Energy (US) Corp. acquired them in 2008, the annual output was averaging only 8 MW (Van Gundy et al., 2010). Therefore a major task was to restore the nameplate capacity and increase power production. A comprehensive 3D geophysical model of the geothermal field was created using various data that were collected and analyzed together for the first time, such as geological maps, locations and depths of wells, mud-logging and drilling data, temperature surveys, geophysical logs, LiDAR, resistivity, magnetic anomalies, microgravity, old seismic studies, etc. In addition, in June 2010 a 3D, three-component reflection seismic survey was carried out and is being integrated with existing well and precision gravity data (Echols et al., 2011).

One result of these investigations was the discovery of a steam cap (Van Gundy et al., 2010). In January 2010 a flow test of a former producing well (41-33) dramatically demonstrated that a steam cap had developed beneath it. The location of the steam

cap was associated with contours (Figure 3) marking the largest subsidence indicated by Interferometric Synthetic Aperture Radar using Satellite Imagery (InSAR). The maximum subsidence in the field approaches 2 cm/year and the size of the total subsidence area is significantly larger than the area outlined by the contours shown in Figure 3 (Gary Oppliger, personal communication). The InSAR anomaly marks the hottest and shallowest part of the field. The elevated temperatures actually cover an area with a diameter 4 to 5 times larger than that of the outer InSAR contour shown in Figure 3.

The placement of the Imageair Inc. and UNR seismic survey was targeted to cover the steam cap, to the extent the local landscape and infrastructure permitted. The 1.3 km^2, 100 m spaced high - frequency vertical geophone survey, conducted in March 2010, recorded ambient seismic noise (and available earthquake waveforms) for 3 days. A total of four 12 m-separation seismic lines (named "the 12-m seismic lines") were also deployed (Figure 3). We envision this type of seismic survey as preliminary to, or replacing more expensive active experiments, since is aimed to resolving lateral seismic parameter variations at a resolution of approximately 100 m. Also, through successful analysis of the 12 m seismic lines, it may be possible to detect buried faults.

Our technique is based on seismic interferometry (Draganov et al., 2009; Shapiro et al., 2005, Tibuleac et al., 2009), a new imaging method used to generate subsurface images without larger seismic sources such as explosions and earthquakes. One application of seismic interferometry is to retrieve the impulse response or Green's Function (GF) from crosscorrelation of ambient seismic noise. The ambient-noise autocorrelation at each station is interpreted as the collocated source–receiver elastic wave Green's Function (i.e. the Earth's reflection response).

The method includes four steps, as follows: 1) Analysis of fundamental mode Rayleigh waves from Green's Functions (GFs) extracted from ambient seismic noise cross correlation stacks; 2) Analysis of the GF P-reflection component extracted from ambient-noise autocorrelations; 3) Analysis of the geothermal field characteristics in terms of seismic scattering and ambient-noise spectral content; 4) Application of cross and auto correlation analysis to ambient noise data recorded at pairs of sensors on the 12-m seismic lines to generate virtual shot gathers. In this paper we report encouraging results development of Steps 1 and 2.

RESULTS

1. Analysis of fundamental mode Rayleigh waves from Green's Functions (GFs) extracted from ambient seismic noise cross correlation stacks

By applying cross correlation to ambient noise data recorded at pairs of sensors (A,B, and D stations in Figure 3), deployed at Soda Lake, and stacking the results over a period of time, we generated inter-station GF's, with Rayleigh waves as dominant arrivals. Examples of inter-station GF's obtained on Transects 1 (600 m length) and 2 (shown as white lines in Figure 3) are shown in Figures 4 and 5. Transect 1 includes inter-station paths outside the anomaly (we name "the anomaly"

the region centered on station A1 and shown with InSAR contours in Figure 3). Transect 2 (of 800 m length) crosses the northern part of the anomaly. A preliminary estimation of the velocity of phases which we interpret as fundamental Rayleigh waves shows lower surface wave velocity on Transect 2 at frequencies of 1-5 Hz. We also note more scattering (complex GF's) at stations on Transect 2.

The next step is to use array processing techniques, such as *fk* analysis (frequency-wavenumber) (Tibuleac *et al*, 2009), to estimate Rayleigh - wave phase velocity dispersion curves for ad-hoc sub-arrays of stations. We will invert the dispersion estimates for surface wave velocity models using the Computer Programs in Seismology (CPS3.0) surf96 algorithm (Herrmann and Ammon, 2002).

2) Analysis of the GF P-reflection component extracted from ambient-noise autocorrelations

By applying auto-correlation to ambient noise data recorded at individual sensors we retrieve the earth's reflection response at the location of each sensor. Autocorrelation stacks over three days, from stations on Transect 2 in Figure 1 are shown in Figure 6. The autocorrelation traces will be interpreted in terms of reflection GF phase composition, crustal structure, crust-mantle boundary depth, and crustal reflector properties, using waveform modeling programs available at UNR, such as CPS3.0 or e3D (Larsen, 1996).

3) Analysis of the geothermal field characteristics in terms of seismic scattering and ambient-noise spectral content

Microtremor spectral anomalies in the range of 1-6 Hz have been associated with "partially saturated" hydrocarbon reservoirs (Saenger et al., 2009; Schechinger et al., 2009). Variations in the seismic noise spectral content in the reservoir area have been reported in geothermal areas (Georgsson et al., 2000). These observations suggest that differences between geothermal reservoirs and non-productive areas could be assessed by measuring seismic scattering. We will research possible geothermal reservoir indicators related to seismic scattering, such as: a) the stochastic parameters, such as Hurst number and characteristic length (Pullammanappallil et al., 1997) of the ambient noise autocorrelations and crosscorrelations; b) ambient noise spectral energy differences above the geothermal reservoir, compared with spectral energy measured at positions away from a reservoir for frequency intervals such as 1-3.5 Hz or 1-6 Hz.

4) Application of cross and auto correlation analysis to ambient noise data recorded at pairs of sensors on the 12-m seismic lines to generate virtual shot gathers.

By applying cross-correlation to ambient noise data recorded at pairs of sensors on 12-m seismic lines we will generate virtual shot gathers as if one of the sensors is generating seismic waves, i.e. we will retrieve the earth's reflection response (Draganov et al., 2009). Using only autocorrelation stacks, preliminary results of two recently deployed co-located surveys near Reno: a passive geophone survey, recording ambient noise and an active source geophone survey have shown similar reflectors, at least to 300 m depth, for sensors located 15 m apart (Tibuleac et al., 2010). The sensors in the geophone lines in Figure 3 were located 12 m apart.

SUMMARY

We develop a method designed to resolving lateral seismic parameter variations at a resolution of approximately 100 m, to be applied prior to, or in replacement of more expensive active experiments. Promising results are obtained from analysis of three days of ambient noise recorded at a 1.3 km^2, 100 m spaced high - frequency vertical geophone survey over a steam cap. A preliminary estimation of the velocity of phases which we interpret as fundamental Rayleigh waves shows lower surface wave velocity and higher scattering within the geothermal production field, at frequencies from 1 to 5 Hz.

ACKNOWLEDGMENTS

We thank Jim Echols for assistance with planning and logistics of the experiment, as well as for help with the installation of the geophones in the field. We thank Gary Oppliger, formerly at Magma Energy (US) Corp., who provided geophysical and geological information and the InSAR results. We thank Chris Sladek and the students from the University of Nevada - Reno: Nick Steele, Jay Goldfarb, Susan Konkol, Jessica Pence, Brady Flinchum, Ellen-Hall Patton, Meghan Hanke and Kristin Kohls who helped with the field work and data collection. We thank the Great Basin Center for Geothermal Energy and its former director, Dr. Lisa Shevenell, for logistic support with the field experiment.

REFERENCES

Echols, J., D. Benoit, M. Ohren, G. Oppliger, and T. Van Gundy, 2011. Integration of a 3D-3C reflection seismic survey over a known geothermal resource: Soda Lake, Churchill County, Nevada, *GRC Transactions*, **35** (this volume).

Draganov D., X. Campman, J. Thorbecke, A. Verdel, and K. Wapenaar, 2009. Reflection images from ambient seismic noise, *Geophysics* **74**, A63–A67, 10.1190/1.3193529

Georgsson, L. S., Gudmundur Ómar Fridleifsson, Magnús Ólafsson and Ólafur G. Flóvenz, 2000. The geothermal exploration of the Öxarfjördur high-temperature area, NE-Iceland, *Proceedings World Geothermal Congress 2000 Kyushu - Tohoku, Japan, May 28 - June 10, 2000*, 1157-1162.

Herrmann, R.B., Ammon, C.J., 2002. Computer Programs in Seismology – SurfaceWaves, Receiver Functions and Crustal Structure. Saint Louis University, http://www.eas.slu.edu/People/RBHerrmann/ComputerPrograms.html.

Hill, D.G.; E.B. Layman, C. M. Swift, and S.H. Yungul, 1979. Soda Lake, Nevada, thermal anomaly, *GRC Transactions*, **3**, 303 – 308.

Larsen, S. C., Schultz C. A., 1996. "ELAS3D: 2D/3D elastic finite-difference wave propagation code." Lawrence Livermore National Laboratory, UCRL-MA-121792, 18 p.

Olmsted, F.H., P.A. Glancy, J.R. Harrill, F.E. Rush, and A.S. Van Denburgh, 1975. Preliminary hydrogeologic appraisal of selected hydrothermal systems in northern and central Nevada, *USGS Open File Report,* 75-56.

Olmsted, F.H., A.H. Welch, A.S. Van Denburgh, and S.E. Ingebritsen, 1984. Geohydrology, aqueous geochemistry, and thermal regime of the Soda Lakes and Upsal Hogback geothermal systems, Churchill County, Nevada, *USGS Water Resources Investigations Report,* **84**, 4054.

Pullammanappallil, S., A. Levander, S. Larkin, 1997. Estimation of crustal stochastic parameters from seismic exploration data, *J. Geophys. Res.,* **102**, 15,269-15,286.

Saenger, E. H. & M-A. Lambert & T. Nguyen & S.M. Schmalholz, 2009, http://www.spectraseis.com/jahia/webdav/site/spectraseis/shared/publications/SaengerAmsterdamPassTheory.pdf, 71st EAGE Conference & Exhibition — Amsterdam, The Netherlands, 8 - 11 June 2009.

Schechinger, **,** A. Goertz, B. Artman, 2009. Extracting subsurface information from ambient seismic noise – an example from Germany, *79th Society of Exploration, Geophysicists International Exposition and Annual Meeting* 2009, Houston, Texas, USA, 25 - 30 October 2009, 1617-1621.

Shapiro, N. M., Campillo, M., Stehly, L., and Ritzwoller, M. H., 2005. High-resolution surface wave tomography from ambient seismic noise, *Science*, **307**, 1615-1618.

Tibuleac, I. M., D. H. von Seggern, J. N. Louie, and J. G. Anderson, 2009. High Resolution Seismic Velocity Structure in the Reno Basin from Ambient Noise Recorded by a Variety of Seismic Instruments, *GRC Transactions*, **33**, 143-146.

Tibuleac, I.M.; Pullammanappallil, S.; von Seggern, D. H.; Pancha, A.; Louie, J. N., 2010. Retrieval of Earth's reflection response from ambient seismic noise - a Nevada experiment, *American Geophysical Union, Fall Meeting 2010, abstract #S33A-2071*

Van Gundy, T., G. Oppliger, M. Ohren, D. Benoit, and M. Morrisson, 2010. Utilizing a comprehensive 3-D model to understand, maintain, and expand the Soda Lake geothermal resource, Nevada USA, *GRC Transactions*, **34**, 1185-1189.

FIGURE CAPTIONS

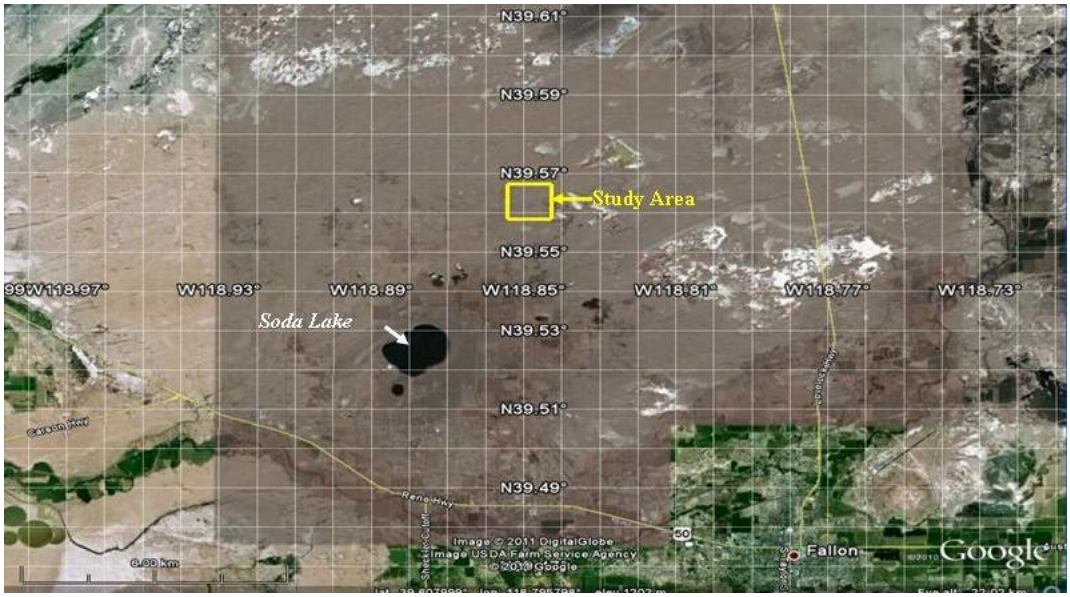

Figure 1. Google Earth map showing Soda Lake and study area (yellow square).

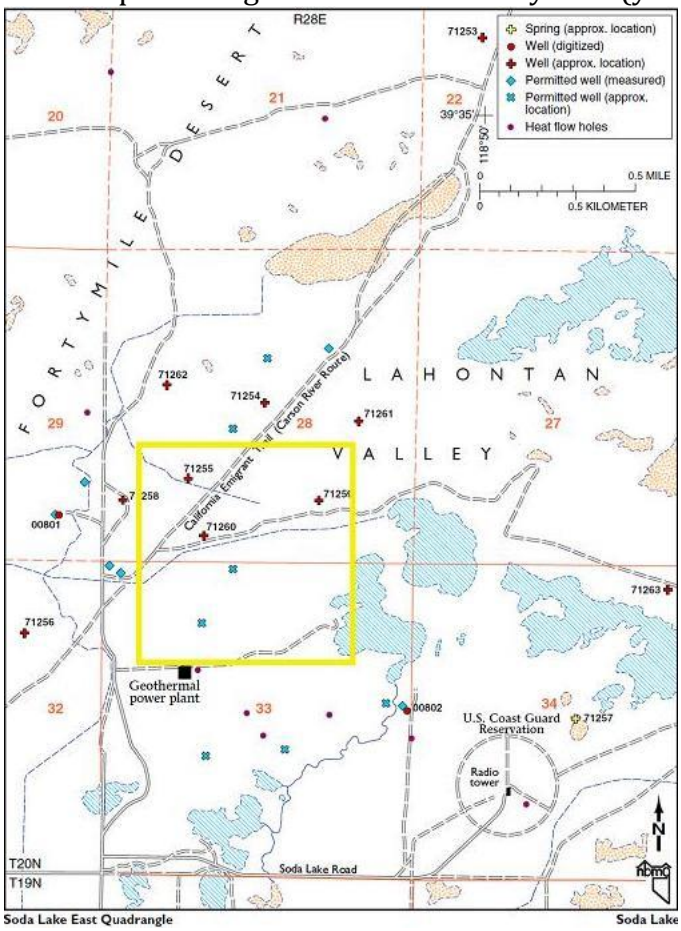

Figure 2. Map of Soda Lake area (from http://www.nbmg.unr.edu/geothermal/). Yellow square outlines study area.

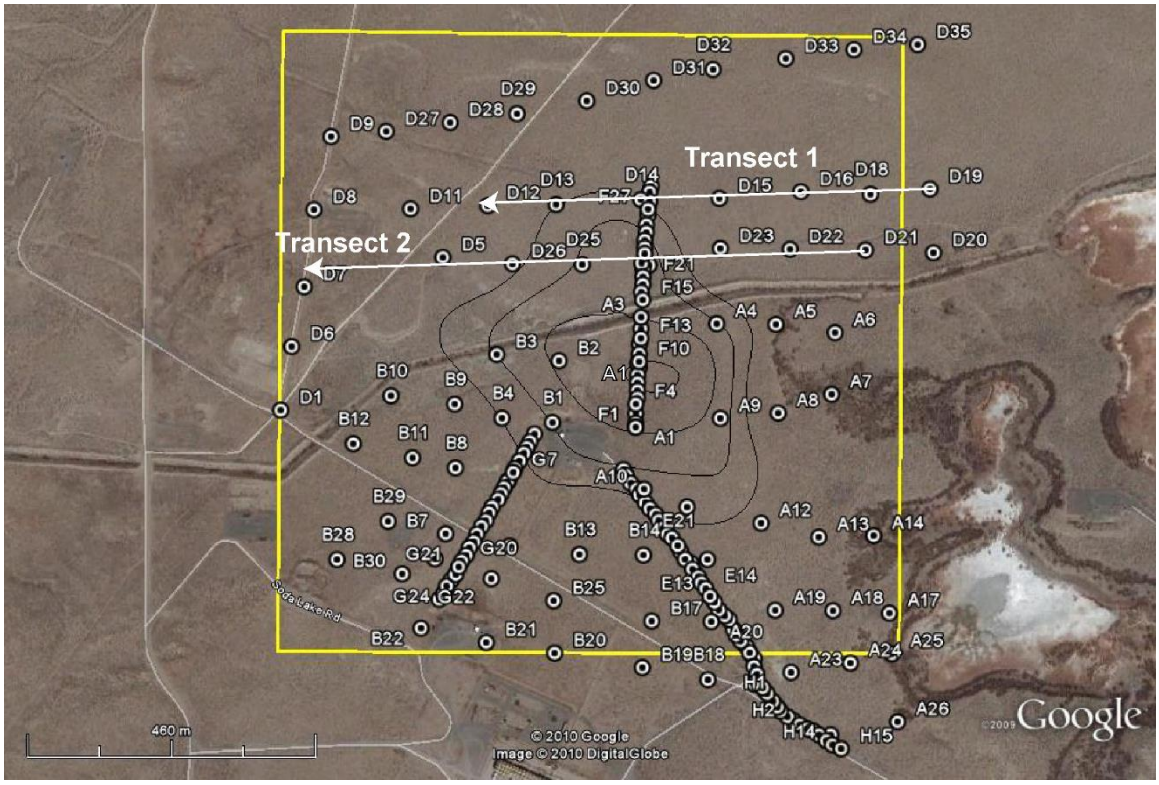

Figure 3. Station location and configuration at Soda Lake. Each station is composed of a high-frequency vertical geophone (4.5 Hz) and a Reftek RT-125 "Texan" digitizer. Contours show subsidence from InSAR analysis of satellite data, with their center considered to be placed above the steam cap (courtesy of Gary Oppliger). The power plant is visible south of study area.

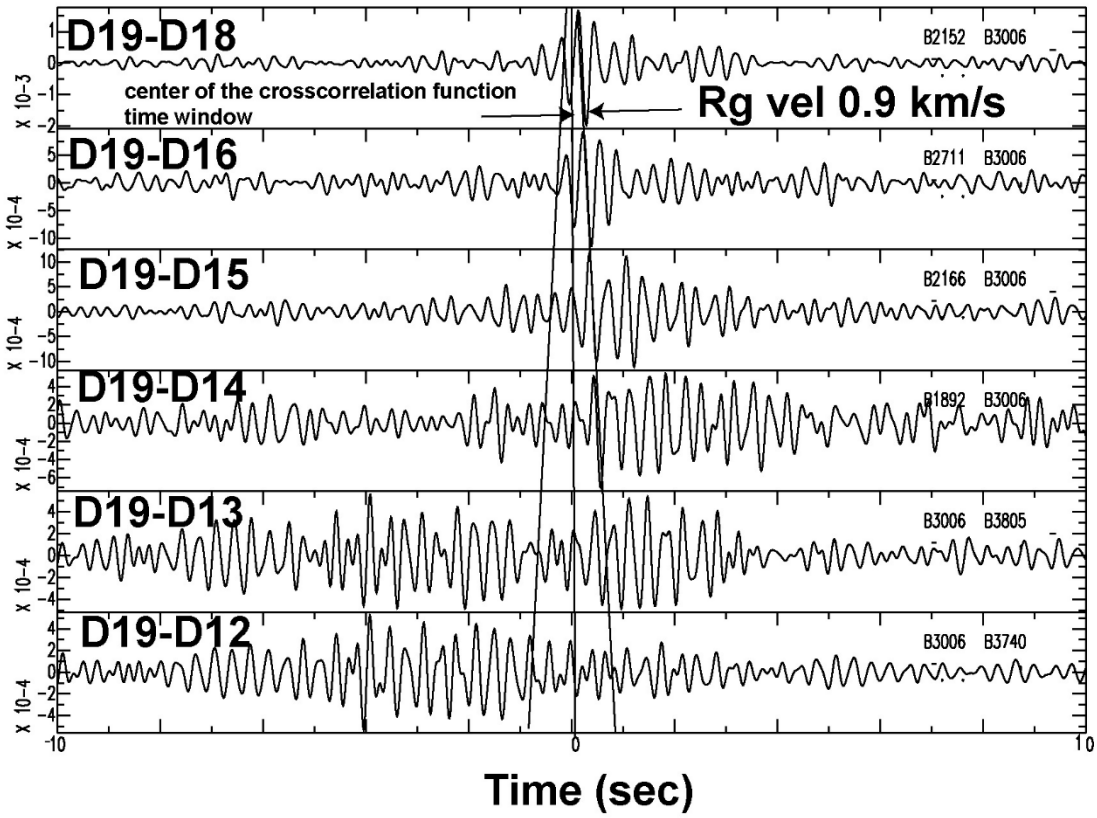

Figure 4. Crosscorrelation stacks for Transect 1 (Figure 1) showing the GF's extracted from D19 waveform crosscorrelations with data recorded at stations D12-D18. The arrival times corresponding to 0.9 km/s velocity are shown on a line, for arrivals interpreted as fundamental Rayleigh waves. The time lag zero corresponds to the center of the crosscorrelation window. In the ideal case, of isotropic ambient noise, the GF's would be symmetrical relative to the center of the crosscorrelation window, with identical causal and a-causal components. In this case, the GF's are identified only on one side of the crosscorrelation function.

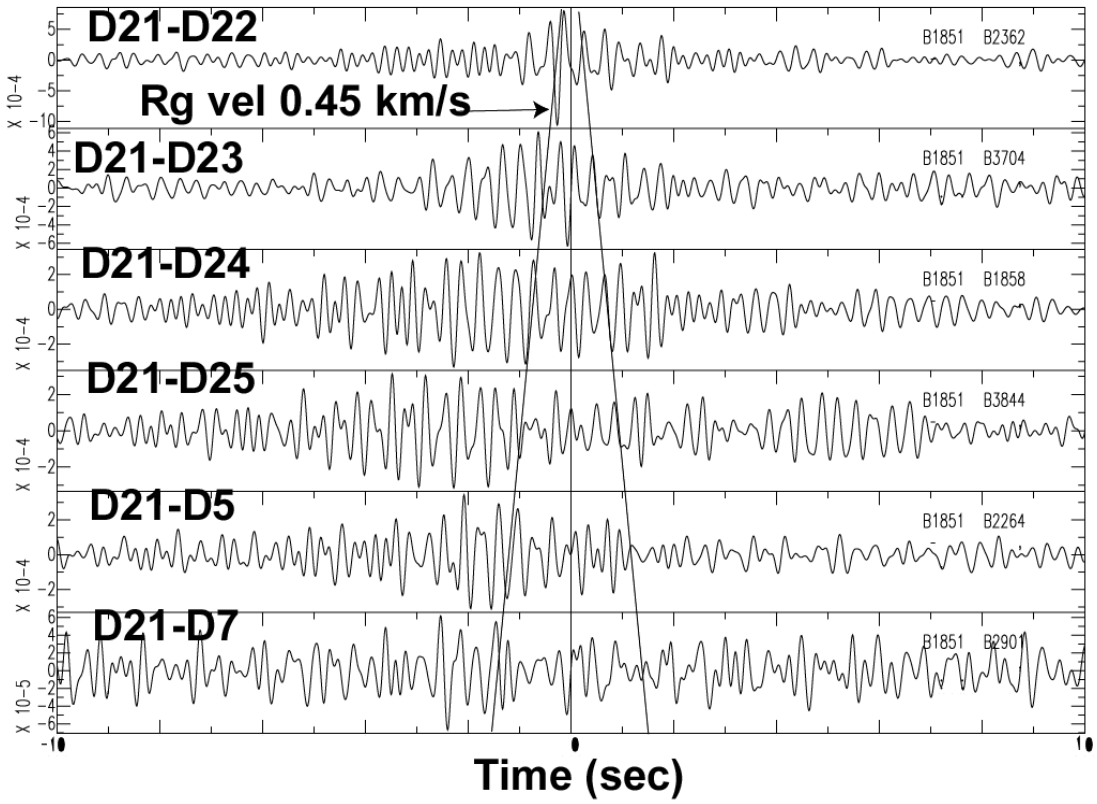

Figure 5. Crosscorrelation stacks for Transect 2 (Figure 1) showing the GF's extracted from D21 waveform crosscorrelations with data recorded at stations D22-D25, D5 and D7. The arrival times corresponding to 0.47 km/s velocity are shown on a line, for arrivals interpreted as fundamental Rayleigh waves. The time lag 0 corresponds to the center of the crosscorrelation window. Like in Figure 2, the GF's are identified only on one side of the crosscorrelation function.

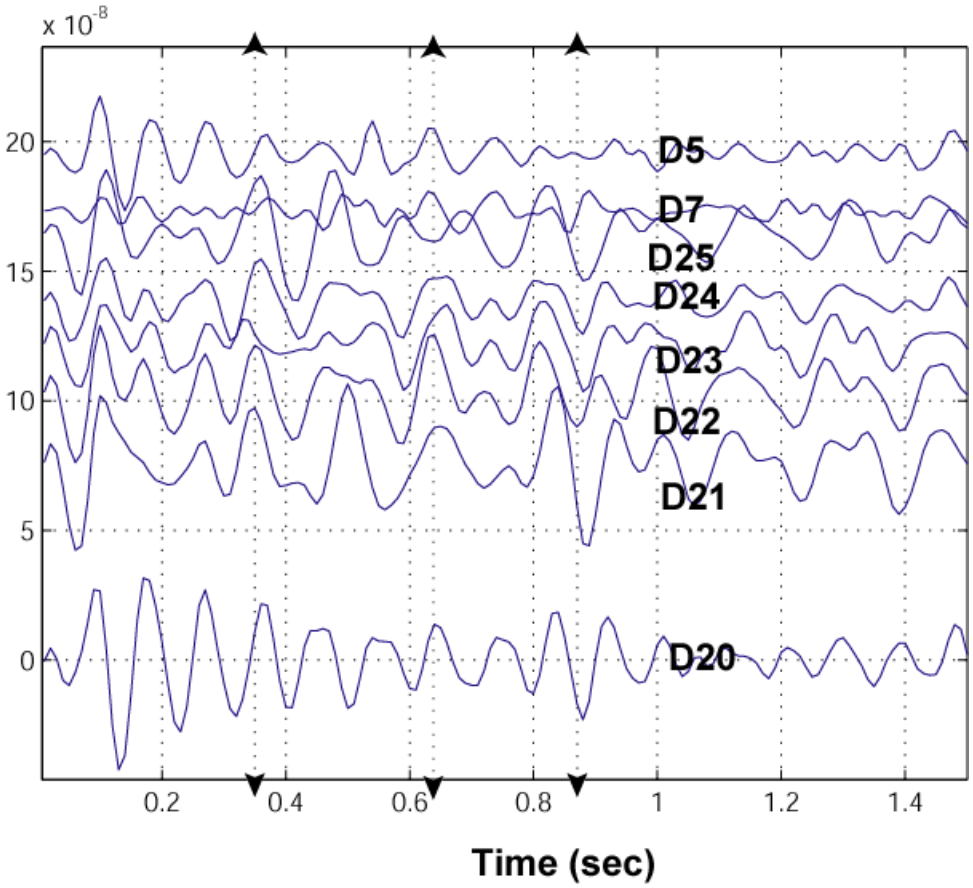

Figure 6. Ambient - noise autocorrelation stacks (weighted) at stations on Transect 2, in a 1.5 sec window. The stations on top of the anomaly (D25-D21) have common arrivals (marked by vertical lines) at ~0.35s, ~ 0.65s, and large arrivals are observed at ~0.85 sec at stations to the NE of the anomaly. Data from more stations is necessary to confirm these arrivals, which we interpret as reflections from subsurface layers. The raw waveforms are processed using automatic gain control in a 0.5 sec window.

B. Final Report Ambient Seismic Noise
1321 114 11GC

Retrieval of reflections from ambient seismic noise - Experiment near Reno, NV

Ileana M. Tibuleac[1], David H. von Seggern[1], Satish Pullammanappallil[2], John N. Louie [1] and Aasha Pancha[2]

Report preparer:
Ileana M. Tibuleac, final version Sept 2011.

(1) Nevada Seismological Laboratory, University of Nevada, Reno NV 89557 (UNR)
(2) Optim, 200 S. Virginia St., suite 560, Reno, NV, 89501 (Optim)

ileana@seismo.unr.edu,vonseg@seismo.unr.edu,satish@optimsoftware.com,
louie@seismo.unr.edu,aasha@nzquakes@gmail.com

SUMMARY

The objective of this study was to deploy a passive high frequency geophone array at the same location as an active source survey, and compare the results of processing three days of ambient noise records to the results of the active source experiment. The deliverable was a database of "segy" records of processed auto- and cross-correlation results, in the form of shot gathers. The final database has been delivered to the sponsor in November 2010 and to IRIS in July 2011. A complete set of codes used to process the data been shared with the sponsor in April 2011. This report also shows results of data processing subsequent to the contract, with the scope of being presented at the American Geophysical Union conference in 2010 and to be used in proposals for additional funding.

INTRODUCTION

The primary objective of our research is to develop, test and calibrate a seismic exploration methodology for fault imaging, using the Earth's reflection response retrieved from crosscorrelations of ambient seismic noise recordings, as a cost-effective exploration method, preliminary or alternative to targeted active source experiments.

The uses of this technology are multiple. Geothermal production relies on an existing, open fracture network for geothermal fluid circulation. Thus, localized, high-resolution geological information is critical for well location and identification of the fracture network. Also, understanding the concealed fault structure and shallow velocity models in urban areas are crucial steps for quantification of seismic hazard, for assessment of potential earthquake occurrence and for resolving the geology that commonly controls water flow. Significant efforts are currently devoted to resolving hidden faults using reflection surveys. Active seismic experiments are highly effective in resolving the subsurface structure, and the fault location, however, these experiments are expensive, since they usually sample more than the target area and involve costly equipment and human resources.

We seek to fulfill these needs through the development, testing and calibration of a new seismic exploration methodology for fault imaging, using the Earth's reflection response retrieved from cross-correlations of ambient seismic noise recordings. We use ambient noise and signal cross-correlation and auto-correlation to recover the surface waves and *P* reflections from ambient noise-derived Green's Functions between pairs of instruments. By applying cross-correlation to ambient noise data recorded at pairs of closely spaced (15 m) sensors along reflection lines, and stacking the results over a period of time, we generate virtual shot gathers as if one of the sensors is generating seismic waves, i.e. we retrieve the earth's reflection response. We envision this non-invasive, cost-effective method as preliminary or alternative to targeted active source experiments.

The new and emerging seismic technique we plan to develop has the potential to be a cost-effective method to identify very small geothermal target areas (such as faults), replacing active experiments, or at least significantly reducing their cost. This information is also important for realistic estimation of reliable urban hazard maps, for reducing the earthquake impact on the population and for communicating the hazards effectively to the affected population.

DATA

More than 350 high frequency seismic sensors with "Texan" digitizers borrowed from IRIS have been used. The dataset (Table 1) was collected in 2010 at a potential geothermal exploration site near Reno, NV (Figure 1). Waveforms have been recorded by two co-located high frequency vertical geophone surveys, one active (by Optim, Inc.) and one passive (funded by Optim Inc. and deployed by UNR). Although

preliminary results, involving minimal data analysis, are positive, further investigations are necessary for the ambient noise method to be used as a stand-alone exploration technique.

METHOD

The technique used in this study is seismic interferometry (Draganov, 2007, 2009; Tibuleac et al., 2011a; Campillo and Paul, 2003; Lobkis and Weaver, 2001; Weaver and Lobkis, 2004), a relatively new imaging method used to generate subsurface images using ambient noise. This technique is based on the theoretical result which states that if A and B are two passive sensors (seismic sensors), the Green's Function (GF), or the signal that B would receive when A is given an impulsive excitation, can be recovered from the temporal cross-correlation of noise received at A and B. This technique is applicable at all frequencies, starting with the high range (MHz) down to 7-15 second period Rayleigh waves, for inter-station distance respectively from millimeters to hundreds of km. Not only the surface wave portion of the Green's function can be retrieved from inter-station ambient noise cross-correlation, but also body-wave reflections (primaries as well as multiples) from layer interfaces (Draganov et al., 2007, 2009).

Algorithms for extracting ambient noise-derived Green's functions (Shapiro and Campillo, 2004; Yang et al., 2009) have been developed for our past NEHRP projects and are used at NSL (Tibuleac et al., 2011a) to derive *P* and *S* velocity models in the Reno Basin, for inter-station distance from 0.5 to 60 km, for different sensor-types and to estimate the P/S reflection component of the Green's Functions extracted from waveform autocorrelations (Tibuleac et al, 2011b). The algorithms are closely following the Bensen et al., (2007) methodology and are using spectral whitening and sign-bit normalization. They are effective in extracting the vertical-component Rayleigh wave fundamental mode, i.e. ground roll, (Figures 2 and 3) for the experiment in Figure 1.

Cross-correlation of continuous records is used to derive surface waves and compressional wave reflections as Green's Functions (GF's) between pairs of stations. We apply auto and cross-correlation to raw ambient noise data recorded at pairs of sensors co-located with an active reflection survey (Figure 1) deployed above a potential geothermal exploration target. Stacking the results over three days, we generate virtual shot gathers as if one of the sensors is generating seismic waves, i.e. we retrieve the earth's reflection response. The results are compared to a co-located active source survey conducted by Optim (Figures 4-6). In Figures 4-6 the noise records were processed with the same geometry as the active source records, were sorted according to CDP (common depth point), and put through the same depth migration process as the active source data, using the same initial velocity model. In order for our new method to be stand-alone, an initial velocity model needs to be derived, before the prestack migration approach (Louie and Pullammanappallil.,

2007; Louie et al., 2008) are applied. To solve this problem, ground roll and autocorrelation information could be used.

We also investigated the use of continuous waveform auto-correlation to image the individual station substructure. Claerbout (1968) showed that for a horizontally layered medium the auto-correlation of the transmission response of a seismic noise source in the subsurface yields the reflection response. Preliminary results obtained at NSL (Tibuleac et al., 2009; Tibuleac et al., 2011b) indicate that the technique has promise, and if successfully used here it will provide additional structural information to aid in the analysis and interpretation of the fault and basin structure. We use auto-correlations (sensors A and B collocated) at all the stations to distinguish reflecting layers beneath each station.

The questions we are currently trying to address are as follows:
1) Can similar seismic-velocity model resolution be obtained for active source and ambient-seismic- noise methods?; 2) What are the differences/similarities between the two approaches?; 3) What are the optimal experiment conditions (such as deployment time length, seismic noise level, waveform frequency content, inter-sensor distance) and processing techniques (such as pre-filtering, amplification, spectral whitening, frequency -wavenumber filters) necessary to attain this goal?; 4) Should the ground roll dispersion be used as a constraint for the initial velocity model?; 5) Can exploration costs be reduced by avoiding active surveys that do not appreciably reduce exploration uncertainty?; 6) Could similar results be obtained in less time, just by running vehicles along the lines?; 7) Are parameters such as stochastic heterogeneity and attenuation useful for geothermal favorability estimation and fault detection?; 8) What information can be extracted from ambient noise autocorrelations?

RESULTS

We have encouraging preliminary results in testing our ambient seismic noise exploration method and in estimation of a shallow (< 1 km deep) seismic velocity model, although no pre-filtering was applied to the waveforms before processing. We have determined that three-day noise surveys can produce similar results (although currently with slightly less resolution) than active surveys for one reflection line which crosses a known fault (line 6), while the results do not match well for a second line, perpendicular to the first (line 4). Thus, further investigations are necessary. We have also determined that useful information for higher resolution preliminary velocity models can be extracted from ambient noise autocorrelations (Figure 6).

There were limitations of the test study, are shown below.
1) Although the interpretation is similar, the resolved seismic-velocity model resolution from ambient noise is lower than the resolution of the model estimated from the active source experiment for line 6. Waveform pre-filtering in a higher frequency band may improve resolution, or whether, as suggested by Irie and Brown,

(2009), and a longer analysis time may be needed to improve the resolution of the passive survey.
2) P-reflection Green's Functions between pairs of seismic stations on line 4 are not very well defined. One possible explanation is noise directionality. Dominant, "bad" vehicle noise may arrive from the highway almost simultaneously at groups of sensors in line 4, since this line is parallel to the road.
3) Despite the relatively successful outcome, the optimal experiment conditions and their dependence on the geology and conditions at the deployment site are still unknown. Further investigations are necessary to estimate the optimal waveform frequency content, inter-sensor distance (also considering the attenuation properties), and deployment time length, the optimal seismic noise level and azimuthal distribution and the best waveform processing techniques (best pre-filter, whether spectral whitening is necessary, the best frequency -wavenumber filters).
4) Further investigations are necessary to determine the extent of information which can be extracted from ambient noise auto-correlations. Waveform modeling is necessary to interpret the autocorrelation-extracted GF's in terms of velocity structure. Also, parameters such as stochastic heterogeneity and attenuation along each line may be useful for fault detection.

SUMMARY

By applying auto and cross correlation to ambient noise data recorded at pairs of sensors deployed in Nevada, above a potential geothermal exploration target, and stacking the results over a period of time, we have generated virtual shot gathers as if one of the sensors is generating seismic waves, i.e. we retrieved the earth's reflection response. Since no active source was used, seismic interferometry has the potential to produce subsurface images cost efficiently. The results are compared to a co-located active source survey conducted by Optim. We have encouraging preliminary results in testing a transportable and cost-effective ambient seismic noise processing methodology to estimate a high resolution shallow (< 1 km deep) seismic velocity model. The next stage of our investigations will be related to extraction of P reflection Green's Function estimation between pairs of seismic stations on line 4 and interpretation in terms of velocity model and fault characteristics.

Acknowledgements

We thank volunteers in the Optim Inc. team Courtney Murphy, Tracy Obarsky, Jorma Perez
and the UNR student team: Nick Steele, Jay Goldfarb, Susan Konkol, Jessica Pence, Brady Flinchum, Ellen-Hall Patton, Meghan Hanke , Kristin Kohls, who helped with the deployment.

Figure 1. Three days of ambient noise were recorded by a deployment of ~350 high-frequency geophones equiped with "Texan" digitizers co-located with an active source survey. The inter-sensor distance was 15 m. Line 4 is parallel to the road, line 6 is perpendicular to the road.

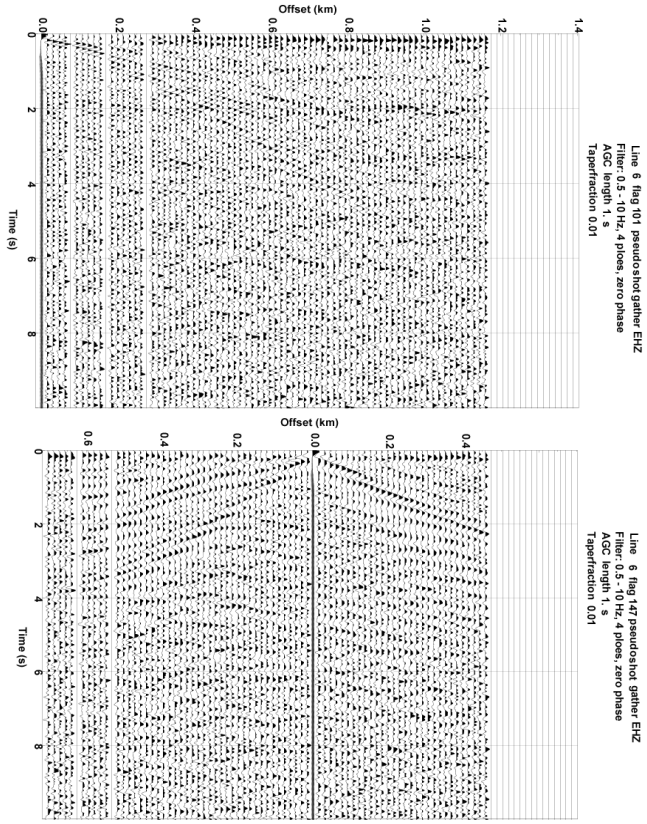

Figure 2. Examples of ground roll resulting from ambient - noise crosscorrelation stacks on line 6 for flag 101 (upper plot) and flag 147 (lower plot). The null lines are for sensors which did not record. No data pre-filtering has been applied before cross-correlations. Average gain control (AGC) was applied on each waveform in 1 sec windows. Windows of 100 s were cross-correlated, however, only the first 10 s are shown,

Figure 3. Examples of ground roll and P arrivals resulting from ambient - noise crosscorrelation stacks on line 4 for flag 101 (upper plot) and flag 189 (lower plot). No data pre-filtering has been applied before cross-correlations. Average gain control (AGC) was applied on each waveform in 1 sec windows.

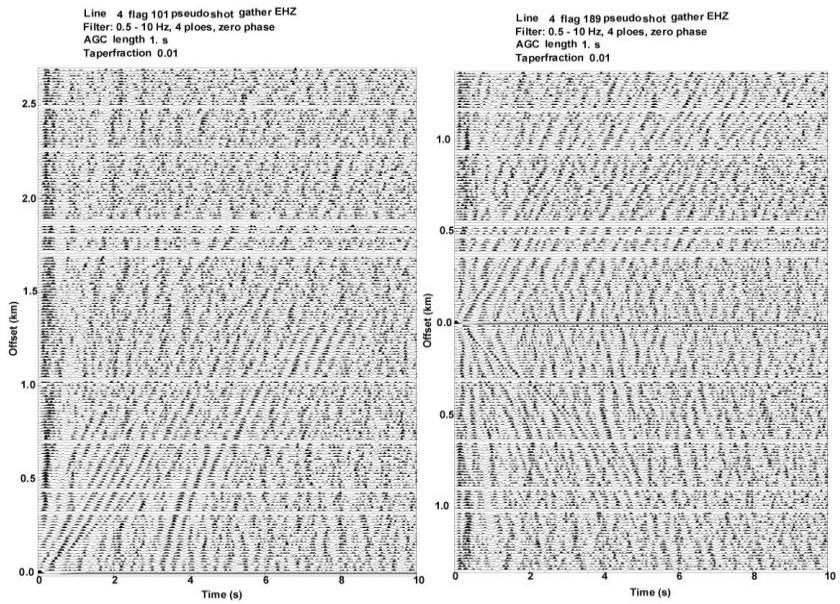
Line 4 flag 101 pseudoshot gather EHZ
Filter: 0.5 - 10 Hz, 4 ploes, zero phase
AGC length 1. s
Taperfraction 0.01
Offset (km)
Time (s)
Line 4 flag 189 pseudoshot gather EHZ
Filter: 0.5 - 10 Hz, 4 ploes, zero phase
AGC length 1. s
Taperfraction 0.01
Offset (km)
Time (s)

LINE 6 AMBIENT-NOISE SURVEY INTERPRETATION

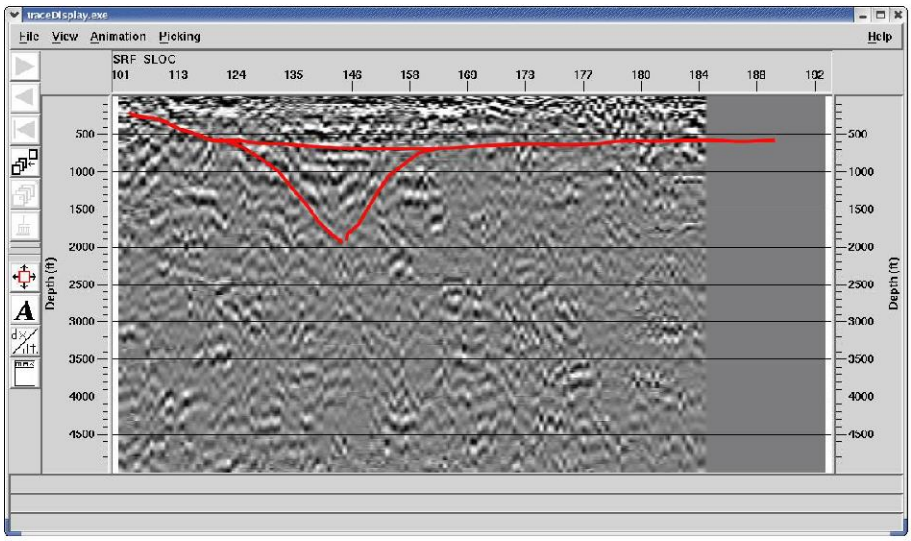

LINE 6 ACTIVE SURVEY INTERPRETATION

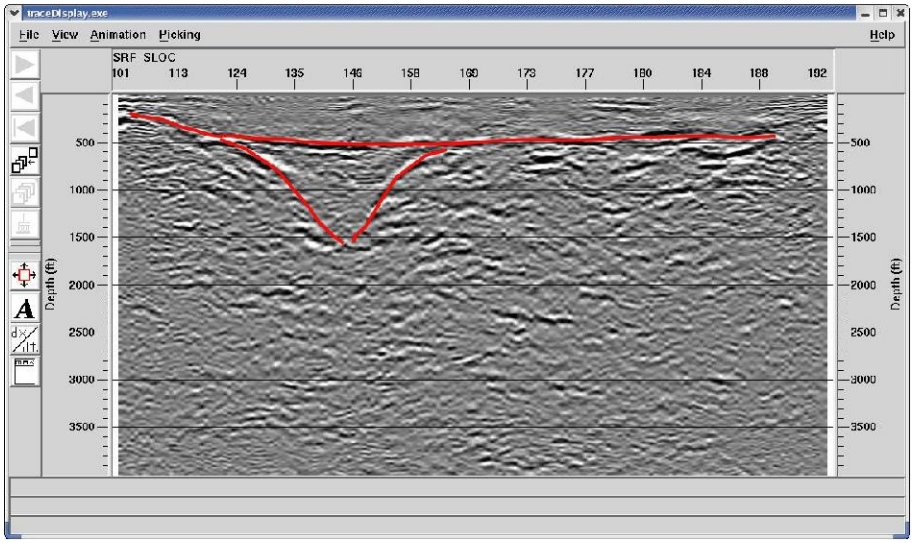

Figure 4. Active source and ambient - noise result comparison for line 6. The noise records were processed with the same geometry as the active source records, were sorted according to CDP (common depth point), and put through the same depth migration process as the active source data, using the same velocity model. Note lower frequencies for the ambient noise survey.

LINE 4 AMBIENT-NOISE SURVEY INTERPRETATION

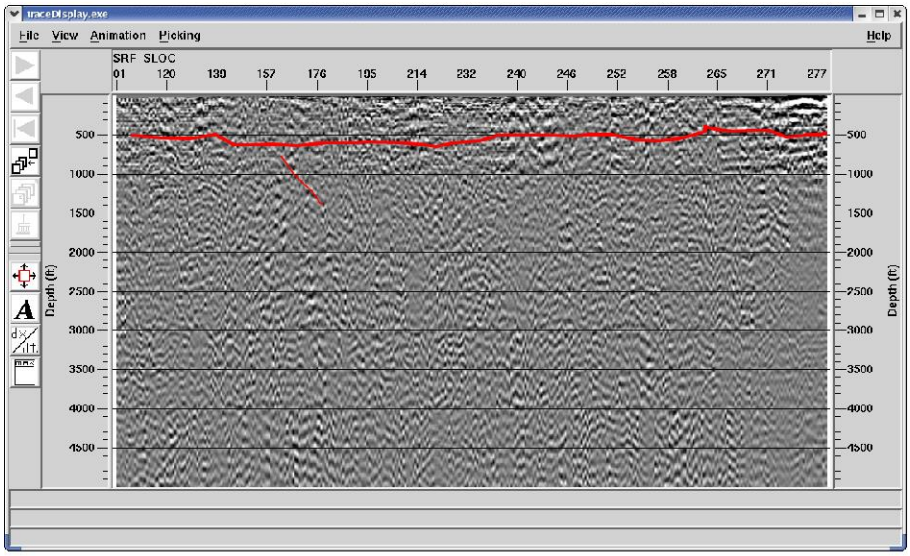

LINE 4 ACTIVE SURVEY INTERPRETATION

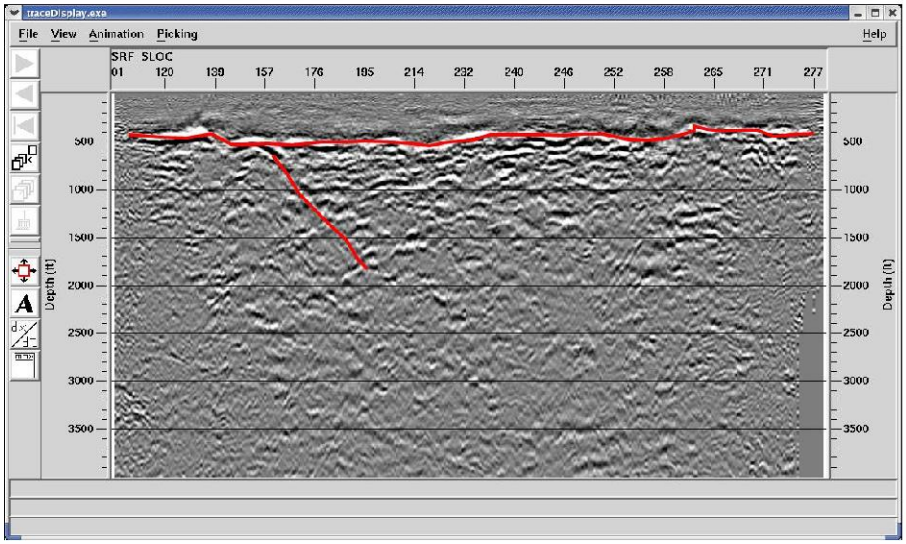

Figure 5. Same as in Figure 2 for line 4. We propose to use further processing to improve the results for this line.

Ambient noise autocorrelations (left) compared to active source results (right)

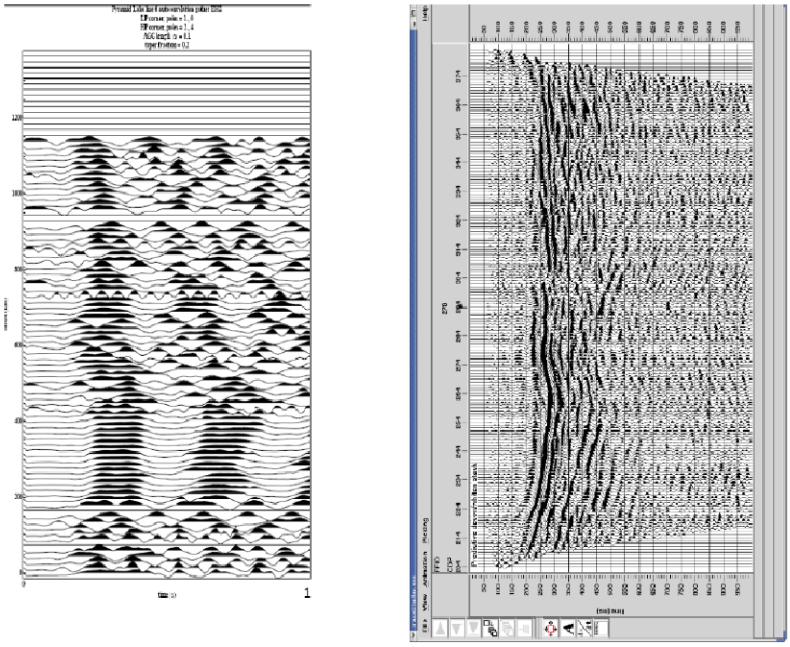

Figure 6. Results of two co-located surveys near Reno: a passive geophone and "Texan" survey, recording ambient noise in the left plot and an active source survey in the right plot. One second of records is represented on the horizontal axis of each plot. Only ambient noise autocorrelations are shown here (left), as a first estimate of the experiment results. The autocorrelation is interpreted as the source–receiver collocated elastic wave Green's function (i.e. the Earth's reflection response). This is only a qualitative assessment of survey result similarity. Despite the difference in frequency content (lower frequency for the noise survey, which was filtered with a zero-phase high pass Butterworth filter at 2 Hz) the reflector at ~ 300 ms is resolved by both surveys and changes in autocorrelations (left) appear to follow the lateral variations shown by the active survey. Automatic gain control (AGC) in the left plot was applied in a window of 0.1 sec on each trace. Sensors in this line are 15 m apart. In the left plot, each trace is the stack of autocorrelations of ambient noise in one-hour windows for records during the three days of deployment. The plot on the right is a common depth point (CDP) stacked section of the active source reflection survey. A trace is shown for every CDP (spacing of approximately 7.5 m) and was derived after refraction statics.

REFERENCES

Draganov D., X. Campman, J. Thorbecke, A. Verdel, and K. Wapenaar, 2009. Reflection images from ambient seismic noise, Geophysics 74, A63–A67, 10.1190/1.3193529

Draganov, D., K. Wapenaar, W. Mulder, J. Singer and A. Verdel, 2007. Retrieval of reflections from seismic background noise measurements, Geophys. Res.Lett. 34, L04305, doi:10.1029/2005GL028735.

D. Halliday and A. Curtis 2008. Seismic interferometry, surface waves, and source distribution. Geophys. J. Int., doi: 10.1111/j.1365-246X.2008.03918

Herrmann, R.B., Ammon, C.J., 2002. Computer Programs in Seismology – SurfaceWaves, Receiver Functions and Crustal Structure. Saint Louis University, http://www.eas.slu.edu/People/RBHerrmann/ComputerPrograms.html.

Gouedard P., L. Stehly1, F. Brenguier, M. Campillo, Y. Colin de Verdiere, E. Larose1, L. Margerin, P. Roux, F. J. Sanchez-Sesma, N. M. Shapiro and R. L. Weaver, 2008. Cross-correlation of random fields: mathematical approach and applications, Geophysical Prospecting, 2008, **56**, 375–393.

Irie, K. and L. Brown, 2009. Extraction and analysis of seismic body waves from ambient noise recorded for crustal imaging in Montserrat, AGU 2009, Paper # V23D-2106, abstract and poster.

Kohler, M. D., T. H. Heaton, and S. C. Bradford (2007), Propagating waves in the steel, moment-frame factor building recorded during earthquakes, Bull. Seismol. Soc. Am., 97, 1334– 1345.

Larose, E., P. Roux, and M. Campillo (2007), Reconstruction of Rayleigh-Lamb dispersion spectrum based on noise obtained from an air-jet forcing, J. Acoust. Soc. Am., 122(6), 3437– 3444.

Leidig, M., R., Brian W. Stump, Jessie L. Bonner, Christopher T. Hayward, Aaron A. Velasco, Diane F., Baker, Heather Hooper, William R. Walter, Xiaoning (David) Yang, Rongmao Zhou, CL Edwards, Marie D. Renwald, and James F. Lewkowicz, 2006. Source phenomenology experiments in Arizona, 26th Seismic Research Review - Trends in Nuclear Explosion Monitoring, pp. 427.

Louie, J. N., and Pullammanappallil, S., 2007, Shallow dip of two Great Basin normal faults demonstrated by shallow seismic reflection with refraction tomography (invited): Eos Trans. AGU, 88(52), Fall Meet. Suppl., Abstract NS23A-07.

Louie, J. N., Pullammanappallil, S., and Honjas, B., 2008, Imaging the geometry of Great Basin normal faults by combining seismic reflection with refraction tomography: presented at the Seismol. Soc. Amer. Annual Meeting, Santa Fe, New Mexico, April 16-18.

Prieto, G. A., and G. C. Beroza, 2008. Earthquake ground motion prediction using the ambient seismic field, Geophys. Res. Lett., 35, L14304, doi:10.1029/2008GL034428.

Shapiro, N. M., Campillo, M., Stehly, L., and Ritzwoller, M. H., 2005. High-resolution surface wave tomography from ambient seismic noise, Science, 307, 1615-1618.

Snieder, R., and E. Safak (2006), Extracting the building response using seismic interferometry: Theory and application to the Millikan Library in Pasadena, California, Bull. Seismol. Soc. Am., 96, 586– 598.

Stehli L., M. Campillo, B. Froment, R. L. Weaver, 2008. Reconstructing Green's function by crosscorrelation of Coda of the Correlation (C^3) of Ambient Seismic Noise, J. Geophys. Res., 113, B11306, doi:10.1029/2008JB005693, 2008

Tibuleac, I. M., D. H. von Seggern, John G. Anderson and J.N. Louie, 2011a. Computing Green's Functions from Ambient Noise Recorded by Narrow-Band Seismometers, Accelerometers, and Analog Seismometers, in press at Seismological Research Letters.;

http://crack.seismo.unr.edu/ileana/GF_ambient_noise_paper_final.pdf

Tibuleac, D. H. von Seggern, and J.N. Louie, 2011b, Crust-mantle boundary reflectors in Nevada from noise auto-correlations, in review at Geophys. J. Int.; http://crack.seismo.unr.edu/ileana/Moho_paper_2010_12_30.pdf

Tibuleac, I. and J. Britton (2006), An Automated Short-Period Surface-Wave Detection Algorithm, Bull. Seis. Soc. Am. 96, 334-343

Yang, Y., M.H. Ritzwoller, F.-C. Lin, M.P. Moschetti, and N.M. Shapiro, 2008. The structure of the crust and uppermost mantle beneath the western US revealed by ambient noise and earthquake tomography, J. Geophys. Res. 113, B12310, doi:10.1029/2008JB005833.

Table 1. List of stations (geophone and digitizer) used in this experiment. For each two lines, the first shows the network name (XT), the digitizer number, the channel name, the start date, the end date, data recovery and number of samples.

- Channel +Station	XT	A1508	ELZ	2010,064,23:00:00	2010,067,21:00:00	100.0%	25200100
- Channel +Station	XT	A1514	ELZ	2010,064,23:00:00	2010,067,21:00:00	100.0%	25200100
- Channel +Station	XT	A1517	ELZ	2010,064,23:00:00	2010,067,21:00:00	100.0%	25200100
- Channel +Station	XT	A1521	ELZ	2010,064,23:00:00	2010,067,21:00:00	100.0%	25200100
- Channel +Station	XT	A1529	ELZ	2010,064,23:00:00	2010,067,21:00:00	100.0%	25200100
- Channel +Station	XT	A1568	ELZ	2010,064,23:00:00	2010,067,20:59:59	100.0%	25200000
- Channel +Station	XT	A1584	ELZ	2010,064,23:00:00	2010,067,21:00:00	100.0%	25200100
- Channel +Station	XT	A1586	ELZ	2010,064,23:00:00	2010,067,21:00:00	100.0%	25200100
- Channel +Station	XT	A1588	ELZ	2010,064,23:00:00	2010,067,21:00:00	100.0%	25200100
- Channel +Station	XT	A1591	ELZ	2010,064,23:00:00	2010,067,21:00:00	100.0%	25200100
- Channel +Station	XT	A1593	ELZ	2010,064,23:00:00	2010,067,20:59:59	100.0%	25200000
- Channel +Station	XT	A1599	ELZ	2010,064,23:00:00	2010,067,21:00:00	100.0%	25200100
- Channel +Station	XT	A1610	ELZ	2010,064,23:00:00	2010,067,21:00:00	100.0%	25200100
- Channel	XT	A1614	ELZ	2010,064,23:00:00	2010,067,21:00:00	100.0%	25200100

+Station - Channel	XT	A1615	ELZ	2010,064,23:00:00	2010,067,21:00:00	100.0%	25200100
+Station - Channel	XT	A1617	ELZ	2010,064,23:00:00	2010,067,21:00:00	100.0%	25200100
+Station - Channel	XT	A1639	ELZ	2010,064,23:00:00	2010,067,21:00:00	100.0%	25200100
+Station - Channel	XT	A1645	ELZ	2010,064,23:00:00	2010,067,21:00:00	100.0%	25200100
+Station - Channel	XT	A1651	ELZ	2010,064,23:00:00	2010,067,21:00:00	100.0%	25200100
+Station - Channel	XT	A1654	ELZ	2010,064,23:00:00	2010,067,21:00:00	100.0%	25200100
+Station - Channel	XT	A1657	ELZ	2010,064,23:00:00	2010,067,21:00:00	100.0%	25200100
+Station - Channel	XT	A1661	ELZ	2010,064,23:00:00	2010,067,21:00:00	100.0%	25200100
+Station - Channel	XT	A1668	ELZ	2010,064,23:00:00	2010,067,21:00:00	100.0%	25200100
+Station - Channel	XT	A1672	ELZ	2010,064,23:00:00	2010,067,21:00:00	100.0%	25200100
+Station - Channel	XT	A1678	ELZ	2010,064,23:00:00	2010,067,21:00:00	100.0%	25200100
+Station - Channel	XT	A1684	ELZ	2010,064,23:00:00	2010,067,21:00:00	100.0%	25200100
+Station - Channel	XT	A1687	ELZ	2010,064,23:00:00	2010,067,21:00:00	100.0%	25200100
+Station - Channel	XT	A1705	ELZ	2010,064,23:00:00	2010,067,21:00:00	100.0%	25200100
+Station - Channel	XT	A1712	ELZ	2010,064,23:00:00	2010,067,21:00:00	100.0%	25200100
+Station							

- Channel +Station	XT	A1715	ELZ	2010,064,23:00:00	2010,067,21:00:00	100.0%	25200100
- Channel +Station	XT	A1731	ELZ	2010,064,23:00:00	2010,067,21:00:00	100.0%	25200100
- Channel +Station	XT	A1735	ELZ	2010,064,23:00:00	2010,067,21:00:00	100.0%	25200100
- Channel +Station	XT	A1752	ELZ	2010,064,23:00:00	2010,067,21:00:00	100.0%	25200100
- Channel +Station	XT	A1761	ELZ	2010,064,23:00:00	2010,067,21:00:00	100.0%	25200100
- Channel +Station	XT	A1764	ELZ	2010,064,23:00:00	2010,067,20:59:59	100.0%	25200000
- Channel +Station	XT	A1768	ELZ	2010,064,23:00:00	2010,067,21:00:00	100.0%	25200100
- Channel +Station	XT	A1786	ELZ	2010,064,23:00:00	2010,067,21:00:00	100.0%	25200100
- Channel +Station	XT	A1791	ELZ	2010,064,23:00:00	2010,067,21:00:00	100.0%	25200100
- Channel +Station	XT	A1793	ELZ	2010,064,23:00:00	2010,067,21:00:00	100.0%	25200100
- Channel +Station	XT	A1795	ELZ	2010,064,23:00:00	2010,067,21:00:00	100.0%	25200100
- Channel +Station	XT	A1802	ELZ	2010,064,23:00:00	2010,067,21:00:00	100.0%	25200100
- Channel +Station	XT	A1803	ELZ	2010,064,23:00:00	2010,067,21:00:00	100.0%	25200100
- Channel +Station	XT	A1808	ELZ	2010,064,23:00:00	2010,067,21:00:00	100.0%	25200100
- Channel +Station	XT	A1815	ELZ	2010,064,23:00:00	2010,067,21:00:00	100.0%	25200100
-	XT	A1816	ELZ	2010,064,23:00:00	2010,067,21:00:00	100.0%	25200100

Channel +Station - Channel	XT	A1819	ELZ	2010,064,23:00:00	2010,067,21:00:00	100.0%	25200100
Channel +Station - Channel	XT	A1832	ELZ	2010,064,23:00:00	2010,067,21:00:00	100.0%	25200100
Channel +Station - Channel	XT	A1837	ELZ	2010,064,23:00:00	2010,067,21:00:00	100.0%	25200100
Channel +Station - Channel	XT	A1838	ELZ	2010,064,23:00:00	2010,067,21:00:00	100.0%	25200100
Channel +Station - Channel	XT	A1851	ELZ	2010,064,23:00:00	2010,067,21:00:00	100.0%	25200100
Channel +Station - Channel	XT	A1858	ELZ	2010,064,23:00:00	2010,067,21:00:00	100.0%	25200100
Channel +Station - Channel	XT	A1870	ELZ	2010,064,23:00:00	2010,067,21:00:00	100.0%	25200100
Channel +Station - Channel	XT	A1887	ELZ	2010,064,23:00:00	2010,067,21:00:00	100.0%	25200100
Channel +Station - Channel	XT	A1892	ELZ	2010,064,23:00:00	2010,067,21:00:00	100.0%	25200100
Channel +Station - Channel	XT	A1895	ELZ	2010,064,23:00:00	2010,067,21:00:00	100.0%	25200100
Channel +Station - Channel	XT	A1902	ELZ	2010,064,23:00:00	2010,067,21:00:00	100.0%	25200100
Channel +Station - Channel	XT	A1903	ELZ	2010,064,23:00:00	2010,067,21:00:00	100.0%	25200100
Channel +Station - Channel	XT	A1909	ELZ	2010,064,23:00:00	2010,067,21:00:00	100.0%	25200100
Channel +Station - Channel	XT	A1920	ELZ	2010,064,23:00:00	2010,067,21:00:00	100.0%	25200100
Channel +Station - Channel	XT	A1928	ELZ	2010,064,23:00:00	2010,067,21:00:00	100.0%	25200100

+Station - Channel	XT	A1939	ELZ	2010,064,23:00:00	2010,067,21:00:00	100.0%	25200100
+Station - Channel	XT	A1948	ELZ	2010,064,23:00:00	2010,067,21:00:00	100.0%	25200100
+Station - Channel	XT	A1950	ELZ	2010,064,23:00:00	2010,067,21:00:00	100.0%	25200100
+Station - Channel	XT	A1951	ELZ	2010,064,23:00:00	2010,067,21:00:00	100.0%	25200100
+Station - Channel	XT	A1952	ELZ	2010,064,23:00:00	2010,067,21:00:00	100.0%	25200100
+Station - Channel	XT	A1973	ELZ	2010,064,23:00:00	2010,067,21:00:00	100.0%	25200100
+Station - Channel	XT	A1980	ELZ	2010,064,23:00:00	2010,067,21:00:00	100.0%	25200100
+Station - Channel	XT	A1981	ELZ	2010,064,23:00:00	2010,067,21:00:00	100.0%	25200100
+Station - Channel	XT	A1982	ELZ	2010,064,23:00:00	2010,067,21:00:00	100.0%	25200100
+Station - Channel	XT	A1992	ELZ	2010,064,23:00:00	2010,067,21:00:00	100.0%	25200100
+Station - Channel	XT	A1994	ELZ	2010,064,23:00:00	2010,066,11:00:00	100.0%	12960100
+Station - Channel	XT	A2038	ELZ	2010,064,23:00:00	2010,067,21:00:00	100.0%	25200100
+Station - Channel	XT	A2063	ELZ	2010,064,23:00:00	2010,067,21:00:00	100.0%	25200100
+Station - Channel	XT	A2074	ELZ	2010,064,23:00:00	2010,067,21:00:00	100.0%	25200100
+Station - Channel	XT	A2078	ELZ	2010,064,23:00:00	2010,067,21:00:00	100.0%	25200100
+Station							

- Channel +Station	XT	A2098	ELZ	2010,064,23:00:00	2010,067,21:00:00	100.0%	25200100
- Channel +Station	XT	A2101	ELZ	2010,064,23:00:00	2010,067,21:00:00	100.0%	25200100
- Channel +Station	XT	A2102	ELZ	2010,064,23:00:00	2010,067,21:00:00	100.0%	25200100
- Channel +Station	XT	A2108	ELZ	2010,064,23:00:00	2010,067,21:00:00	100.0%	25200100
- Channel +Station	XT	A2111	ELZ	2010,064,23:00:00	2010,067,21:00:00	100.0%	25200100
- Channel +Station	XT	A2114	ELZ	2010,064,23:00:00	2010,067,21:00:00	100.0%	25200100
- Channel +Station	XT	A2116	ELZ	2010,064,23:00:00	2010,067,21:00:00	100.0%	25200100
- Channel +Station	XT	A2119	ELZ	2010,064,23:00:00	2010,067,21:00:00	100.0%	25200100
- Channel +Station	XT	A2121	ELZ	2010,064,23:00:00	2010,067,21:00:00	100.0%	25200100
- Channel +Station	XT	A2126	ELZ	2010,064,23:00:00	2010,067,21:00:00	100.0%	25200100
- Channel +Station	XT	A2135	ELZ	2010,064,23:00:00	2010,067,21:00:00	100.0%	25200100
- Channel +Station	XT	A2136	ELZ	2010,064,23:00:00	2010,067,21:00:00	100.0%	25200100
- Channel +Station	XT	A2137	ELZ	2010,064,23:00:00	2010,067,21:00:00	100.0%	25200100
- Channel +Station	XT	A2138	ELZ	2010,064,23:00:00	2010,067,21:00:00	100.0%	25200100
- Channel +Station	XT	A2141	ELZ	2010,064,23:00:00	2010,067,21:00:00	100.0%	25200100
-	XT	A2152	ELZ	2010,064,23:00:00	2010,067,20:59:59	100.0%	25200000

Channel +Station - Channel	XT	A2166	ELZ	2010,064,23:00:00	2010,067,21:00:00	100.0%	25200100
Channel +Station - Channel	XT	A2171	ELZ	2010,064,23:00:00	2010,067,21:00:00	100.0%	25200100
Channel +Station - Channel	XT	A2175	ELZ	2010,064,23:00:00	2010,067,21:00:00	100.0%	25200100
Channel +Station - Channel	XT	A2189	ELZ	2010,064,23:00:00	2010,067,21:00:00	100.0%	25200100
Channel +Station - Channel	XT	A2199	ELZ	2010,064,23:00:00	2010,067,21:00:00	100.0%	25200100
Channel +Station - Channel	XT	A2204	ELZ	2010,064,23:00:00	2010,067,21:00:00	100.0%	25200100
Channel +Station - Channel	XT	A2234	ELZ	2010,064,23:00:00	2010,067,21:00:00	100.0%	25200100
Channel +Station - Channel	XT	A2237	ELZ	2010,064,23:00:00	2010,067,21:00:00	100.0%	25200100
Channel +Station - Channel	XT	A2248	ELZ	2010,064,23:00:00	2010,067,21:00:00	100.0%	25200100
Channel +Station - Channel	XT	A2264	ELZ	2010,064,23:00:00	2010,067,21:00:00	100.0%	25200100
Channel +Station - Channel	XT	A2362	ELZ	2010,064,23:00:00	2010,067,21:00:00	100.0%	25200100
Channel +Station - Channel	XT	A2364	ELZ	2010,064,23:00:00	2010,067,21:00:00	100.0%	25200100
Channel +Station - Channel	XT	A2406	ELZ	2010,064,23:00:00	2010,067,21:00:00	100.0%	25200100
Channel +Station - Channel	XT	A2431	ELZ	2010,064,23:00:00	2010,067,21:00:00	100.0%	25200100
Channel +Station - Channel	XT	A2448	ELZ	2010,064,23:00:00	2010,067,21:00:00	100.0%	25200100

+Station - Channel	XT	A2459	ELZ	2010,064,23:00:00	2010,067,21:00:00	100.0%	25200100
+Station - Channel	XT	A2467	ELZ	2010,064,23:00:00	2010,067,21:00:00	100.0%	25200100
+Station - Channel	XT	A2480	ELZ	2010,064,23:00:00	2010,067,21:00:00	100.0%	25200100
+Station - Channel	XT	A2487	ELZ	2010,064,23:00:00	2010,067,21:00:00	100.0%	25200100
+Station - Channel	XT	A2499	ELZ	2010,064,23:00:00	2010,067,21:00:00	100.0%	25200100
+Station - Channel	XT	A2501	ELZ	2010,064,23:00:00	2010,067,21:00:00	100.0%	25200100
+Station - Channel	XT	A2502	ELZ	2010,064,23:00:00	2010,067,21:00:00	100.0%	25200100
+Station - Channel	XT	A2503	ELZ	2010,064,23:00:00	2010,067,21:00:00	100.0%	25200100
+Station - Channel	XT	A2509	ELZ	2010,064,23:00:00	2010,067,21:00:00	100.0%	25200100
+Station - Channel	XT	A2510	ELZ	2010,064,23:00:00	2010,067,21:00:00	100.0%	25200100
+Station - Channel	XT	A2515	ELZ	2010,064,23:00:00	2010,067,21:00:00	100.0%	25200100
+Station - Channel	XT	A2522	ELZ	2010,064,23:00:00	2010,067,21:00:00	100.0%	25200100
+Station - Channel	XT	A2523	ELZ	2010,064,23:00:00	2010,067,21:00:00	100.0%	25200100
+Station - Channel	XT	A2524	ELZ	2010,064,23:00:00	2010,067,21:00:00	100.0%	25200100
+Station - Channel	XT	A2544	ELZ	2010,064,23:00:00	2010,067,21:00:00	100.0%	25200100
+Station							

- Channel +Station	XT	A2571	ELZ	2010,064,23:00:00	2010,067,21:00:00	100.0%	25200100
- Channel +Station	XT	A2576	ELZ	2010,064,23:00:00	2010,067,21:00:00	100.0%	25200100
- Channel +Station	XT	A2577	ELZ	2010,064,23:00:00	2010,067,21:00:00	100.0%	25200100
- Channel +Station	XT	A2587	ELZ	2010,064,23:00:00	2010,067,21:00:00	100.0%	25200100
- Channel +Station	XT	A2597	ELZ	2010,064,23:00:00	2010,067,21:00:00	100.0%	25200100
- Channel +Station	XT	A2612	ELZ	2010,064,23:00:00	2010,067,21:00:00	100.0%	25200100
- Channel +Station	XT	A2644	ELZ	2010,064,23:00:00	2010,067,21:00:00	100.0%	25200100
- Channel +Station	XT	A2647	ELZ	2010,064,23:00:00	2010,067,21:00:00	100.0%	25200100
- Channel +Station	XT	A2651	ELZ	2010,064,23:00:00	2010,067,21:00:00	100.0%	25200100
- Channel +Station	XT	A2653	ELZ	2010,064,23:00:00	2010,067,21:00:00	100.0%	25200100
- Channel +Station	XT	A2656	ELZ	2010,064,23:00:00	2010,067,21:00:00	100.0%	25200100
- Channel +Station	XT	A2657	ELZ	2010,064,23:00:00	2010,067,21:00:00	100.0%	25200100
- Channel +Station	XT	A2659	ELZ	2010,064,23:00:00	2010,067,20:59:59	100.0%	25200000
- Channel +Station	XT	A2667	ELZ	2010,064,23:00:00	2010,067,21:00:00	100.0%	25200100
- Channel +Station	XT	A2676	ELZ	2010,064,23:00:00	2010,067,21:00:00	100.0%	25200100
-	XT	A2677	ELZ	2010,064,23:00:00	2010,067,21:00:00	100.0%	25200100

Channel +Station - Channel	XT	A2678	ELZ	2010,064,23:00:00	2010,067,21:00:00	100.0%	25200100
Channel +Station - Channel	XT	A2679	ELZ	2010,064,23:00:00	2010,067,21:00:00	100.0%	25200100
Channel +Station - Channel	XT	A2685	ELZ	2010,064,23:00:00	2010,067,21:00:00	100.0%	25200100
Channel +Station - Channel	XT	A2688	ELZ	2010,064,23:00:00	2010,067,21:00:00	100.0%	25200100
Channel +Station - Channel	XT	A2689	ELZ	2010,064,23:00:00	2010,067,21:00:00	100.0%	25200100
Channel +Station - Channel	XT	A2692	ELZ	2010,064,23:00:00	2010,067,21:00:00	100.0%	25200100
Channel +Station - Channel	XT	A2696	ELZ	2010,064,23:00:00	2010,067,21:00:00	100.0%	25200100
Channel +Station - Channel	XT	A2702	ELZ	2010,064,23:00:00	2010,067,21:00:00	100.0%	25200100
Channel +Station - Channel	XT	A2711	ELZ	2010,064,23:00:00	2010,067,21:00:00	100.0%	25200100
Channel +Station - Channel	XT	A2714	ELZ	2010,064,23:00:00	2010,067,21:00:00	100.0%	25200100
Channel +Station - Channel	XT	A2716	ELZ	2010,064,23:00:00	2010,067,21:00:00	100.0%	25200100
Channel +Station - Channel	XT	A2721	ELZ	2010,064,23:00:00	2010,067,21:00:00	100.0%	25200100
Channel +Station - Channel	XT	A2724	ELZ	2010,064,23:00:00	2010,067,21:00:00	100.0%	25200100
Channel +Station - Channel	XT	A2744	ELZ	2010,064,23:00:00	2010,067,21:00:00	100.0%	25200100
Channel +Station - Channel	XT	A2762	ELZ	2010,064,23:00:00	2010,067,21:00:00	100.0%	25200100

+Station-Channel	XT	A2767	ELZ	2010,064,23:00:00	2010,067,21:00:00	100.0%	25200100
+Station-Channel	XT	A2768	ELZ	2010,064,23:00:00	2010,067,21:00:00	100.0%	25200100
+Station-Channel	XT	A2802	ELZ	2010,064,23:00:00	2010,067,21:00:00	100.0%	25200100
+Station-Channel	XT	A2809	ELZ	2010,064,23:00:00	2010,067,21:00:00	100.0%	25200100
+Station-Channel	XT	A2841	ELZ	2010,064,23:00:00	2010,067,21:00:00	100.0%	25200100
+Station-Channel	XT	A2848	ELZ	2010,064,23:00:00	2010,067,21:00:00	100.0%	25200100
+Station-Channel	XT	A2852	ELZ	2010,064,23:00:00	2010,067,21:00:00	100.0%	25200100
+Station-Channel	XT	A2868	ELZ	2010,064,23:00:00	2010,067,21:00:00	100.0%	25200100
+Station-Channel	XT	A2871	ELZ	2010,064,23:00:00	2010,067,21:00:00	100.0%	25200100
+Station-Channel	XT	A2877	ELZ	2010,064,23:00:00	2010,067,21:00:00	100.0%	25200100
+Station-Channel	XT	A2882	ELZ	2010,064,23:00:00	2010,067,21:00:00	100.0%	25200100
+Station-Channel	XT	A2900	ELZ	2010,064,23:00:00	2010,067,21:00:00	100.0%	25200100
+Station-Channel	XT	A2903	ELZ	2010,064,23:00:00	2010,067,21:00:00	100.0%	25200100
+Station-Channel	XT	A2922	ELZ	2010,064,23:00:00	2010,067,21:00:00	100.0%	25200100
+Station-Channel	XT	A2934	ELZ	2010,064,23:00:00	2010,067,21:00:00	100.0%	25200100
+Station							

- Channel +Station	XT	A2936	ELZ	2010,064,23:00:00	2010,067,21:00:00	100.0%	25200100
- Channel +Station	XT	A2937	ELZ	2010,064,23:00:00	2010,067,21:00:00	100.0%	25200100
- Channel +Station	XT	A2943	ELZ	2010,064,23:00:00	2010,067,21:00:00	100.0%	25200100
- Channel +Station	XT	A2945	ELZ	2010,064,23:00:00	2010,067,21:00:00	100.0%	25200100
- Channel +Station	XT	A2948	ELZ	2010,064,23:00:00	2010,067,21:00:00	100.0%	25200100
- Channel +Station	XT	A2982	ELZ	2010,064,23:00:00	2010,067,21:00:00	100.0%	25200100
- Channel +Station	XT	A2983	ELZ	2010,064,23:00:00	2010,067,21:00:00	100.0%	25200100
- Channel +Station	XT	A3003	ELZ	2010,064,23:00:00	2010,067,21:00:00	100.0%	25200100
- Channel +Station	XT	A3004	ELZ	2010,064,23:00:00	2010,067,21:00:00	100.0%	25200100
- Channel +Station	XT	A3005	ELZ	2010,064,23:00:00	2010,067,21:00:00	100.0%	25200100
- Channel +Station	XT	A3006	ELZ	2010,064,23:00:00	2010,067,21:00:00	100.0%	25200100
- Channel +Station	XT	A3008	ELZ	2010,064,23:00:00	2010,067,21:00:00	100.0%	25200100
- Channel +Station	XT	A3009	ELZ	2010,064,23:00:00	2010,067,21:00:00	100.0%	25200100
- Channel +Station	XT	A3508	ELZ	2010,064,23:00:00	2010,067,21:00:00	100.0%	25200100
- Channel +Station	XT	A3604	ELZ	2010,064,23:00:00	2010,067,21:00:00	100.0%	25200100
-	XT	A3617	ELZ	2010,064,23:00:00	2010,067,21:00:00	100.0%	25200100

Channel +Station - Channel	XT	A3620	ELZ	2010,064,23:00:00	2010,067,21:00:00	100.0%	25200100
Channel +Station - Channel	XT	A3621	ELZ	2010,064,23:00:00	2010,067,21:00:00	100.0%	25200100
Channel +Station - Channel	XT	A3627	ELZ	2010,064,23:00:00	2010,067,21:00:00	100.0%	25200100
Channel +Station - Channel	XT	A3634	ELZ	2010,064,23:00:00	2010,067,21:00:00	100.0%	25200100
Channel +Station - Channel	XT	A3636	ELZ	2010,064,23:00:00	2010,067,21:00:00	100.0%	25200100
Channel +Station - Channel	XT	A3638	ELZ	2010,064,23:00:00	2010,067,21:00:00	100.0%	25200100
Channel +Station - Channel	XT	A3660	ELZ	2010,064,23:00:00	2010,067,21:00:00	100.0%	25200100
Channel +Station - Channel	XT	A3704	ELZ	2010,064,23:00:00	2010,067,21:00:00	100.0%	25200100
Channel +Station - Channel	XT	A3709	ELZ	2010,064,23:00:00	2010,067,21:00:00	100.0%	25200100
Channel +Station - Channel	XT	A3711	ELZ	2010,064,23:00:00	2010,067,21:00:00	100.0%	25200100
Channel +Station - Channel	XT	A3712	ELZ	2010,064,23:00:00	2010,067,21:00:00	100.0%	25200100
Channel +Station - Channel	XT	A3713	ELZ	2010,064,23:00:00	2010,067,21:00:00	100.0%	25200100
Channel +Station - Channel	XT	A3724	ELZ	2010,064,23:00:00	2010,067,21:00:00	100.0%	25200100
Channel +Station - Channel	XT	A3740	ELZ	2010,064,23:00:00	2010,067,21:00:00	100.0%	25200100
Channel +Station - Channel	XT	A3747	ELZ	2010,064,23:00:00	2010,067,20:59:59	100.0%	25200000

+Station - Channel	XT	A3757	ELZ	2010,064,23:00:00	2010,067,21:00:00	100.0%	25200100
+Station - Channel	XT	A3760	ELZ	2010,064,23:00:00	2010,067,21:00:00	100.0%	25200100
+Station - Channel	XT	A3770	ELZ	2010,064,23:00:00	2010,067,21:00:00	100.0%	25200100
+Station - Channel	XT	A3776	ELZ	2010,064,23:00:00	2010,067,21:00:00	100.0%	25200100
+Station - Channel	XT	A3779	ELZ	2010,064,23:00:00	2010,067,21:00:00	100.0%	25200100
+Station - Channel	XT	A3788	ELZ	2010,064,23:00:00	2010,067,21:00:00	100.0%	25200100
+Station - Channel	XT	A3790	ELZ	2010,064,23:00:00	2010,067,21:00:00	100.0%	25200100
+Station - Channel	XT	A3795	ELZ	2010,064,23:00:00	2010,067,21:00:00	100.0%	25200100
+Station - Channel	XT	A3798	ELZ	2010,064,23:00:00	2010,067,21:00:00	100.0%	25200100
+Station - Channel	XT	A3802	ELZ	2010,064,23:00:00	2010,067,21:00:00	100.0%	25200100
+Station - Channel	XT	A3804	ELZ	2010,064,23:00:00	2010,067,21:00:00	100.0%	25200100
+Station - Channel	XT	A3805	ELZ	2010,064,23:00:00	2010,067,21:00:00	100.0%	25200100
+Station - Channel	XT	A3822	ELZ	2010,064,23:00:00	2010,067,21:00:00	100.0%	25200100
+Station - Channel	XT	A3834	ELZ	2010,064,23:00:00	2010,067,21:00:00	100.0%	25200100
+Station - Channel	XT	A3839	ELZ	2010,064,23:00:00	2010,067,21:00:00	100.0%	25200100
+Station							

- Channel +Station	XT	A3840	ELZ	2010,064,23:00:00	2010,067,21:00:00	100.0%	25200100
- Channel +Station	XT	A3844	ELZ	2010,064,23:00:00	2010,067,21:00:00	100.0%	25200100
- Channel +Station	XT	A3845	ELZ	2010,064,23:00:00	2010,067,21:00:00	100.0%	25200100
- Channel +Station	XT	A3852	ELZ	2010,064,23:00:00	2010,067,21:00:00	100.0%	25200100
- Channel +Station	XT	A3865	ELZ	2010,064,23:00:00	2010,067,20:59:59	100.0%	25200000
- Channel +Station	XT	A3871	ELZ	2010,064,23:00:00	2010,067,21:00:00	100.0%	25200100
- Channel +Station	XT	A3882	ELZ	2010,064,23:00:00	2010,067,21:00:00	100.0%	25200100
- Channel +Station	XT	A3887	ELZ	2010,064,23:00:00	2010,067,21:00:00	100.0%	25200100
- Channel +Station	XT	A3888	ELZ	2010,064,23:00:00	2010,067,21:00:00	100.0%	25200100
- Channel +Station	XT	A3918	ELZ	2010,064,23:00:00	2010,067,21:00:00	100.0%	25200100
- Channel +Station	XT	A3921	ELZ	2010,064,23:00:00	2010,067,21:00:00	100.0%	25200100
- Channel +Station	XT	A3936	ELZ	2010,064,23:00:00	2010,067,21:00:00	100.0%	25200100
- Channel +Station	XT	A3944	ELZ	2010,064,23:00:00	2010,067,21:00:00	100.0%	25200100
- Channel +Station	XT	A3947	ELZ	2010,064,23:00:00	2010,067,21:00:00	100.0%	25200100
- Channel +Station	XT	A3951	ELZ	2010,064,23:00:00	2010,067,21:00:00	100.0%	25200100
-	XT	A3986	ELZ	2010,064,23:00:00	2010,067,21:00:00	100.0%	25200100

Channel +Station - Channel	XT	A3988	ELZ	2010,064,23:00:00	2010,067,21:00:00	100.0%	25200100
Channel +Station - Channel	XT	A3994	ELZ	2010,064,23:00:00	2010,067,21:00:00	100.0%	25200100
Channel +Station - Channel	XT	A3999	ELZ	2010,064,23:00:00	2010,067,21:00:00	100.0%	25200100
Channel +Station - Channel	XT	A4009	ELZ	2010,064,23:00:00	2010,067,21:00:00	100.0%	25200100
Channel +Station - Channel	XT	A4015	ELZ	2010,064,23:00:00	2010,067,21:00:00	100.0%	25200100
Channel +Station - Channel	XT	A4031	ELZ	2010,064,23:00:00	2010,067,21:00:00	100.0%	25200100
Channel +Station - Channel	XT	A4037	ELZ	2010,064,23:00:00	2010,067,21:00:00	100.0%	25200100
Channel +Station - Channel	XT	A4041	ELZ	2010,064,23:00:00	2010,067,21:00:00	100.0%	25200100
Channel +Station - Channel	XT	A4052	ELZ	2010,064,23:00:00	2010,067,21:00:00	100.0%	25200100
Channel +Station - Channel	XT	A4058	ELZ	2010,064,23:00:00	2010,067,21:00:00	100.0%	25200100
Channel +Station - Channel	XT	A4063	ELZ	2010,064,23:00:00	2010,067,21:00:00	100.0%	25200100
Channel +Station - Channel	XT	A4066	ELZ	2010,064,23:00:00	2010,067,21:00:00	100.0%	25200100
Channel +Station - Channel	XT	A4068	ELZ	2010,064,23:00:00	2010,067,21:00:00	100.0%	25200100
Channel +Station - Channel	XT	A4076	ELZ	2010,064,23:00:00	2010,067,21:00:00	100.0%	25200100
Channel +Station - Channel	XT	A4094	ELZ	2010,064,23:00:00	2010,067,21:00:00	100.0%	25200100

+Station
- XT A4095 ELZ 2010,064,23:00:00 2010,067,21:00:00 100.0% 25200100
Channel
+Station

APPENDIX 3

RECEIVER LOCATIONS

Table A3-1. Line receiver locations

Station	Latitude (deg)	Longitude (deg)	Active survey receiver number	Altitude (m)
W1	39.57437	-118.8803705	7958	1217.8
W2	39.5742	-118.8800508	7959	1217.8
W3	39.57402	-118.8797311	7960	1217.6
W4	39.57385	-118.8794115	7961	1216.8
W5	39.57367	-118.8790953	7962	1216.9
W6	39.5735	-118.8787745	7963	1217.4
W7	39.57332	-118.8784583	7964	1218.9
W8	39.57315	-118.8781375	7965	1217
W9	39.57297	-118.877819	7966	1216.5
W10	39.5728	-118.8775005	7967	1217.4
W11	39.57263	-118.877182	7968	1216.6
W12	39.57245	-118.8768623	7969	1217.9
W13	39.57228	-118.876545	7970	1219
W14	39.5721	-118.8762277	7971	1220.1
W15	39.57193	-118.875908	7972	1219.6
W16	39.57175	-118.8755896	7973	1218.3
W17	39.57158	-118.8752734	7974	1217.8
W18	39.57141	-118.8749514	7975	1217.7
W19	39.57123	-118.874633	7976	1217.5
W20	39.57106	-118.8743157	7977	1219
W21	39.57088	-118.873996	7978	1218.4
W22	39.57071	-118.8736787	7979	1218.1
W23	39.57053	-118.8733567	7980	1217.6
W24	39.57036	-118.8730371	7981	1216.5
W25	39.57018	-118.872721	7982	1216.7
W26	39.57001	-118.8724025	7983	1217.1
W27	39.56984	-118.8720817	7984	1216.4
W28	39.56966	-118.8717632	7985	1215.8
W29	39.56949	-118.8714471	7986	1215.5
W30	39.56931	-118.8711286	7987	1215.6
W31	39.56914	-118.8708113	7988	1217
W32	39.56899	-118.8704709	7989	1216.5
W33	39.56884	-118.8701362	7990	1217.5
W34	39.56868	-118.8697981	7991	1217.8
W35	39.56853	-118.8694611	7992	1219.4
W36	39.56838	-118.8691206	7993	1219.2
W37	39.56823	-118.8687848	7994	1218.7
W38	39.56808	-118.8684478	7995	1219
W39	39.56793	-118.868112	7996	1217.8
W40	39.56777	-118.8677739	7997	1216.1
W41	39.56762	-118.8674357	7998	1217.4

Station	Latitude (deg)	Longitude (deg)	Active survey receiver number	Altitude (m)
W42	39.56747	-118.8670999	7999	1216.9
W43	39.56732	-118.8667618	8000	1218.3
W44	39.56716	-118.866426	8001	1217.7
W45	39.56701	-118.8660867	8002	1216.2
W46	39.56686	-118.8657497	8003	1217.4
W47	39.56671	-118.8654116	8004	1217.5
W48	39.56656	-118.8650769	8005	1217.3
W49	39.5664	-118.8647155	8006	1216.5
W50	39.56625	-118.8644019	8007	1216.5
W51	39.5661	-118.8640649	8008	1215.4
W52	39.56595	-118.8637268	8009	1214.7
W53	39.5658	-118.8633898	8010	1214.5
W54	39.56564	-118.8630529	8011	1214.4
W55	39.56549	-118.8627136	8012	1214.9
W56	39.56534	-118.862379	8013	1215.4
W57	39.56519	-118.862042	8014	1215.1
W58	39.56504	-118.8617027	8015	1215.6
W59	39.56488	-118.861367	8016	1215.3
W60	39.56473	-118.86103	8017	1214.9
W61	39.56458	-118.8606942	8018	1215.3
W62	39.56443	-118.8603573	8019	1215.1
W63	39.56428	-118.860018	8020	1214.8
W64	39.56413	-118.8597393	8021	1213.9
W65	39.56397	-118.8593441	8022	1215
W66	39.56382	-118.859013	8023	1215
W67	39.56366	-118.8586772	8024	1215.6
W68	39.56351	-118.8583403	8025	1216.3
W69	39.56336	-118.8580022	8026	1217.3
W70	39.56321	-118.8576618	8027	1217.9
W71	39.56306	-118.8573214	8028	1218.2
W72	39.56291	-118.8569821	8029	1218.1
W73	39.56276	-118.8566464	8030	1217.6
W74	39.5626	-118.8563106	8031	1216.7
W75	39.56245	-118.8559725	8032	1215.8
W76	39.5623	-118.8556333	8033	1215.6
W77	39.56215	-118.8552952	8034	1216.2
W78	39.562	-118.8549559	8035	1215.8
W79	39.56185	-118.8546179	8036	1214.1
W80	39.5617	-118.8542833	8037	1213.3
W81	39.56155	-118.8539452	8038	1213
W82	39.56139	-118.8536036	8039	1212.7
W83	39.56124	-118.8532656	8040	1212.7

Station	Latitude (deg)	Longitude (deg)	Active survey receiver number	Altitude (m)
W84	39.56108	-118.8529379	8041	1212.4
W85	39.56093	-118.852601	8042	1212.5
W86	39.56078	-118.8522641	8043	1212.6
W87	39.56063	-118.8519272	8044	1213
W88	39.56048	-118.8515903	8045	1212.8
W89	39.56033	-118.8512522	8046	1214.4
W90	39.56017	-118.8509153	8047	1215.5
W91	39.56002	-118.8505773	8048	1215.9
W92	39.55987	-118.8502404	8049	1217
W93	39.55972	-118.8499035	8050	1217
W94	39.55957	-118.8495677	8051	1216.5
W95	39.55941	-118.8492297	8052	1216.1
W96	39.55926	-118.8488939	8053	1216.2
W97	39.55911	-118.8485571	8054	1216
W98	39.55895	-118.8482167	8055	1215.9
W99	39.5588	-118.8478809	8056	1216.3
W100	39.55865	-118.8475429	8057	1216.1
W101	39.5585	-118.847206	8058	1215.7
W102	39.55835	-118.846868	8059	1215.3
W103	39.5582	-118.8465299	8060	1215.6
W104	39.55805	-118.8461942	8061	1215.8
W105	39.55789	-118.8458631	8062	1216.2
W106	39.55774	-118.8455193	8063	1215.3
W107	39.55759	-118.8451847	8064	1212.1
W108	39.55743	-118.8448455	8065	1211.8
W109	39.55728	-118.8445086	8066	1212
W110	39.55713	-118.8441741	8067	1212.6
W111	39.55698	-118.8438384	8068	1213.8
W112	39.55683	-118.8434992	8069	1214.7
W113	39.55668	-118.8431612	8070	1214.6
W114	39.55652	-118.842822	8071	1214.7
W115	39.55637	-118.8424863	8072	1213.3
W116	39.55622	-118.8421482	8073	1213.5
W117	39.55607	-118.8418114	8074	1213.4
W118	39.55592	-118.8414757	8075	1213.8
W119	39.55576	-118.8411353	8076	1212.3
W120	39.55561	-118.8408043	8077	1211.9
W121	39.55546	-118.8404616	8078	1212.1
W122	39.55531	-118.8401271	8079	1212.6
8080	39.55516	-118.8397902	8080	1212.8
8081	39.55498	-118.8394347	8081	1210.4
8082	39.55485	-118.8391142	8082	1211.6

Station	Latitude (deg)	Longitude (deg)	Active survey receiver number	Altitude (m)
8083	39.5547	-118.8387774	8083	1213.6
8084	39.55455	-118.8384417	8084	1214.3
8085	39.55441	-118.8381351	8085	1214.1
NO	39.55424	-118.8377657		1214
NO	39.55409	-118.8374311		1214.3
NO	39.55394	-118.8370931		1214.7

Table A3-2. Array receiver locations

	Internal GPS	**Lat**	**Long**			**Handheld GPS**	**Lat**	**Long**
Station	**Degrees**	**Minutes**	**Degrees**	**Minutes**	**Elevation**	**Degrees**		**Degrees**
A85	N 39		W 118			N 39.57245		W 118.87691
A84/86?	N 39		W 118					
A84						N 39.57138		W 118.87485
A83	N 39	34.1459	W 118	51.8482	1209	N 39.56907		W 118.86413
A82	N 39	34.5013	W 118	51.1922	1206	N 39.57501		W 118.85321
A81	N 39	34.9218	W 118	51.578	1204	N 39.58203		W 118.85963
A101	N 39	34.297	W 118	51.2084	1212	N 39.57180		W 118.85346
A102						N 39.56897		W 118.85852
A80	N 39	34.9053	W 118	51.9779	1207			
A79	N 39	34.9171	W 118	52.3542	1208			
A78	N 39	34.8126	W 118	52.77012				
A75	N 39	33.8716	W 118	52.4984	1221	N 39.56456		W 118.87500
A73	N 39	34.0632	W 118	52.7661	1213			
A72?	N 39	34.143	W 118	53.01123	1102			
A72?	N 39	34.9814	W 118	53.0758	1215			
A71	N 39	34.266	W 118	53.3583	1216			
A65	N 39	33.5003	W 118	51.4729		N 39.55830		W 118.85783
A64						N 39.54986		W 118.86576
A63	N 39	33.2133	W 118	52.0644	1219	N 39.55354		W 118.86774
A61	N 39	33.487	W 118	52.1672		N 39.55811		W 118.86943
A611?						N 39.56055		W 118.87510

A60E?						N 39.56784		W 118.85317
A60W?						N 39.55688		W 118.87364
A59						N 39.56784		W 118.85318
A56	N 39	33.2301	W 118	51.2597	1208			
A501	N 39	33.8718	W 118	50.4217	1202			
A49	N 39	33.6286	W 118	50.825	1206			
A48	N 39	33.5972	W 118	50.2191	1210			
A47	N 39	33.4158	W 118	50.061	1213			
A46	N 39	33.0833	W 118	49.4707	1210			
A45	N 39	33.1645	W 118	49.3449	1206			
A43	N 39	33.6912	W 118	49.3826	1209			
A42	N 39	32.8616	W 118	50.4437	1206			
A41	N 39	32.8595	W 118	50.7899	1205			
A40	N 39	33.0088	W 118	51.8053	1209			
A391	N 39	33.4165	W 118	51.1483	1211			
A38	N 39	33.7034	W 118	51.5941				
A37	N 39	33.6971	W 118	51.9551				
W32	N 39	34.139	W 118	52.2313		N 39.569		W 118.87049
W37	N 39	34.0879	W 118	52.1067		N 39.56807		W 118.86843
W50	N 39		W 118			N 39.56625		W 118.86439
W55	N 39	33.9272	W 118	51.7645		N 39.56545		W 118.86273
W61	N 39	33.8747	W 118	51.64527		N 39.56457		W 118.86069

APPENDIX 4

PROPOSED SOLUTIONS FOR IMPROVED P-ARRIVAL EXTRACTION

4.1 Pre-filtering in narrow, empirically chosen frequency bands may enhance P-arrivals only when the cultural noise is very high. As suggested by Draganov et al., 2013, a new approach to the database analysis was evaluated, to specifically search for P-arrivals by crosscorrelating the ambient noise and signal in the frequency band 6-24 Hz, which was estimated as the frequency band of observed GF P-arrivals. The sample rate was increased to 250 sps (versus 125 sps used in this study) and the window length was 3s (vs 6s in the investigations above). In Figure A4.1 A-B are represented the GFs extracted after pre-filtering from 6-24 Hz, with virtual source station W65, and receivers along the line, for the duration of the experiment, using all the data. The station pairs are at in the same distance range from W65, to the north (A) and to the south (B). Figure 4A.1 C-D shows the GFs extracted from at the same stations pairs as in A and respectively B, however, when the waveforms were processed after a pre-filter of 0.4 Hz high-pass, eight poles, zero-phase Butterworth filter.

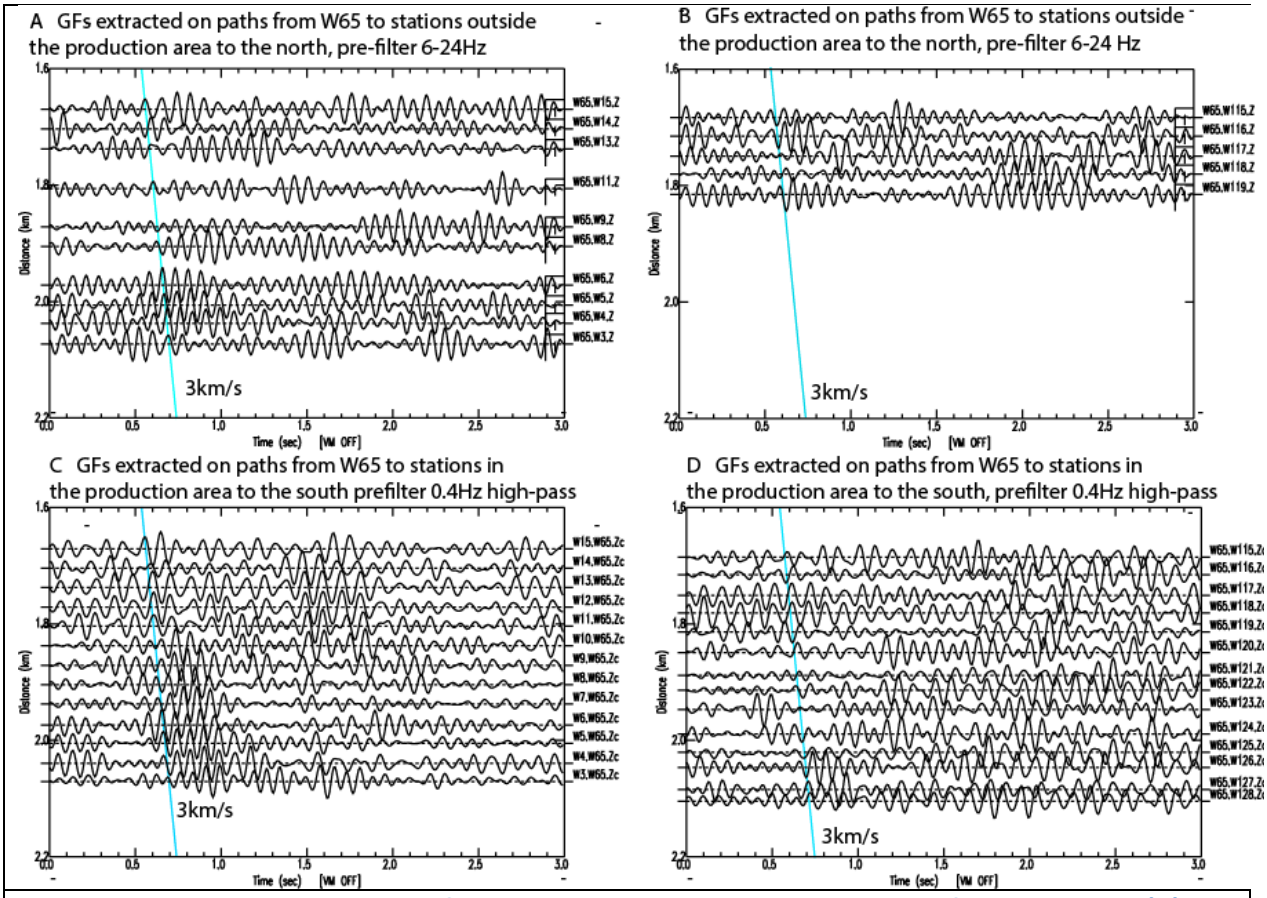

Figure A4.1 shows a comparison of ambient – noise analysis when the pre-filter is 6-24 Hz (A) and when the pre-filter is 0.4Hz Butterworth zero phase, eight-pole high-pass (B). The arrivals near the 3km/s time lag (blue line in all plots) are interpreted as P-arrivals. Note that when the cultural noise is low, pre-filtering from 6-24 Hz results in lower signal-to-noise (SNR) arrivals, however, in the production area, pre-filtering from 6-24 Hz results in higher SNR arrivals at least for some station pairs. In Figure 71B some of the GFS are missing because the waveforms were rejected by the stacking algorithms.

4.2 Using the crosscorrelations of the coda of the crosscorrelations (or C^3) is a method developed first by Stehli et al. 2008, which has significant potential to improve the results. Figure A4.2 shows preliminary results of P-extraction, after cutting the last 1 s of the GFs from selected stations, and crosscorrelating all the waveforms with W59. Note that in this figure some of the southern (production area) stations show "ringing" in a narrow frequency band, however, many crosscorrelations are symmetrical in Figure A4.2A, which is expected when applying C^3 (Zhang and Yang, 2013). This figure also shows the advantage of choosing similar daily GFs to stack. The GF similarity is assessed by crosscorrelating the daily crosscorrelations from 0.2 to 0.4 s from zero time lag, after filtering from 7 to 16 Hz and choosing the waveforms with crosscorrelation maxima exceeding a threshold of 0.05.

A. Record section for two-sided GF waveforms extracted from crosscorrelation of the coda of crosscorrelations (coda from 2s to 3s from the origin time). The initial GFs have been estimated after daily GFs were selected prior to stacking. All coda waveforms were crosscorrelated with the coda of the GF extracted between W65 and W59. The results should show GFs from W59 to all the other stations. Blue: GFs between W59 and stations to the south of W65; Black: GFs extracted between W59 and stations to the north of W65 ; Yellow: GFs for which no arrival has been identified by an analyst. The blue lines show 4 s time lags.

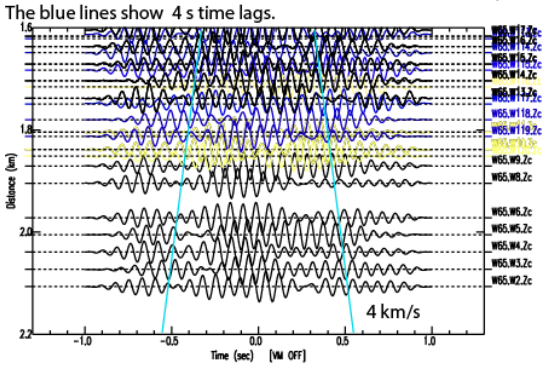

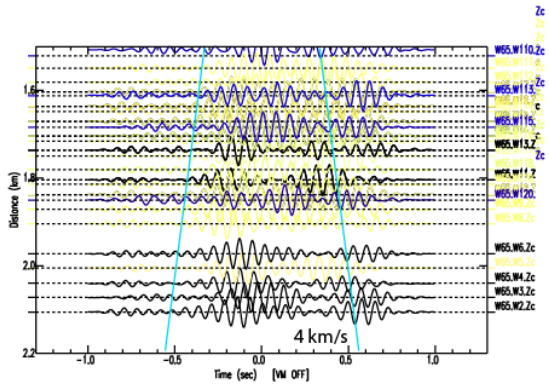

B. Record section for two-sided GF waveforms extracted from crosscorrelation of the coda of crosscorrelations (coda from 2s to 3s from the origin time). All the available daily GFs have been used. All the initial, cut from 2s to 3s GF waveforms were crosscorrelated with the GF extracted between W65 and W59. The results should be GFs from W59 to all the other stations arriving from 3-4km/s. Blue: GFs between W59 and stations to the south of W65; Black: GFs extracted between W59 and stations to the north of W65 ; Yellow: GFs for which no arrival has been identified by an analyst. The blue lines show 4 s time lags.

Figure A4.2 The potential of the C^3 method. A. Selected stations of one of the 127 record sections which would be stacked to obtain a virtual shot gather for station W59. Note symmetrical waveforms and thus better results are obtained when (A) the initial GFs are selected based on waveform similarity prior to stacking, compared to (B) when all the initial GF's are stacked.

APPENDIX 5

OPTIM, INC. REPORT

Technical Report in Support of

Development of a low cost method to estimate the seismic signature of a geothermal field from ambient seismic noise analysis

Prepared for

Ileana Tibuleac, PhD
University of Nevada, Reno
1664 N. Virginia St. MS 174
Reno, NV, 89557

Purchase Order No: 115GC000057
Subaward No: UNR-13-76
UNR Account No: 1320-114-11HR

By

Optim, Inc.
200 South Virginia Street
Suite 560
Reno, NV 89501
www.optimsoftware.com
Contact: satish@optimsoftware.com

May 2015

TABLE OF CONTENTS

1.0 INTRODUCTION

Optim participated and completed the work described in this report as part of Tasks 4, 5 and 12 (described below) of the DOE project entitled "Development of a low cost method to estimate the seismic signature of a geothermal field from ambient seismic noise analysis". Tasks involved generating P-wave velocity model from active source seismic reflection data acquired along the same line as the ambient noise data, using the model to do a pre-stack depth migration on both active and ambient noise data and estimating stochastic and attenuation parameters from the migrated section, respectively.

The study area (Figure 1) is a relatively well-characterized geothermal resource in Fallon, Nevada, where evaluation and calibration of the new exploration method is possible (Tibuleac and Eneva, 2011).

Optim was provided with shot gathers from the active source survey recording along "Line 2" (Figure) as well as virtual shot gathers generated from ambient noise recordings (Tibuleac et al., 2013)

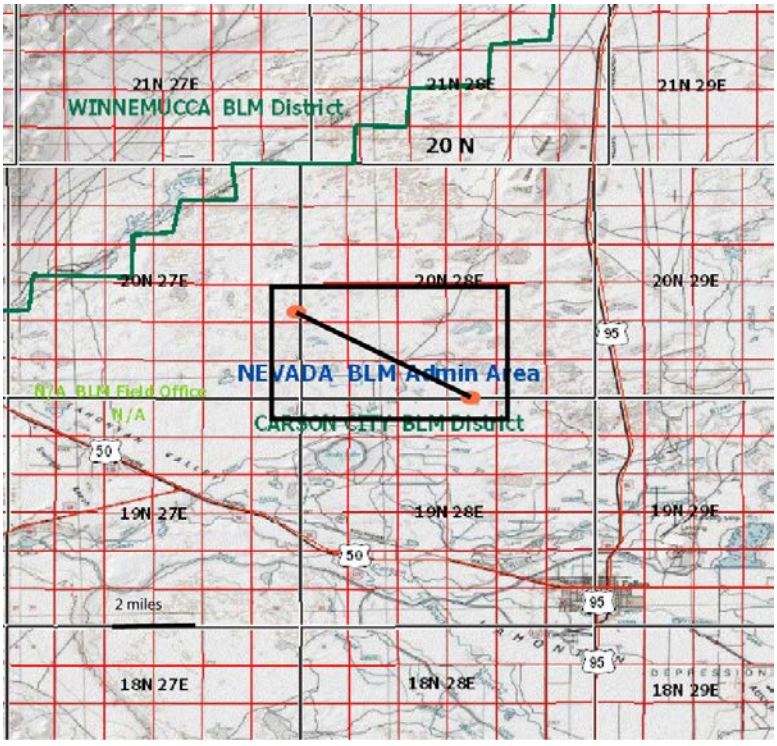

Figure 1: General location map showing the seismic survey location along which both active source and ambient noise data was acquired. Data from this line was used for the analyses described in this report.

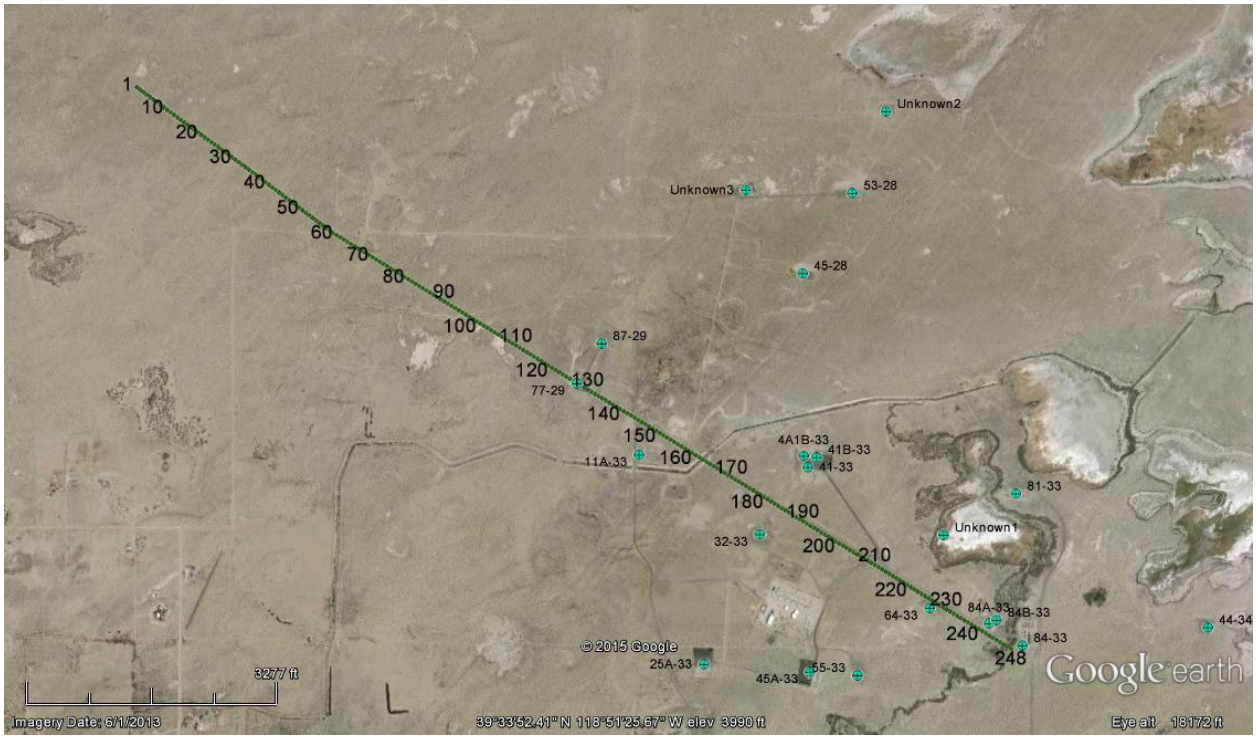

Figure 2: Google Earth images showing orientation of Line 2. The numbers shown are common depth points (CDP). They have a spacing of about 16.5 m and will be used to as reference for the seismic sections including in this report. CDP 1 is to the NW and CDP 248 is to the SE.

2.0 REFLECTION DATA PROCESSING

During this task, we first derived P-wave velocity model from the active source data recorded along Line 2 and then used it in a pre-stack depth migration to directly image the reflectors in depth. The same model derived from the active source data was used for processing the ambient noise data as well. The S-wave velocity information derived from group-velocity dispersion analysis of the ambient noise data will also be used to process the data (after converting to P-wave velocities) at a later time and so those results are not included in this report.

Velocity modeling was done using Optim's SeisOpt® Simulated Annealing Optimization method. SeisOpt® optimization uses only first arrivals from the raw data to accurately predict subsurface velocity structure. First-arrivals are the strongest and easiest events to pick on a seismogram, especially in laterally complex or volcanic environments that usually characterize geothermal environments. These models are then extended in depth. We then use this velocity model in a depth migration to place the reflection amplitudes in their correct position in the subsurface. It is important to note that the accuracy and resolution of the velocity model is a dependent on the acquisition parameters, specifically the geophone spacing. Based in previous studies performed by Optim, SeisOpt® velocity models alone can be a reliable indicator of structure, and sometimes zones of permeability within geothermal anomalies.

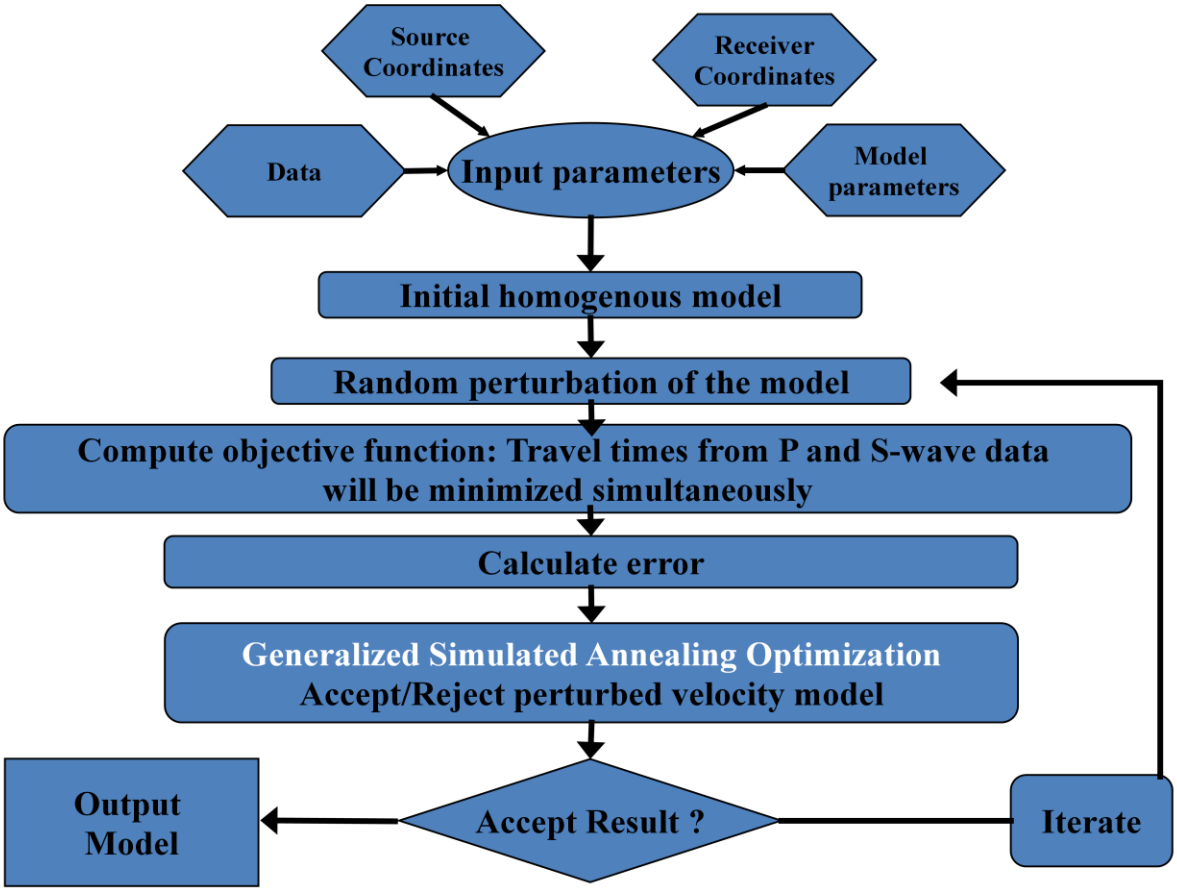

Figure 3: Flow chart showing the SeisOpt® velocity optimization process.

Simulated annealing is a Monte-Carlo estimation process that can match P-wave arrival times to a velocity model even where sophisticated non-linear inversion methods may fail (Pullammanappallil and Louie, 1993; Pullammanappallil and Louie, 1994). The algorithm works by randomly perturbing an arbitrary starting model until the synthetic seismic wave travel times computed through it match the travel time picks from the new data. New models producing less travel time error are accepted for further enhancements, and models having increased error can be accepted conditionally based on their total error. As annealing proceeds, conditional acceptance becomes less and less likely. Unlike linear, iterative inversions, simulated annealing optimization will find the global velocity solution while avoiding local error minimums. It is also completely insensitive to the starting velocity model, removing the interpreter bias may be involved in a prospect.

The velocity model obtained from first arrivals is extended in depth by first enhancing the coherence of deeper reflection.

Velocity models obtained by the above process are then used as input for the Kirchhoff pre-stack depth migration algorithm, which is the second processing technique. The pre-stack migration algorithm uses the velocity models for accurate calculation of travel times down to and up from every point within the reflection data volume.

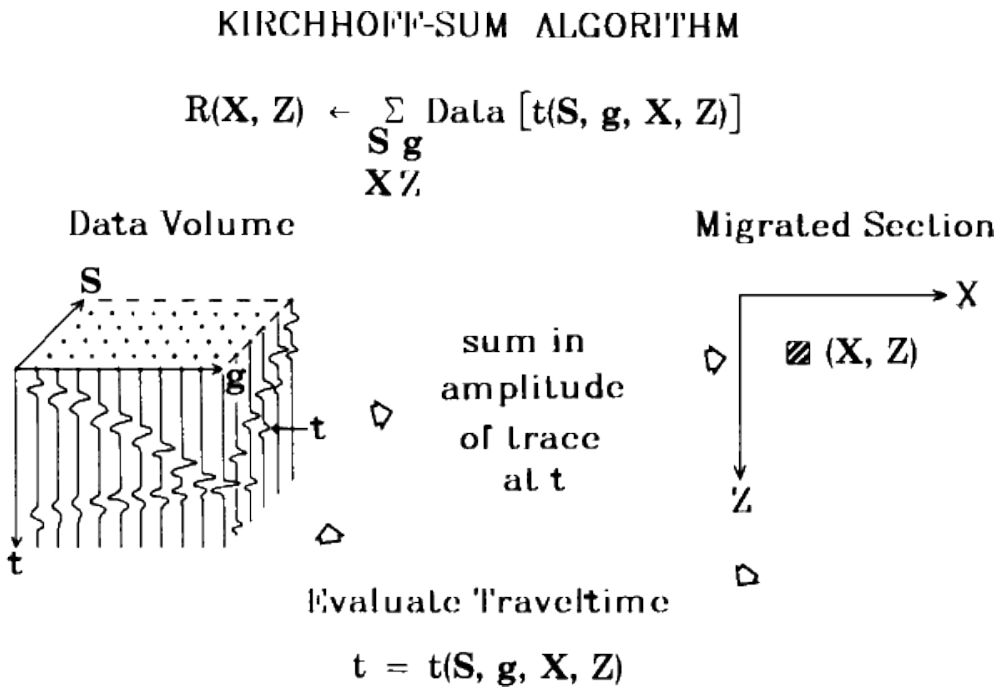

Figure 4: Schematic showing the Kirchhoff pre-stack depth migration (PSDM) process.

It produces images by summing the value of seismograms within the data volume at discrete points of time, based on travel-time calculations through the velocity model. Given a model that characterizes the velocity structure, the pre-stack migration can produce images from seismic data that has no visible signs of reflective coherency. Because pre-stack migration is free of assumptions about dip of bedding and structure, it will create images that reveal the true-depth location and geometry of permeable features in any orientation (Louie and Qin, 1991).

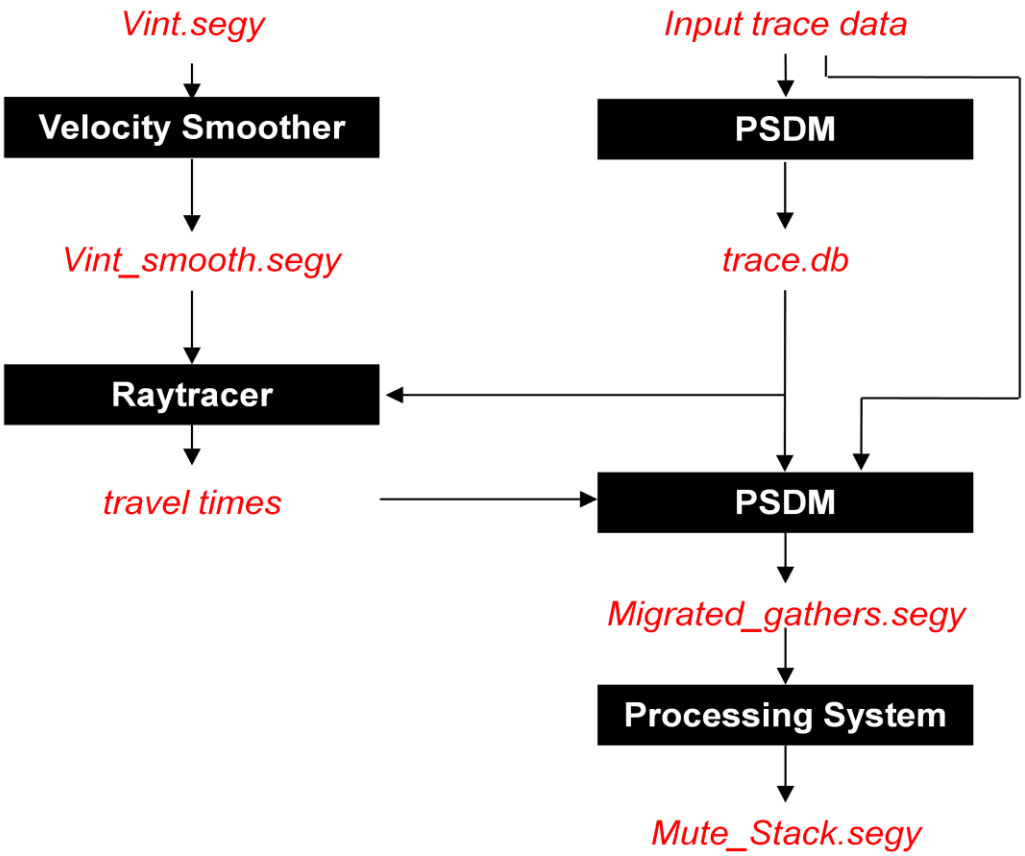

Figure 5: Flow chart showing the PSDM process.

The combined approach utilizing SeisOpt® velocity optimization and depth migration objectively evaluates the subsurface velocity structure, which may include significant horizontal velocity gradients, to accurately image permeable features within geothermal fields.

Figure 6 shows the P-wave velocity model obtained from the active source reflection data. Not the strong lateral velocity variations and in particular the “dip” in velocities at the center of the line. P-wave velocities range from 1,850 m/s to 4,500m/s. The relative lower velocities between CDP’s 120 and 180 are probably caused either due to fracturing or faulting.

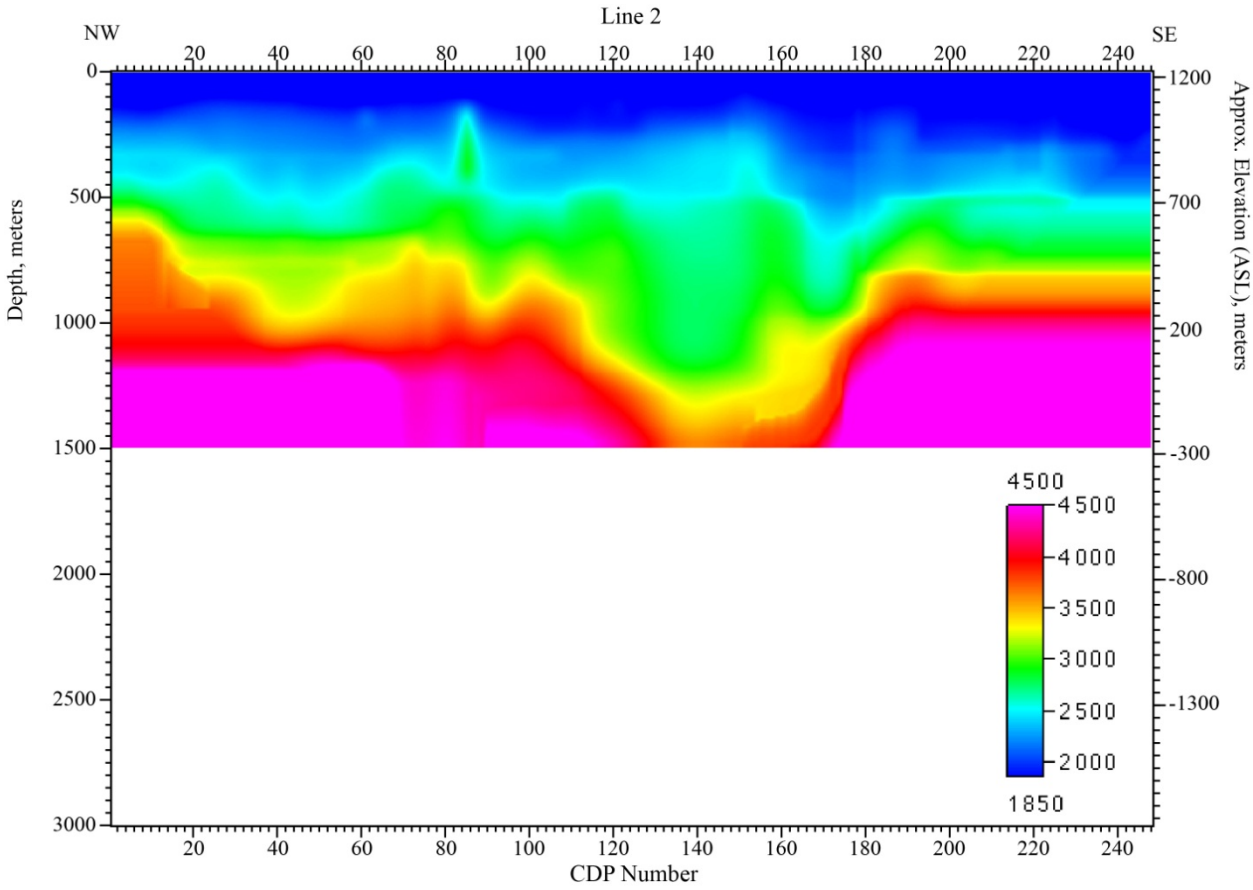

Figure 6: P-wave velocity model derived using SeisOpt® velocity optimization of data from active source data recording along Line 2. Note the lower velocities between CDP's 120 and 180.

The velocity model is then used to obtain the pre-stack depth migration image shown in Figure 7 and 8 for the active source data and Figures 9 and 10 for the ambient noise data. The same processing was applied to both data sets.

The migration of the active source data shows horizontal to sub-horizontal reflectors that truncate against a "dome" shaped structure between CDP's 120 and 180. This structure corresponds to the area that has the relatively low P-wave velocity. The resolution is good down to 2,300m or so before we start seeing deterioration of the image quality.

On the other hand, the ambient noise data does not show the dome shaped structure very well. We can see presence of dipping reflectors near CDP 120 and 180 and horizontal reflections truncating against it but the image resolution deteriorates rapidly below 1,000m or so. Deeper reflections are hard to discern

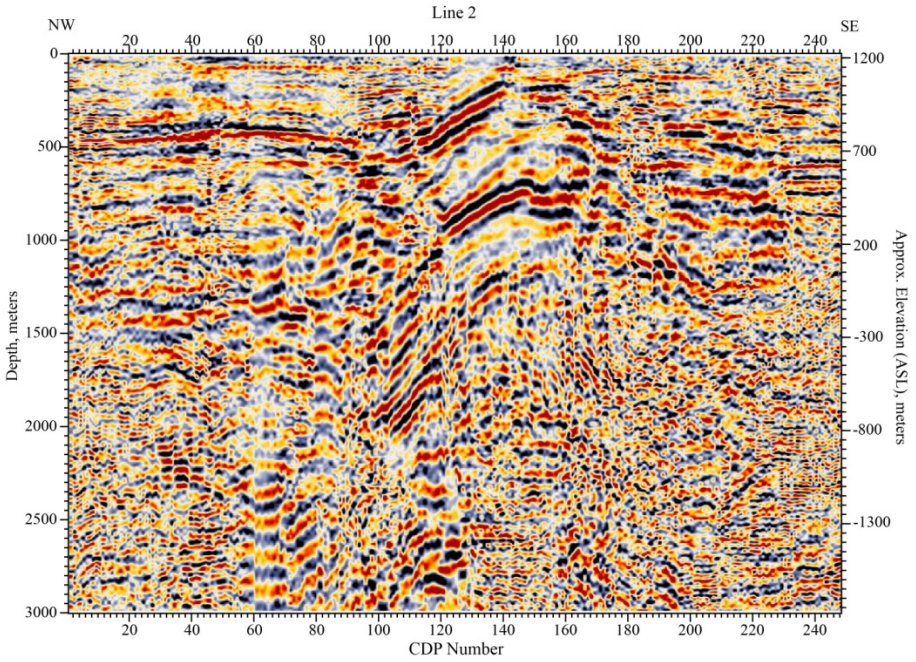

Figure 7: Pre-stack depth migration using the active source data recorded along Line2.

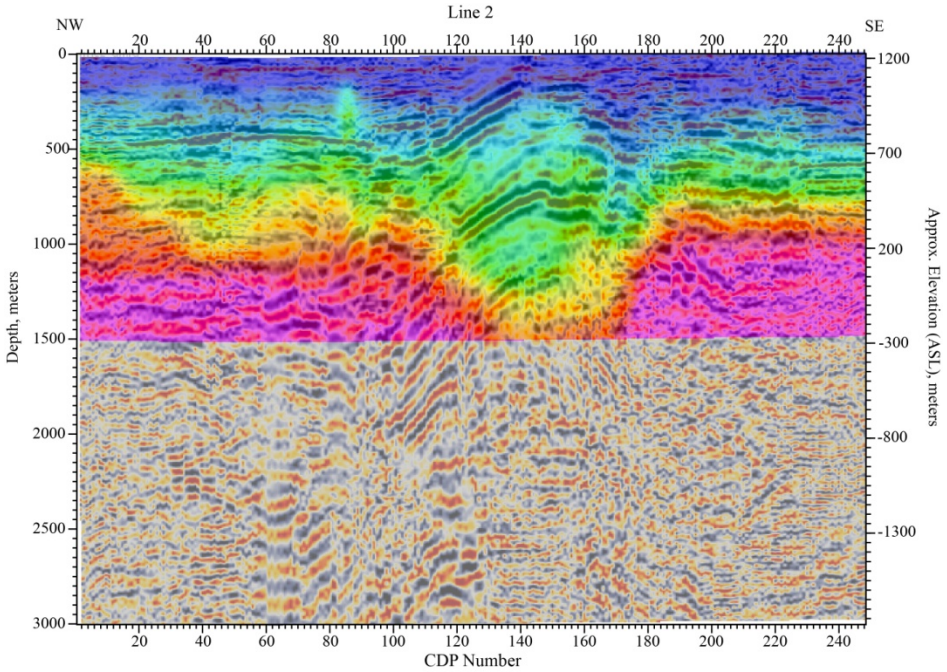

Figure 8: P-wave velocity model overlain on the depth migrated section shown in Figure 7. The doming of reflectors corresponds to the relative low velocity zone between CDP's 120 and 180

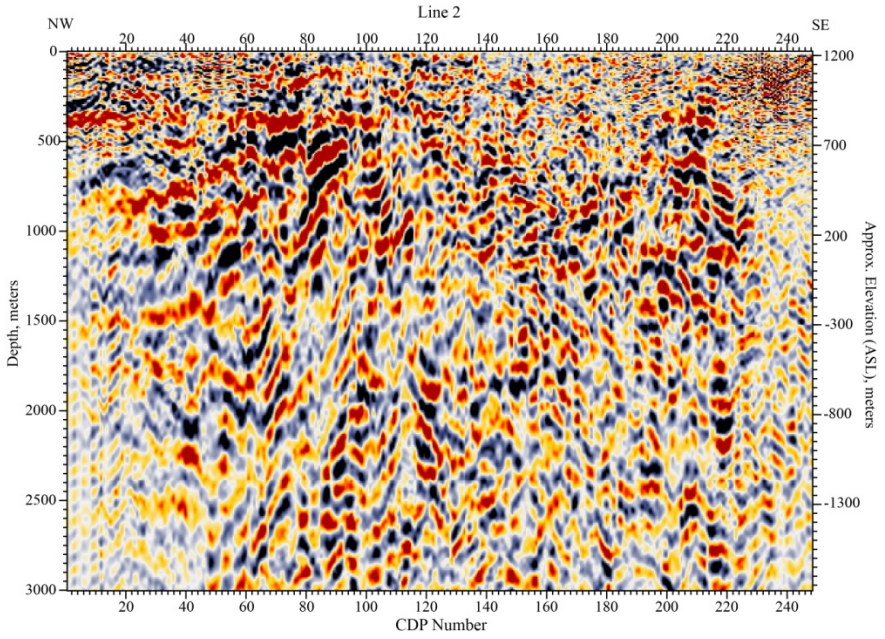

Figure 8: Pre-stack depth migration using the ambient noise data recorded along Line2.

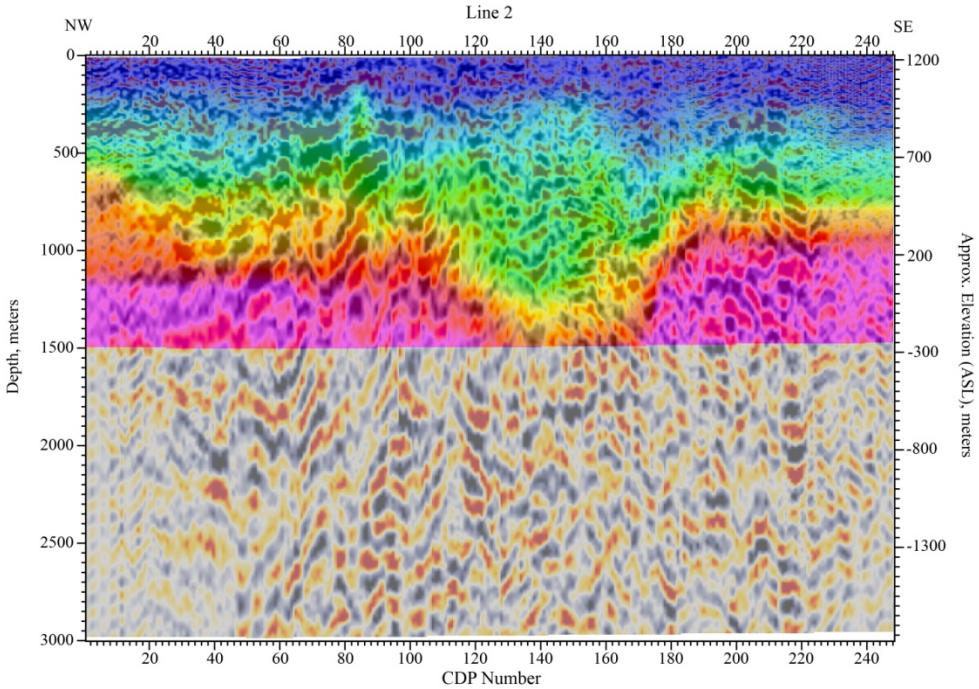

Figure 10: P-wave velocity model overlain on the depth migrated section shown in Figure 9. The resolution of the image deteriorates below 1,000m but shallower data show the horizontal and dipping reflections similar to those see in the active source data (Figure 8).

3.0 ESTIMATING OF STOCHASTIC PARAMETERS

We estimate stochastic parameters from the depth migrated sections obtained from both active and ambient noise data. The estimated parameters include correlation length and Hurst number. The objective is to see if there are similarities in the estimated parameters between the two sections and whether these provide additional information that could be used as indicators of permeability within the subsurface.

We start with the assumption the depth migrated images reveal heterogeneities that represent a von Karman heterogeneity distribution (Carpentier et al., 2010). The process begins by loading the migrated depth section. Once loaded, a normalized 2D autocorrelation function is computed in an N x M window, using user provided window parameters. The windows are shifted by 25 percent of the window height and width to produce an array of overlapping autocorrelation matrices. To aid in selecting the proper window size, the program provides a spectrum analyzer function. An example spectrum is illustrated in Figure 11 below.

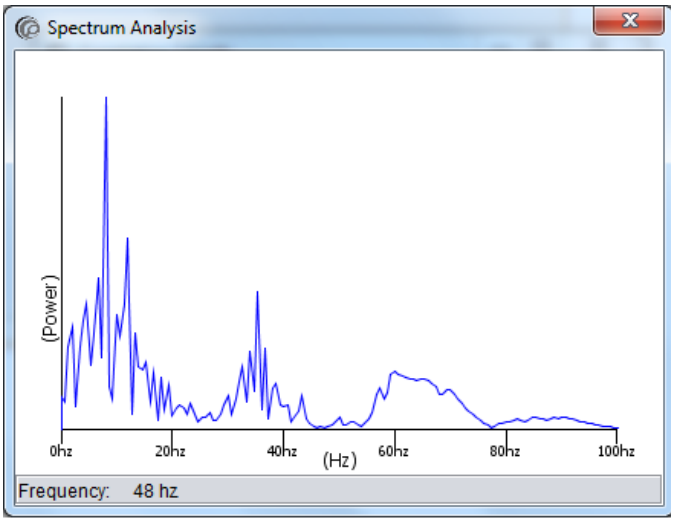

Figure 11: Example power spectrum

Given the proper window size, the following 2D autocorrelation function is computed.

Where $p(x_i,z_j)$ is a 2D seismic field in common midpoint (CMP) and time, l is the horizontal lag and τ is the vertical or time lag. From the resulting 2D autocorrelation array, $\Phi(l,0)$ is selected as the average lateral autocorrelation function for the entire 2D matrix.

The next step is an optional dip correction to the average lateral autocorrelation functions. This is done by interpolating along a line rotated by an incremental dip angle. The line at the dip angle producing a maximum amount of elongation is selected as representing the dip-corrected autocorrelation function (Hurich, 2003)

The lateral correlation functions are used to estimate the von Karman parameters, correlation length and Hurst number. The misfit function for the parameters is assumed to be:

where $LSQ(a_x,v)$ is the least-squares misfit as a function of a_x and v. $\Phi_i(l,0)$ are the observed datapoints of $\Phi(l,0)$ and $C_i(r)$ is (from Goff and Jordan, 1988):

where is the second modified Bessel function of fractional order, and r the weighted lateral autocorrelation lag, defined as x/a_x. $G_v(0)$ is defined as

and is the gamma function.

A grid-search is used to determine the 1D von Karman function that minimizes the misfit function (Figure 13).

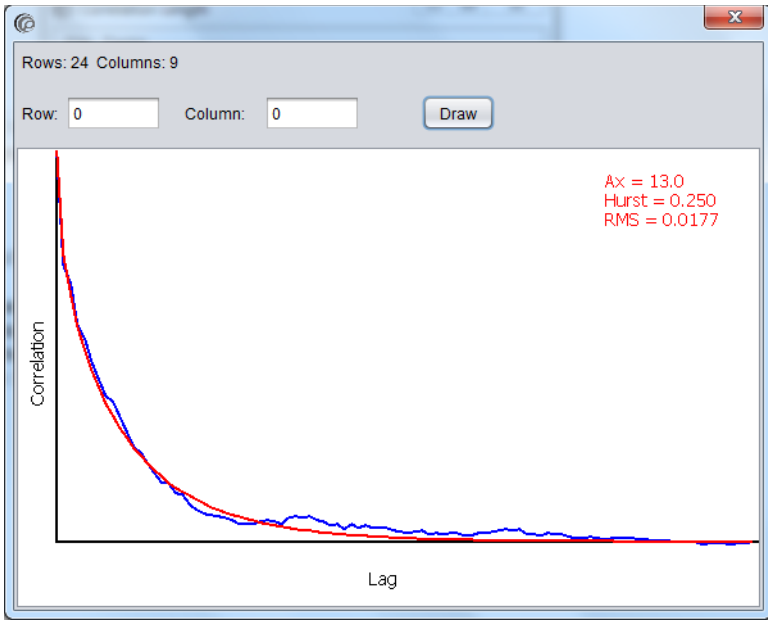

Figure 13: von Karman function estimation

Once the von Karman parameters are estimated for each lateral autocorrelation window, the parameters are assigned to the center of the window. This produces a 2D parameter array that can be used as input to a gridding routine to fill in the remainder of the 2D seismic line. The gridding is accomplished with a 2D cubic spline interpolation with no smoothing.

Figures 14 and 15 show the correlation length parameter derived from the active source depth migration shown in Figure 6. Figure 16 and 17 shows the correlation length parameter derived from the ambient noise depth migrated section shown in Figure 8.

For all plots the correlation length varies from 20 which are shown blue colors to the maximum of 170 shown in red/purple colors. Figure 15 shows how the high correlation length (red/purple colors) match the horizontal and sub-horizontal reflectors while the dipping and incoherent reflectors have a low correlation length (blue). It is interesting to note some deeper horizontal reflectors shown in the yellow.

Even though the depth migrated image from the ambient noise data (Figure 8) was not as clean as from the active source data, the correlation lengths derived from it look remarkably similar to the section from the active source data (compare Figure 14 and 16).

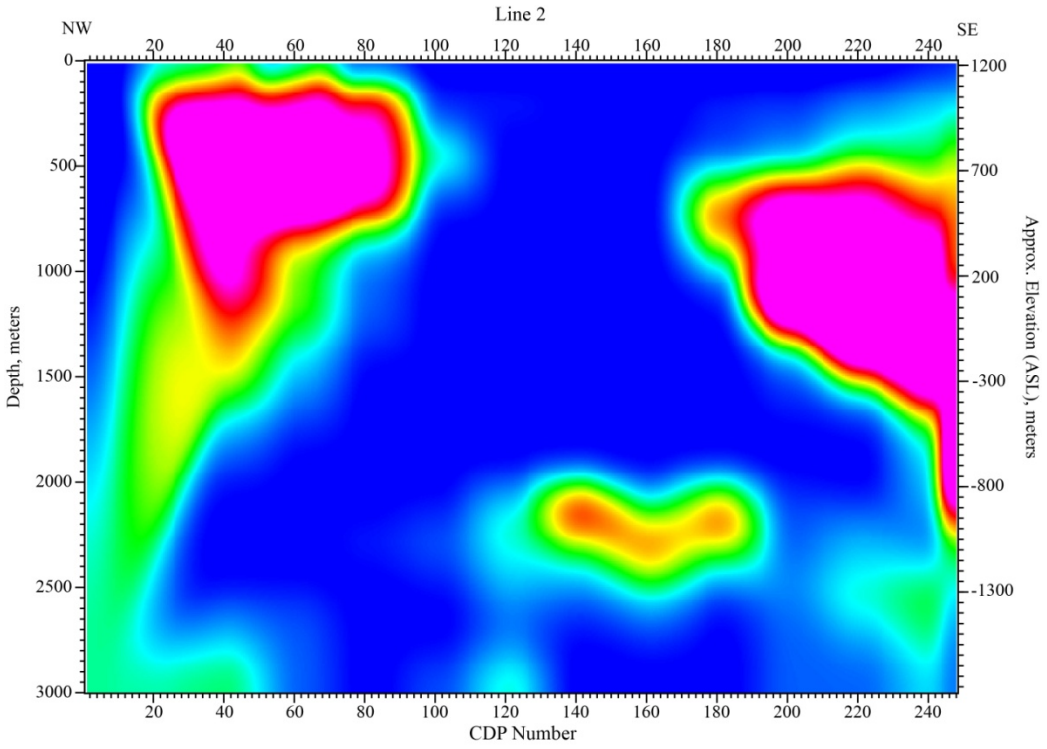

Figure 14: Estimation of correlation length stochastic parameter from the active source depth migrated image shown in Figure 6.

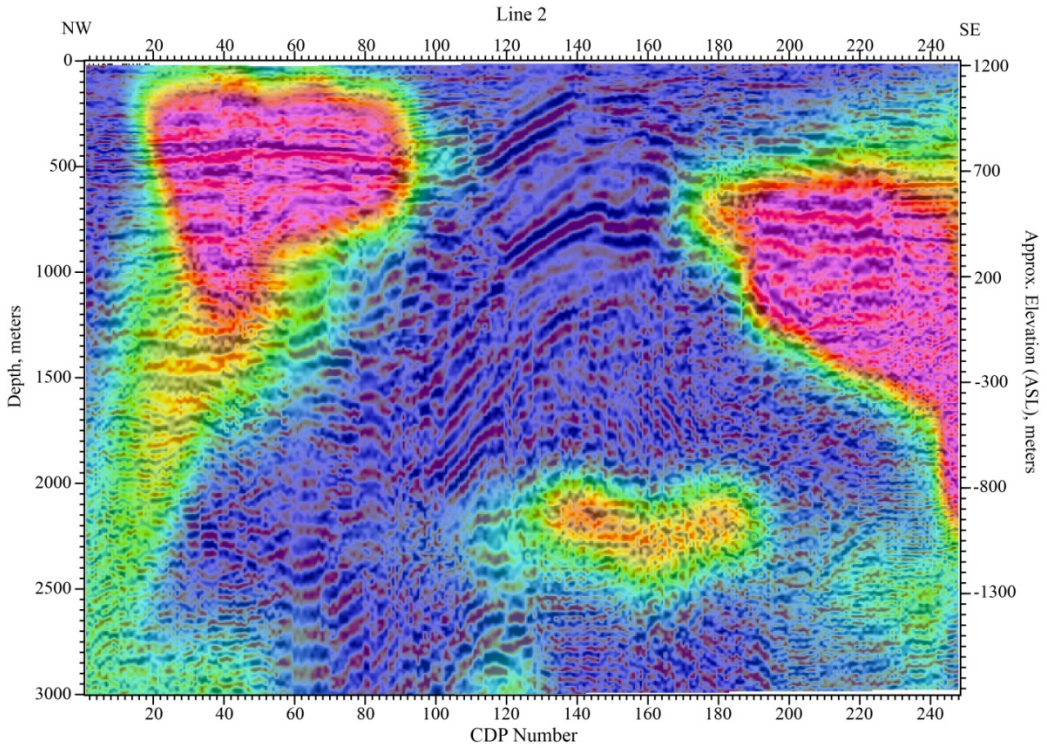

Figure 15: Correlation length estimate overlain on the depth migration. Note how the high correlation length values (red/purple) match the horizontal reflectors whilst the blue, low correlation values overlay the dipping and incoherent reflectors.

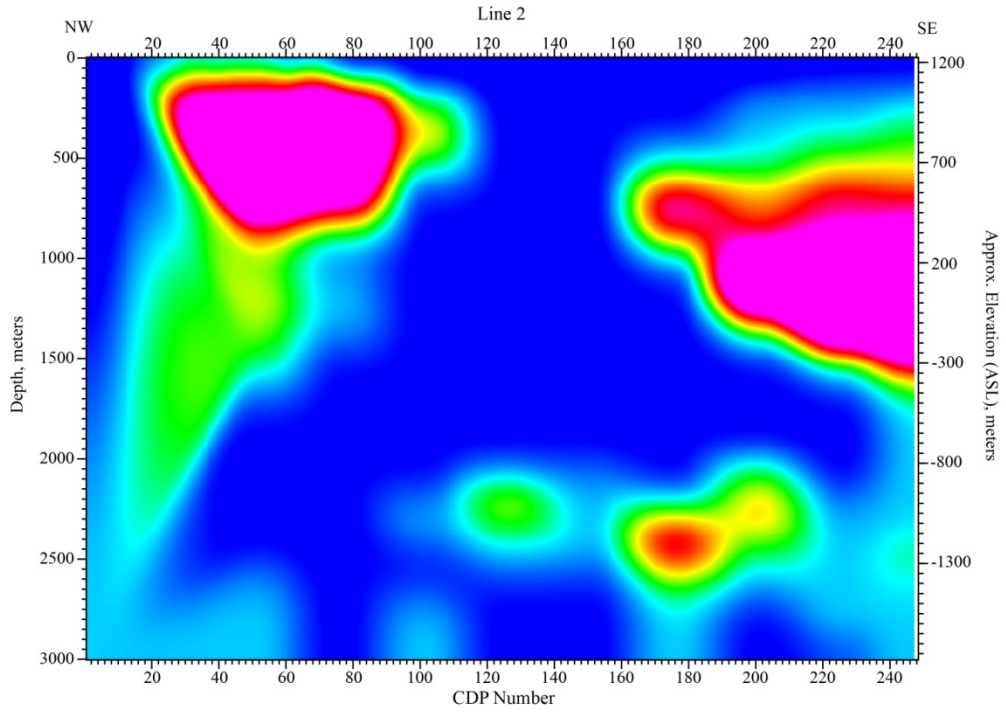

Figure 16: Estimation of correlation length stochastic parameter from the ambient noise depth migrated image shown in Figure 8.

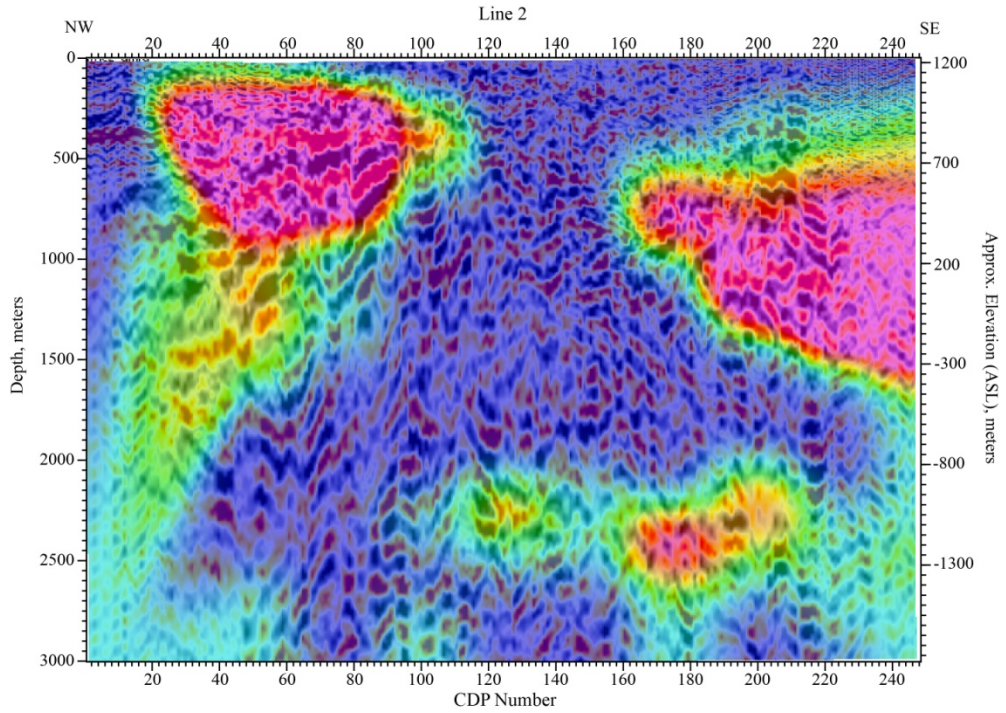

Figure 17: Correlation length estimate overlain on the depth migration. Note how the high correlation length values (red/purple) match the horizontal reflectors whilst the blue, low correlation values overlay the dipping and incoherent reflectors.

The other stochastic parameter we estimated was the Hurst number. The Hurst number is related to the fractal dimension of the media. Lower the Hurst number higher the fractal dimension. The objective was to map its variations to see how they correlate with the anomalous zones.

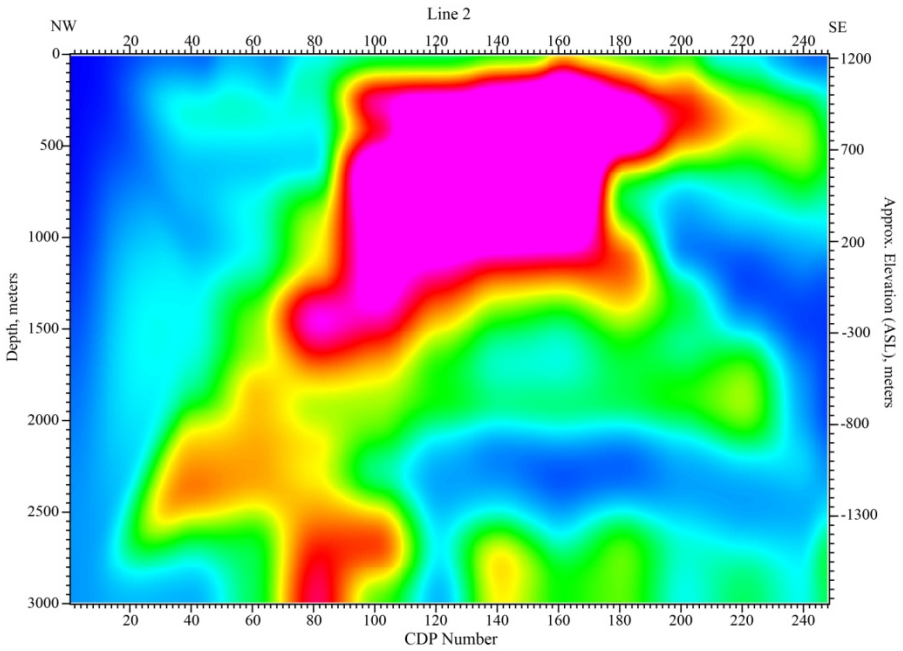

Figure 18: Hurst number variations determined from the active source depth migrated data shown in Figure 6. The values vary from 0 (blue) to 1 (red).

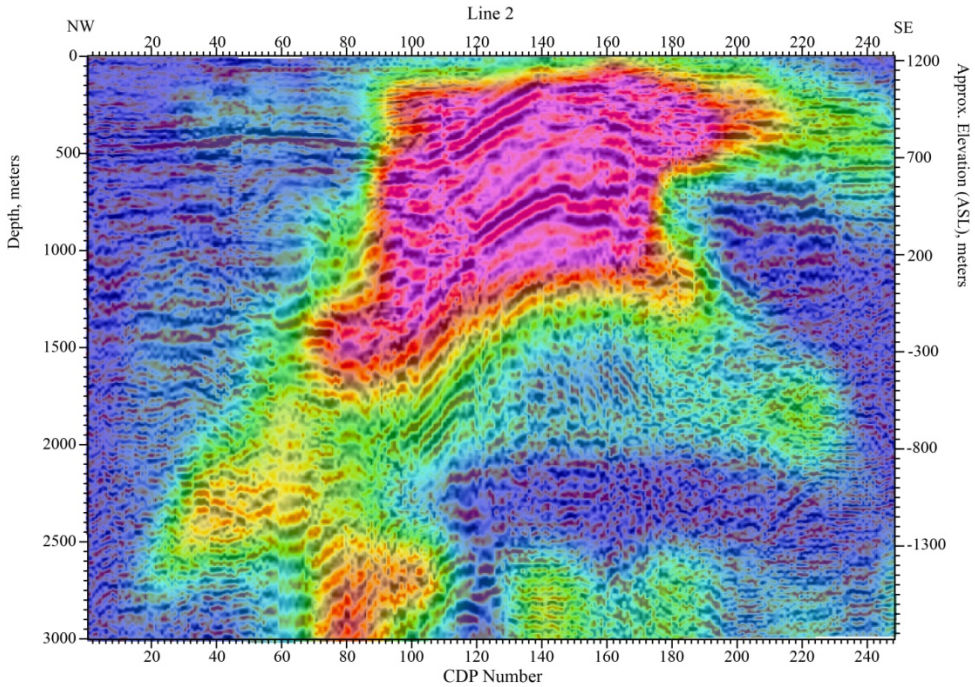

Figure 19: Hurst number variations overlain on the active source depth migrated image. The high Hurst number matches very well the strongly dipping reflectors.

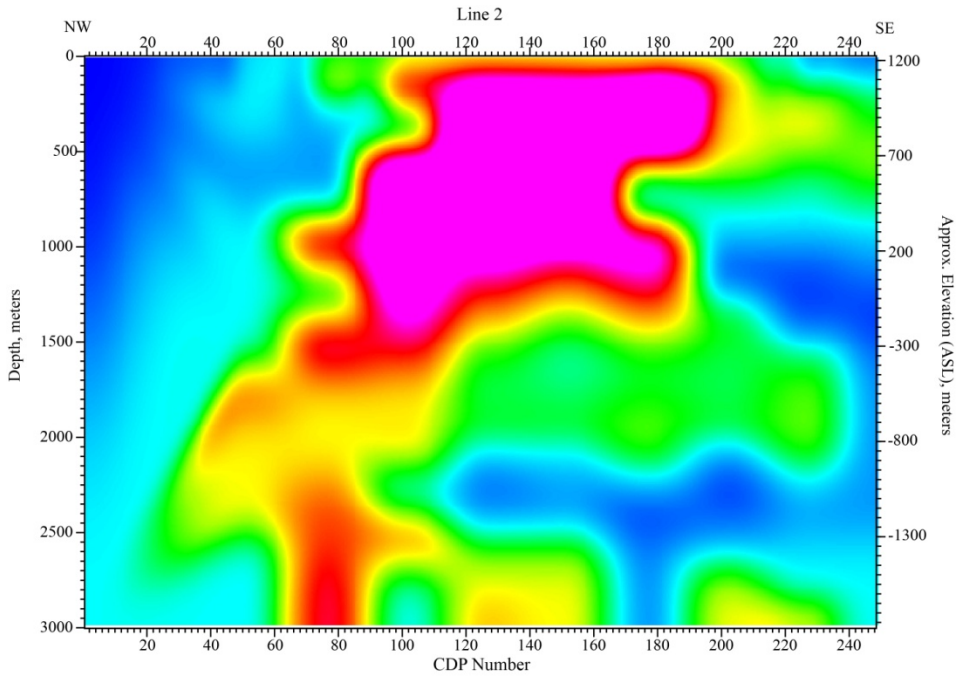

Figure 20: Hurst number variations determined from the ambient source depth migrated data shown in Figure 6. The values vary from 0 (blue) to 1 (red).

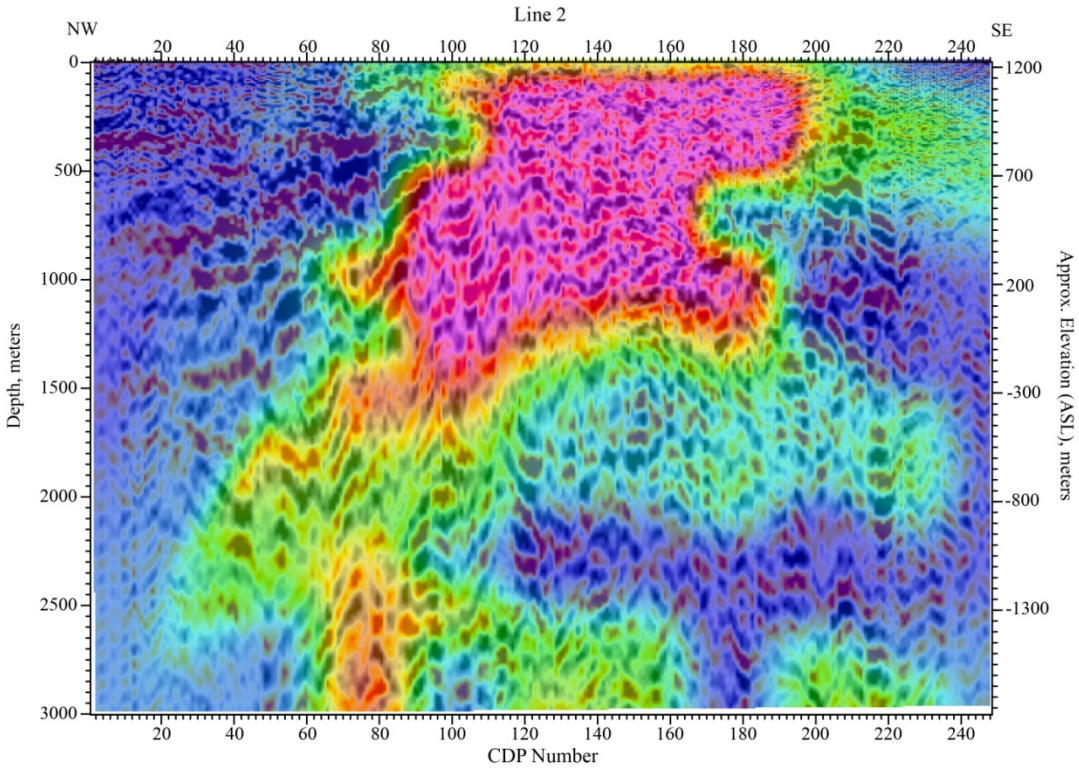

Figure 21: Hurst number variations overlain on the ambient noise depth migrated image. The high Hurst numbers match very well the strongly dipping reflectors.

Like the correlation length estimation, the Hurst number estimates from the active source and ambient noise migrated data compare remarkably well. The high Hurst numbers highlight the strongly dipping reflectors. They reveal a NW dipping fabric that seem to extends in depth. It highlights the area where the subhorizontal reflectors truncate against this “dome” shaped structures.

4.0 ESTIMATING Q

For this task we endeavor to make some calculations on the attenuation properties. Once again the analysis is performed on the depth migrated sections obtained from both the ambient noise and active source data.

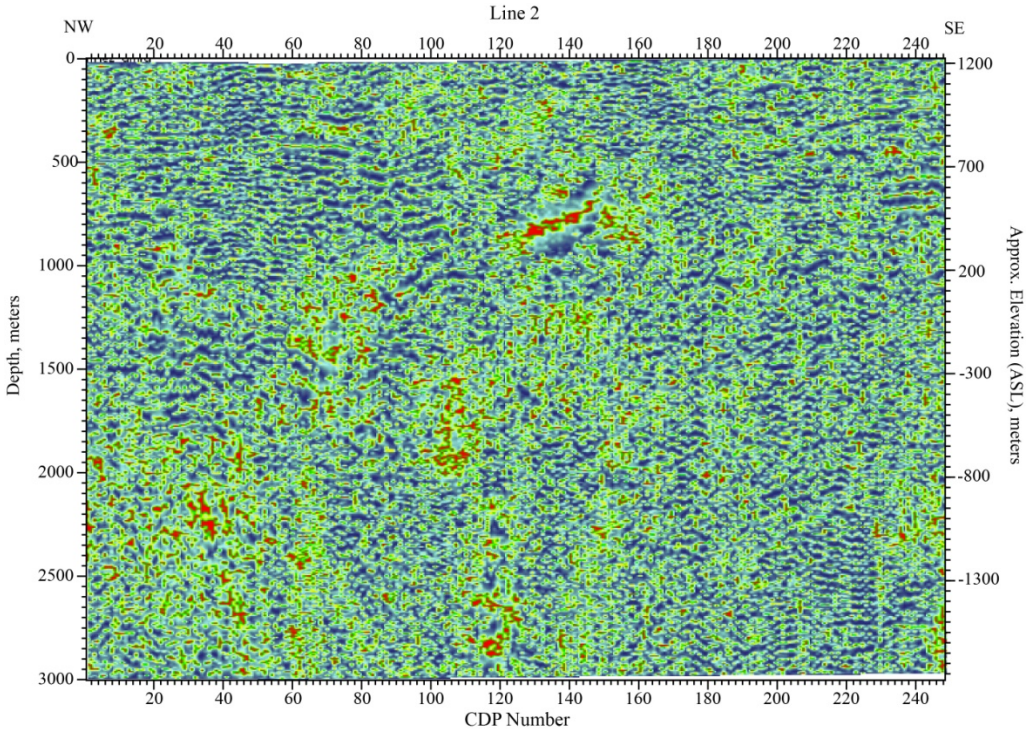

Figure 22: Q estimated from instantaneous frequency analysis of the active source depth migrated section. The red colors represent higher attenuation. No patterns can be discerned except for the a high attenuation observed at CDP 140 and depth of about 500m. It is along one of the strong dipping reflectors.

The attenuation parameter we estimate is the instantaneous Q. To obtain this we first calculate the instantaneous frequency at the sample location. The instantaneous frequency attribute responds to both wave propagation effects and depositional characteristics, hence it is a physical attribute and can be used as an effective discriminator.

$$f(t) = \frac{1}{2\pi}\phi'(t)$$

The Q factor is then the instantaneous frequency divided by the bandwidth:

$$q(t)= 0.5(-\pi.freq(t)/decay(t))$$

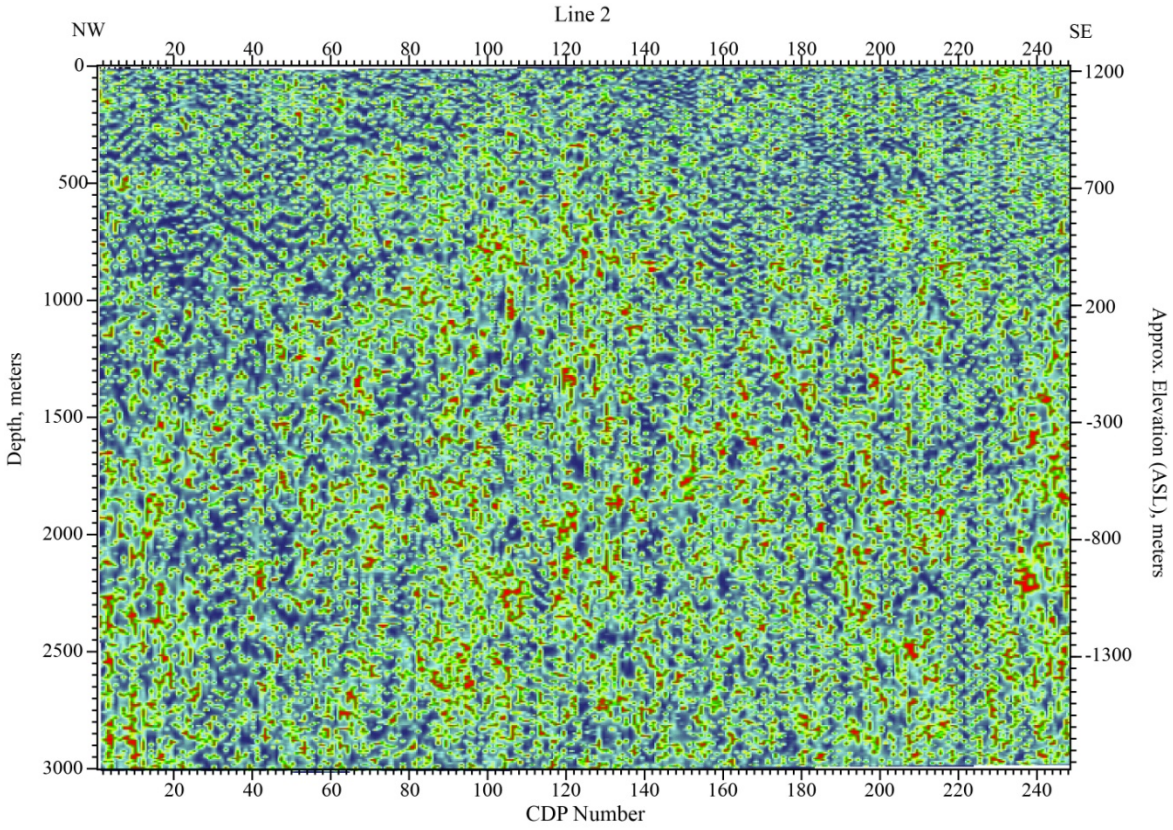

Figure 23: Q estimated from instantaneous frequency analysis of the ambient noise depth migrated section. The red colors represent higher attenuation. No patterns can be discerned from this image.

5.0 REFERENCES

Carpentier, S.F.A., K. Roy-Chowdhury, C. A. Hurich, Mapping correlation lengths of lower crustal heterogeneities together with their Bayesian uncertainty estimates, 2010, ftp://ftp.geo.uu.nl/pub/people/kabir/DSS-08/DSS_LITHO.pdf

Goff, J.A. and T.H. Jordan (1988), Stochastic modeling of seafloor-morphology: Inversion of seabeam data for second order statistics. J. Geophys. Res., 93(6):13,589–13,608.

Hurich, C. (2003). *Heterogeneity in the crust and upper mantle: nature, scaling, and seismic properties*, chapter The Nature of Crustal Seismic Heterogeneity: A Case Study From the Grenville Province, pages 299.320. Kluwer Academic Publishers, New York, U.S.A.

Louie, J.N., and Qin, J., 1991, Subsurface imaging of the Garlock fault, Cantil Valley, California: Journal of Geophysical Research, B., Solid Earth and Planets, v. 96, p. 14,461-14,479.

Pullammanappallil, S.K., and Louie, J.N., 1993, Inversion of Seismic reflection traveltimes using a nonlinear optimization scheme: Geophysics, v. 58, No. 11, p. 1607-1620.

Pullammanappallil, S.K., and Louie, J.N., 1994, A generalized simulated-annealing optimization for inversion of first arrival times: Bulletin of the Seismological Society of America, v. 84, p. 1397-1409. 61pp.

Pullammanappallil, S.K., Honjas, W., Unruh, J. R., and Monastero, F. C., 2001, Use of advanced data processing techniques in the imaging of the Coso geothermal field: Proceedings, 26th Workshop on Geothermal Reservoir Engineering, Stanford, California.

Tibuleac, I., and M. Eneva, 2011, Seismic Signature of the Geothermal Field at Soda Lake, Nevada, from Ambient Noise Analysis, *GRC Transactions*, **35**, 1767-1772.

Tibuleac, I., Pullammanappallil, S., Faulds, J., and McLachlan, H., 2013, Development of a low cost method to estimate the seismic signature of a geothermal field from ambient seismic noise analysis, GRC Transactions.

Unruh, J.R., Monastero, F.C. and Pullammanappallil, S.K., 2008, The Nascent Coso Metamorphic Core Complex, East-Central California: Brittle Upper Plate Structure Revealed by Reflection Seismic Data - International Geology Review, 50, 1–25